CONTENTS

Page

INTENTIONALLY LEFT BLANK

TABLES

Page

INTENTIONALLY LEFT BLANK

FIGURES

Page

FIGURES (Continued)

Page

FIGURES (Continued)

FIGURES (Continued)

Page

2.3.5 In-Drift Physical and Chemical Environment

[NUREG-1804, Section 2.2.1.3.3.3: AC 1(1) to (10), (12), AC 2(1) to (4), AC 3(1) to (4), (6), AC 4, AC 5]

The information presented in this section (2.3.5) addresses the requirements of proposed 10 CFR 63.114(a)(1) through (a)(7) and (b) for conducting a performance assessment in the area of the in-drift physical and chemical environment. This section also provides information that addresses specific acceptance criteria in Section 2.2.1.3.3.3 of NUREG-1804.

Sections 2.3.3, 2.3.4, 2.3.5, 2.3.7, and 2.3.11 collectively provide information that addresses the requirements of proposed 10 CFR 63.114(a)(1) through (a)(7) and (b), as well as specific acceptance criteria in Section 2.2.1.3.3 of NUREG-1804 in the area of water movement into and through the emplacement drift. Sections 2.3.3, 2.3.4, 2.3.5, and 2.3.7 present information regarding the quantity of water movement through the repository.

The purpose of Section 2.3.5 is to describe the in-drift environment, including key aspects of the quantity and quality of water in the environment, for intact and collapsed drifts. The quantity of water seeping into the emplacement drift is discussed in Section 2.3.3, for the time period that the near-field conditions are affected by thermal processes as well as for the long-term ambient conditions. Movement of water into the rubble formed by emplacement drift collapse in the event of a low-probability seismic event, is discussed primarily in Section 2.3.3, with some related discussion in Section 2.3.4. The temperature and relative humidity conditions associated with that collapse are described in Section 2.3.4. Section 2.3.5 describes the quantity of water within the emplacement drift that condenses on the drift wall. Section 2.3.7 discusses water movement within the emplacement drift, including the quantity of water contacting engineered barrier features and waste forms. The impact of an igneous intrusion on the drift seepage abstraction is provided in Section 2.3.3.

The quality or chemistry of water contacting engineered barrier features and waste forms is discussed in the three sections: Sections 2.3.5, 2.3.7, and 2.3.11. With regard to the nominal and seismic scenario classes, this section (2.3.5) discusses the chemistry of the water contacting the following engineered barrier features: drip shield, waste package surface, and invert. For conditions of liquid flow from breached waste packages into the invert, the chemistry of water along the invert transport pathway is represented by in-package chemistry as discussed in Section 2.3.7. Section 2.3.7 also covers the chemistry of water inside the waste package and contacting the waste form. Seepage water chemistry for the igneous event scenario class is discussed in Section 2.3.11.

This section (2.3.5) also describes the temperature and relative humidity histories for intact and collapsed drifts and briefly describes the approach to coupled processes in the near-field and in-drift environments.

The models and abstractions in this section (2.3.5) describe aspects of the total system performance assessment (TSPA) that can potentially affect dose, with the exception of coupled processes described in Section 2.3.5.2, which are not included in TSPA but are addressed in response to specific acceptance criteria.

With regard to the in-drift physical and chemical environment, this section presents:

- Data from the site and surrounding region, uncertainties and variabilities in parameter values, and alternative conceptual models used in the analyses
- Specific features, events, and processes (FEPs) included in the analyses with technical bases for inclusion
- Specific chemical and physical processes taking into consideration their effects on annual dose and the technical bases for inclusion of the processes
- Technical bases for models used in the performance assessment.

The information provided in this section, the corresponding requirement of proposed 10 CFR 63.114, and the acceptance criteria of NUREG-1804, Section 2.2.1.3.3.3, are presented below. With regard to Acceptance Criterion 1(12), no formal peer reviews were used to support development of the current models discussed in this section (Section 2.3.5). Also, this section does not discuss the approach used for data qualification. However, scientific analyses, model development, and data qualification activities were conducted in accordance with project procedures that comply with Quality Assurance Program requirements. The project procedures governing data qualification are consistent with NUREG-1298 (Altman et al. 1988) in keeping with Acceptance Criterion 1(12). With regard to Acceptance Criterion 3(6), no expert elicitations were directly used to develop the technical basis for the information presented in this section. With regard to Acceptance Criterion 4(5), the equivalent continuum modeling approach (Pruess et al. 1990) is not used in the models described in Section 2.3.5. Three acceptance criteria from NUREG-1804, Section 2.2.1.3.3.3, are not referenced below for the following reasons. Acceptance Criterion 1(11) and Acceptance Criterion 3(5) pertain to criticality, which is excluded from the TSPA (Section 2.2.1.4.1). Acceptance Criterion 2(5) pertains to microbial activity, which is addressed in Sections 2.2.1 (Table 2.2-5) and 2.3.6.3.3.2.

SAR Section	Information Category	Proposed 10 CFR Part 63 Reference	NUREG-1804 Reference
2.3.5	In-Drift Physical and Chemical Environment	63.114(a)(1) 63.114(a)(2) 63.114(a)(3) 63.114(a)(4) 63.114(a)(5) 63.114(a)(6) 63.114(a)(7) 63.114(b) 63.342(a) 63.342(c)	Section 2.2.1.3.3.3: Acceptance Criterion 1(1) Acceptance Criterion 1(2) Acceptance Criterion 1(3) Acceptance Criterion 1(4) Acceptance Criterion 1(5) Acceptance Criterion 1(6) Acceptance Criterion 1(7) Acceptance Criterion 1(8) Acceptance Criterion 1(9) Acceptance Criterion 1(10) Acceptance Criterion 1(12) Acceptance Criterion 2(1) Acceptance Criterion 2(2) Acceptance Criterion 2(3) Acceptance Criterion 2(4) Acceptance Criterion 3(1) Acceptance Criterion 3(2) Acceptance Criterion 3(3) Acceptance Criterion 3(4) Acceptance Criterion 3(6) Acceptance Criterion 4 Acceptance Criterion 5
2.3.5.1	Summary and Overview	Not applicable	Not applicable
2.3.5.2	Approach to Coupled Processes	63.114(a)(1) 63.114(a)(2) 63.114(a)(3) 63.114(a)(4) 63.114(a)(5) 63.114(a)(6) 63.114(a)(7) 63.342(a)	Section 2.2.1.3.3.3: Acceptance Criterion 1(1) Acceptance Criterion 1(2) Acceptance Criterion 1(4) Acceptance Criterion 1(5) Acceptance Criterion 1(6) Acceptance Criterion 1(8) Acceptance Criterion 2(4) Acceptance Criterion 4(4) Acceptance Criterion 5(3)

SAR Section	Information Category	Proposed 10 CFR Part 63 Reference	NUREG-1804 Reference
2.3.5.3	Near-Field Chemistry Model	63.114(a)(1) 63.114(a)(2) 63.114(a)(3) 63.114(a)(4) 63.114(a)(5) 63.114(a)(6) 63.114(a)(7) 63.114(b) 63.342(c)	Section 2.2.1.3.3.3: Acceptance Criterion 1(1) Acceptance Criterion 1(2) Acceptance Criterion 1(3) Acceptance Criterion 1(4) Acceptance Criterion 1(5) Acceptance Criterion 1(7) Acceptance Criterion 1(8) Acceptance Criterion 1(9) Acceptance Criterion 1(10) Acceptance Criterion 2(1) Acceptance Criterion 2(2) Acceptance Criterion 3(1) Acceptance Criterion 3(2) Acceptance Criterion 3(3) Acceptance Criterion 3(4) Acceptance Criterion 4(1) Acceptance Criterion 4(2) Acceptance Criterion 4(3) Acceptance Criterion 4(4) Acceptance Criterion 5(3)
2.3.5.4	In-Drift Thermal-Hydrologic Environment	63.114(a)(1) 63.114(a)(2) 63.114(a)(3) 63.114(a)(4) 63.114(a)(5) 63.114(a)(6) 63.114(a)(7) 63.114(b) 63.342(c)	Section 2.2.1.3.3.3: Acceptance Criterion 1(1) Acceptance Criterion 1(2) Acceptance Criterion 1(3) Acceptance Criterion 1(4) Acceptance Criterion 1(5) Acceptance Criterion 1(6) Acceptance Criterion 1(7) Acceptance Criterion 1(8) Acceptance Criterion 1(9) Acceptance Criterion 1(10) Acceptance Criterion 2(1) Acceptance Criterion 2(2) Acceptance Criterion 2(3) Acceptance Criterion 2(4) Acceptance Criterion 3(1) Acceptance Criterion 3(2) Acceptance Criterion 3(3) Acceptance Criterion 3(4) Acceptance Criterion 4(1) Acceptance Criterion 4(2) Acceptance Criterion 4(3) Acceptance Criterion 4(4) Acceptance Criterion 5(1) Acceptance Criterion 5(3)

SAR Section	Information Category	Proposed 10 CFR Part 63 Reference	NUREG-1804 Reference
2.3.5.5	In-Drift Chemical Environment Models	63.114(a)(1) 63.114(a)(2) 63.114(a)(3) 63.114(a)(4) 63.114(a)(5) 63.114(a)(6) 63.114(a)(7) 63.114(b) 63.342(c)	Section 2.2.1.3.3.3: Acceptance Criterion 1(1) Acceptance Criterion 1(2) Acceptance Criterion 1(3) Acceptance Criterion 1(4) Acceptance Criterion 1(5) Acceptance Criterion 1(6) Acceptance Criterion 1(7) Acceptance Criterion 1(8) Acceptance Criterion 1(10) Acceptance Criterion 2(1) Acceptance Criterion 2(2) Acceptance Criterion 2(4) Acceptance Criterion 3(1) Acceptance Criterion 3(2) Acceptance Criterion 3(3) Acceptance Criterion 3(4) Acceptance Criterion 4(1) Acceptance Criterion 4(2) Acceptance Criterion 4(3) Acceptance Criterion 4(4) Acceptance Criterion 5
2.3.5.6	Conclusions	Not applicable	Not applicable

In some instances, the acceptance criteria in the table above are addressed in multiple sections of the SAR. Acceptance criteria in NUREG-1804 Section 2.2.1.3.3.3 are addressed by one or more of Sections 2.2, 2.3.3 to 2.3.7, 2.3.11, and 2.4, as described below.

Acceptance Criterion 1:

- **Acceptance Criteria 1(1) and 1(2)**—The portions of these acceptance criteria pertaining to the quantity of water contacting the Engineered Barrier System (EBS) are addressed in Sections 2.3.3, 2.3.5, and 2.3.7. The portions of these acceptance criteria pertaining to the chemistry of water contacting the EBS are addressed in Sections 2.3.5, 2.3.7, and 2.3.11. Consistency and integration of abstractions supporting the TSPA is discussed in Section 2.4.

- **Acceptance Criterion 1(3)**—The portion of this acceptance criterion related to the quantity of water contacting the EBS is addressed by Sections 2.3.3, 2.3.5, and 2.3.7. The portion related to the degradation or corrosion of the waste packages and how these phenomena affect TSPA abstractions is addressed in Sections 2.3.4, 2.3.6, and 2.3.7. The portion addressing the chemistry of the water is addressed in Sections 2.3.5, 2.3.7, and 2.3.11.

- **Acceptance Criterion 1(4)**—The portion of this acceptance criterion related to thermal-hydrologic effects is addressed in Sections 2.3.3 and 2.3.5. Thermal-mechanical effects are addressed in Section 2.3.4. The effects of thermal-hydrologic-chemical and

thermal-hydrologic-mechanical processes on the volume of seepage are excluded from TSPA (Section 2.2.1) based on modeling described in Section 2.3.5.2. The thermal-hydrologic-chemical effects on the chemistry of seepage are addressed in Section 2.3.5. Thermal-chemical effects on the waste forms are addressed in Section 2.3.7. The effects of physical couplings for the igneous scenario are discussed in Section 2.3.11.

- **Acceptance Criterion 1(5)**—The portion of this acceptance criterion pertaining to the technical bases for TSPA assumptions and approximations for modeling coupled thermal-hydrologic-mechanical-chemical effects on seepage and flow is addressed in Sections 2.3.3, 2.3.5, and 2.3.7. The portion of the acceptance criterion pertaining to the waste package chemical environment and the chemical environment for radionuclide release is discussed in Sections 2.3.5, 2.3.7, and 2.3.11. Consistency relative to implementation of abstractions in TSPA is addressed in Section 2.4.

- **Acceptance Criterion 1(6)**—The portion of this acceptance criterion pertaining to expected ranges of environmental conditions within the emplacement drifts is addressed in Section 2.3.5; conditions that promote corrosion of the engineered barrier features are addressed in Sections 2.3.5, 2.3.6, and 2.3.7. Section 2.3.11 discusses the expected environmental conditions for the igneous scenario.

- **Acceptance Criterion 1(7)**—The portion of this acceptance criterion addressing the quantity and chemistry of water contacting the EBS and waste forms is addressed in Sections 2.3.3, 2.3.5, 2.3.7, and 2.3.11. Consistency with EBS design and other engineered features is addressed within these sections as well as Section 2.4, which discusses consistency and integration of abstractions supporting the TSPA.

- **Acceptance Criterion 1(8)**—The technical bases for inclusion of applicable thermal-hydrologic-mechanical-chemical couplings and FEPs are addressed in Sections 2.3.3, 2.3.5, 2.3.7, and 2.3.11.

- **Acceptance Criterion 1(9)**—The inclusion of performance-affecting processes observed in thermal-hydrologic tests is addressed in Sections 2.3.3, 2.3.5, and 2.3.7. For example, liquid reflux is discussed in Sections 2.3.3 and 2.3.5.

- **Acceptance Criterion 1(10)**—Modes of corrosion are addressed in Section 2.3.6, and their effect on the quantity and chemistry of water entering the EBS and contacting waste forms is addressed in Sections 2.3.5 and 2.3.7.

- **Acceptance Criterion 1(11)**—The technical basis for screening criticality events is addressed in Section 2.2.1.

- **Acceptance Criterion 1(12)**—With regard to the quantity and chemistry of water contacting the engineered barriers and waste forms, no formal peer reviews were used to support this aspect of the development of models discussed in Sections 2.3.3, 2.3.5, 2.3.7, and 2.3.11. While the approach to data qualification is not discussed directly, the data qualification activities were conducted in accordance with project procedures that comply

with Quality Assurance Program requirements. The project procedures governing data qualification are consistent with NUREG-1298 (Altman et al. 1988).

Acceptance Criterion 2:

- **Acceptance Criterion 2(1)**—Justification for geologic, hydrologic, and geochemical values used to represent the quantity and chemistry of water contacting the EBS and waste forms is provided in Sections 2.3.3, 2.3.5, 2.3.7, and 2.3.11.

- **Acceptance Criterion 2(2)**—The portion of this acceptance criterion pertaining to thermal-hydrologic-mechanical-chemical coupled processes that affect seepage and flow is addressed in Sections 2.3.3, 2.3.5, and 2.3.7. Portions pertaining to the EBS chemical environment are addressed in Sections 2.3.5, 2.3.7, and 2.3.11.

- **Acceptance Criterion 2(3)**—Thermal-hydrologic tests are addressed in Sections 2.3.3 and 2.3.5.

- **Acceptance Criterion 2(4)**—The approach to analyzing water contact with the EBS features is addressed in Sections 2.3.5, 2.3.7, and 2.3.11.

- **Acceptance Criterion 2(5)**—Microbial effects on waste package corrosion are addressed in Section 2.3.6. Other microbial effects are excluded (Section 2.2.1).

Acceptance Criterion 3:

- **Acceptance Criterion 3(1)**—This criterion pertains to using defensible model inputs that reasonably account for uncertainties and variabilities and do not cause risk to be under-represented. The portion of this acceptance criterion pertaining to water quantity is addressed in Sections 2.3.3, 2.3.5, and 2.3.7. The portion of this acceptance criterion pertaining to chemistry is addressed in Sections 2.3.5, 2.3.7, and 2.3.11.

- **Acceptance Criterion 3(2)**—The portion of this acceptance criterion pertaining to the technical basis for parameter values and assumptions used in TSPA calculations of the quantity and chemistry of water contacting the EBS and waste forms is addressed in Sections 2.3.3, 2.3.5, 2.3.7, and 2.3.11.

- **Acceptance Criteria 3(3) and 3(4)**—Portions of these acceptance criteria pertaining to seepage and thermal-hydrologic effects are addressed in Sections 2.3.3 and 2.3.5. Portions related to the chemistry of water contacting features of the EBS are addressed in Section 2.3.5 and 2.3.11. Thermal-mechanical effects are addressed in Section 2.3.4. Effects of thermal-hydrologic-chemical and thermal-hydrologic-mechanical processes on the volume of seepage are excluded from TSPA, based on modeling described in Section 2.3.5.2. Portions of the acceptance criteria related to flow through the EBS and the chemical environment for radionuclide release are addressed in Sections 2.3.7 and 2.3.11.

- **Acceptance Criterion 3(5)**—Section 2.2.1 addresses criticality, which is excluded from the TSPA.

- **Acceptance Criterion 3(6)**—With regard to the quantity and chemistry of water contacting the engineered barriers and waste forms, no expert elicitations were directly used to support this aspect of the development of models discussed in Sections 2.3.3, 2.3.5, 2.3.7, and 2.3.11.

Acceptance Criterion 4:

- **Acceptance Criteria 4(1), 4(2), and 4(3)**—These acceptance criteria pertain to alternative conceptual models and conceptual model uncertainty. Sections 2.3.3, 2.3.5, and 2.3.7 address water quantity, and Sections 2.3.5, 2.3.7, and 2.3.11 address water chemistry.

- **Acceptance Criterion 4(4)**—The effects of thermal-hydrologic-mechanical-chemical coupled processes were addressed in the assessment of alternative conceptual models. Sections 2.3.3, 2.3.4, 2.3.5, 2.3.7, and 2.3.11 describe the alternative conceptual models and provide rationale for selection of the preferred models for implementation in the TSPA.

- **Acceptance Criterion 4(5)**—The equivalent continuum modeling approach (Pruess et al. 1990) was not used for the models described in Sections 2.3.3, 2.3.5, and 2.3.7. The models in Sections 2.3.3 and 2.3.7 used a single- or dual-continuum approach. The models in Section 2.3.5 used a dual-continuum approach.

Acceptance Criterion 5:

- **Acceptance Criterion 5(1)**—This acceptance criterion pertains to consistency between abstraction models implemented by TSPA, process models, and/or to empirical observations. Sections 2.3.3, 2.3.5, and 2.3.7 address water quantity, and Sections 2.3.5, 2.3.7, and 2.3.11 address water chemistry.

- **Acceptance Criterion 5(2)**—The portion of this acceptance criterion pertaining to coupled process effects on abstractions for seepage and flow is addressed in Sections 2.3.3, 2.3.5, and 2.3.7. Effects of coupled processes on abstractions related to the EBS chemical environment and the chemical environment for radionuclide release are addressed in Sections 2.3.5, 2.3.7, and 2.3.11.

- **Acceptance Criterion 5(3)**—Codes and models used to simulate coupled thermal-hydrologic-mechanical-chemical effects on seepage and flow, engineered barrier chemical environment, and the chemical environment for radionuclide release are prepared in accordance with quality assurance procedures for software development and qualification and for model validation. Discussion of models, and software used to implement the models, including references to detailed supporting information, is provided in Sections 2.3.3, 2.3.4, 2.3.5, 2.3.7, and 2.3.11 for the topics covered by this acceptance criterion.

2.3.5.1 Summary and Overview

Section 2.3.5 presents an integrated conceptual basis for modeling the in-drift physical and chemical environment and describes a broad base of supporting information. The purpose is to describe and justify the in-drift physical and chemical environment models used in TSPA, particularly the multiscale thermal-hydrologic model, the in-drift condensation model, the near-field chemistry model, and the in-drift seepage dilution/evaporation model (Figure 2.3.5-1).

The models developed in Section 2.3.5 are used to represent the physical and chemical conditions in the repository emplacement drifts, which determine the manner in which the features of the EBS work together in conjunction with the natural barriers. The EBS and the in-drift environment are depicted in Figure 2.3.5-2. As described in Section 2.1.2.2.2, the EBS features prevent or substantially reduce the release of radionuclides from the waste and prevent or substantially reduce the rate of movement of radionuclides from the repository to the accessible environment.

The chemical and physical environment that develops in the repository drifts is determined, in part, by the features and processes that comprise the unsaturated zone component of the Upper Natural Barrier (Table 2.2-5). Some of the key included processes that affect the emplacement drift environment in this way are evaluated in Section 2.3.5:

- **Heat Generation in the EBS**—Heat produced from radioactive decay affects the thermal-hydrologic-mechanical-chemical environment in the emplacement drifts. Models developed in Section 2.3.5 include thermal-hydrologic effects on the drift environment, thermal-hydrologic-chemical effects on seepage, and evaporative evolution of water in the in-drift chemical environment. These processes affect the quantity and chemistry of water that may enter the emplacement drifts and contact the drip shields, waste packages, and waste forms.

- **Geosphere Dryout Due to Waste Heat (EBS and Host Rock)**—Heat from radioactive decay of the waste causes temperatures in the emplacement drifts to be high enough to produce dryout in the geosphere around the emplacement drifts. Although this process is transient, it is significant for the period of time during which the temperatures at the drift wall exceed the boiling point of water, which at the repository elevation is approximately 96°C. Entry of water into the drift is inhibited by moisture redistribution due to boiling and transport of water vapor to cooler regions and by imbibition of percolating water into the dry matrix. Coupled processes involved in geosphere dryout are described in Section 2.3.5.2. Diversion of unsaturated flow in the host rock during the dryout period is described in Section 2.3.3.3.

- **Thermal Effects on Flow in the EBS**—Thermal effects on hydrologic processes are included in models of in-drift thermal hydrology in Section 2.3.5.4 and seepage models in Section 2.3.3. These models determine the amount and distribution of moisture (both liquid and vapor) in the drift and on waste packages. The rates of diffusion and advection predicted to occur through the EBS are determined by the thermal-hydrologic and seepage conditions in the emplacement drift.

Within the emplacement drift feature of the EBS, a number of included processes are associated with characteristics that are important to barrier capability (Table 2.1-3). These include heat generation in the EBS, discussed above. In addition, the following key processes, related to the in-drift physical and chemical environment and important to barrier capability, are evaluated in Section 2.3.5:

- **Chemistry of Water Flowing into the Drift**—The chemistry of seepage water is evaluated in the near-field chemistry model described in Section 2.3.5.3. The chemistry of the water in the emplacement drift determines the potential for localized corrosion of the waste package outer barrier and, in the event of waste package failure, can affect the chemical environment inside the waste package and control the stability of radionuclide-bearing colloids and radionuclide solubility in the invert.

- **Chemical Characteristics of Water in Drifts**—The chemical characteristics of water in the drift are affected by seepage, condensation, capillary flow from the host rock, evaporation, and other thermal-chemical processes in the drift that are functions of the thermal-hydrologic environment. Models for evaluating the evolution of the in-drift chemical environment and representing effects of these processes are presented in Section 2.3.5.5.

- **Unsaturated Flow in the EBS**—Unsaturated flow occurs in the emplacement drift due to seepage or condensation processes. The nature of this flow has been included in the abstractions for flow and transport through the EBS features. Unsaturated flow limits advective transport of radionuclides and other chemical species (for example under intact drip shields), facilitates isolation of water from the waste packages and waste forms, and is therefore important to barrier capability.

- **Thermal Effects on Chemistry and Microbial Activity in the EBS**—The in-drift temperature substantially affects the evolution of in-drift chemistry and is important to the capability of the engineered barrier. The effect of temperature on microbial activity in the drift does not significantly impact barrier capability because microbial activity will be limited by environmental factors. The potential for microbially influenced corrosion of the waste package outer barrier is included, although it does not significantly impact barrier capability.

- **Localized Corrosion on Waste Package Outer Surface Due to Deliquescence**—Deliquescence is the process in which soluble minerals, usually salts, condense liquid from water vapor and dissolve to form brines. Although deliquescence of salts on the waste package surface is expected to occur, this process has been excluded from TSPA because the effects of such deliquescence have been determined to be insignificant to performance (Table 2.2-5, FEP 2.1.09.28.0A, Localized corrosion on waste package outer surface due to deliquescence). The physiochemical characteristics of brines produced through deliquescence of minerals in deposited dusts are not expected to generate an environment favorable for the initiation of localized corrosion and propagation for Alloy 22 (UNS N06022) waste packages. In addition, at elevated temperatures (greater than 120°C), only small quantities of brine will form from the available dust, and brine volume will limit the extent of localized corrosion damage should it initiate.

The time period over which the EBS functions can be divided into stages for discussion of the corrosion environment. The first stage is dryout, which begins during preclosure as a result of forced ventilation and continues following closure during the period when host-rock temperatures are above 100°C. No seepage occurs during this stage due to vaporization (Section 2.3.3.3) and capillary diversion effects (Section 2.3.3.2). This dryout stage corresponds to the preclosure, heat-up, and initial cooldown periods discussed in the description of localized corrosion process (Section 2.3.6.4.1). The second stage is a transition stage when rock temperatures are below 100°C, waste package surface temperatures are near 100°C, and localized corrosion is possible under certain geochemical conditions. Capillary diversion remains active, and near-field rock will rewet. Seepage is possible during this stage (as a function of percolation flux, rock properties, and state of drift degradation), and if waste packages are exposed to seepage, then localized corrosion may result. This second stage corresponds to the middle cooldown stage in the discussion of localized corrosion (Section 2.3.6.4.1), where the waste package surface is above, and the drift wall temperature is below the boiling point of water. Finally, the third stage is the period when the rock temperature and the temperature of the waste package surface are well below 100°C, reducing the likelihood of localized corrosion. Capillary diversion remains effective, and relative humidity within the drift increases to approximately 70% or greater, with many waste package locations approaching 100%. This third stage corresponds to the final stage of evolution in the discussion of localized corrosion (Section 2.3.6.4.1). Additional discussion of stages of repository thermal evolution as they affect modeling of drift-wall condensation is provided in Section 2.3.5.4.2.1. Evolution of the chemical and physical environment in the drift during these stages is the subject of Section 2.3.5.

Section 2.3.5.2 discusses the approach to the evaluation of coupled processes and provides information about where incorporation of the various processes is discussed. Thermal-hydrologic and certain thermal-hydrologic-chemical responses are included in the modeling of the in-drift physical and chemical environment and in the TSPA. Thermal-hydrologic-mechanical responses, and some thermal-hydrologic-chemical responses, are also evaluated, although their effects are excluded from the TSPA (Section 2.2.1, Table 2.2-5).

Development of the near-field chemistry model is described in Section 2.3.5.3. The primary role of this model is to describe the composition of seepage, for use in simulating the in-drift chemical environment (Section 2.3.5.5). Evolution of water and gas compositions in the near-field host rock due to coupled thermal, hydrologic, and chemical processes influences the composition of potential seepage water and the associated gas-phase composition in the emplacement drifts. The near-field chemistry model does not address redissolution of salts deposited during the boiling period, but this transient effect occurs during rewetting of the near-field host rock, when liquid saturations are low and seepage does not occur. After the drift crown temperature falls below the boiling point of water, potential seepage waters are likely to be dilute. Further discussion of redissolution of precipitates is provided in Sections 2.3.5.2.3, 2.3.5.3, and 2.2.1 (Table 2.2-5, FEP 2.2.08.04.0A, Re-dissolution of precipitates directs more corrosive fluids to waste packages). The near-field chemistry model also describes the evolution of CO_2 in the drift environment and its uncertainty.

Evolution of thermal-hydrologic conditions in the drift and host rock is described in Section 2.3.5.4, including the effects of in-drift natural convection and condensation. The multiscale thermal-hydrologic model (Section 2.3.5.4.1) predicts above-boiling conditions in the host rock for up to 1,345 years. Peak waste package temperatures are predicted to be approximately 107°C to

211°C depending on waste package thermal output and location within the repository for thermal loading described in the postclosure thermal reference case. Thermally driven natural convection will cause axial and radial convection cells to develop in the emplacement drifts. Water vapor transport from hotter to cooler parts of the drifts will cause condensation to occur. Condensation is shown to be correlated with waste packages that have lower heat output, with repository edge locations, and with percolation flux in the host rock, all three of which promote lower temperatures (Section 2.3.5.4.2). Whereas the multiscale model represents the thermal performance of the repository based on a repeating unit cell of waste package types, based on a postclosure thermal reference case (SNL 2007a, Section 6.4.2[a]), Section 2.3.5.4.3 addresses the effects from a range of thermal loading estimated from further consideration of the likely repository waste stream and of waste handling operations.

Section 2.3.5.5 describes the modeling and analyses conducted to determine the chemistry of seepage after it enters the repository drifts and contacts the drip shield and, potentially, the waste packages. The chemistry of seepage water is modified by evaporation, which is determined by the temperature and relative humidity calculated by the multiscale thermal-hydrologic model (Section 2.3.5.4). Response surfaces representing the chemistry of evaporated seepage originating at the drift crown and invert are developed. Modeling of evaporative evolution of potential seepage waters shows that corrosive calcium and magnesium-chloride brines are not expected to form. As noted above, although deliquescence-induced brine formation is expected to occur, this process has been excluded from TSPA because the effects of such deliquescence have been determined to be insignificant to performance.

Role of In-Drift Chemical and Physical Environment in Total System Performance Assessment—Figure 2.3.5-3 schematically shows the information flow from the foundation of field and laboratory data, through the process and abstraction models representing the in-drift chemical and physical environment, and finally to the TSPA. The primary process model evaluating in-drift physical conditions is the multiscale thermal-hydrologic model, with the in-drift condensation model playing a secondary role. Evaluation of the in-drift chemical environment at the process model level begins with the near-field chemistry model, which characterizes the chemistry of water that can potentially enter the drift. Results from the near-field chemistry model are used in a series of seepage evaporation analyses conducted with the in-drift precipitates/salts model. Results from these analyses are abstracted in the seepage evaporation abstraction for use in the TSPA. Results from the near-field chemistry model are also used to develop the in-drift CO_2 gas abstraction for use in the TSPA.

Figure 2.3.5-1 displays the information transfer among the principal model components of the TSPA nominal scenario class model. The in-drift physical and chemical environment models described in Section 2.3.5 calculate the range of thermal, hydrologic, and chemical environments expected in the repository emplacement drifts. Figure 2.3.5-1 shows the integration of other TSPA components with these models, which are represented in the TSPA model (in the figure) as the EBS thermal-hydrologic environment, the EBS chemical environment, and the drift seepage and drift wall condensation submodels. TSPA uses some or all of the outputs from the models described in Section 2.3.5, consisting of temperatures, relative humidity values, water chemistries, and in-drift CO_2 pressures, to calculate general corrosion and the potential occurrence of localized corrosion of the waste package outer barrier, colloid stability, and radionuclide solubility. These model outputs are also used to model EBS flow and transport.

The in-drift chemical environment models described in Section 2.3.5.5 provide response surfaces for in-drift evaporated seepage water compositions including pH, ionic strength, and other compositional data for water contacting the waste package and evolving in the invert. The multiscale thermal-hydrologic model (Section 2.3.5.4.1) provides temperature and relative humidity within the drift and in the host rock along each emplacement drift in the repository. The temperature and relative humidity are used in the TSPA to determine water compositions in the drift through use of the response surfaces (lookup tables) that represent in-drift seepage water compositions. The in-drift condensation model, described in Section 2.3.5.4.2, provides TSPA with the likelihood of drift wall condensation at various waste package locations. When that likelihood is nonzero, the model provides the magnitude of condensation, which is correlated with the percolation rate. The TSPA treats condensation as another source of liquid water that can potentially contact the drip shield or waste package in EBS flow calculations (Section 2.3.7.12).

Features, Events, and Processes Evaluated in the Models Related to In-Drift Physical and Chemical Environment—The FEPs included in the models described in this section are summarized in Tables 2.3.5-1 through 2.3.5-3. Some of the FEPs included in this section are also included in models related to climate and infiltration, unsaturated zone flow, and seepage. Cross-references are provided to the sections where the FEP is included. The complete set of TSPA FEPs, both included and excluded, is discussed in Section 2.2.1 (Table 2.2-5).

Design Features and Components Evaluated in the Models Related to In-Drift Physical and Chemical Environment—Design features important to determining the initial and boundary conditions for representing the quantity and chemistry of water are included in the models described in Section 2.3.5. These features include the configuration of subsurface facilities (as described in Section 1.3.4) which is used in Sections 2.3.5.3 and 2.3.5.4, and the EBS configuration (Sections 1.3.4 and 1.5.2) and subsurface ventilation (Section 1.3.5), which are explicitly represented in the multiscale thermal-hydrologic model described in Section 2.3.5.4. The models also take into account repository closure and the installation of drip shields (Section 1.3.6). Thermal loading in these models is represented by a postclosure thermal reference case corresponding to the nominal thermal loading condition (Section 1.3.1.2.5) and also by the range of anticipated thermal loading discussed in Section 2.3.5.4.3.

2.3.5.2 Approach to Coupled Processes

[NUREG-1804, Section 2.2.1.3.3.3: AC 1(1), (2), (4), (5), (6), (8), AC 2(4), AC 4(4), AC 5(3)]

This section focuses on the effects of coupled processes on the thermal, hydrologic, mechanical, and chemical environment in the near-field host rock and the emplacement drifts. As indicated in the following subsections, some of these coupled processes are included in TSPA, and some are excluded. The excluded thermal-hydrologic-mechanical-chemical processes are covered in detail here because of the emphasis given to these in NUREG-1804, Section 2.2.1.3.3. Note that processes that affect radionuclide transport in the EBS and the host rock are addressed in Sections 2.3.7 and 2.3.8, respectively.

General Description of Coupled Processes—Processes that combine the effects of two or more different types of physical or chemical variables simultaneously to produce an observable result are defined as coupled processes. One variable may directly affect another, without back-coupling

(one-way) (Manteufel et al. 1993, Section 2), or two variables may affect each other resulting in couplings in both directions (two-way). For cases in which multiple variables are involved, one-way or two-way couplings may be important between any two variables (Manteufel et al. 1993, Sections 3 and 4).

2.3.5.2.1 Coupled Processes

[NUREG-1804, Section 2.2.1.3.3.3: AC 1(1), (2), (4), (6), (8), AC 2(4)]

Coupled processes in the host rock are described using a framework based on evaluation of the possible one-way relationships between binary combinations of thermal, hydrologic, chemical, and mechanical processes (Manteufel et al. 1993, Section 2). The following processes are included in the near-field models described in Sections 2.3.3 and 2.3.5 (additional section references are provided where appropriate): evaporation, condensation, buoyancy-driven unsaturated flow, liquid water dripping, gravity-driven heat pipes, thermal stress (Section 2.3.4), thermal effects on chemical equilibria and reaction rates, effects of flow and transport on chemical reactions and conditions, effects of flow processes on transport (Sections 2.3.7.12, 2.3.8, and 2.3.9), mineral deposition in fractures, saturation effects on rock strength (Section 2.3.4), and stress corrosion cracking of metals (Section 2.3.6). Some of the one-way couplings described above are parts of two-way couplings (e.g., evaporation and condensation are thermal effects on hydrology, and gravity-driven heat pipes are hydrologic effects on heat transfer). These coupled processes are included in process models described here, although the consequences of some of these processes are excluded from TSPA (e.g., thermal-hydrologic-mechanical processes, as described in Section 2.3.5.2.2, are excluded from TSPA).

Thermal-hydrologic processes are included in the models developed for thermal seepage (Section 2.3.3.3) and in the multiscale thermal-hydrologic model (Section 2.3.5.4.1), which describes in-drift temperature and relative humidity for TSPA. Thermal-hydrologic models include the processes of heat, two-phase multicomponent mass flow, evaporation, and condensation. Thermal-hydrologic-chemical processes affect the chemical evolution of waters in the host rock; these waters can potentially seep into the emplacement drifts and are described for TSPA by the near-field chemistry model (Section 2.3.5.3). The near-field chemistry model includes thermal-hydrologic processes plus the chemical processes of dissolution, precipitation, diffusion, and reactions involving gas-phase species. Thermal-hydrologic-mechanical processes affect the temperature and flow patterns around the drifts; modeling performed to evaluate thermal-hydrologic-mechanical processes is described in Section 2.3.5.2.2. Treatment of important coupled processes in the host rock for models that support TSPA is consistent with the conclusions of Manteufel et al. (1993, Section 2.11).

Thermally driven coupled processes at Yucca Mountain can also be categorized based on duration of the effects. Reversible processes (e.g., drying and long-term rewetting) recover to preemplacement conditions after decay of the thermal pulse. These processes are modeled using knowledge of site characteristics, with boundary conditions (e.g., climate and associated net infiltration) modified to represent future conditions. Irreversible changes to flow and transport pathways, involving chemical dissolution and precipitation, remain in effect after the thermal pulse. Irreversible changes in flow characteristics of the near-field host rock are predicted to occur, but the effects on the quantity of water contacting the engineered barrier features are not included in TSPA because they are bounded by the seepage abstraction used in TSPA (Sections 2.3.3 and 2.3.5.2.3).

Section 2.2.1 addresses the inclusion or exclusion from the TSPA of FEPs, some of which involve coupled processes. In addition to the coupled processes discussed above, other coupled processes have been evaluated and are not included in the TSPA, including chemical interactions with ground support materials (Table 2.2-5, FEP 2.1.06.01.0A, Chemical effects of rock reinforcement and cementitious materials in the EBS), microbial activity (Table 2.2-5, FEP 2.1.10.01.0A, Microbial activity in EBS; and Section 2.3.6), radiolysis (Table 2.2-5, FEP 2.1.13.01.0A, Radiolysis), and redissolution of soluble salts (Table 2.2-5, FEB 2.2.08.04.0A, Re-dissolution of precipitates directs more corrosive fluids to waste packages; and Section 2.3.5.2.3). Coupled processes that are included in the TSPA include salt precipitation with direct transport (Section 2.3.5.5.4.2), colloidal stability and transport (Section 2.3.7), and rock mass degradation (Section 2.3.4). The description of the corrosion environment addresses the chemical changes associated with the temperature and humidity conditions at the surfaces of the drip shield and waste package, including reaction with gas-phase CO_2 and the precipitation and possible deliquescence of soluble salts (Sections 2.3.5.5 and 2.2.1).

Onsager Coupled Processes—Another conceptual framework for considering coupled processes is in terms of Onsager coupled processes, which are represented by a matrix of first-order relationships (Table 2.3.5-4). These fundamental coupled processes can occur even if the associated physical or chemical properties of the medium are temporally or spatially invariant. As reflected in Table 2.3.5-4, Onsager processes are driven by gradients of thermodynamic state variables such as temperature, pressure, chemical potential, and electrical potential. For each coupled process, a linear coefficient relates the gradient of the thermodynamic state variable to the flux.

Onsager processes can be categorized as direct processes (i.e., main diagonal of Table 2.3.5-4) or indirect processes (i.e., off-diagonal of Table 2.3.5-4). The effects of direct processes such as Darcy flow and Fickian diffusion are expected to dominate and overwhelm the effects of indirect processes, which are small because the magnitudes of the associated potential gradients or fluxes in the host rock are small or because the linear coefficient for the effect is small. In fact, the existence of indirect processes is generally known from controlled experiments, rather than from observations in nature. Some of the indirect processes listed in Table 2.3.5-4, such as chemical osmosis (observed in clays or zeolites) may be observable in response to heating the host rock at Yucca Mountain, but the effects of these processes are not significant to repository performance (Table 2.2-5). Direct processes are included in the models that support the TSPA (SNL 2007b, Section 6.4).

2.3.5.2.2 Thermal-Hydrologic-Mechanical Coupled Processes

[NUREG-1804, Section 2.2.1.3.3.3: AC 1(1), (2), (4), (5), AC 2(4), AC 4(4), AC 5(3)]

The impacts of thermal-hydrologic-mechanical coupled processes were analyzed at both the site-scale and the drift-scale levels (BSC 2004a, Sections 6.5 and 6.6; BSC 2005a, Sections 6.5.12 and 6.5.13). In general, thermal-mechanical–induced stresses at the repository level act across fractures causing decreased vertical permeability, while outside the heated region near the ground surface, reduction in horizontal stresses tends to open vertical fractures causing increased vertical permeability. The impact of these processes on site-scale flow in the unsaturated zone is described in Section 2.3.2.4. On the basis of these modeling studies, changes in drift-scale and site-scale hydrologic properties induced by thermal-hydrologic-mechanical processes are concluded to have

no significant impact on vertical percolation flux through the repository horizon and no significant effect on seepage into the emplacement drifts, and are therefore excluded from TSPA (Table 2.2-5, FEP 2.2.10.04.0A, Thermo-mechanical stresses alter characteristics of fractures near repository; also FEP 2.2.10.05.0A, Thermo-mechanical stresses alter characteristics of rocks above and below the repository).

Model Description—The modeling framework for the drift-scale thermal-hydrologic-mechanical model is based on the thermal-hydrologic seepage model (Section 2.3.3), which is based on the ambient seepage models (Section 2.3.3.2). The drift-scale thermal-hydrologic-mechanical model combines a thermal-hydrologic simulation code (TOUGH2) with a thermal-mechanical modeling code (FLAC3D). The drift-scale thermal-hydrologic-mechanical simulations focus on thermally induced stress changes and the resulting impacts on host-rock properties and the flow field (BSC 2004a, Section 8.1). The modeling framework for the site-scale model is based on the site-scale thermal-hydrologic model (BSC 2005a, Sections 6.1 through 6.3) and combines the same simulation codes, to focus on the potential for coupled thermal-hydrologic-mechanical processes to perturb the unsaturated zone flow field.

The drift-scale and site-scale thermal-hydrologic-mechanical models evaluate the effects of thermal hydrologic-mechanical-coupled processes on flow in the host rock, and provide the basis for excluding these effects from the TSPA (Section 2.2.1). The drift-scale thermal-hydrologic-mechanical model also develops disturbed-zone permeability changes associated with excavation, which are accommodated by the uncertainty distributions on rock permeability that are used by the drift seepage abstraction (Section 2.3.3). Modeling of drift-scale thermal-mechanical coupled processes to evaluate mechanical degradation and seismic effects is addressed in Section 2.3.4.

Model Results—Simulations of drift-scale thermal-hydrologic-mechanical effects for the Topopah Spring Tuff middle nonlithophysal (Tptpmn) and lower lithophysal (Tptpll) host-rock units generally show decreases in vertical permeability as a result of temperature-induced stresses near the drift openings, while the horizontal permeability remains essentially unchanged from initial post-excavation values (BSC 2004a, Sections 6.5.4, 6.5.5, 6.6.1, and 6.6.2). These changes in permeability indicate that water flow in the host rock would be more readily diverted around the drift openings, decreasing the potential for seepage (Section 2.3.3). The site-scale model results show increased vertical permeability within approximately the upper 150 to 200 m (BSC 2005a, Figures 6.5.12-1 and 6.5.12-3) that is not reflected in the drift-scale thermal-hydrologic-mechanical model results (BSC 2004a, Figures 6.5.4-1 and 6.6.1-2). These two sets of comparisons indicate that thermal-hydrologic- mechanical models produce nearly identical vertical liquid flux fields as those calculated by thermal-hydrologic models that lack the mechanical coupling.

Model Support—Major support for the drift-scale thermal-hydrologic-mechanical model is provided by the results of the Drift Scale Test, which are described in Section 2.3.3. The thermal-hydrologic-mechanical response of the rock mass in the Drift Scale Test is represented in rock mass displacement data and air permeability data measured during the Drift Scale Test heating phase. Model-data comparisons (BSC 2004a, Section 7.4) show that the drift-scale thermal-hydrologic-mechanical model adequately reflects observed trends and predicts the changes in air permeability within one order of magnitude. Both the simulated and measured changes are small compared to the natural variability in fracture permeability, which spans four

orders of magnitude in each host rock unit (Section 2.3.3.2.3.6) (BSC 2004a, Section 7.1.4). These comparisons provide confidence that the drift-scale thermal-hydrologic-mechanical model justifies the exclusion of these effects from the TSPA (BSC 2004a, Section 7.4.3).

2.3.5.2.3 Thermal-Hydrologic-Chemical Coupled Processes

[NUREG-1804, Section 2.2.1.3.3.3: AC 1(1), (2), (4), (5), (8), AC 2(4), AC 4(4), AC 5(3)]

The primary purpose for the thermal-hydrologic-chemical seepage model is support for the near-field chemistry model (Section 2.3.5.3). Insights gained from the model are also used in screening justifications for FEPs related to coupled processes as summarized in Section 2.2.1, for example, excluded FEP 2.2.08.04.0A, Re-dissolution of precipitates directs more corrosive fluids to waste packages. This section briefly describes this model and summarizes model results that have contributed to understanding of coupled processes.

This section describes the analyses done to understand the effects of thermal-hydrologic-chemical processes on the occurrence and composition of seepage. The thermal-hydrologic-chemical seepage model includes the processes of mineral dissolution and precipitation, with multiphase, nonisothermal unsaturated flow and transport. All but the fastest chemical reactions are modeled as being kinetically limited, with rates that depend on the temperature and the state of aqueous saturation with respect to minerals. Local aqueous chemistry is controlled by the state of chemical equilibrium with respect to mineral phases, the effective surface areas of minerals in contact with water, the rates of mineral dissolution and precipitation, the aqueous and gaseous fluxes, and the rates of evaporation and condensation (SNL 2007c, Section 6.2.1.2). Mineral dissolution and precipitation lead to spatially heterogeneous changes in porosity of the rock. Porosity changes cause changes in hydrologic properties, which affect the occurrence and composition of seepage (SNL 2007c, Section 6.2.1.4).

Model Description—The thermal-hydrologic-chemical seepage model is a two-dimensional, drift-scale, numerical model of a dual-permeability system (SNL 2007c, Section 8.1). The dual-permeability modeling approach is consistent with the thermal-hydrologic seepage model (Section 2.3.3.3.3) and the multiscale thermal-hydrologic model (Section 2.3.5.4.1). Stratigraphic data and rock properties used to construct the model are taken from the unsaturated zone flow model and the unsaturated zone calibrated properties model (Section 2.3.2). The thermal-hydrologic-chemical seepage model is consistent with the three-dimensional mineralogical model (SNL 2007c, Section 4.1.6; BSC 2004b). Net infiltration fluxes applied at the top boundary of the model grid represent the mean of the 30th percentile infiltration map for present-day, monsoonal, and glacial-transition climatic conditions (SNL 2007c, Section 4.1.4). Other input data include dimensions and other characteristics of EBS features, thermal loading, and thermodynamic and kinetic parameters from scientific literature sources (SNL 2007c, Section 4.1).

The geochemical system used by the thermal-hydrologic-chemical seepage model includes a suite of aqueous components representing the major components in Yucca Mountain pore waters and minerals; the major primary solid phases (minerals and glass) occurring in geologic units at Yucca Mountain, and possible secondary alteration minerals; and the gas-phase components CO_2, water vapor, and air (the noncondensable components in the gas phase, excluding CO_2). Initial mineral

types and abundances were estimated using qualitative identification, x-ray diffraction measurements on cores reported in the Yucca Mountain mineralogical model (BSC 2004c, Section 4.1.1), and analyses of fracture surfaces (SNL 2007c, Section 6.2.2.2). Minerals included in the model as possible precipitates were determined from field observations of thermal alteration (Vaniman et al. 2001) corroborated by simulations of water–rock interaction (SNL 2007c, Section 6.2.2.2). The model is designed to simulate evaporatively concentrated waters with ionic strength less than 4 molal. At ionic strengths greater than 4 molal or liquid saturation less than 10^{-5}, the model uses a dryout mineral assemblage to represent the behavior of soluble salts (SNL 2007c, Section 6.4.5). When moisture returns, the salts are redissolved using kinetic rate expressions.

The thermal-hydrologic-chemical seepage model simulates the evolution of the compositions of fracture waters, minerals, and gas throughout the host rock around an emplacement drift (i.e., in the matrix and fractures). Simulation results are used to represent the composition of potential seepage water and the gas-phase composition of gas that can enter the drift (SNL 2007c, Section 6.5). Potential seepage water compositions are taken from high-flux zones proximal to and above the drift (SNL 2007c, Section 6.5.5.4); predicted in-drift gas compositions are taken from values in drift wall gridblocks.

Model Results—To evaluate the effect of mineral precipitation and dissolution on flow, results of ambient and thermal-hydrologic simulations are evaluated first, and then compared to results from similar thermal-hydrologic-chemical simulations (SNL 2007c, Section 6.5; SNL 2007d, Section 6.6). In all cases, the long-term reduction of permeability is caused primarily by the deposition of silica from evaporative concentration at the boiling front, as well as minor calcite precipitation caused by the increased temperature (retrograde solubility) (SNL 2007c, Section 6.5.5.3). The short-term permeability decrease is caused by the precipitation of salts upon dryout at the boiling front (SNL 2007c, Section 6.5.5.3). These salts readily dissolve as the boiling front collapses back toward the drift wall. They consist primarily of halite, which accounts for much of the short-term reduction of fracture porosity, and other salts in lesser amounts (SNL 2007c, Section 6.5.5.3).

The effect of porosity changes on the vertical liquid flux within the near-field host rock above the drift is minor (SNL 2007c, Section 6.5.5.3 and Figure 6.5-5). This is attributable to the high initial permeability of host rock, and the coupling of porosity changes with capillary pressure in the model (Leverett scaling; SNL 2007c, Section 6.4.4.4). Leverett scaling is a realistic response that increases capillarity when the porosity and permeability decrease as a result of mineral precipitation. Additional sensitivity testing of the effects of Leverett scaling and heterogeneity of hydrologic properties on seepage behavior and composition is discussed below.

The base case thermal-hydrologic-chemical seepage model described above (SNL 2007c, Section 6.5) simulates the composition of waters in the host rock but does not actually simulate the hydrologic process of seepage into drifts. This is because the capillary rock properties and the typical infiltration rates used in this model, while representative, produce liquid saturations below the theoretical threshold for seepage (SNL 2007c, Section 6.4.8). To address this limitation and investigate the relationship between seepage composition and seepage occurrence, the base case model was modified to integrate features of the thermal-hydrologic seepage model (Section 2.3.3.3.3) to investigate both the quantity and chemistry of seepage together in the same

simulations (SNL 2007d, Section 6.4). The remainder of this section describes the results of the sensitivity analyses performed using this approach.

Heterogeneity Effects and In-Drift Seepage Composition—Sensitivity studies were performed to evaluate the impact of spatial heterogeneity in fracture permeability and capillarity on the evolution of thermal-hydrologic-chemical processes affecting the quantity and chemistry of seepage (SNL 2007d). The thermal-hydrologic-chemical seepage model described above was modified to incorporate heterogeneity in fracture permeability using a distribution function similar to that used in developing the seepage abstraction (Section 2.3.3.2.3.6). Heterogeneity in fracture properties was introduced in two ways: (1) calculating the capillary strength from the initial fracture permeability using Leverett scaling relations (SNL 2007d, Section 6.3); and (2) varying the initial fracture capillary-strength parameters for different realizations of the same fracture permeability distribution, covering a wide range of fracture capillary-strength parameters. The results of these studies show that thermal-hydrologic-chemical processes are not likely to cause seepage that exceeds the occurrence frequency or magnitude predicted by the ambient seepage model and that the composition of seepage will be dilute.

The fracture capillary-strength parameter of the host rock ($1/\alpha$) is a key parameter in determining whether seepage will occur (Section 2.3.3.2.3.6). The sensitivity studies started with the base case capillary-strength values from the unsaturated zone calibrated properties model (Section 2.3.2.4.1.2; SNL 2007d, Section 6.4.11.4). Additional simulations were performed in which the fracture capillary-strength parameter was set to a value consistent with the seepage abstraction (Section 2.3.3.2.3.6) to demonstrate the impact on the magnitude of seepage from not including capillary heterogeneity while including permeability heterogeneity. This was done to test whether the incorporation of spatially heterogeneous Leverett scaling is consistent with the conceptual basis for the ambient seepage model (and its calibrated parameters). Another set of additional simulations was performed in which a spatially uniform initial value for the fracture capillary-strength parameter was estimated using an iterative approach intended to find the minimum value for the fracture capillary strength that prevents ambient seepage. Both of these studies are discussed in the following paragraphs. Seepage into the drifts is also determined by percolation flux in the rock. The sensitivity studies described here included two sets of time-varying infiltration boundary conditions (mean flux and 10 × the mean flux) to demonstrate whether or not seepage occurs and, when it does occur, to predict the quantity and chemistry of seepage.

When fracture permeability heterogeneity is included in the conceptual model but capillarity is assumed homogeneous (i.e., Leverett scaling is not included), the selected base-case fracture capillary-strength parameter does not predict seepage to occur with either the present-day mean or ten times the present-day mean infiltration flux (SNL 2007d, Section 6.6). However, with inclusion of both permeability and capillarity heterogeneity in the conceptual model through Leverett scaling (SNL 2007d, Section 6.3), seepage may occur locally. When seepage occurs (particularly with larger infiltration fluxes), ambient seepage is greater than for thermal-hydrologic or thermal-hydrologic-chemical simulations (using the same heterogeneous distributions). This result is important because it shows that the ambient seepage abstraction used in the TSPA, which does not include effects from thermal-hydrologic-chemical processes, conservatively overestimates the magnitude of seepage.

The iterative estimation procedure involved adjusting the uniform fracture capillary-strength parameter so that seepage occurs for ambient conditions using the present-day mean infiltration flux, then increasing it slightly so that seepage does not occur, and running the ambient, thermal-hydrologic, and thermal-hydrologic-chemical simulations for both the present-day mean, and 10 × the present-day mean infiltration flux values (SNL 2007d, Section 6.7). This process gives an estimate of the results that would be obtained by recalibrating the ambient seepage model used in TSPA, using a new conceptual model that includes Leverett scaling. Using the developed capillary-strength values, thermal-hydrologic and thermal-hydrologic-chemical simulations confirmed that the occurrence frequency and magnitude of seepage are both less than predicted by the ambient seepage model.

The sensitivity study integrated features of the thermal-hydrologic-chemical seepage model with the calibrated ambient seepage model used for TSPA, allowing direct examination of seepage chemistry for conditions when seepage is predicted to occur. The composition of such "in-drift" seepage was compared to compositions extracted from the model grid for the base case model (SNL 2007d, Section 6.6). The results show that "in-drift" seepage is dilute and closely comparable (within the model uncertainty) to compositions selected from within the host rock.

Model Support—The base case thermal-hydrologic-chemical seepage model was adapted to simulate the Drift Scale Test (SNL 2007c, Section 7.1). The Drift Scale Test model implements all the same conceptual processes but with initial conditions and boundary conditions specific to the test. It is used to support understanding of the important thermal-hydrologic-chemical processes during heating of the host rock under repository-relevant conditions, as revealed by the compositions of gas and water samples, as well as thermal-hydrologic observations. Model support is also provided by simulations of laboratory water-rock interaction tests that used samples of the repository host rock (SNL 2007c, Section 7.2). Model simulations are validated by comparison with the direction and magnitude of changes in aqueous species concentrations measured at elevated temperatures during this test. In addition, a fracture-sealing laboratory experiment was simulated (SNL 2007c, Section 7.3). The modeled location and amounts of amorphous silica precipitated are comparable to the location and amounts observed in the experiment.

While these sensitivity tests involving permeability and capillary heterogeneity indicate that irreversible changes in the flow characteristics of the near-field host rock will occur, the changes are likely to result in decreased seepage. The seepage response is bounded by the ambient seepage abstraction used in TSPA (Section 2.3.3.2). Given that the quantity of water contacting the engineered barrier is not adversely impacted, changes to flow and seepage due to thermal-hydrologic-chemical processes are excluded from the TSPA (Section 2.2.1).

2.3.5.3 Near-Field Chemistry Model

[NUREG-1804, Section 2.2.1.3.3.3: AC 1(1) to (5), (7) to (10), AC 2(1), (2), AC 3(1) to (4), AC 4(1) to (4), AC 5(3)]

The primary role of the near-field chemistry model is to provide the near-field gas and water chemistries for use in simulating the in-drift chemical environment (Section 2.3.5.5). The evolution of water and gas compositions in the near-field host rock due to coupled thermal, hydrologic, and chemical processes influences the composition of potential seepage water and the associated

gas-phase composition in the emplacement drifts (SNL 2007b, Section 6.3.2). These near-field gas and water chemistries are inputs needed to generate the seepage evaporation abstraction used by TSPA (Section 2.3.5.5).

The near-field chemistry model provides the in-drift CO_2 range and compositional information about seepage to the seepage evaporation abstraction (Section 2.3.5.5). The seepage evaporation abstraction represents how these waters evolve and generates ionic strength, pH, and concentrations of Cl^- and NO_3^- for in-drift waters. The TSPA uses these values to evaluate the potential occurrence of localized corrosion of the waste package outer barrier, colloid stability and radionuclide solubilities in the invert, and solubilities in the waste package (CO_2 pressures only). The information provided by the near-field chemistry model mostly controls the resulting pH and gas-phase CO_2. Ionic strength is determined mostly by the seepage evaporation abstraction, which simulates evaporation. Chloride and nitrate for in-drift waters are adjusted in the seepage evaporation abstraction to represent the range of uncertainty for pore waters sampled from the host rock.

As described in this section, the final results of the near-field chemistry model are the outcome of a series of documented activities, including the following (SNL 2007b):

- **Generation of Input Parameters—**Parameter values, parameter ranges, uncertainty distributions, and bounding assumptions are based on site-specific field measurements, laboratory experiments, process-level modeling studies, and scientific literature data. Section 2.3.5.3.2 describes how data are used, interpreted, and synthesized into parameters for the near-field chemistry model. Uncertainty and variability in input parameters such as thermodynamic data, kinetic data, initial water and gas compositions, initial mineralogy, and percolation fluxes are also discussed. As presented in Section 2.3.5.3.3.4, the near-field chemistry model propagates parametric uncertainty and variability in the simulations supporting TSPA.

- **Model Development and Results—**Model development and its technical basis, including determination of computational domain, initial and boundary conditions, assumptions, and approximations, are discussed in Section 2.3.5.3.3. Section 2.3.5.3.3.3 describes the overall model results, while Section 2.3.5.3.3.4 describes the evaluation of limitations and uncertainties of the near-field chemistry model to ensure that their treatment contributes to appropriate representation of risk.

- **Model Support—**As discussed in Section 2.3.5.3.3.5, comparisons with ambient pore-water strontium isotopic and major element compositions, with predictions from the independently-developed thermal-hydrologic-chemical seepage model, and with gas-phase data from the Drift Scale Test were used as the primary means of model support.

2.3.5.3.1 Conceptual Description

[NUREG-1804, Section 2.2.1.3.3.3: AC 1(1), (2)]

The conceptual understanding of thermal-hydrologic processes involving seepage and flow and the evolution of thermal-hydrologic conditions in the drift is discussed in Section 2.3.3.3 and 2.3.5.4,

respectively. This section focuses on the additional model components (inputs and processes) used to evaluate thermal-hydrologic-chemical processes and how water–rock interactions in the evolving thermal setting affect the composition of pore and fracture waters that could enter the repository as seepage.

2.3.5.3.1.1 Matrix Pore-Water Composition

Matrix pore-water composition is an important input to coupled chemical process models for the repository host rock. Pore-water geochemical data have been collected throughout the geologic units at Yucca Mountain. These data show that there are consistent compositional changes with increasing depth. Relevant initial pore-water compositions for use in near field process modeling are from repository-level lithologic units because it is water–rock interactions within these units that are being modeled. The repository lies within the Topopah Spring welded (TSw) hydrologic unit, including the upper lithophysal (Tptpul), middle nonlithophysal (Tptpmn), lower lithophysal (Tptpll), and lower nonlithophysal (Tptpln) units (Table 2.3.2-2). Pore-water compositions from these units were chosen to represent the initial pore-water compositions in the near-field chemistry model (SNL 2007b, Sections 6.3.2.3 and 6.6). Section 2.3.5.3.2.2.1 provides further discussion of the suite of measured pore-water compositions.

2.3.5.3.1.2 Thermal-Hydrologic-Chemical Processes

The chemical evolution of waters, gases, and minerals is intimately coupled to the thermal-hydrologic processes related to percolation through the thermal field and matrix-fracture diffusion. The distribution of liquid water determines where mineral dissolution and precipitation can occur and where direct interaction can occur between matrix pore waters and fracture waters. Figure 2.3.5-4 shows the relationship between thermal, hydrologic, and geochemical processes occurring in the rock as the pore waters percolate downward through the thermal field above the drift (SNL 2007b, Figure 6.3-1).

As water percolates downward through the TSw unit toward the heated repository, as depicted in Figure 2.3.5-4, the increase in temperature affects mineral solubilities, the kinetics of alkali feldspar dissolution, and the partitioning of CO_2 between the aqueous and vapor phases. The solution composition changes as the water moves downward, and the composition reaching the drift is a function of the starting water composition, the percolation flux, which determines the rate of transport to the drift, and the thermal profile encountered along the flow pathway through time (SNL 2007b, Section 6.3.2.4).

Specific effects of thermal-hydrologic processes on water chemistry depend on the intrinsic characteristics of the dissolved species and the types of chemical reactions in which they are involved. The behaviors of the major species are as follows (SNL 2007b, Section 6.3.2.6):

- Cl^- and NO_3^- are conservative species, the relative concentrations of which are not affected during downward transport to the drift because mineral phases containing these species are highly soluble and do not precipitate. Precipitation of salts will occur in the dryout zone around the drift, but these are rapidly re-dissolved when the drift wall rewets and have only a transient effect on potential seepage water chemistry (Section 2.3.5.2.3).

- Ca^{2+} concentrations are affected primarily by calcite dissolution and precipitation, by feldspar dissolution, and by precipitation of secondary phases such as clays and zeolites.

- Mg^{2+} concentrations are affected by dissolution of feldspar and subsequent precipitation of secondary magnesium-bearing clay minerals. Although magnesium-bearing clay minerals (illite, celadonite, montmorillonite) are included in the near-field chemistry model, the lack of significant magnesium zeolites above the repository drifts (Bish et al. 2003, p. 1893) made it unnecessary to include these phases in the model.

- Na^+ and K^+ are more conserved in solution than the divalent ions as the pore waters percolate downward, and concentrations are mainly controlled by feldspar dissolution reactions and precipitation of clays and zeolites.

- SiO_2(aq) concentrations are controlled by precipitation and dissolution of amorphous silica. Silica solubilities increase with temperature, and SiO_2(aq) concentrations increase as pore waters percolate downward through the thermal zone above the drift.

- CO_2 concentrations in the gas phase through the rock column above the drift are controlled by equilibrium with the local aqueous phase. CO_2 gas concentrations are strongly dependent upon the temperature profile above the drift, because CO_2 partitions more strongly into the gas phase at higher temperatures. Also important is feldspar dissolution, which increases the solution alkalinity and pH, offsetting the effects of increasing temperature with respect to gas-phase CO_2. Calcite, through dissolution and precipitation, acts as a source/sink for aqueous carbonate and gas-phase CO_2.

In the near-field chemistry model, most mineral precipitation and dissolution reactions are modeled as being controlled by thermodynamic equilibrium between the solid and aqueous phases. The principal mineral phases in the Topopah Spring Tuff are alkali feldspar and silica polymorphs. Mixed-composition alkali feldspar is a high-temperature igneous phase that cannot reach saturation at lower temperatures and will not precipitate; its dissolution is modeled as being kinetically limited, with a rate that is a function of temperature (Section 2.3.5.3.3.2.5). Hence, species concentrations in solution at any given time and location are largely controlled by the equilibrium thermodynamic condition, the feldspar dissolution rate, and the percolation flux, which determines the water–rock contact time (SNL 2007b, Section 6.3.2.4).

The near-field chemistry model treats percolating waters moving through the rock as "plug flow." Pore-water velocity is a function of percolation flux, porosity, and saturation, but there is no discrimination of fracture versus matrix flow. This implementation requires that the rate of equilibration between fracture waters and waters in the rock matrix be rapid relative to the rate of downward transport, and was confirmed with simulations using the finite element heat and mass transfer code, FEHM. The FEHM code explicitly calculates transport through connected matrix and fracture continuums, using rock and fracture hydrologic properties consistent with other unsaturated zone hydrologic models. FEHM model results yielded virtually identical transport times as the plug flow implementation in the near-field chemistry model (Section 2.3.5.3.3.2.7).

Effects of Infiltration and Climate Changes—Future climate changes are represented in the model by changing percolation fluxes to represent changes in infiltration rates, affecting

pore-water velocities and water–rock contact times, and hence, the relative impact of feldspar dissolution on water chemistry (SNL 2007b, Section 6.3.2.4.5). Percolation fluxes are evaluated parametrically, allowing water composition to be calculated at any location across the repository footprint, as a function of percolation flux (Sections 2.3.5.3.3.2.1 and 2.3.5.3.3.2.7).

Hydrologic Property Changes in Fractures and Matrix—As water percolates downward toward the drift, mineral-water reactions result in precipitation and dissolution of minerals in fractures and in the tuff matrix. Because the molar volumes of minerals created by hydration reactions (e.g., feldspars reacting with water to form zeolites or clays) are commonly greater than the molar volumes of the reactant minerals, the reactions lead to porosity reduction. However, because dissolution rates for silicate minerals are slow, the predicted extent of alteration is minor. Thermochronology of alteration phases and fracture minerals in the Topopah Spring Tuff indicates that most secondary phases formed at somewhat elevated temperatures (40°C to 100°C) that persisted for millions of years after tuff emplacement (SNL 2007b, Section 6.12.2.2). Given that only a tiny fraction of the devitrified rhyolitic core of the tuff altered to secondary minerals during that time interval, significant changes in the rock matrix and fracture porosity in the rock section above the boiling zone around the drift are not expected. Mineral precipitation, primarily silica, calcite, and more soluble salts, is anticipated in the boiling zone proximal to the drift; however, sensitivity analyses carried out using the thermal-hydrologic-chemical seepage model indicate that these have limited effect on either the occurrence or composition of seepage (Section 2.3.5.2.3).

2.3.5.3.2 Data and Data Uncertainty

[NUREG-1804, Section 2.2.1.3.3.3: AC 1(2), (3), (8), AC 2(1), (2), AC 3(1) to (4)]

This section describes the data sources used to develop the near-field chemistry model with references to supporting documents. Development of input parameters and uncertainties in input parameters that could affect water and gas compositions are also summarized.

2.3.5.3.2.1 Data Sources

The geologic setting at Yucca Mountain has been studied extensively and characterized using information gathered from surface outcrops, boreholes, and the Exploratory Studies Facility (ESF). These studies provide both conceptual bases and integrated sets of model parameters for unsaturated zone flow and transport models. The near-field chemistry model is consistent with the geologic framework model for the site (BSC 2004d), the three-dimensional mineralogical model (BSC 2004c), drift-scale calibrated thermal-hydrologic properties (Section 2.3.2.4.1.2.3), and the unsaturated zone flow model (Section 2.3.2.3).

Additional site-specific data include starting pore-water compositions, chosen from Topopah Spring Tuff pore-water analyses, and the ambient geothermal gradient, derived from borehole temperature data. Other data sources include scientific literature sources for thermodynamic data, and design information such as drift dimensions and thermal loading, repository layout, and ventilation efficiency (Section 1.3). Design information used by the near-field chemistry model, and associated constraints placed on the design through implementation of this model in TSPA, are identified in Section 2.2.1 (Table 2.2-3).

2.3.5.3.2.2 Input Parameter Development

This section describes input parameters utilized in the near-field chemistry model including stratigraphic data, hydrologic and thermal data, percolation flux values, mineralogy, fracture and matrix pore-water gas chemistry, and design information. Uncertainties in input parameters that could affect calculated water and gas compositions are also summarized with references to supporting sensitivity studies.

2.3.5.3.2.2.1 Input Parameter Descriptions

The near-field chemistry model requires the following types of input parameters (SNL 2007b, Section 4.1):

Stratigraphic Data—The near-field chemistry model domain consists of the devitrified rhyolitic core of the Topopah Spring Tuff—units Tptpul, Tptpmn, Tptpll, and Tptpln. The model domain extends from the top of the Tptpul to the repository level (SNL 2007b, Section 6.3.2.4). A vertical dimension of 200 m is used; this is a representative average stratigraphic thickness for this interval over the repository footprint, based on data from *Geologic Framework Model (GFM2000)* (BSC 2004d).

Hydrologic and Thermal Properties—The devitrified rhyolite core of the Topopah Spring Tuff is treated as a single unit in the near-field chemistry model. Hydrologic properties of this unit are the thickness-weighted averages of the values for each of the four repository host lithologic units, extracted from the unsaturated zone calibrated properties model (Section 2.3.2.4.1). The use of a single set of values for these four units was verified by comparison with FEHM model simulations in which all four units were explicitly included (Section 2.3.5.3.3.2.7).

Thermal properties for the modeled rock column are based on those for the Tptpll unit, because the majority of the repository lies within this unit. Using thermal properties for the Tptpll assures representative modeling of the steep thermal gradient proximal to the drifts. Rock thermal conductivity values are evaluated parametrically, using the 10th percentile, mean, and 90th percentile values for the wet and dry values for the Tptpll. This range of values is broadly consistent with the in-drift condensation model (Section 2.3.5.4.2) and the multiscale thermal-hydrologic model (Section 2.3.5.4.1), as it covers most of the modeled range for all four repository host units.

Percolation Flux Values—Percolation fluxes are handled parametrically in the near-field chemistry model. The flux values are derived from the unsaturated zone flow model, which assumes steady-state flow conditions and generates 16 three-dimensional flow fields for four different infiltration boundary conditions (using the 10th, 30th, 50th, and 90th percentile infiltration maps) for the three different climate states and the post-10,000-year period. The three climate states are present-day climate for the first 600 years after waste emplacement, monsoonal climate for the period 600 to 2,000 years after emplacement, and glacial-transition climate for the period 2,000 to 10,000 years after emplacement (SNL 2008a, Section 5.1.4); the post-10,000-year period has a defined percolation flux range, rather than a defined climate.

Twenty different sets of percolation flux values are used in the near-field chemistry model, each consisting of four values, representing the three different climate states and the post-10,000-year period. To generate the percolation flux sets, cumulative distribution functions of the percolation fluxes were generated for each climate state, combining data from all four infiltration boundary condition scenarios. The four percolation flux values representing the same probability of occurrence for each climate state were combined into a single set, with the twenty sets representing probabilities at 5% intervals from 2.5% to 97.5%.

Mineralogy—The near-field chemistry model is based upon thermodynamic calculations performed using a slightly modified version of the project "Pitzer" thermodynamic database for concentrated solutions. Although the near-field chemistry model does not itself predict the occurrence of concentrated solutions, the Pitzer database was used to maintain consistency with the seepage evaporation abstraction (Section 2.3.5.5), which receives inputs from the near-field chemistry model. The database was modified for use in the near-field chemistry model to include a mixed sodium-potassium alkali feldspar, representing the TSw matrix feldspar. In addition, trace amounts of iron were removed from the formulas of several versions of the zeolite mineral clinoptilolite, so that they were not inhibited from forming in the near-field chemistry model, which does not include iron in the chemical species considered. Hundreds of other mineral phases in the database are implicitly included in the model, including many zeolite and clay phases, which are commonly represented as end-member or simplified compositions (SNL 2007b, Section 6.3.2.6); however, only a few of these are predicted to form in the near-field chemistry model.

The tuff matrix is comprised almost entirely (>95%) of alkali feldspar and silica polymorphs, including tridymite, cristobalite, and quartz (BSC 2004b, Table 6-2). Common fracture-coating minerals are calcite and opal. Alkali feldspar is incorporated explicitly in the near-field chemistry model and is allowed to dissolve at a kinetically limited rate but does not saturate or precipitate, as mixed-composition igneous feldspars are not stable at the relatively low temperatures expected around the drift. The silica polymorphs, including opal, are represented in the near-field chemistry model by amorphous silica. Percolating pore waters are assumed to be in equilibrium with amorphous silica; none of the other silica phases are allowed to precipitate. This is based on the observation that ambient pore waters have aqueous silica concentrations higher than those predicted by assuming equilibrium with any of the less soluble silica polymorphs. Also, aqueous silica concentrations in geothermal systems in general are higher than predicted by equilibrium with the less soluble silica phases.

The pore waters are also held at equilibrium with calcite, which is common in fracture coatings throughout the Topopah Spring Tuff. Also, because calcite displays decreasing solubility with increasing temperature, geothermal waters are nearly always in equilibrium with calcite (Stefansson and Arnorsson 2000).

Initial Matrix Pore-Water and Gas Chemistry—The geochemical system used by the near-field chemistry model also includes aqueous components and CO_2 in the gas phase. Aqueous

species included in this model are the major components of the pore waters, and the components in major rock-forming minerals considered in the model.

In the near-field chemistry model, the initial CO_2 partial pressure in the gas phase in the rock is assumed to be 10^{-3} bar, on the basis of CO_2 concentrations near 1,000 ppm measured in the wall rock in the initial stages of the Drift Scale Test (SNL 2007b, Section 4.1.7). These values are corroborated by CO_2 measurements in borehole USW UZ-1, which vary little from 10^{-3} bar throughout the TSw unit (Yang et al. 1996).

Because the goal of the near-field chemistry model is to evaluate the composition of potential seepage into the emplacement drifts, actual pore-water compositions from the repository-level lithostratigraphic units are used as model inputs. In order to ensure that the entire range of possible pore waters was appropriately considered, all available pore-water analyses from the repository host units were evaluated for quality, and statistically evaluated to determine a small set of measured waters that represents the characteristics of all measured waters that passed the quality screening analysis (SNL 2007b, Section 6.6).

The screening analysis evaluated ninety compositional analyses for TSw pore waters that were complete with respect to major aqueous species; waters missing pH data, bicarbonate concentrations, or silica concentrations were included in the analysis because values for these parameters can be derived when the samples are pre-equilibrated for use in the near-field chemistry model (SNL 2007b, Section 6.6). The screening analysis revealed that many of the pore waters have relatively poor charge balances (Figure 2.3.5-5) and exhibit a consistent anion deficiency, the magnitude of which correlates with other compositional parameters; larger charge balance errors are associated with high Ca^{2+} and HCO_3^- concentrations (Figure 2.3.5-6). A correlation with NO_3^-/Cl^- ratio was also observed (Figure 2.3.5-7). In addition, many of the pore-water analyses, including many with good charge balances, indicate equilibrium with calcite at pCO_2 values far in excess of the observed in situ values of 10^{-3} bars (Figure 2.3.5-8, upper). Hence, they are supersaturated with calcite at the nominal repository pCO_2 of 10^{-3} bars. The waters plot on a line of equal calcite/bicarbonate normality, indicating that the increase in bicarbonate concentrations is being balanced by Ca^{2+} and suggesting that calcite dissolution is occurring. Natural surface waters also tend to plot along this line and some show elevated pCO_2 values, which have been attributed to CO_2 generation by microbial degradation of organic materials in river water (see lower figure in Figure 2.3.5-8; Stumm and Morgan 1996).

A deficiency of anions is not unusual in sedimentary formation water analyses, where it is commonly attributed to the presence of organic acids (Palandri and Reed 2001), which occur in the deprotonated, anionic forms at near-neutral pH. Organic acids were not included in early TSw pore-water analyses, but recent TSw pore-water analyses have found elevated levels of organic acids, specifically propionic acid, in several samples, suggesting that this may be the cause of the poor charge balances in many TSw waters (SNL 2007b, Section 6.6.3).

Propionic acid is a byproduct of microbial fermentative processes and is only produced under reducing conditions. Other chemical trends observed in the pore waters also provide evidence of microbial activity. Samples most strongly affected by elevated CO_2 concentrations also show proportionally lower nitrate and sulfate concentrations, consistent with the development of anoxic conditions and microbial denitrification/sulfate reduction processes. In situ conditions in the TSw

are oxic; all unsaturated zone gas phase analyses have yielded atmospheric levels of oxygen (SNL 2007b, Section 6.6.3; Thorstenson et al. 1990). Also, organic acids are rapidly metabolized by microbes under oxidizing conditions, and could not persist long in the oxidizing environment of the unsaturated zone (e.g., the measured amounts could not represent organic material percolating down from surface soils). Hence, it is unlikely that reducing conditions were present in the rock. However, microbial activity could have resulted in reducing conditions in the borehole cores after collection because they were tightly wrapped in plastic and sealed in core tubes, which were in turn plastic-wrapped.

The clearest evidence for microbial activity in the core tubes comes from the equilibrium CO_2 pressures calculated from measured pore-water concentrations, which are much higher than the 10^{-3} bar measured in situ. The predicted pCO_2 values correlate with the measured pH, with higher partial pressures corresponding to lower pH (SNL 2007b, Figure 6.6-7). This is entirely consistent with microbial activity resulting in buildup of CO_2 in the sealed, plastic-wrapped core tube. As the CO_2 built up in the gas phase, the pore water absorbed CO_2 and became more acidic, resulting in calcite dissolution.

Microbial activity during core storage modifies water compositions and also results in artifacts being introduced into the water compositions when they are pre-equilibrated for use in the near-field chemistry model. Thus, screening criteria were chosen both to evaluate analysis quality and the degree of modification by microbial processes. Two screening criteria, based on the charge balance (±10% was considered acceptable) and on the calculated pH upon equilibration, proved sufficient to screen out affected waters, reducing the total number of analyses to 34. The calculated pH criterion is a proxy for predicted elevated pCO_2 values (or alternatively, the degree of calcite supersaturation at an assumed pCO_2 of 10^{-3} bars) and can be applied even if the water analysis lacks measured pH or HCO_3^- data. The results of the screening analysis are shown on a Piper diagram in Figure 2.3.5-7, on which the Topopah Spring Tuff pore-water analyses are plotted.

Trace element data for the pore waters provide confidence in the screening criteria; strontium and manganese concentrations discriminate well between the screened-in and screened-out pore waters. Several processes associated with microbial activity could explain the observed enrichment in strontium and manganese in the screened-out waters, including calcite or manganese-oxide dissolution due to increasing acidity as CO_2 builds up in the sealed cores, and stabilization of desorbed or ion-exchanged strontium and manganese in solution by complexation with organic acids (SNL 2007b, Section 6.6.4). The results of the screening analysis are shown on a Piper diagram in Figure 2.3.5-9, on which the Topopah Spring Tuff pore-water analyses are plotted.

The number of starting waters necessary to capture the variation in the measured waters was determined by statistical analysis of waters that passed the screening analysis. When the pore waters evaporate or boil, the compositional evolution of the waters is controlled by the relative proportions of the various cations and anions in the starting water (i.e., ratios, not concentrations) (SNL 2007b, Section 6.3.3.1). Should these waters seep onto the surface of a drip shield or hot waste package, the composition of the resulting brine could affect the initiation of corrosion (Section 2.3.6). Therefore, prior to performing a cluster analysis of the 34 Topopah Spring Tuff pore waters that survived the screening analysis, thermodynamic simulations were performed to simulate evaporative concentration of the fluids to an activity of water of 0.74. At this degree of concentration, highly soluble salts (e.g., chlorides and nitrates) did not precipitate, but many less soluble minerals did,

resulting in differentiation of the waters. The statistical method of principal component analysis was then used to determine that the remaining water analyses formed four chemically distinct clusters. Then, representative waters from each group were chosen by selecting those nearest to the cluster centroid (SNL 2007b, Section 6.6.5). The effectiveness of the grouping analysis is shown in Figure 2.3.5-10, where the predicted evaporative evolution of the pore waters is shown with respect to pH and calcium, two solution parameters that are sensitive to mineral precipitation over a wide range of degrees of evaporation. The four groups evolve into distinct trends, but the members of each group evolve similarly. The evolution of the Cl^-/NO_3^- ratio with evaporation, for each of the 34 waters, is shown in Figure 2.3.5-11. The initial values reflect the measured pore-water values and show the range in Cl^-/NO_3^- ratios in the waters that passed the screening analysis. A discrete distribution of the Cl^-/NO_3^- values in each of the four water groups is sampled by TSPA in determining the in-drift chemical environment (Section 2.3.5.5.4.3). The four representative water compositions are used as starting water compositions for the near-field chemistry model, which provides potential seepage water compositions to the in-drift chemical environment models.

The groups and their representative waters are described below. The chemistry of the unevaporated representative waters is given in Table 2.3.5-5 (representative evaporated pH ranges are taken from *Engineered Barrier System: Physical and Chemical Environment* (SNL 2007b, Figure 6.6-17)).

Group 1—Group 1 waters account for 21 of the 34 analyses and evaporatively evolve into sodium-potassium-nitrate-chloride, high pH (pH 9-10) brines. The representative water is from borehole SD-9, depth interval 1,184.7–1,184.8 ft.

Group 2—Group 2 is the second largest group, comprising 7 of the 34 waters. This group evaporatively evolves into calcium-rich, nitrate-rich brines with slightly acidic pH values of 6–7. The representative water was extracted from a core sample from borehole Thermal K-017 in the ESF, interval 26.5–26.9 ft.

Group 3—Group 3 comprises three waters, all representing a single underground location. They evolve into slightly acidic (pH 6–7) calcium-rich, chloride-rich brines. The representative water is from Alcove 5 in the Enhanced Characterization of the Repository Block (ECRB) Cross-Drift, borehole HD-PERM-3, interval 34.8–35.1.

Group 4—Group 4 also contains three waters, which evolve into sodium-potassium-nitrate-chloride brines of near-neutral pH. The representative water is from Alcove 5 in the ECRB Cross-Drift, borehole HD-PERM-3, interval 56.7–57.1.

Regardless of the number of waters in each group, or the number of separate sampling locations represented, each representative pore water is given equal weight in the model. This is done in order to avoid overweighting groups that contain more pore-water analyses, but from only a single location or a few locations. This approach conservatively over-represents the potentially corrosive Group 3 waters, which have the highest Cl^-/NO_3^- ratios, as there are only three waters from a single location in this group.

Using the four starting waters for near-field chemistry model simulations ensures that the full range of compositional variation in the pore waters has been captured. In addition, in order to capture the entire range of observed Cl^-/NO_3^- ratios, potentially an important parameter for TSPA, the seepage

evaporation abstraction samples discrete distributions of the Cl^-/NO_3^- ratios exhibited by the waters in each group (SNL 2007b, Section 6.12.3). Thus, when these water compositions (Section 2.3.5.3.3.2.8) are modified by amounts of water–rock interaction covering the entire range predicted by the near-field chemistry model, the results represent the full range of potential seepage compositions. These values are used as the starting compositions for the seepage evaporation abstraction (Section 2.3.5.5.2), which provides the TSPA with the potential range of water compositions that result from evaporation and dilution within the drift.

The starting time, temperature, and location of potential seepage water in the stratigraphic column above the drift are functions of the potential seepage time at the drift wall, the percolation flux, and the evolution of the thermal field through time. The near-field chemistry model evaluates the degree of water–rock interaction for seepage at any given time after repository closure by integrating over the flow path taken by that seepage to reach the drift. The flow path is back-calculated for a given seepage time and percolation flux history, starting at the drift wall and moving backwards in time and up the stratigraphic section to the starting point. The initial CO_2 partial pressure is determined by re-equilibrating the representative pore water, while maintaining equilibrium with calcite and amorphous silica, at the starting temperature (SNL 2007b, Section 6.3.2.4.6).

Initial Fracture Water Chemistry—The starting waters for the near-field chemistry model are sampled from the available matrix pore-water analyses for the repository host units of the Topopah Spring Tuff. Using multiple lines of evidence, fracture water chemistries are shown to be similar to the matrix pore waters, although no fracture water compositions have been measured directly.

As discussed in Section 2.3.5.3.3.2.7, flow and transport modeling of the TSw unit above the repository also suggests that equilibration of matrix and fracture waters is rapid relative to downward transport throughout much of the host rock mass. The near-field chemistry model uses a plug flow model for transport, calibrated to the results from one-dimensional unsaturated zone transport simulations using the finite element heat and mass transfer code FEHM, which explicitly models matrix-fracture transport and matrix diffusion. The FEHM model domain included the four TSw repository host rock units (Section 2.3.5.3.1.1), each with the hydraulic and capillary properties taken from the calibrated rock properties set developed by the unsaturated zone flow model (Section 2.3.2), which are derived from field-based measurements of rock porosities and ambient rock saturations. The FEHM simulations were performed at percolation fluxes ranging from 1 mm/yr to 100 mm/yr, covering the general range of fluxes predicted to occur within the repository footprint (SNL 2007b, Table 6.3-1). Prior to calibration of the plug flow results to the FEHM results, median breakthrough times for the two methods varied by no more than 15%. Also, regardless of whether the particles were initially injected into the fractures or the matrix in the FEHM simulations, the predicted breakthrough curves were virtually identical. Both of these results indicate that, for the parameter values in the unsaturated zone calibrated hydrologic properties set, matrix-fracture interactions are rapid relative to downward transport, and it is reasonable to assume that fracture and matrix pore waters are in compositional equilibrium (SNL 2007b, Section 6.3.2.3).

The strontium isotopic composition of fracture-lining calcite from the TSw unit also supports rapid matrix-fracture equilibration. The calcite displays a microstratigraphy, with $^{87}Sr/^{86}Sr$ ratios that systematically increase from the earliest deposited to the outermost layers (Paces et al. 2001), with the outermost calcite layers having $^{87}Sr/^{86}Sr$ values similar to those of the present-day matrix pore waters. This trend reflects precipitation from water in isotopic equilibrium with matrix pore waters

(Marshall and Futa 2001) that have an isotopic signature that reflects incorporation of strontium released by dissolution of the rhyolitic tuff matrix. The $^{87}Sr/^{86}Sr$ ratio of the tuff matrix changed significantly through time due to the relatively rubidium-rich, strontium-poor composition of the unit. Thus, the strontium isotopic data from fracture-lining calcite indicate that matrix and fracture waters in the TSw are in isotopic, and therefore chemical, equilibrium.

Uranium-series isotopic data also indicate fracture-matrix water equilibrium. Gascoyne et al. (2002) examined fractured tuff samples from the Sundance and Drill Hole Wash Fault zones intersected in the ESF and unfractured tuff samples from the ECRB Cross-Drift. They found that both exhibited equivalent whole-rock deficiencies of ^{234}U relative to ^{238}U indicating that fractured rock does not necessarily represent a "fast path" with respect to transport. Fractures could still represent preferred flow pathways, however, if equilibration between matrix and fracture waters is rapid relative to downward flow.

Uranium isotopic data from fracture minerals also show evidence of extensive matrix-fracture interactions (Paces et al. 2001). $^{234}U/^{238}U$ isotopic data indicate that deposition of opal and calcite in unsaturated zone fractures was a continuous rather than an intermittent process, with a long-term, stable source of ^{234}U being provided to the fracture waters. The fracture minerals exhibited no pedogenic signature with respect to uranium isotopes, suggesting that complete equilibration between matrix and fracture waters had occurred prior to reaching the depths from which the mineral samples were collected. Paces and Neymark (2004) note that deep unsaturated zone pore waters exhibit the same degree of uranium isotopic disequilibrium as that measured for fracture minerals (and presumed fracture waters) and for the perched waters at the base of the TSw. Because matrix waters percolate very slowly though the rock, and are exposed to large mineral surface areas relative to fracture waters, which only contact the fracture surface, the matching uranium isotopic signatures indicate rapid diffusive/advective equilibration of matrix and fracture waters.

Thus, both FEHM modeling of flow and transport using the unsaturated zone calibrated hydrologic properties set, and field measurements of water and mineral isotopic data, indicate rapid equilibration of matrix and fracture waters relative to downward transport and support the use of matrix pore-water compositions as starting waters for the near-field chemistry model (SNL 2007b, Section 6.3.2.3).

Emplacement Drift and Engineered Barrier System Design Data—The near-field chemistry model uses repository design data (Section 1.3) consistent with other models used in TSPA, including the multiscale thermal-hydrologic model (Section 2.3.5.4.1) and the in-drift condensation model (Section 2.3.5.4.2). These parameters are listed in Table 1.9-9 and include the geologic location (Parameter Number 01-01); the repository layout, including the waste package end-point coordinates (Parameter Number 01-02); the emplacement drift spacing (Parameter Number 01-13) and diameter (Parameter Number 01-10); the waste package line load and thermal limits (Parameter Number 05-03); and the subsurface ventilation period of 50 years (Parameter Number 06-01). The assumed ventilation efficiency during the ventilation period is also consistent with the multiscale thermal-hydrologic and in-drift condensation models.

2.3.5.3.2.2.2 Input Parameter Uncertainty

Uncertainties in the input parameters can affect the calculated water and gas compositions. Other sources of uncertainty were evaluated during the development of the near-field chemistry model and found to have negligible effect on model results. The principal method of incorporating uncertainty in the input parameters into the near-field chemistry model is by sampling a range of input values.

Uncertainty in Starting Pore-Water Compositions—Initial compositions of pore waters in the Topopah Spring Tuff were developed from field and laboratory measurements. Uncertainty and variability are reflected in the four starting water compositions implemented in the near-field chemistry model. In addition, the within-group variability in the chloride:nitrate ratio is explicitly incorporated into TSPA by the in-drift seepage evaporation abstraction, which samples discrete distributions of this parameter for each of the four water groups. The potential use of pore waters from the Paintbrush Tuff nonwelded hydrogeologic unit (PTn), which overlies the TSw hydrogeologic unit, was evaluated as an alternative conceptual model (Section 2.3.5.3.3.1).

Uncertainty in Rock Thermal Properties—Uncertainty in rock thermal conductivity values is incorporated into the model by use of three different sets of wet/dry thermal conductivity values, consistent with the values used in other project models, including the multiscale thermal-hydrologic model (Section 2.3.5.4.1) and the in-drift condensation model (Section 2.3.5.4.2). The three sets of values represent the 10th percentile, mean, and 90th percentile values of the wet and dry thermal conductivity of the Tptpll unit, based on laboratory measurements (SNL 2007b, Section 6.3.2.4.3).

The effect of uncertainties in the extent and shape of the thermal field above the drift on the degree of water–rock interaction are explicitly included in the near-field chemistry model through use of a range of values for the rock thermal conductivity and by calculating the thermal field at many locations throughout the repository, resulting in a large number of possible thermal histories (SNL 2007b, Section 6.3.2.4.3). Percolation fluxes are taken from models that include representation of uncertainty, and are implemented by parametrically sampling suites of climate state-dependent percolation flux rates, covering the entire range of fluxes predicted by the unsaturated zone flow model (Section 2.3.2). The TSPA uses location-specific flux rates and thermal histories to select the appropriate near-field chemistry output for use at each waste package location.

Uncertainty in Ambient Feldspar Dissolution Rate—Most uncertainty in the near-field chemistry model is combined into the calculation of the amount of feldspar that dissolves as water percolates downward to the repository drift. This value is referred to as the water–rock interaction parameter, and it is used in calculating the composition of potential seepage at the drift wall. It is most strongly a function of the ambient feldspar dissolution rate, calculated from the mass fraction of secondary aluminosilicate alteration products (clays and zeolites) in the rock. Sources of uncertainty in the water–rock interaction parameter include uncertainty in the following: (1) the average mineral abundances (both feldspar secondary minerals) for the four repository units; (2) the water–rock ratio, due to uncertainties in rock properties such as porosity, ambient saturation (including the use of ambient saturation levels for the thermal case), and grain density; and (3) the timing of alteration because much of the secondary mineral formation occurred early

in the history of the tuff when temperatures were elevated and thus does not represent feldspar dissolution under ambient conditions. Other sources of uncertainty in the water–rock interaction parameter value lie in the estimation of the activation energy for feldspar dissolution, which determines the temperature-dependence of the reaction, and in treating transport as plug flow. These uncertainties, and how they are propagated through the near-field chemistry model, are described below.

Uncertainty in Rock Hydrologic Properties and Mineralogy—Within the near-field chemistry model, the four repository host units are represented as a single lithology, with rock properties (mineral abundances, ambient matrix saturation, rock grain density, and porosity) that represent the averaged properties of the four units, weighted by the average thickness of each unit over the area of the repository footprint.

Each averaged value is determined by generating synthetic data sets using the mean and standard deviation for each of the four repository host units. Then, the synthetic data are weighted according to the thickness of the unit and added together to generate a combined distribution, from which the mean and standard deviation for the averaged lithology are determined.

Uncertainty in the Ambient Feldspar Dissolution Rate Due to Timing and Conditions of Alteration—The four repository host units comprising the densely welded, rhyolitic center of the Topopah Spring Tuff within the repository block, are entirely devitrified (Vaniman et al. 1996) and contain only minor amounts of alteration products. Because there is no glass in these units, the secondary minerals that are present must have formed by alteration of feldspars within the devitrified tuff. It is these units, extending to about 200 m above the repository, which form the model domain of the near-field chemistry model (Section 2.3.5.3.3.2.1). Paragenesis of fracture minerals in this part of the stratigraphic section indicates that, as with the altered vitric zones near the water table, most clay and zeolite formation appears to have occurred early in the history of the tuff (Paces et al. 2001, p. 8), at temperatures above ambient. Hence, the ambient feldspar dissolution rate is significantly slower than that estimated assuming all the secondary minerals in these units formed at ambient temperatures.

The possible range of ambient feldspar dissolution rates can be evaluated by taking advantage of the knowledge that most of the alteration occurred at temperatures between 40°C and 100°C (Levy and O'Neil 1989, p. 324) and also that the dependence of the alteration rate on temperature is defined by an Arrhenius relationship (e.g., the 96°C rate is approximately 59 times the 23°C rate). The total feldspar dissolved (and the amount of secondary minerals formed) is the sum of that dissolved at elevated temperatures and that dissolved at ambient conditions. The ambient rate can be calculated as a function of how long elevated temperatures might have persisted. The maximum bound for the ambient feldspar dissolution rate is calculated by assuming that all secondary minerals formed at ambient conditions. The minimum bound is calculated by assuming that the tuff has always been at elevated temperature; in this case, all feldspar dissolved at elevated temperature, and the dissolution rate calculated using the entire abundance of secondary minerals is the high temperature dissolution rate. The Arrhenius relationship can then be used to calculate the relevant ambient rate. For instance, if 96°C conditions persisted over the entire history of the tuff, then all the secondary minerals formed at 96°C, and the ambient rate is equal to 1/59 of the rate calculated using all the secondary minerals.

While the amount of secondary minerals that formed at elevated temperatures versus ambient conditions cannot be determined with accuracy, the possible range of ambient alteration rates can be estimated from the available information on the thermal history of the tuff. The tuff probably took no more than several thousand years to cool after eruption but was reheated to near-boiling temperatures by magmatic heat during Timber Mountain group volcanism at 11.4 Ma (Whelan et al. 2006, Figure 8). U-Pb and (U-Th)/He dating of secondary minerals and fluid inclusion geothermometry (Wilson et al. 2003, p. 1171; Evans et al. 2005, p. 1103) indicate that the tuff cooled slowly after that, remaining above 80°C for a few million years and reaching ambient temperatures only four to five million years ago. Utilizing the known thermal history of the tuff and the timing of alteration, the possible range of the ambient feldspar dissolution rate, per kilogram of tuff, is estimated.

Propagation of Uncertainty in the Feldspar Dissolution Rate into the Near-Field Chemistry Model—The feldspar dissolution rate per kilogram of tuff is converted to the rate per liter of water using the water–rock mass ratio calculated from the rock hydrologic properties. A distribution of values for the feldspar dissolution rate per liter of water is created by generating synthetic data sets for the per-kilogram dissolution rate and the rock porosity, saturation, and grain density and randomly combining them. The resulting distribution is best represented as a beta distribution (Harr 1987, Section 2.3), defined by a mean, standard deviation, and maximum and minimum values. The mean value, 1.14×10^{-15} mol/L per sec, is used within the near-field chemistry model to calculate the nominal water–rock interaction parameter value.

The uncertainty in the ambient alkali feldspar dissolution rate scales linearly with uncertainty in the water–rock interaction parameter value. Therefore, a beta distribution for the water–rock interaction parameter value can be generated from that of the feldspar dissolution rate, using the nominal water–rock interaction parameter value and the mean. The beta distribution parameters are passed to TSPA, which samples them once per realization. In this fashion, uncertainty in rock properties and in the temperature and timing of alteration is propagated through the near-field chemistry model to TSPA.

The uncertainties in two additional input parameters used to calculate the water–rock interaction parameter value were evaluated but found to have little effect and are not propagated into the near-field chemistry model. The uncertainty in the water–rock interaction parameter value due to the activation energy (E_a) for feldspar dissolution is a function of temperature, and its effect is small relative to the combined uncertainty in the feldspar dissolution rate. The plug flow implementation of transport used by the near-field chemistry model is calibrated against FEHM breakthrough curves at percolation flux values of 1, 3, 10, 30, and 100 mm/yr to ensure that predicted residence times are representative. After adjusting the percolation fluxes, the uncertainty in the water–rock interaction parameter values due to the spread in the breakthrough times indicated by the FEHM simulations was evaluated and found to be insignificant, averaging only about 2.5% (1σ). It is not incorporated into the net uncertainty in the water–rock interaction parameter that is applied by TSPA.

2.3.5.3.3 Model and Model Uncertainty

[NUREG-1804, Section 2.2.1.3.3.3: AC 1(1), (2), (4), (5), (7) to (10), AC 3(1) to (4), AC 4(1) to (4), AC 5(3)]

This section discusses the assumptions and describes the model domain and boundary conditions for the development of the near-field chemistry model. Results of simulations performed with the model are reviewed. These simulations provide the basis for the in-drift chemical abstractions described in Section 2.3.5.5. Limitations in the model are summarized, and results of an evaluation of uncertainties in input parameters, numerical methods, and approximations are described, with reference to supporting documents. Comparisons to ambient pore-water compositional and strontium isotopic data and to data from the Drift Scale Test are described and contribute to confidence in the results of the near-field chemistry model.

2.3.5.3.3.1 Model Development and Alternative Conceptualizations

The near-field chemistry model evaluates the effect of water–rock interactions on water chemistry as waters percolate downward through the thermal field to the drift. It incorporates several simplifying modeling choices, such as aqueous phase-gas phase equilibrium (Section 2.3.5.3.3.2.9) and plug flow (Section 2.3.5.3.3.2.7). It does not address near-drift processes such as mineral precipitation associated with boiling or the transient compositional effects of redissolution of precipitated salts on matrix and fracture waters when the drift wall rewets. The thermal-hydrologic-chemical seepage model (Section 2.3.5.2.3) is used to evaluate some of the effects of drift-proximal mineral precipitation and dissolution. Results of that model provide confidence that processes in the boiling zone do not significantly affect seepage conditions or have more than a transient effect on potential seepage water compositions (Section 2.3.5.2.3).

Two alternative conceptual models are considered for the near-field chemistry model. In the first, pore waters from the PTn are evaluated as starting waters for the near-field chemistry model (SNL 2007b, Section 6.11.1). Near-field chemistry model simulations using a PTn starting water showed that the predicted seepage water chemistry fell within the range of results generated using TSw pore waters. However, because the PTn waters were not sampled from the base of that unit and reflect varying degrees of reaction with the vitric component in that unit, they exhibit a wider variation in chemistry than the TSw pore waters (SNL 2007b, Section 7.1.2) and were excluded from consideration as starting waters for the near-field chemistry model. Exclusion of these waters is also supported by the observation that matrix and fracture waters in the TSw equilibrate rapidly (Section 2.3.5.3.2.2.1), making it unlikely that unaltered PTn waters could reach the repository level.

In the second alternative conceptual model, potential seepage water compositions were calculated while treating feldspar as an equilibrium phase, as opposed to treating it as a phase which can only dissolve at a kinetically limited rate (SNL 2007b, Section 6.11.1). This approach was rejected because (1) the feldspar present in the rock is a mixed sodium-potassium phase, and mixed feldspars are high-temperature phases which, unlike pure end-members, cannot precipitate, and hence cannot be at equilibrium with the water at low temperatures; and (2) even if mixed feldspars could form at low temperatures, precipitation of other aluminosilicates (clays and zeolites) prevents them from saturating in pore water as it percolates downward through the unsaturated zone.

2.3.5.3.3.2 Model Description

This section provides an overview of the near-field chemistry model, a description of model assumptions, and a description of the model domain and boundary conditions. Table 2.3.5-1 summarizes the FEPs included in this model (SNL 2007b, Section 6.14).

Model Overview—The near-field chemistry model analyzes the effects of thermal-hydrologic-chemical processes on water chemistry as it percolates downward through the Topopah Spring Tuff to the drift. Major feeds for the model are ambient pore-water compositions, mineralogy and rock properties for the repository host rock units, and repository design features such as repository layout and drift heat loads. The model provides potential seepage water compositions and CO_2 concentrations in the gas phase within the drift to the in-drift chemical environment models (Section 2.3.5.5), which evaluate the effect of in-drift processes on water chemistry.

The major processes simulated by the near-field chemistry model are shown in Figure 2.3.5-4. As percolating water moves through the evolving thermal field above the drift, it interacts with minerals in the rock, maintaining equilibrium with calcite and silica phases, and dissolving alkali feldspar, while precipitating out secondary mineral phases. The rate of feldspar dissolution is a function of the temperature at any location along the percolation path and is calculated using a temperature-dependent dissolution rate. The dissolution rate is estimated for ambient conditions from the degree of alteration that the tuff has undergone since it erupted, 12.8 million years ago, and adjusted for temperature using literature data for the activation energy for feldspar dissolution. Little evaporation or degassing occurs as the water moves downward, until it reaches the near-field host rock around the drift, where water vapor and gas can readily escape into the drift, and water vapor is transported axially to cooler locations where it condenses. During the thermal period, evaporation occurs at an evaporation front at the drift wall or further from the drift opening where rock at low moisture saturation adjoins more distal rock at higher saturation. During the boiling period, this boundary corresponds to the boiling zone around the drift. At later times, it corresponds to the drift wall and fractures extending outward from the drift, close enough to be in gas-phase equilibrium with it. The pCO_2 in the drift is provided as a range, the maximum value representing equilibrium with the water at the evaporation front, and the minimum being the ambient value at the drift level, with dilution by water vapor generated by evaporation of water at the evaporation front around the drift (SNL 2007b, Section 6.3.2.8).

The near-field chemistry model implements a conduction-only heat transfer model similar to the smeared-source, mountain-scale, thermal-only (SMT) submodel of the multiscale thermal-hydrologic model (Section 2.3.5.4.1) and consistent with the in-drift condensation model (Section 2.3.5.4.2). Flow through the unsaturated zone above the drift is modeled using an optimized plug flow approach that does not explicitly include matrix-fracture interactions; however, comparisons with simulations performed using both the finite element heat and mass transfer code FEHM and the reactive transport code TOUGHREACT, which do include matrix-fracture interactions, confirm the validity of this approach (Sections 2.3.5.3.3.2.7 and 2.3.5.3.3.5.3).

The aqueous basis species considered in the model are H^+, Ca^{2+}, Mg^{2+}, Na^+, K^+, $SiO_2(aq)$, SO_4^{2-}, HCO_3^-, Cl^-, NO_3^-, F^-, and Al^{3+}. The qualified project database for concentrated solutions, a Pitzer

database (Section 2.3.5.5.2), is used for thermodynamic calculations, and all aqueous complexes and ion-pair interactions incorporated into that database, which combine these basis species, are implicitly included in the near-field chemistry model. A simplified mineralogy is used for the devitrified rhyolitic tuff, consisting of alkali feldspar (approximately 60 wt % of the tuff), amorphous silica (representing the silica polymorphs cristobalite, tridymite, quartz, and opal, which comprise approximately 35 wt % of the tuff), and calcite (less than 1 wt % of the tuff, but important chemically). Secondary minerals that are allowed to form are those in the Pitzer database, including a suite of clays and zeolites, and the end-member feldspars albite and microcline. Minerals that do not form under repository conditions (e.g., high-temperature igneous and metamorphic minerals) are suppressed (SNL 2007b, Section 6.2.4.1).

2.3.5.3.3.2.1 Assumptions, Model Domain, and Boundary Conditions

Key Assumptions—This section addresses assumptions built into the near-field chemistry model. These assumptions include the following:

- **Near-Field Chemistry Model Results, Calculated for a Repository in the Tptpll Lithologic Unit, Apply to all Host-Rock Lithologies**—Near-field chemistry model results are calculated assuming the repository is located in the Tptpll unit but are assumed to apply across the entire repository. This assumption is supported by the use of a range of thermal conductivity values that spans much of the range for the other host rock units, and by the compositional uniformity of the host rock units (Peterman and Cloke 2002). In addition, the four starting waters represent the observed range of matrix pore-water compositions, including analyses of samples from three of the four host-rock units (Tptpmn, Tptpll, and Tptpul).

- **Measured Pore-Water Compositions Adequately Represent the Actual Range of Initial Water Compositions in the Natural System**—Measured pore-water compositions from pore-water samples are used to determine the four initial water compositions for the near-field chemistry model. The measured pore-water compositions are assumed to adequately represent the actual range of pore-water compositions in the natural system. There are two bases for this assumption. First, while pore-water samples are not available from all possible locations in the repository, samples are available from all of the host-rock units. Second, the chemical similarity of the host-rock units makes large variations in concentrations of non-conservative aqueous species unlikely (SNL 2007b, Section 5.2.1).

- **Transport Through the Model Domain is Treated as Plug Flow**—Pore-water migration times through the near-field chemistry model domain are calculated assuming plug flow through a single unit with rock properties (porosity, saturation, grain density) representing the thickness-weighted average of the values for the four repository host units. This assumes that matrix-fracture interactions (advective and/or diffusive equilibration) are rapid relative to downward transport, that vertical dispersion is minimal, and that the averaged rock properties adequately represent the four units. The plug flow assumption is based on a comparison to modeling results using the transport modeling code FEHM and on strontium and uranium isotopic data collected from pore

waters and mineral coatings in fractures. The basis for the plug-flow assumption was described in Section 2.3.5.3.2.2.1.

- **Feldspar Dissolution Rate is Solely a Function of Temperature**—The feldspar dissolution rate implemented by the near-field chemistry model is assumed to vary solely with temperature, as a function of the activation energy for feldspar dissolution. This assumes that the rate is not a function of solution composition (e.g., saturation index, pH), and also that the accessible feldspar surface area does not change over the modeled period. The basis for the first assumption is that the mixed sodium-potassium alkali feldspar used in the near-field chemistry model is more soluble than either end-member feldspar; hence, it cannot reach saturation in solution (Stefansson and Arnorsson 2000). Also, feldspar dissolution rates are relatively insensitive to pH over the range from pH 3 to pH 9 (Helgeson et al. 1984; Lasaga et al. 1994). The basis for the second assumption is the thermal history of the tuff. The Topopah Spring Tuff is 12.8 million years old, and underwent a prolonged period of elevated temperatures (several millions of years) in its early history (SNL 2007b, Section 6.12.2.2.1). During the entire history of the tuff, only a few percent of the feldspar altered to form secondary minerals. Since the thermal pulse around the drift will only last a few thousands to tens of thousands of years, there is little chance that repository heating induced feldspar dissolution, or precipitation of secondary minerals, will significantly alter the bulk mineralogy of the tuff or the available feldspar surface area (SNL 2007b, Sections 5.2.4).

Model Domain and Boundary Conditions—With respect to the model for the thermal field above the drift, the near-field chemistry model domain encompasses the entire repository footprint. The temperature profile in the rock at each drift location is calculated by summing the thermal contribution from all 108 repository drifts. Hence, edge effects are explicitly incorporated into the model. Vertically, the thermal model extends upward to the surface, 300 meters above the drift. The initial (and final) temperature conditions throughout the model domain are based on a geothermal gradient calculated from temperature data measured in borehole SD-12. The land surface is held isothermal at 17°C by utilizing the method of images (Section 2.3.5.3.3.2.6), while the ambient temperature at the repository level is 23.4°C. The thermal model is a semi-infinite continuum model, so the lower boundary condition is an infinite extension of the homogeneous medium (SNL 2007b, Section 6.3.2.4.3).

The chemical-hydrologic domain of the near-field chemistry model is the devitrified core of the Topopah Spring Tuff, extending from the top of the Tptpul to the repository level, a vertical distance of 200 meters, on average, over the repository footprint. Initial pore-water compositions are those of the representative waters of the four compositional groups (Section 2.3.5.3.2.2.1); the initial CO_2 concentration in the rock is the ambient value of 10^{-3} bars. The pore-water and gas-phase compositions return to these values in the long term (tens to hundreds of thousands of years), once the repository wall temperature drops below 24°C. As with other coupled process models including the multiscale thermal-hydrologic model, four successive percolation fluxes, corresponding to three climate states (present-day (0 to 600 years), monsoonal (600 to 2,000 years), glacial transition (2,000 to 10,000 years), and the post-10,000-year period, are used (Section 2.3.5.3.2.2.1). The near-field chemistry model implements these by changing the flux when each climate state boundary is crossed. Geographic variation in the percolation fluxes is handled parametrically; the model generates results for twenty different sets of the four successive percolation fluxes. TSPA

chooses the relevant results by interpolating between percolation flux sets that bound the values for the waste package location being evaluated (SNL 2007b, Section 6.15.1).

2.3.5.3.3.2.2 Starting Pore-Water Compositions

Prior to using the representative pore-water compositions described in Section 2.3.5.3.2.2.1, the compositions were charge balanced using the EQ3/6 thermodynamic speciation and solubility code. This was accomplished by adjusting the H^+ concentrations while fixing the bicarbonate concentration to be in equilibrium with a partial pressure of CO_2 of 10^{-3} bars, the typical ambient partial pressure throughout the Topopah Spring Tuff. Charge-balancing is required prior to using the waters for thermodynamic modeling. It was also necessary because one of the four starting waters, the HD-PERM-3 sample from Alcove 5 (SNL 2007b, Table 4.1-3), did not have a measured value for bicarbonate. Aluminum concentrations were not measured for the pore waters, and were estimated by adjusting aluminum concentration to be in equilibrium with alkali feldspar ($Na_{0.51}K_{0.46}Ca_{0.03}Al_{1.03}Si_{2.97}O_8$, Section 2.3.5.3.3.2.5), the most abundant aluminosilicate in the tuff. This resulted in slight supersaturation with respect to several aluminosilicates, but this was deemed preferable to *a priori* assuming equilibrium with any alteration minerals. In the succeeding equilibration step, trace amounts of stellerite, the most supersaturated phase, precipitated. This reduced the aluminum concentrations slightly but had no significant effect on other components in solution. For the Group 4 representative water, the aqueous silica concentration was not measured, and was calculated assuming equilibrium with amorphous silica. A second equilibration step at the starting temperature was used to precipitate out any minerals that saturated in the original calculation (SNL 2007b, Section 6.3.2.3).

2.3.5.3.3.2.3 Water–Rock Interactions

A major process affecting pore water as it percolates through the rock is interaction with the minerals in the tuff. Primary silicate minerals such as silica polymorphs and alkali feldspar dissolve, releasing components into solution, while secondary minerals such as calcite, opal, clays, and zeolites dissolve and precipitate. These water–rock interactions modify the water composition as it percolates downward. Because heating within the PTn is limited, any change in the degree of water–rock interaction relative to the ambient case in the PTn is minimal, and only water–rock interactions in the TSw are considered. By far the most abundant minerals in this unit are silica polymorphs (quartz, tridymite, cristobalite/opal-CT), accounting for 30% to 40% of the total, and alkali feldspar, accounting for about 60% of the total. Alteration phases such as zeolites and clays, and opal and calcite in fractures, are minor but widespread constituents (BSC 2004b, Table 6-2).

2.3.5.3.3.2.4 Treatment of Calcite and Silica Polymorphs

Modeling water–rock interactions requires deciding how to treat each of these minerals. Calcite is a widely distributed phase in the fractures, comprising between 0.01% and 0.41% of the total rock mass in the four repository lithologic units (BSC 2004b, Table 6-2). Also, it precipitates as pore waters percolate downward toward the drifts and warm, because of the retrograde solubility of the mineral (Langmuir 1997, p. 205). Hence, it is likely to be present throughout the model domain. Although some components in solution can inhibit calcite precipitation if present in high concentrations, in general, calcite precipitates and dissolves readily. Because it is present throughout the system, and its precipitation/dissolution is not usually kinetically controlled, calcite

is treated as being present and at equilibrium with the waters at all times. This is consistent with the general observation that calcite is at saturation in geothermal systems (Figure 2.3.5-12).

Several silica phases are present in the Topopah Spring Tuff, including quartz, tridymite/cristobalite, and opal. Ambient pore waters in the repository host rock units contain about 50 mg L^{-1} SiO_2(aq), but thermodynamic simulations show that this concentration is too high to be in equilibrium with quartz or cristobalite, and less than that required to be in equilibrium with amorphous silica. General trends in low-temperature (less than 100°C) geothermal waters indicate that this is a typical condition (Figure 2.3.5-13). In the near-field chemistry model, percolating waters are treated as being in equilibrium with SiO_2(am). While this treatment results in slightly elevated aqueous silica concentrations relative to the ambient case, it is justified because amorphous silica will precipitate around the drift during the thermal period and hence is likely to be present in the geologic system as it cools. Also, amorphous silica dissolution has little effect on pH over the range of pH values likely to be encountered in this system, and dissolved silica does not interact significantly with most other species in solution. Clay and zeolite precipitation is limited by aluminum concentrations in solution, which are many orders of magnitude lower than silica. Only aqueous magnesium concentrations are significantly affected by aqueous silica concentrations, through precipitation of amorphous/crystalline sepiolite or amorphous antigorite. Even ambient silica concentrations are sufficient to limit magnesium concentrations by precipitation of magnesium-silicates, and silica concentrations can only rise with increasing temperature (silica phases exhibit prograde solubility). While silica concentrations could potentially affect the dissolution rate of alkali feldspar by driving up the saturation index with respect to this species, this effect is negligible because precipitation of zeolites, clays, and/or end-member feldspars limits aqueous concentrations of other components in alkali feldspar and keeps the alkali feldspar from approaching saturation (SNL 2007b, Section 6.3.2.4.1). Hence, this treatment of silica is reasonable and is consistent with the relative unimportance of silica to the model parameters that are important to the downstream in-drift seepage evaporation abstraction and to TSPA.

2.3.5.3.3.2.5 Treatment of Alkali Feldspar

Alkali feldspars are the most abundant mineral phases in the tuff. Alkali feldspars that form within a magma chamber or form by devitrification of the tuff matrix at elevated temperatures may be present initially as a single phase but will unmix as the tuff cools, with potassium-rich (sanidine) and sodium-rich (anorthoclase) cryptoperthitic layers segregating out. However, the degree of unmixing and the composition of the potassium- and sodium-rich lamellae that form are functions of the cooling rate. X-ray diffraction studies (Bish and Vaniman 1985) determined that alkali feldspars in the Topopah Spring Tuff are partially unmixed but exhibit a highly variable degree of solid solution and sample-to-sample variability. Because the degree of exsolution is highly variable, use of separate potassium-rich and sodium-rich feldspar phases is unwarranted, and a single feldspar composition ($Na_{0.51}K_{0.46}Ca_{0.03}Al_{1.03}Si_{2.97}O_8$) is used in the near-field chemistry model. This feldspar composition is based on the average normative albite, orthoclase, and anorthite abundances in the TSw hydrogeologic unit (Peterman and Cloke 2002). Use of the normative abundances to estimate the representative alkali feldspar composition is justified because the total normative feldspar abundance almost exactly matches the average modal feldspar abundance in the unit (BSC 2004b, Table 6-2), determined by x-ray diffraction analysis of borehole cores.

Volcanic alkali feldspars are undersaturated in groundwaters and geothermal waters (Stefansson and Arnorsson 2000) because the high-temperature disordered forms of feldspar are more soluble than the lower temperature polymorphs and because volcanic feldspars exhibit considerable solid solution, and the mixed phases have higher solubilities than the pure feldspar end-members. Hence, pore waters can never be saturated with respect to alkali feldspar, and dissolution of this phase must be treated as a kinetically limited process, as opposed to an equilibrium process.

In order to treat feldspar dissolution as a kinetic process, a dissolution rate for the feldspar must be assigned. The common approach for quantifying mineral dissolution rates generally requires using pure mineral dissolution rates developed in laboratory experiments and then estimating available mineral reactive surface areas. However, laboratory-derived mineral dissolution rates have been shown to be up to several orders of magnitude higher than field-measured dissolution rates (White 1995, Table 7). In addition, estimating mineral reactive surface areas is difficult, and the two commonly used approaches, estimating the surface area geometrically and using measured gas adsorption (Brunauer-Emmett-Teller) surface area, commonly yield results that vary by one to three orders of magnitude. In addition, no measurements of gas adsorption surface areas are available for Yucca Mountain tuffs. For these reasons, a feldspar dissolution rate was estimated for ambient conditions from Yucca Mountain-specific mineralogic data. This rate is calculated from the observed abundances of aluminum-containing alteration products (i.e., clays and zeolites) in the repository units. Because these units are entirely devitrified (Vaniman et al. 1996), feldspar dissolution is the only possible source for the aluminum in these phases, and the very low solubility of aluminum in neutral groundwaters ensures that aluminum is conserved in the solid phases and is not significantly removed in aqueous form. Hence, the aluminum mass balance allows the calculation of an average ambient feldspar dissolution rate, over the age of the Topopah Spring Tuff, from the alteration phases. This value is a maximum because, as discussed in Section 2.3.5.3.2.2.2, much of the alteration occurred at elevated temperatures (Levy and O'Neil 1989). Using the average abundance of smectite clays and zeolites in each of the four repository units, the observed alteration assemblage requires that 7.6×10^{-2} moles of alkali feldspar per kilogram of tuff have dissolved. Given that the age of the Topopah Spring Tuff is 12.8 Ma (Sawyer et al. 1994), this yields a dissolution rate of 5.94×10^{-9} mol/(kg tuff) per year. Using a water–rock ratio of 19.6 kg/L calculated using the rock properties (porosity, saturation, and grain density) for the four repository host units, this yields a feldspar dissolution rate of 3.7×10^{-15} mol/L per second. This value is not actually the ambient rate, as much of the alteration occurred under elevated temperature conditions early in the history of the tuff. Given knowledge of the thermal history of the tuff, it is possible to constrain the ambient feldspar dissolution rate to a range of values, the mean value for which is 1.14×10^{-15} mol/L per second (Section 2.3.5.3.2.2.2). This value is used in the near-field chemistry model calculations of the water–rock interaction parameter, and the uncertainty in the dissolution rate is captured by scaling it to an uncertainty in the water–rock interaction parameter value, which is passed to TSPA (Section 2.3.5.3.2.2.2).

The ambient (23.4°C) feldspar dissolution rate is modified for temperature as percolating waters move downward through the thermal field above the drift. The temperature dependence of this reaction is calculated using the Arrhenius relationship and a literature-derived activation energy for feldspar dissolution of 49 kJ/mol (SNL 2007b, Section 6.3.2.4.2).

The actual amount of alkali feldspar that will dissolve is a function of the transport time and the temperature profile the water experiences along the flow path to the drift. To determine this, it is

necessary to model the thermal gradient above the drift through time, and to determine the temperature profile encountered by water as it percolates slowly downward to the drift crown.

2.3.5.3.3.2.6 Modeling the Evolution of the Thermal Field

Because of the time required for percolation to occur, the instantaneous thermal gradient above the drift is not representative of the temperature profile that a packet of water would experience as it percolates downward to the drift. However, if thermal profiles from the drift to the surface can be calculated for several points in time during the repository history, then the temperature along the flow path through time can be estimated by interpolation between the point-in-time profiles.

The evolution of the thermal field through time was calculated using the same thermal model as that used in the in-drift condensation model (Section 2.3.5.4.2). The method uses a conduction-only heat dissipation model, implementing a line source solution derived from the transient solution for a continuous point source in an infinite medium (Carslaw and Jaeger 1959). Using the principle of superposition, the contribution from all 108 drifts, plus the natural geothermal gradient, is summed in calculating the thermal profile above the drift at each location evaluated. The land surface is assumed to be 300 m above the drift center depth at the center of the footprint. The land surface is held isothermal by utilizing the method of images, in which a thermal sink of strength equal to each source is reflected across the isothermal plane (SNL 2007e, Section 6.3.5.1.1). The contribution of the geothermal gradient is based on analysis of borehole temperature data from borehole SD-12. The near-field chemistry model uses a repository depth of 300 m; the predicted geothermal gradient ranges from 17°C at the land surface to 23.4°C at the repository level (SNL 2007b, Section 6.3.2.4.3). The thermal line load used in these calculations, the geothermal gradient, and the repository layout are all consistent with both the multiscale thermal-hydrologic model (Section 2.3.5.4.1) and in-drift condensation model (Section 2.3.5.4.2).

The model treats the stratigraphy above the repository as a single unit, with the thermal properties of the Tptpll rock unit. Thermal conductivities were calculated from wet and dry conductivities using an average value of 90.5% for the host rock saturation. The calculations were repeated three times, using three different sets of wet and dry thermal conductivities, to capture uncertainty in these parameters (SNL 2007b, Section 6.3.2.4.3). This is consistent with the implementation of thermal conductivities in other unsaturated zone thermal-hydrologic models, including the multiscale thermal-hydrologic model (Section 2.3.5.4.1) and the in-drift condensation model (Section 2.3.5.4.2).

The calculations were done in seven drifts located throughout the repository, at 16 locations through each drift. The locations of the drifts considered are shown in Figure 2.3.5-14. Thermal gradient profiles were generated at 41 points in time, from repository closure (50 years) to 1 million years.

An example of the results for one location and one set of rock thermal conductivity values is given in Figure 2.3.5-15. The thermal profiles initially exhibit a strong thermal gradient near the drift; over time, as heat is conducted upwards, the gradient becomes more linear, with only a slight steepening near the repository wall. If the drift wall remains above the boiling temperature of water for several hundred years, as in this example, then a nearly stable gradient will evolve and persist until the end of the boiling period. Once the drift wall drops below the boiling point of water, the temperature gradient begins to decrease while still being largely linear except for very close to the

drift. Given sufficient time, the temperature gradient would evolve to the geothermal gradient at the repository (SNL 2007b, Section 6.3.2.4.3).

The temperature profile encountered by a packet of water moving downward to the drift does not resemble these thermal gradients, which represent the gradient at any single point in time. The water takes a relatively long time to reach the drift, and the thermal gradient evolves. Hence, the water will follow a time-temperature path that crosses these instantaneous thermal profiles. However, that path can be calculated from the thermal profiles by interpolating between the different profiles as a function of time and depth, with the two parameters being correlated by the percolation flux rate. The thermal profiles in Figure 2.3.5-15 extend to the land surface because they are calculated assuming that the temperature at the land surface is isothermal (i.e., T = 17°C). Only those parts of the profiles from 0 to 200 m above the drift are used in the near-field chemistry model.

2.3.5.3.3.2.7 Modeling Flow Through the TSw

Defining the flow path also requires modeling the flow velocity through the TSw. The near-field chemistry model determines flow velocities at any given flux by using an assumption of plug flow and assuming a wetted porosity equal to the ambient condition. In this case, the transport time is equal to:

$$\text{Plug flow transport time, yr} = \text{Distance traveled, m} \div \text{Velocity, m/yr} \qquad \text{(Eq. 2.3.5-1)}$$

where

$$\text{Velocity, m/yr} = (\text{Perc. flux, mm/yr} \div 1000) \times 1/(\text{Sat.} \times \theta) \qquad \text{(Eq. 2.3.5-2)}$$

where saturation (Sat.) and porosity values (θ) are averages of ambient values for the four repository units (Tptpul, Tptpmn, Tptpll, and Tptpln), weighted by the average thickness of each unit over the repository footprint from the geologic framework model (Section 2.3.5.3.2.2.1).

The percolation flux values used in the near-field chemistry model range from less than 1 mm/yr to nearly 100 mm/yr and are based on fluxes at the PTn/TSw boundary predicted by the unsaturated zone flow model calibrated flow fields (Section 2.3.2). Cumulative distribution functions for the percolation flux values were used to define twenty sets of percolation flux rates (at probability intervals of 0.05), each containing a value for each of the four climate states: present-day, monsoonal, glacial-transition, and post-10,000-year (Section 2.3.5.3.2.2.1).

The use of a plug flow model with averaged rock properties, assuming ambient saturation, is a simplification that does not consider that the different units in the TSw have different hydrologic properties and that actual matrix and fracture saturations (and hence the rock water content and water flow velocity) will be functions of the percolation flux. To evaluate the appropriateness of this assumption with respect to flow rates and residence times, hydrologic simulations were performed using the finite element heat and mass transfer code FEHM. The FEHM simulations used a more

complex stratigraphic column corresponding to a repository center location, with separate sets of hydrologic properties for each of the units in the Topopah Spring Tuff. The simulations were run in particle tracking mode, for five different percolation fluxes: 1, 3, 10, 30, and 100 mm/yr (SNL 2007b, Section 6.3.2.4.4). A matrix diffusion coefficient 3.47 x 10^{-11} m^2/s was used. This value is consistent with those used for weakly sorbing radionuclides (Section 2.3.8, Table 2.3.8-9) in the repository host units.

Transport times based upon the plug flow implementation are slightly faster than the mean breakthrough times predicted by the FEHM modeling, with the relative difference being greater at higher percolation fluxes (Figure 2.3.5-16). It is possible that this difference is due to an increase in rock saturation with increasing percolation flux. However, the difference is less than 15% in all cases, providing confidence in the plug flow implementation for calculating flow rates in the Topopah Spring Tuff. Although the differences between the FEHM mean breakthrough values and the values calculated using plug flow are relatively minor, a minor adjustment was implemented in the near-field chemistry model to further reduce the difference. The FEHM results were used to calibrate the plug flow implementation; percolation fluxes are modified internally to the near-field chemistry model to result in plug flow transport times that match the FEHM results (SNL 2007b, Section 6.3.2.4.4).

Initial FEHM simulations were generated by injecting particles into the fracture continuum at the top of the model. Additional simulations were run in which the particles were injected into the matrix. The breakthrough times for each of the five percolation fluxes were nearly identical in the two cases, varying by only a few percent. The breakthrough curves for both sets of FEHM calculations, varying by a maximum of 15% from the plug flow values, provide an important conclusion with respect to fracture matrix interactions. Because the FEHM calculations so closely match the plug flow approximation and because of the reciprocity exhibited when the particles are injected into the fracture or the matrix, fracture-matrix exchange must be rapid relative to downward transport through the Topopah Spring Tuff (Section 2.3.5.3.2.2.1).

2.3.5.3.3.2.8 Calculating the Amount of Feldspar Dissolved as Water Percolates through the Thermal Field

In this section, the ambient feldspar dissolution rate, the dissolution rate temperature dependence, the model for the thermal field, and the plug flow model for transport through the TSw are combined to evaluate the amount of feldspar that dissolves as the water percolates downward through the TSw to the repository level.

The general process for determining the amount of feldspar dissolved involves discretizing the flow path into several sections and determining an average temperature and residence time for each section. Then the amount of feldspar dissolved is calculated using a temperature-dependent feldspar dissolution rate, based on the activation energy relationship described in Section 2.3.5.3.3.2.5 and the average temperature for the interval. This is done for each interval, and then the total feldspar dissolved is summed up over the entire flow path. Once the starting point is identified, the flow path and temperatures are calculated from the thermal field and the percolation rates used, checking whether climate state boundaries are crossed and adjusting the percolation fluxes accordingly. The results of this calculation are shown in Figure 2.3.5-17 for three locations in the repository, corresponding to three different thermal histories. The first (a) is a cool location, where the drift wall

does not exceed the boiling temperature of water; the second (b) is an average location, where the drift wall exceeds the boiling temperature of water for about 700 years; and the third (c) is a hot location, where the drift wall exceeds boiling for about 1,400 years. The amount of feldspar dissolved rises sharply after closure as the thermal field expands outward around the drift and then falls slowly as the thermal field collapses. The amount of feldspar dissolved varies with the percolation flux and is larger for lower percolation fluxes (e.g., longer residence times), and the peak in the amount dissolved shifts to higher times as percolation flux rate decreases. In locations where a boiling front develops (b and c), the feldspar dissolution rates nearly match during the boiling period; however, after the boiling period, feldspar dissolution rates decrease more slowly in the hotter case. To determine possible seepage water compositions, the calculated amount of feldspar is numerically titrated into a starting water composition and brought to the temperature of interest (SNL 2007b, Section 6.3.2.4.5).

To summarize, water–rock interactions in the thermal zone above the drift are modeled by considering three principal minerals. Calcite is a common fracture mineral in the Topopah Spring Tuff, and waters passing through the rock are treated as being in equilibrium with this phase, based on the observation that geothermal waters are always at saturation with respect to this phase. The tuff itself consists almost entirely of silica polymorphs and alkali feldspars, and, in addition, opal is a common fracture mineral. In the near-field chemistry model, water percolating through the thermal envelope above the drift is treated as being at equilibrium with amorphous silica. This slightly overestimates aqueous silica concentrations at ambient conditions; however, assuming equilibrium with tridymite, cristobalite, or quartz would underestimate aqueous silica concentrations. Alkali feldspar initially present in the tuff has exsolved to varying degrees to alternating potassium- and sodium-rich lamellae. Because the degree of exsolution is variable and because the two phases formed are not pure end-members but vary widely in composition, the alkali feldspars are treated as a single phase, with a kinetically limited dissolution rate, in the near-field chemistry model.

The amount of feldspar dissolved is a primary parameter in determining the composition of potential seepage waters, and it is implemented in the near-field chemistry model as the water–rock interaction parameter, which is tabulated through time as a function of two location-specific parameters, the thermal history and the percolation fluxes. For use in the TSPA, the range of water–rock interaction parameter values is discretized into 11 values. Pore-water compositions are calculated for these 11 values and then interpolated as necessary for intermediate amounts of feldspar dissolution (SNL 2008b, Section 6.3.4.3.1).

2.3.5.3.3.2.9 Liquid-Gas Exchange along the Flow Path

Liquid-gas phase exchange as percolating water moves downward toward the heated repository could have an effect on the composition of the water. Two potentially important processes to consider are evaporation (loss of water vapor) and CO_2 exchange.

Evaporation cannot be an important process as water percolates downward through the thermal gradient, until the drift, or the dryout zone around the drift, is reached. The reason for this is because the ambient liquid water saturation levels in the rock are high (approximately 80%) and will increase as the temperature gradient is established and as hotter, vapor-saturated gas from zones closer to the repository moves upward along fractures and cools, condensing water. Saturation will

also increase at the higher percolation fluxes expected in future climate states. High saturations leave little room for a gas phase, and because of the large volume change associated with the transition from water to water vapor, significant vapor loss is impossible. Vapor transport is orders of magnitude more effective in fractures than in the matrix, but the fracture porosity is only approximately 0.01. At temperatures below boiling, the capacity of air to hold water is lower, and an even larger volume of atmosphere would be required; at 79°C, 1 L of water would saturate over 2,700 L of air. In addition, once a temperature gradient is established, the relative humidity at any point will be close to 100%. This is because the saturation vapor pressure at higher temperatures is greater than at lower temperatures. Water vapor moving down the temperature gradient to lower temperatures will keep the whole system on the temperature-water vapor saturation curve. At 100% relative humidity, with a limited volume of gas, little evaporation or degassing can occur, and water will not significantly concentrate or degas until it hits the low saturation zone around the drift and vapor can be lost into the drift (SNL 2007b, Section 6.3.2.5).

As water percolates downward through the thermal field and heats up, CO_2 is partitioned into the gas phase. This is offset by the effects of feldspar dissolution, which raises the alkalinity and reduces the degree of partitioning into the gas phase. The relative rates of these two processes are important because the degree to which the gas phase acts as an open system (i.e., the amount of CO_2 that would be lost or gained by gas phase advection and mixing) is unknown. Given that matrix saturations are high and fracture porosity is low, it is assumed for the near-field chemistry model that gas phase transport is limited, except for the area immediately around the drift where loss into the drift can occur. Therefore, the gas phase composition at any location in the rock column is determined by assuming equilibrium with the aqueous composition, rather than being controlled by gas phase advection and mixing. This approach is justified because the aqueous phase represents a huge reservoir for CO_2 relative to the gas phase (Yang 2002). Also, the impact of this approach with respect to the in-drift chemical environment (Section 2.3.5.5) is captured in part by providing a range of values for CO_2 within the drift (Section 2.3.5.3.3.2.11).

2.3.5.3.3.2.10 Predicting the Composition of Potential Seepage Waters

To summarize the near-field chemistry model, percolating pore water moves up a temperature gradient as it approaches the drift but does not evaporate or degas significantly until water hits the isotherm representing the saturation temperature for the in-drift vapor pressure; even if that temperature is below the boiling point of water, some of the percolating water evaporates and the residual liquid becomes concentrated at that point. The water just behind the evaporation front is represented by pore water at the temperature of the interface, in equilibrium with a gas phase pCO_2 predicted by ramping the water up to temperature in a closed system (i.e., no degassing), while maintaining equilibrium with calcite and amorphous silica, and titrating in an amount of feldspar determined by the thermal field and flux-dependent flow velocities. The water vapor pressure is maintained at *p*SAT as the temperature increases, so no evaporation occurs. The near-field chemistry model predicts the composition of potential seepage water at the evaporation front, providing starting water compositions for the seepage evaporation model (Section 2.3.5.5). The evaporation front corresponds to the boiling front (96°C) during the boiling period; its location is determined by interpolation between the thermal profiles described in Section 2.3.5.3.3.2.6. Once the drift wall temperature drops below boiling, it corresponds to a location at or near the drift wall (SNL 2007b, Section 6.3.2.4.5).

2.3.5.3.3.2.11 The In-Drift Gas Composition

The in-drift atmosphere consists of air that has diffused or advected into the drift from the surrounding rocks, diluted by water vapor generated by evaporation in the near-field host rock. The amount of dilution can be readily estimated from the vapor pressure of water in the drift, obtained from the output of the multiscale thermal-hydrologic model (SNL 2008a). Carbon dioxide in the drift atmosphere comes from two sources. The first is CO_2 that is released from pore water as it evaporates in the near-field host rock. The amount of CO_2 that is released can be calculated from the molar ratio of carbon to H_2O in the pore water at the evaporating water interface. About half of the inorganic carbon in the water will be released during evaporation to dryness; the rest will precipitate as carbonate minerals (SNL 2007b, Section 6.3.2.8).

The second source of CO_2 is in the gas phase that diffuses or advects into the drift. This is more difficult to constrain. Two bounding cases are used (SNL 2007b, Section 6.3.2.8):

- **Minimum CO_2 Concentration in the Drift—**In this bounding case, gas movement into and out of the drift, and through the mountain, occurs readily through fractures. The CO_2 concentration in the air fraction entering the drift is equal to the ambient CO_2 concentration in the mountain at the repository level (10^{-3} bars; Section 2.3.5.3.2.2.1). The contribution of this to the total CO_2 in the drift atmosphere is equal to this concentration times the mole fraction of air in the drift. Using the ambient CO_2 concentration and summing the CO_2 entering the drift in air with that released as water evaporates at the evaporation front yields a lower bound concentration for CO_2 in the drift.

- **Maximum CO_2 Concentration in the Drift—**Behind the evaporation front, the gas phase fugacity is set to equilibrium with the aqueous phase at the temperature of the evaporation interface, assuming that the water moved up the temperature gradient to the interface without degassing. Treating the drift as a closed system, the in-drift pCO_2 would equal this value, which is an upper bound for CO_2 in the drift.

Combining the lower and upper bounds for the in-drift pCO_2 yields the possible range of CO_2 concentrations in the drift at any given time step. This range is sampled by the TSPA model once per realization, and the relative offset from the nominal value (10^{-3} bars) is carried through the entire time history for that realization (SNL 2007b, Section 6.15.1).

2.3.5.3.3.3 Model Results

In the near-field chemistry model, most mineral precipitation and dissolution reactions are modeled by assuming thermodynamic equilibrium between the solid and aqueous phases. Alkali feldspar dissolution, which has the strongest effect on water composition, is modeled as being kinetically limited, with a rate that is a function of temperature. Hence, species concentrations in solution at any given time and location are largely controlled by the amount of feldspar dissolved along the flow pathway to that point. The strongest controls on this parameter are the temperature profile along the flow path (the temperature at any point controls the feldspar dissolution rate), and the percolation flux, which determines the water–rock contact time (SNL 2007b, Section 6.3.2.6).

To illustrate the calculation of the amount of feldspar dissolved, a simplified example is provided. This example uses a thermal history based on the mean thermal conductivity value, at the location corresponding to a central location in Drift 1 in Figure 2.3.5-14. For this example, a single percolation flux of 4 mm/yr is assumed to apply for all climate periods. The calculation of the water–rock interaction parameter value is performed for potential seepage waters intersecting the drift wall at five different times in the repository history: 2,000, 4,000, 6,000, 10,000, and 20,000 years.

First, the starting elevation above the drift and a starting time are calculated for each case using the percolation flux and the plug flow implementation (Section 2.3.5.3.3.2.7). For the shorter two seepage times, the percolating water starts at about 73 and 145 m above the drift because the time since closure is less than the length of time required to travel 200 m at the given percolation flux (about 5,500 years); the starting time is 50 years (corresponding to the end of the ventilation period). For the later three seepage times, the percolating waters start at the top of the modeled section, 200 m above drift center, at starting times corresponding to the seepage time minus the travel time of 5,500 years. The total distance traveled is discretized into 19 locations (in this example) through time, and the temperature is determined by interpolation between the point-in-time thermal profiles (Figure 2.3.5-15), as a function of time and elevation above the drift. The resulting temperature-flow pathways are shown in Figure 2.3.5-18.

Once a discretized set of temperatures along the flow path has been determined, each pair of adjacent temperatures is averaged, and the average value is used to calculate a temperature-dependent feldspar dissolution rate applicable to the interval between the two points. This rate is used to calculate the amount of feldspar that dissolves as the water percolates through the interval, and total dissolution along the flow path is calculated by summing cumulatively along the flow path. This is shown in Figure 2.3.5-19 for the same five flow pathways shown in Figure 2.3.5-18. The cumulative amount of feldspar dissolved is the water–rock interaction parameter value and is used, in conjunction with the starting water and the drift wall temperature, to determine the composition of potential seepage at the drift wall, as discussed in Section 2.3.5.3.4.

As pore waters percolate downward through the TSw, the types of secondary minerals that form depend on the amount of feldspar that dissolves. The near-field chemistry model predicts the following reactions occur, with increasing amounts of alkali feldspar dissolved:

At low amounts of feldspar dissolved, the following reaction occurs (SNL 2007b, Eq. 6.3-19):

$$\underset{\text{(alkali feldspar)}}{2Na_{0.5}K_{0.5}AlSi_3O_8} + Ca^{2+} + SiO_2(aq) + 7H_2O \rightarrow \underset{\text{(stellerite)}}{½Ca_2Al_4Si_{14}O_{36}{:}14H_2O} + K^+ + Na^+ \quad \text{(Eq. 2.3.5-3)}$$

As this reaction occurs, Ca^{2+} is depleted from solution, and K^+ and Na^+ increase. The solution becomes undersaturated with respect to calcite, and calcite begins to dissolve. The total reaction becomes (SNL 2007b, Eq. 6.3-20):

$$\underset{\text{(alkali feldspar)}}{2Na_{0.5}K_{0.5}AlSi_3O_8} + \underset{\text{(calcite)}}{CaCO_3} + H^+ + SiO_2(aq) + 7H_2O \rightarrow \underset{\text{(stellerite)}}{\tfrac{1}{2}Ca_2Al_4Si_{14}O_{36}{:}14H_2O} + K^+ + Na^+ + HCO_3^-$$

(Eq. 2.3.5-4)

This reaction results in an increase in pH and solution alkalinity with increasing feldspar dissolution; Ca^{2+} concentrations continue to drop as bicarbonate concentrations increase.

Eventually, as greater amounts of feldspar dissolve, K^+ builds up in solution and a potassium-bearing clay phase saturates. In the near-field chemistry model, the potassium-phase is the mineral celadonite, and the reaction becomes (SNL 2007b, Eq. 6.3-21):

$$\underset{\text{(alkali feldspar)}}{6Na_{0.5}K_{0.5}AlSi_3O_8} + \underset{\text{(calcite)}}{2CaCO_3} + 2Mg^{2+} + 4SiO_2(aq) + 16H_2O \rightarrow \underset{\text{(stellerite)}}{Ca_2Al_4Si_{14}O_{36}{:}14H_2O} + \underset{\text{(celadonite)}}{2KMgAlSi_4O_{10}(OH)_2} + K^+ + 3Na^+ + 2CO_2$$

(Eq. 2.3.5-5)

Once celadonite begins to precipitate, further dissolution of feldspar results in a drop in the pH. However, the amount of magnesium in solution is limited. With continued feldspar dissolution, this reaction rapidly becomes inhibited by lack of Mg^{2+}, and the reaction shown in Equation 2.3.5-4 once again becomes dominant. At even higher degrees of feldspar dissolution—only rarely predicted by the near-field chemistry model—sodium- and potassium-bearing zeolites such as phillipsite can saturate and begin to precipitate (SNL 2007b, Section 6.3.2.6).

With respect to the secondary minerals that are predicted to form by the near-field chemistry model, it should be noted that clays and zeolites are compositionally complex minerals that are represented in the thermodynamic database as single, compositionally fixed phases. In the reactions described above, it is appropriate to consider the secondary minerals as representing, progressively, sinks for aluminum and calcium (stellerite); aluminum, potassium, and magnesium (celadonite); and aluminum, sodium, potassium, and calcium (phillipsite) in the near-field chemistry model. While the actual minerals that form may not be chemically identical to the species in the database, the general trends described above are expected to be maintained (SNL 2007b, Sections 6.3.2.6 and 7.1.2.3).

In addition to the reaction of feldspar to form secondary minerals, other processes occur due to the increase in temperature as the water percolates downward. The effect of the increase in temperature is to cause calcite to precipitate, while feldspar dissolution consumes calcite (Equations 2.3.5-4 and 2.3.5-5 above). The relative rates of these two reactions determine whether calcite is predicted to precipitate or dissolve. For ambient conditions, very small amounts of calcite either precipitate or

dissolve. In the simulations for TSPA, calcite is generally predicted to dissolve because of the increase in the feldspar dissolution rate at elevated temperatures (SNL 2007b, Section 6.3.2.6).

Specific effects of thermal-hydrologic processes on water chemistry depend on the intrinsic characteristics of the dissolved species and the types of chemical reactions in which they are involved. The expected behaviors of the major species have already been discussed in Section 2.3.5.3.1.2; in general, the aqueous species most sensitive to processes modeled by the near-field chemistry model are Ca^{2+} and Mg^{2+}, and to a lesser extent, Na^{+} and K^{+}.

With respect to parameters important to TSPA, the most important effects of the processes modeled by the near-field chemistry model, feldspar dissolution and secondary mineral precipitation, are on the pH and the potential pCO_2 range within the drift. The thermal envelope around the drift heats percolating waters, resulting in degassing of CO_2 and an increase in the partial pressure of CO_2 in the gas phase, which is used to represent the maximum pCO_2 in the drift. This is offset by dissolution of alkali feldspar which raises the pH, resulting in partitioning of CO_2 into the aqueous phase. Because feldspar dissolution rates are slow, the temperature effect dominates, and, in general, predicted maximum pCO_2 values in the drift are higher at greater temperatures (SNL 2007b, Section 6.3.2.4.6). The abundance of divalent ions (Ca^{2+} and Mg^{2+}) is an important parameter in the seepage evaporation abstraction, as these ions determine (in part) whether water evaporatively evolves toward acidic calcium chloride-type brines, neutral to moderately acidic sulfate brines, or basic carbonate brines (Section 2.3.5.5.1). Feldspar dissolution and secondary mineral precipitation consume calcium and magnesium from solution and increase the pH, eventually resulting in waters that evaporate to form basic carbonate brines (SNL 2007b, Section 6.13.5.2). Because of the effect on pH, increased water–rock interaction makes potential seepage waters more benign with respect to initiation of localized corrosion of the waste package outer barrier (SNL 2007f, Section 6.4.4.6).

Chloride and nitrate are conserved in the near-field chemistry model, and chloride and nitrate concentrations do not change as the water percolates downward. Similarly, within the seepage evaporation abstraction, chloride-nitrate ratios do not change until a salt phase containing one of these species precipitates (SNL 2007b, Section 6.12.3). However, the relative abundances of the cations in solution determine which salt phase will precipitate and at what relative humidity salt precipitation will occur. Thus, the processes modeled by the near-field chemistry model, which affect cation concentrations, have a significant effect on the relative humidity at which nitrate- or chloride-containing salts precipitate. This is an important TSPA parameter, because TSPA initiates localized corrosion of the Alloy 22 waste package outer barrier if conditions for salt precipitation and, potentially, physical separation of salts from remaining brine, are predicted to occur (Section 2.3.5.5.4.3).

2.3.5.3.3.4 Model Limitations, Approximations, and Uncertainty

Model Limitations—The near-field chemistry model is subject to several limitations. One limitation is that the model inputs are developed using averaged rock hydrologic properties and mineralogies, and transport through the model domain is implemented as plug flow, rather than modeling discrete fracture and matrix interactions. Fast pathways are not considered. As such, it represents the average response for flow transport times through the host rock and not the response to fine-scale temporal or spatial variability. Nonetheless, comparisons of model results with observed mineralogic and pore-water compositional data, as well as measured data from the Drift

Scale Test (Section 2.3.5.3.3.5.3) indicate that the near-field chemistry modeling approach using averaged properties provides an adequate representation of the chemical composition of water that could potentially seep into emplacement drifts, and the composition of the gas phase in the drifts (SNL 2007b, Section 7.4). In addition, hydrologic modeling with FEHM that explicitly included fracture-matrix interactions and used unsaturated zone calibrated hydrologic properties consistent with those used by other unsaturated zone thermal-hydrologic and flow and transport models, demonstrated that fracture-matrix exchange is rapid relative to downward flow, providing confidence in the plug flow approach (Section 2.3.5.3.3.2.7).

An additional limitation of the near-field chemistry model is that it does not incorporate the effects of mineral precipitation and dissolution on hydrologic properties of the rock and does not evaluate the effects of salt precipitation in the dryout zone and re-dissolution when that zone rewets. These processes have been evaluated by the thermal-hydrologic-chemical seepage model. Hydrologic property changes are found to have no significant effect on predicted seepage compositions or on conditions of seepage as represented for TSPA (Section 2.3.5.2.3). Salt re-dissolution during the rewetting period is a short-term transient process that is not significant to repository performance (Table 2.2-5, excluded FEP 2.2.08.04.0A, Re-dissolution of precipitates directs more corrosive fluids to waste packages), and has been shown not to significantly impact seepage composition (Section 2.3.5.2.3).

The near-field chemistry model uses a conduction-only heat transfer solution for calculating the thermal field above the drift; advective and radiative processes are not considered, nor is heat transfer associated with liquid or vapor movement. This approximation captures the most important mode of heat transfer, and is consistent with the implementation for the thermal field in the in-drift condensation model (Section 2.3.5.4.2) and also with the implementation of heat transfer in the submodels of the multiscale thermal-hydrologic model (SNL 2008a, Sections 5.2.1 and 5.2.2).

Propagation of Uncertainty—The input parameters, numerical methods, and approximations used in developing the near-field chemistry model contribute to uncertainties in model output (SNL 2007b, Section 6.12.2.2). Input parameter uncertainties are propagated through the model as described in Section 2.3.5.3.2.2. Uncertainties in the thermal field around the drift are incorporated by (a) use of three different thermal conductivities, in a manner consistent with the multiscale thermal-hydrologic model; and (b) evaluation of the development and evolution of the thermal field at many different locations throughout the repository footprint (SNL 2007b, Section 6.3.2.4.3). Because the near-field chemistry model generates many different thermal histories, which are matched to the most similar multiscale thermal-hydrologic model thermal history, this approach also incorporates model uncertainties with respect to the use of the conduction-only heat transfer solution for the thermal field.

The majority of the uncertainty in the model inputs is incorporated into the predicted amount of feldspar dissolved (the water–rock interaction parameter value; Section 2.3.5.3.2.2.2). Uncertainty in input parameters such as mineral abundances in the repository units, rock hydrologic properties, and timing and temperature of alteration, are incorporated directly into the water–rock interaction parameter value by sampling a distribution around the predicted value. Model uncertainties in the use of the plug flow approximation are evaluated by comparison with FEHM model results and found to be minor; they are reduced further by calibrating the plug flow results to match the FEHM model results (SNL 2007b, Section 6.12.2.3).

The near-field chemistry model parametrically evaluates the effect of percolation flux rates, and the changes in climate states and infiltration rates that control the percolation fluxes and provides a table of water–rock interaction parameter values as a function of sets of percolation flux values. The uncertainty in these parameters is implemented by the TSPA.

2.3.5.3.3.5 Model Support

To build confidence, several components of the near-field chemistry model were evaluated by comparison to ambient pore-water isotopic and major element compositions, measured gas and pore-water data from the Drift Scale Test, and the results of the thermal-hydrologic-chemical seepage model (Section 2.3.5.2.3). Each of these provides support for different components of the near-field chemistry model. Depth-related variations in the strontium isotopic composition of the tuff and pore waters are used to provide support for the alkali feldspar dissolution rate used in the near-field chemistry model (SNL 2007b, Section 7.1.1); trends in pore-water composition support both the alkali feldspar dissolution rate used and the general chemical reactions (e.g. secondary minerals formed) predicted by the model (SNL 2007b, Section 7.1.2); Drift Scale Test gas compositions provide confidence in the predicted range of in-drift CO_2 concentrations (SNL 2007b, Section 7.1.4); and comparison to thermal-hydrologic-chemical simulations using TOUGHREACT provide confidence in the simplified transport features of the near-field chemistry model, as well as the general chemical reactions predicted (SNL 2007b, Section 7.1.3).

2.3.5.3.3.5.1 Strontium Isotopic Data

As water percolates through the unsaturated zone, it reacts with minerals in the rock. The devitrified rhyolitic core of the TSw, which is the model domain for the near-field chemistry model, is enriched in ^{87}Sr relative to the pore water, so reaction with the tuff results in a systematic increase in the $^{87}Sr/^{86}Sr$ ratio of the pore water as it percolates through this part of the geologic section. Because the devitrified rhyolitic tuff consists almost entirely of silica polymorphs and feldspar (SNL 2007b, Section 4.1.6), and silica polymorphs contain no significant strontium, the trends in pore-water isotopic composition can be used to estimate the rate of feldspar dissolution in the geologic interval considered in the near-field chemistry model (SNL 2007b, Section 7.1.1). Although calcite is present in the rock and typically contains a few hundred mg/kg strontium (Paces et al. 2001, Appendix 3), it contributes little to the total strontium concentration in the rock because it is present in only small amounts. It does not contribute at all to the rate of strontium release by the rock because it precipitates rather than dissolves as the percolating water moves downward through the rock.

The trend of increasing pore water $^{87}Sr/^{86}Sr$, or $\delta^{87}Sr$ (a normalized representation of $^{87}Sr/^{86}Sr$) with depth has been used to estimate pore-water flow velocities and rates of whole-rock dissolution along the entire flow path through the unsaturated zone (Johnson and DePaolo 1994; Marshall and Futa 2001). To evaluate the feldspar dissolution rate in the rhyolitic center of the TSw, the same approach was used, although the form and parameterization were slightly modified to represent dissolution of a single mineral phase, and the isotopic data were limited to the geologic section of interest.

The approach used to evaluate feldspar dissolution rates is based on the formalism presented by Johnson and DePaolo (1994), who derive a specialized case of the transport equation for evaluating the change in the strontium isotopic composition in the groundwater, incorporating a

source term representing strontium release by mineral dissolution and a sink representing mineral precipitation. If dispersion is negligible relative to advective transport, and steady state is assumed, the general equation simplifies to the following (SNL 2007b, Eq. 7.1-7):

$$R_{feldspar} = \frac{\left(\frac{\partial \delta_{porewater}}{\partial z}\right) v}{W_{feldspar} M (\delta_{feldspar} - \delta_{porewater}) \left(\frac{c_{feldspar}}{c_{porewater}}\right)} \qquad \text{(Eq. 2.3.5-6)}$$

where $R_{feldspar}$ is the feldspar dissolution rate; $W_{feldspar}$ is the mass fraction of feldspar in the rock, measured from field data; M is the rock:water mass ratio, calculated from measured rock hydrologic properties; feldspar and pore water are the feldspar and starting pore-water values for $\delta^{87}Sr$; $c_{feldspar}$ and $c_{porewater}$ are the strontium concentrations in the feldspar and pore water; and $\partial\delta_{porewater}/\partial z$ is the observed change in isotopic composition of the pore water with depth. Finally, the velocity of the pore water, v, is treated parametrically in this analysis and is calculated for percolation flux values ranging from 1 mm/yr to 15 mm/yr using the plug flow implementation of the near-field chemistry model. This range was chosen because it represents the most probable range of values for fluxes at the PTn/TSw boundary for the present-day climate state.

Strontium isotopic data from two boreholes through the TSw, SD-7 and SD-12, were used in this evaluation. Isotopic data were collected for core samples of the rock units throughout the geologic section and also for soluble salts leached from crushed core samples. Measured rock $\delta^{87}Sr$ values were used for the feldspar, because it is the only phase containing significant strontium, and the concentration of strontium in the feldspar was calculated from the measured rock concentration and the mass fraction of feldspar in the rock. The assumed pore water $\delta^{87}Sr$ values are those measured for the core leachate, and the pore water strontium concentration is calculated from the leachate values and rock-water mass ratio. The pore water strontium concentration is the value with the greatest uncertainty in the analysis and this was carried through to evaluate its importance.

The strontium isotopic data for the pore waters from the entire sampled depth interval of these boreholes are shown in Figure 2.3.5-20. The upper and lower boundaries for the section representing the devitrified core of the TSw, which is the near-field chemistry model domain, are shown. The $\delta^{87}Sr$ values for the pore water increase systematically with depth across this interval. Rock $\delta^{87}Sr$ values are not shown but are always higher than the pore-water values in the rhyolitic center of the TSw, covering a range of 8 to 12 per mil and decreasing gradually with depth. In general, the pore-water values tend to evolve toward the rock values in any part of the section. The relationship is more complex in higher units in the geologic section because the latitic parts of the PTn and upper TSw have lower $\delta^{87}Sr$ values and possibly because of extensive zeolitization and scavenging of soil-derived strontium from the percolating waters in the PTn.

The feldspar dissolution rates estimated from the strontium isotopic data are compared to the near-field chemistry range in Figure 2.3.5-21. For the near-field chemistry model, the feldspar dissolution rate is implemented as a beta distribution, with a mean value of 5.6×10^{-17} mol/(kg tuff) per second and maximum and minimum values of 1.0×10^{-16} mol/(kg tuff) per second and

1.3×10^{-17} mol/(kg tuff) per second, respectively (SNL 2007b, Section 7.1.1.4). The rates calculated using strontium isotopic data from boreholes SD-7 and SD-12 vary as a function of the assumed percolation flux; the range in Figure 2.3.5-21 corresponds to fluxes from 1 mm/yr to 15 mm/yr. For SD-7, the dissolution rates vary from 8.4 10^{-17} mol/(kg tuff) per second (percolation flux 1 mm/yr) to 1.3×10^{-15} mol/(kg tuff) per second (percolation flux 15 mm/yr). For SD-12, the rates vary from 1.1×10^{-16} mol/(kg tuff) per second (percolation flux 1 mm/yr) to 1.6×10^{-15} mol/(kg tuff) per second (percolation flux 15 mm/yr). The rates from the two boreholes are very similar and are slightly higher than those used in the near-field chemistry model. However, the difference is generally less than an order of magnitude, and at percolation fluxes of a few millimeters per year, which are most consistent with the inferred age of the waters in the lower TSw (5,000–10,000 years; Yang 2002, Table 2), the near-field chemistry model and strontium ranges overlap. If the uncertainty in the input data for the strontium isotope calculations is included (lighter shaded region in Figure 2.3.5-21), then there is even greater overlap between the rates derived from the two methods.

Although the feldspar dissolution rates determined from the strontium data are generally slightly higher than the range used by the near-field chemistry model, the ranges overlap. The dissolution rates vary by less than an order of magnitude, providing corroboration for the feldspar dissolution rates used.

2.3.5.3.3.5.2 Prediction of Ambient Pore-Water Compositional Trends and Alteration Mineral Assemblages

As pore waters percolate downward through the geologic section, their compositions change. Viewed on a unit-to-unit basis, these changes are subtle and are masked by the low sampling density, the variable thickness of the overlying rock units that percolating water has contacted, and the effect of combining water analyses from different depths within the unit itself. Despite these complications, general trends in pore-water composition between waters in the PTn hydrogeologic unit and the waters in the underlying TSw are observed, which can be used to evaluate the general processes modeled and chemical reactions predicted by the near-field chemistry model. All pore-water analyses used in this comparison passed the screening analysis for microbial activity during core storage that is discussed in Section 2.3.5.3.2.2.1.

The near-field chemistry model predicts potential seepage water compositions by (1) implementing a thermal gradient calculated using a conduction-only line source heat flow solution, modified for the natural geothermal gradient; (2) assuming the water is in equilibrium with calcite and amorphous silica; (3) summing the amount of alkali feldspar that dissolves into water as it percolates downward, using a temperature-dependent feldspar dissolution rate; (4) implementing transport as a function of percolation flux, using plug flow; and (5) assuming that the aqueous phase controls the local pCO_2. The same general approach is used to predict ambient compositional trends as waters percolate through the TSw, but there is no thermal overprint; the ambient geothermal gradient based on temperature data from borehole SD-12 (SNL 2007b, Section 6.3.2.4.3) is used. The predicted geothermal gradient changes from 19.1°C at the top of the devitrified core of the TSw (100 m) to 23.4°C at the repository level, 300 m below the surface.

Transport times through the TSw are assumed to be about 10,000 years based on ^{14}C residence times from borehole gas analysis calculated by Yang (2002, Table 2). This is also in agreement with

estimates, based on pore-water hydrogen isotope data, that waters at the base of the TSw are more than 10,000 years old and isotopically reflect the cooler climate of the last ice age. Because pore-water samples from the TSw come from all levels in the unit, this age is assumed to be the maximum transport time. The pCO_2 at the top of the Tptpul is assumed to be 10^{-3} bar (0.1%) based on the measured CO_2 concentrations in borehole UZ-1 over the time interval from 1988 to 1994 (SNL 2007b, Figure 7.1-5). The pCO_2 is not held fixed but rather is assumed to remain in equilibrium with the aqueous phase as the water percolates downward.

The reactions that are predicted to occur in the near-field chemistry model are discussed in (Section 2.3.5.3.3.3). As small amounts of feldspar dissolve, stellerite ($Ca_2Al_4Si_{14}O_{36}$:$14H_2O$) precipitates and alkali feldspar and calcite are dissolved (Equation 2.3.5-4). This reaction results in increased pH and solution alkalinity with increasing feldspar dissolution. At higher amounts of feldspar dissolution, celadonite ($KMgAlSi_4O_{10}(OH)_2$) begins to precipitate, consuming aqueous Mg^{2+} as well (Equation 2.3.5-5). Once celadonite begins to precipitate, further dissolution of feldspar results in a drop in the pH. However, the amount of magnesium in solution is limited, and with continued feldspar dissolution, this reaction rapidly becomes inhibited by lack of Mg^{2+}, and Equation 2.3.5-4 once again becomes dominant. At levels of feldspar dissolution higher than those observed under ambient conditions, sodium and potassium-bearing zeolites such as phillipsite can saturate and precipitate.

In addition to the reaction of feldspar to form secondary minerals, other processes occur due to the temperature change as the water percolates downward. Even in the ambient case, these reactions are significant with respect to the water composition. The increase in temperature causes CO_2 to degas from solution, and the rise in pCO_2 results in a slight decrease in pH. A very small amount of calcite precipitates due to the retrograde solubility of this mineral. Both calcium and carbonate concentrations decrease, while there is a slight increase in the silica concentration because silica polymorphs are more soluble with increasing temperature.

The predicted trends in water chemistry are shown in Figure 2.3.5-22. In each of these plots, PTn waters are plotted with TSw waters. The TSw waters are divided into those from the upper two rhyolitic units (the Tptpul and Tptpmn) and the lower two units (Tptpll and Tptpln) to illustrate that the chemical differences between the PTn and TSw waters are not solely due to glass dissolution in the PTn; the same chemical trends are observed between the upper and lower TSw samples. The predicted evolutionary paths of the waters are also indicated, assuming feldspar dissolution rates equal to the mean and maximum rates used in the near-field chemistry model; the maximum rate is about twice the mean rate of 1.1×10^{-15} mol/L per second (Section 2.3.5.3.3.2.5). Also shown are the evolutionary paths using feldspar dissolution rates of 5 times the mean rate. Potassium is the most sensitive measure of feldspar dissolution in the pore waters, because, although potassium and sodium are released at an equal rate by alkali feldspar dissolution, the initial aqueous potassium concentrations are much lower than the sodium concentrations, so the relative change in concentration is greater. Calcium is also quite sensitive, as it is depleted from solution by precipitation of stellerite and is also affected by the change in calcite solubility due to the geothermal gradient. Potassium and calcium concentrations in PTn and TSw waters are plotted against each other in Figure 2.3.5-22 (upper). TSw data are shown for an equilibration temperature of 23.4°C. The TSw data represents samples from throughout the unit, so the actual temperature would have ranged from 19.1°C to 23.4°C, however, effect of the temperature is minor relative to the difference between PTn and TSw waters. Also shown are the evolutionary pathways for the PTn waters,

assuming the mean, maximum, and 5 times the mean near-field chemistry model feldspar dissolution rates, and a 10,000-year transport time. The PTn waters are systematically more calcium-rich and potassium-poor than the TSw water. The calculated evolutionary paths illustrate that the major components of the near-field chemistry model (feldspar dissolution, equilibrium with calcite, and the local gas phase being controlled by equilibrium with the water) can account for the general compositional changes observed in the pore waters, and simulations using the mean and the maximum near-field chemistry model feldspar dissolution rates accurately predict the degree of change. In this plot, the simulations using 5 times the mean near-field chemistry model feldspar dissolution rate over-predict the degree of compositional change.

The ratio of divalent to monovalent cations is plotted against the total carbon concentration in Figure 2.3.5-22 (lower). The predicted evolution of the PTn waters at feldspar dissolution rates consistent with, or slightly larger than, the baseline near-field chemistry model rates is consistent with observed pore water compositional trends. The lower TSw waters suggest a slightly higher dissolution rate, although this may be due to differences in the composition of Pleistocene relative to modern infiltration. The near-field chemistry model predictions capture the general compositional trends observed in the pore water. An inflection for some of the 5 × simulations occurs when celadonite starts to precipitate and the pH begins to drop and captures the upturn in the data at lower values of the divalent/monovalent ion ratio. The lower TSw samples are well predicted by this inflection, and this might indicate that the near-field chemistry model feldspar dissolution rate is slightly low. However, the possibility that the difference between the PTn waters and the TSw waters might be in part due to glass dissolution in the PTn, or in the upper TSw, must be considered. The PTn waters were not collected at the base of that unit, but throughout it.

Predicted CO_2 partial pressures and pH values through the TSw offer some constraint on the feldspar dissolution rate. Model predictions for gas-phase CO_2 concentrations were compared with the measured field data borehole USW UZ-1. In general, the measured data cluster tightly around 0.1% CO_2 (10^{-3} bars) and show almost no variation throughout the rhyolitic TSw section, the exception being the measured data at a depth of about 160 meters below the PTn, which indicate a slightly lower pCO_2 than the data sets from other levels. The model pCO_2 predictions for the mean and maximum near-field chemistry model rates are consistent with the measured values from borehole UZ-1. However, for simulations using higher feldspar dissolution rates, 5 times and 10 times the mean rate, predicted pCO_2 values are significantly below the observed range. This is because the higher rates result in a relatively large increase in alkalinity, and CO_2 partitions into the aqueous phase.

Similarly, for the range of feldspar dissolution rates implemented in the near-field chemistry model, the predicted pH values are similar to the measured range, which varies from 6.7 to 8.3. However, at feldspar dissolution rates of 5 to 10 times higher than the mean near-field chemistry model, predicted values fall between 8.0 and 8.5, and a few samples in the 10 × case exceed 9.0. Thus, measured pH and CO_2 partial pressure data are more consistent with the range of feldspar dissolution rates implemented by the near-field chemistry model than with rates 5 to 10 times higher.

Observed Mineral Assemblages—The near-field chemistry model assumes pore-water equilibrium with respect to calcite and amorphous silica. This approach is justified in Section 2.3.5.3.3.2.4 on the basis of generally observed trends in geothermal fields. The

observation of calcite and opal on fracture surfaces throughout the TSw (Paces et al. 2001, p. 7), and the abundance of other silica polymorphs in the matrix of the tuff corroborates the use of these phases.

Calcite precipitates as water percolates downward through the TSw unit under ambient conditions and has been doing so for millions of years (Paces et al. 2001). This is probably due to the geothermal gradient; the increase in temperature with depth lowers the solubility of calcite. The observation of calcite precipitation provides limits on possible rates of feldspar dissolution because the alteration reactions consume calcium from solution and result in calcite dissolution. Simulations with no feldspar dissolution predict minor amounts of calcite precipitation due to the geothermal gradient. Using the near-field chemistry model mean feldspar dissolution rate, minor calcite dissolution is generally predicted, although in a few cases precipitation occurs. However, using feldspar dissolution rates of 5 times and 10 times the mean near-field chemistry model rate, calcite is predicted to dissolve at amounts corresponding to approximately 0.1 and 0.5 millimoles per liter, respectively. Hence, the observation of calcite precipitation under ambient conditions suggests that the near-field chemistry model mean feldspar dissolution rate might be a maximum value and that rates of 5 times and 10 times the mean near-field chemistry model rate are too fast to be representative of the ambient case.

The near-field chemistry model predicts the formation of the alteration phases stellerite ($Ca_2Al_4Si_{14}O_{36}:14H_2O$); celadonite ($KMgAlSi_4O_{10}(OH)_2$); and, at the highest amounts of feldspar dissolved, phillipsite ($K_{0.7}Na_{0.7}Ca_{1.1}Al_{3.6}Si_{12.4}O_{32}:12.6H_2O$). Zeolites are commonly observed associated with vitric horizons at Yucca Mountain, especially near the water table. These are mostly clinoptilolite and mordenite, although heulandite and chabazite are also found in the zeolitic zones. The near-field chemistry model does not predict the formation of these phases, but they appear to be dominantly associated with alteration of the vitric zones at Yucca Mountain, and the model domain considered by the near-field chemistry model is the devitrified rhyolitic core of the TSw, which contains no glass. Zeolites are much less abundant in the devitrified TSw rhyolite, but within this zone, stellerite is common in fractures (Bish et al. 2003). It covered over 40% of the fracture surface in borehole core ESF-HD-TEMP-2 (SNL 2007g) and has been observed as a significant component of the tuff in borehole UZ-16, where it comprises, on the average, 3% of the rock, for an interval of over 100 m (Chipera et al. 1995). At the latter location, concomitant decreases in feldspar suggest that stellerite may have formed at the expense of feldspar by scavenging calcium out of groundwater, exactly the reaction predicted by the near-field chemistry model. These common occurrences of stellerite in the devitrified rhyolite offer corroboration of one of the dominant reactions predicted by the near-field chemistry model.

Celadonite has not been observed at Yucca Mountain. Commonly observed clay minerals at Yucca Mountain include illite and smectite. Illite is chemically and structurally very similar to celadonite; both are potassium- and magnesium-bearing clays, capable of having varying amounts of (Mg + Al) substituting for (K + Si) in the structure. The predicted occurrence of celadonite as opposed to illite may be a function of the particular fixed compositions present in the thermodynamic database used in the model. Celadonite is defined as $KMgAlSi_4O_{10}(OH)_2$, and illite, as $K_{0.6}Mg_{0.25}Al_{1.8}Al_{0.5}Si_{3.5}O_{10}(OH)_2$. Given the potential compositional variation within these minerals, and the fact that they are represented in the thermodynamic database as single, compositionally-fixed phases, these two phases can be considered more or less equivalent, both representing sinks for aluminum, potassium, and magnesium in the near-field chemistry model.

Smectites are not predicted to form in the near-field chemistry model, although they are observed as a common alteration product in the rock. This may be a database limitation; several smectite clays are in the thermodynamic database, but they are fixed compositions, usually end-member compositions, which may not saturate under conditions when a mixed-phase would. Alternatively, the smectite minerals may have formed early in the history of the tuff, when high temperatures persisted for at least a few million years, and the conditions of secondary mineral formation may have differed from the modeled conditions.

As with the clays, the zeolites have very complex, variable compositions that are represented in the database as a few fixed-composition phases. Phillipsite is represented in the database as $K_{0.7}Na_{0.7}Ca_{1.1}Al_{3.6}Si1_{2.4}O_{32}$:12.6$H_2O$. Although it has been observed as a rare mineral associated with altered vitric material at Yucca Mountain (Bish et al. 2003, p. 1893), other zeolites such as clinoptilolite, heulandite, mordenite, and chabazite are more common. These minerals are present in the thermodynamic database as single species or, for clinoptilolite, as a few end-members. Given the simplicity of the representations in the database, it is most accurate to think of these potassium- and sodium-bearing zeolites as a group, representing mineral sinks for potassium and sodium once the solution saturates with respect a given zeolite. Phillipsite is the solubility-limiting phase that is predicted to form first; if it is suppressed, other sodium, potassium, (±calcium) zeolites will form. Hence, phillipsite represents the sodium- and potassium-bearing zeolites as a group, and its predicted occurrence is corroborated by the general observation of sodium-potassium-calcium-bearing zeolites as secondary minerals at Yucca Mountain.

2.3.5.3.3.5.3 Comparisons to the Thermal-Hydrologic-Chemical Seepage Model

The near-field chemistry model calculates the interaction between percolating pore waters and the rock matrix of the TSw in order to represent the time-dependent chemistries of fluids entering the drift. Another model that has been used to investigate similar processes is the thermal-hydrologic-chemical seepage model (Section 2.3.5.2.3; SNL 2007c). The thermal-hydrologic-chemical seepage model evaluates these processes at only a single drift location at a time and is not used for TSPA because it does not readily allow incorporation of spatial variability in thermal history, rock properties, or percolation fluxes into the performance assessment model. In addition, it does not evaluate the effects of axial transport, and the degree to which cooler drift-end locations act as sinks for water vapor, and for CO_2. While the near-field chemistry model also does not explicitly model axial transport, the effects of this process with respect to in-drift CO_2 pressures are captured by the bounding approach used. The thermal-hydrologic-chemical seepage model is primarily used to corroborate the near-field chemistry model, and evaluate the impact of mineral dissolution/precipitation in the rock surrounding the drift on the conditions of occurrence and composition of potential seepage for FEP screening arguments (Section 2.3.5.2.3). In this section, the thermal-hydrologic-chemical seepage model is used to corroborate the near-field chemistry model by comparing results generated using many of the same input values.

An overview of the thermal-hydrologic-chemical seepage model is provided in Section 2.3.5.2.3. Although both the near-field chemistry and the thermal-hydrologic-chemical seepage models predict the composition of potential seepage into the repository drifts, they differ significantly in terms of implementation. The thermal-hydrologic-chemical seepage model is fully coupled, estimating multiphase mass transport by simultaneously solving mass balance, mass action, and kinetic equations affecting all dissolved and gas phase (in particular CO_2) species; the near-field

chemistry model predicts dissolved phase transport under bounding CO_2 scenarios. The thermal-hydrologic-chemical seepage model relies on a dual-continuum model prediction of fluid flow, while the near-field chemistry uses a plug-flow approximation, optimized by calibration against dual-continuum FEHM simulations. The thermal-hydrologic-chemical seepage model attempts to predict how reaction-induced changes in rock porosity might affect whole rock permeability; the near-field chemistry holds rock hydrologic properties constant. The near-field chemistry model uses a field-based feldspar alteration rate and assumes equilibrium with calcite and amorphous silica to predict pore-water evolution; the thermal-hydrologic-chemical seepage model implements kinetically-limited mineral dissolution/precipitation rates, based on laboratory measurements combined with reactive surface areas based on geometric calculations, and reduced to account for the generally slower rates observed in field studies (White 1995, Table 7). The near-field chemistry model generates time-dependent fluid chemistries at 16 locations in each of seven drifts distributed across the repository footprint; the thermal-hydrologic-chemical seepage model uses a model grid representing a two-dimensional perpendicular slice across the drift at a single location. Neither of the two models actually predicts seepage compositions but instead sample the composition of waters just behind the evaporation front (see sensitivity analyses in Section 2.3.5.2.3 for an exception to this). The thermal-hydrologic-chemical seepage model samples pore-water compositions at the highest flux zone proximal to the drift crown, incorporating the effects of boiling, evaporation, and condensation; the near-field chemistry model focuses primarily on fluid-rock interactions as the pore water percolates through the TSw to the evaporation front around the drift and does not incorporate boiling and condensation effects. Neither model explicitly considers ion exchange onto clays or zeolites, but both consider these implicitly, as the databases used for both models include many end-member clay and zeolite phases. Finally, neither model explicitly considers gas phase axial transport through the drift, but the near-field chemistry model considers this possibility in assessing the uncertainty on pCO_2.

The near-field chemistry and thermal-hydrologic-chemical seepage models have been independently derived and are implemented with different software. However, both models use many of the same inputs to maintain consistency with other unsaturated zone thermal-hydrologic flow and transport models. Both models implement the same thermal loading, initial rock hydrologic properties based on the unsaturated zone calibrated properties set, rock mineralogies based on the field data as abstracted in the geologic framework model, and the same starting water compositions. The only major inputs to the near-field chemistry model that do not match those used in the thermal-hydrologic-chemical seepage model are the feldspar dissolution rate and the activation energy (*Ea*) for feldspar dissolution. The range of feldspar dissolution rates used in the near-field chemistry model, which is based on site-specific data and is corroborated by the pore-water strontium isotopic data (Section 2.3.5.3.3.5.1) and which is also propagated through the model to include uncertainty, is considered more representative. In order to do a relevant comparison between the two models, the near-field chemistry model was run using the thermal-hydrologic-chemical seepage model feldspar dissolution rate and *Ea* values. The thermal-hydrologic-chemical seepage model implements two feldspar compositions, one representing the matrix "sanidine" in the TSw, equivalent to the alkali feldspar in the near-field chemistry model, and the other representing the trace plagioclase phenocrysts in the TSw. The "sanidine" rate was used in this comparison. The thermal-hydrologic-chemical seepage model feldspar dissolution rate is approximately seven times the near-field chemistry rate at 23.4°C and because of a higher activation energy for feldspar dissolution, approximately 21 times the near-field chemistry model rate at 96°C.

The final input parameters for the models are the infiltration fluxes; the values used were 7.96 mm/yr (0 to 600 years), 12.89 mm/yr (600 to 2,000 years), and 20.45 mm/yr (2,000 to 10,000 years, extended to 100,000 years), values representing the means for the 30th percentile infiltration maps for the present-day, monsoonal, and glacial transition climate states, respectively. The starting water for both simulations was the Group 3 representative water (ESF-HD-PERM-3/34.8-35.1/Alcove 5). Thermal histories were matched by calculating the thermal measure (the sum of the drift wall boiling time in years and the maximum drift wall temperature in degrees Celsius) for the thermal-hydrologic-chemical seepage model simulation and using it to select the set of near-field chemistry model output with the most closely matching thermal measure (Section 2.3.5.3.4).

The results of the comparison are shown in Figure 2.3.5-23. At any given point in time in the figure, a range of compositions is shown for the thermal-hydrologic-chemical seepage model data, representing the six highest-flux nodes above the drift-locations likely to represent possible crown seepage into the drift. Also shown are the potential seepage water compositions predicted by the near-field chemistry model, using the same feldspar dissolution rate and activation energy used by the thermal-hydrologic-chemical seepage model. The near field chemistry model does not model condensation or evaporation, so for comparison purposes all parameters values in Figure 2.3.5-23 are normalized to the concentration of chlorine, which is conserved in both models. The near-field chemistry model incorporates an uncertainty in the water–rock interaction parameter value; results are shown in Figure 2.3.5-23 for the mean, maximum, and minimum water–rock interaction parameter values at each time step, defining the uncertainty range that is sampled by the TSPA model. For the line representing the maximum water–rock interaction parameter value, results are not predicted if the water–rock interaction parameter value exceeds the maximum value evaluated by the near-field chemistry model. This is not a conceptual limitation but rather a limitation on the range of feldspar dissolution rates used to calculate water–rock interaction parameter values in the near-field chemistry model. This limitation occurs at the maximum of the thermal period when host rock temperatures exceed the boiling point of water, and seepage does not occur (Section 2.3.3.3). The near-field chemistry model was not designed to represent such conditions because it does not include the processes of evaporation and condensation.

Mean predicted sodium and potassium profiles from the thermal-hydrologic-chemical seepage model and near-field chemistry model outputs are similar, and generally within 50% of each other throughout each simulation. Sodium and potassium profiles (and to a lesser extent, pH) largely result from temperature-dependent feldspar alteration. The general agreement points to the importance of feldspar dissolution to the geochemical evolution predicted by both the thermal-hydrologic-chemical seepage and near-field chemistry models. Feldspar dissolution affects the pH by raising solution alkalinity, and the resulting increased bicarbonate concentrations depress calcium because of limiting calcite solubility. Predicted pH values diverge during the boiling period, but are within 0.4 units of each other in the critical post-drift wall boiling period (seepage does not occur until boiling ceases at the drift wall approximately 1,300 years after closure for the considered repository-center location). Calcium levels are affected by calcite equilibrium, pH, and equilibria with calcium-bearing silicate phases, the same factors that control predicted CO_2 levels in the near-field chemistry model. Although general trends in predicted calcium levels are the same between the two models over the whole time span, the otherwise close agreement does not exist from approximately 400 to 4,000 years. Over this time interval, the thermal-hydrologic-chemical seepage model predicts lower calcium values. This is due to the higher pH values and carbonate

concentrations predicted by the model during this time interval, limiting calcium concentrations by precipitation of calcite. All of these differences can largely be traced back to differences in the predicted CO_2 concentrations described later in this section. However, the uncertainty bands in the near-field chemistry results capture most features of the thermal-hydrologic-chemical seepage model results, with one exception discussed below.

Near-field chemistry model-predicted silicon/chlorine values are a factor of three to eight times higher than those predicted by the thermal-hydrologic-chemical seepage model, possibly reflecting kinetic limitations on the dissolution rates of amorphous silica and other silica polymorphs in the thermal-hydrologic-chemical seepage model; both models use the same thermodynamic data for SiO_2(am). Note that the pH, buffering capacity, and potential corrosivity of seepage are relatively insensitive to dissolved SiO_2(aq) levels.

To compare the pCO_2 data from the near-field chemistry model with that from the thermal-hydrologic-chemical seepage model, equivalent data in terms of spatial location and thermal history must be extracted from their respective outputs. The near-field chemistry model provides potential seepage water compositions through time, from which maximum and minimum values of in-drift pCO_2 are calculated for the in-drift seepage dilution/evaporation abstraction, while the thermal-hydrologic-chemical seepage model provides a single time history of the in-drift pCO_2.

The near-field chemistry model and thermal-hydrologic-chemical seepage model predictions for pCO_2 are shown in Figure 2.3.5-24. The near-field chemistry model pCO_2 range captures the thermal-hydrologic-chemical seepage model results for most for the first 1,200 years. The results for the period from 50 to 100 years do not match, but this is in part because only 50- and 100-year data points were calculated for the near-field chemistry model. Over the 50 to 100-year time interval, the thermal-hydrologic-chemical seepage model predicts pCO_2 values that are lower than the amount of CO_2 which would be released by the boiling pore water. Once the drift wall temperature drops below boiling, after 1,200 years, the thermal-hydrologic-chemical seepage model predicts a rapid rise in pCO_2 exceeding the maximum range of the near-field chemistry model for several thousands of years. At longer times, both models eventually converge back to their starting values, although this is somewhat above 10^{-3} bars for the thermal-hydrologic-chemical seepage model. The differences between the two models are attributed to differences in the transport assumptions, particularly the effect of axial gas-phase transport in the drift on pCO_2. In the thermal-hydrologic-chemical seepage model, water vapor displaces most of the non-condensable gases in the drift during the initial boiling period, resulting in very low partial pressures of CO_2; in a three-dimensional model, axial transport and condensation of water vapor in the cooler parts of the drift results in lower relative humidity values in the drift, and less displacement of non-condensable gases (SNL 2008a, Section 7.8[a]). After the boiling period in the thermal-hydrologic-chemical seepage model, CO_2 concentrations in the drift increase markedly as displaced CO_2 migrates back to the drift. In a three-dimensional drift, condensation of cooler water at the drift ends will provide a sink for the CO_2, limiting buildup.

The thermal-hydrologic-chemical seepage model CO_2 predictions show similar behavior to the near-field chemistry model minimum pCO_2 values during the boiling period and transition, then show similar behavior to the near-field chemistry model maximum pCO_2 values at longer times. Thus, for the thermal-hydrologic-chemical seepage model, the composition of the gas phase is

controlled dominantly by the boiling process during the boiling period, and by equilibrium with the fluid phase in the rock after the boiling period. Because the effect of axial transport on the gas phase composition is poorly constrained, the near-field chemistry model uses these cases as end-members, and does not attempt to refine predicted in-drift CO_2 concentrations further.

2.3.5.3.3.5.4 Comparison to Drift Scale Test Gas Phase Data

In this section, measured data from the Drift Scale Test are compared to results predicted by the near-field chemistry model. The Drift Scale Test was carried out in the ESF. It was a large-scale test to evaluate the coupled thermal, hydrologic, chemical, and mechanical processes that take place in unsaturated fractured tuff over a range of temperatures (approximately 25°C to 200°C). The Drift Scale Test consisted of a 50-m-long drift, 5 m in diameter, with nine heaters placed axially in the drift to simulate waste packages. Secondary heaters were placed in boreholes extending outward from the drift, to simulate the effects of adjacent drifts. The Drift Scale Test heaters were activated on December 3, 1997, and switched off on January 14, 2002, and since that time the test area has been slowly cooling. Water and gas samples were collected from packed borehole intervals surrounding the drift. The Drift Scale Test borehole water compositions do not provide a useful comparison for the near-field chemistry model, because the near-field chemistry model does not model the processes of condensation and evaporation, which are the dominant processes affecting the borehole waters. Feldspar dissolution is too slow a process to affect the water compositions over the duration of the Drift Scale Test.

Drift Scale Test gas phase data and borehole and drift wall temperature data were used to corroborate the near-field chemistry model in-drift pCO_2 predictions. Gas samples were collected from packed-off intervals in boreholes extending through the heated zone around the drift. Additional gas samples were taken from the observation drift, which did not significantly heat, and from the heated drift itself, after the boiling period. Gas samples were collected from February 9, 1998, to November 29, 2005. Prior to evaluating the Drift Scale Test gas phase CO_2 data, the raw data were corrected for condensation of water vapor from the gas phase during sampling, as well as for a systematic analytical error in some measurements.

Corrected gas-phase CO_2 concentrations are shown in Figure 2.3.5-25. Three different pCO_2 data sets, borehole, in-drift, and observation drift, are shown. One borehole data set, from borehole BH-185 is plotted separately; this borehole has consistently higher pCO_2 values than the other boreholes. These values presumably represent pCO_2 levels in equilibrium with pore waters in the rock, although the degree of connection with the drift is not known. The in-drift pCO_2 data shown were collected only after the drift wall cooled back below boiling. The observation drift was open to the atmosphere and did not significantly heat up during the test; measured pCO_2 values average $10^{-3.42}$, essentially identical to the current atmospheric levels. After the heaters were turned off, as the drift and the surrounding rock cooled, the range of observed pCO_2 data narrowed.

The near-field chemistry model predicts a range of pCO_2 values as a function of (1) the starting water; (2) the amount of feldspar dissolution; and (3) the temperature at the evaporation front (either 96°C, or the drift wall temperature). The maximum value of that range is predicted on the basis of equilibrium with the predicted pore-water compositions at the temperature at the evaporation front. The minimum value assumes that the in-drift atmosphere is a mixture of air with the ambient repository-level pCO_2 (10^{-3} bars) and water vapor generated by evaporation of the pore

water at the evaporation front, which releases some CO_2 as it evaporates (Section 2.3.5.3.3.2.11). With respect to the Drift Scale Test, at any given time, the predicted near-field chemistry maximum value should bound the upper range of the observed data, which represents equilibrium with the local pore water, while the predicted near-field chemistry minimum value should bound the lower range of the observed data, representing dilution by water vapor.

Two possible choices for the starting water were considered, the Group 3 and Group 4 representative waters, both of which were collected from the HD-PERM boreholes in Alcove 5, near the site of the Drift Scale Test. Both yielded virtually identical results, so the results using the Group 4 water are presented in Figure 2.3.5-25.

The range of pCO_2 values was calculated by sampling the TSPA lookup tables for in-drift pCO_2, which are generated by the near field chemistry model. The pore-water composition must be estimated, and this requires estimating the amount of feldspar dissolved over the course of the Drift Scale Test experiment. A maximum bound on the amount dissolved was calculated using the mean near-field chemistry model feldspar dissolution rate and assuming eight years of water–rock contact (the total gas sampling interval) at 96°C, the maximum temperature at the evaporation front. The calculated amount of feldspar dissolved was too small to be significant, so the predicted range of CO_2 pressures is based on calculations with the unaltered starting water.

For borehole gas samples, the temperature used in the analysis was the nearest measured value from that borehole. Within the drift, the temperatures associated with each gas sample are from a single sensor, located approximately at the center of the 50-meter heated drift.

Two pCO_2 values predicted by the near-field chemistry model are calculated at each time step, by using the drift wall temperature, or 96°C if the drift wall temperature exceeds boiling, to query the CO_2 lookup tables provided to TSPA for Group 4 water with no alkali feldspar added. The results of this calculation are shown in Figure 2.3.5-25a. The near-field chemistry model maximum pCO_2 curve captures nearly all of the data, with two exceptions. Several points early in the heating history exceed the predicted values, and the data from one borehole toward the end of the heated drift, BH-185, are consistently higher than the other data, and are outside of the predicted range. It is not clear why this one location yields higher values than all others; however, over this end of the drift, a cast-in-place concrete liner, 20 cm thick, was used as ground support (CRWMS M&O 1998, Section 3.4). The presence of the liner would have affected gas-phase transport, and may have resulted in the formation of high pH, carbonate charged waters that degassed CO_2 upon evaporation. Such a process is not relevant to the repository, as there will be no cementitious materials in the emplacement drifts. Cementitious materials are limited to (Tables 1.3.6-1 and 1.3.6-2): (1) shotcrete in the emplacement drift turnouts, exhaust intersections, and other non-emplacement openings; (2) grout for rock bolt placement in non-emplacement drifts and turnout intersections; and (3) cement in the ground support for the access mains, exhaust mains, shafts, and ramps. Standoffs from the shotcrete portions of the turnouts and exhaust drift intersections (Table 1.9-9, Parameter 01-18) will limit heating of these parts of the drift.

The near-field chemistry model minimum pCO_2 curve captures the variation during the boiling period; it appears to under-predict the data, but it must be remembered that samples collected at temperatures above boiling, which would have had the largest degree of dilution and the lowest pCO_2 values, are not included in this analysis. However, after the boiling period, the near-field

chemistry model minimum curve does not capture the spread of the data; the lower bound converges too rapidly back to the ambient value of 10^{-3} bars.

One likely explanation for this is that the air that moved back into the system as it cooled was not representative of the gas phase in the host rock but rather represented atmospheric air that was drawn around the drift scale test bulkhead. Current atmospheric pCO_2 values are about $10^{-3.42}$ bars, as opposed to the 10^{-3} bars observed in the gas phase in the host rock. In Figure 2.3.5-25b, the near-field chemistry model range is recalculated assuming that the non-condensable gas phase moving back into the drift has a pCO_2 of $10^{-3.42}$ bars, and the behavior of the data, especially the in-drift data after the drift wall boiling period, is better captured. Note that the upper bound does not change, as it is not sensitive to the assumed pCO_2 in the non-condensable fraction of the gas phase. The model-data comparisons in Figure 2.3.5-25b provide corroboration for the in-drift pCO_2 range implemented by the near-field chemistry model. Note that this does not suggest that a pCO_2 of $10^{-3.4}$ bars would be more appropriate than 10^{-3} bars for use in the near-field chemistry model; Drift Scale Test heating was terminated abruptly, resulting in rapid cooling and condensation of water vapor, and requiring relatively rapid air flow into the system to maintain atmospheric pressure. Thus, atmosphere from the ventilated drift was drawn through the rock around the bulkhead. These conditions do not apply to the repository itself, which will cool slowly and after closure will likely be more isolated from the atmosphere.

2.3.5.3.3.5.5 Summary of Near-Field Chemistry Model Confidence Building Activities

Four comparisons with model and measured data provide corroboration for different aspects of the near-field chemistry model.

Strontium Isotopes—Pore-water isotopic ratios vary systematically with depth through the rhyolitic core of the TSw due to dissolution of feldspar in the tuff. The observed variation was used to estimate a feldspar dissolution rate which is similar to, and corroborates, that used in the near-field chemistry model, which was calculated independently from the mass fraction of secondary aluminosilicates in the tuff.

Trends in Ambient Pore-Water Composition and Secondary Mineral Assemblages—General trends in ambient pore-water and gas phase compositions are captured by the near-field chemistry model and provide corroboration for the feldspar dissolution rate used in the model and for the general transport model and the geochemical reactions predicted. Additional corroboration is offered by comparison with observed secondary mineral assemblages in the TSw devitrified rhyolite section, which are broadly consistent with the alteration products predicted by the near-field chemistry model; the importance of reactions involving stellerite is especially well supported. In addition, the range of possible feldspar dissolution rates used in the model is constrained by the observation that calcite precipitates in the ambient system.

Comparison to Thermal-Hydrologic-Chemical Seepage Model—The near-field chemistry model relies on a field-calibrated feldspar dissolution rate that is lower than that used by the thermal-hydrologic-chemical seepage model, and it will always predict less reaction with the host rock. However, when simulations of the two models using comparable feldspar dissolution rates are compared, predicted trends in seepage water chemistry are similar. The general similarity in

the predictions provides confidence that both models capture the primary processes critical to the chemistry of seepage. Both models indicate that feldspar dissolution is the dominant control on water chemistry; uncertainty in this important parameter is explicitly implemented in the TSPA implementation of the near-field chemistry model. The suite of secondary aluminosilicates that is predicted to form by each model differs, in part because of use of different thermodynamic data. However, both suites apparently capture the general behavior of the alteration minerals as sinks for aluminum, calcium, and magnesium, and at higher amounts of feldspar dissolution, potassium and sodium. The largest values for pCO_2 predicted by the thermal-hydrologic-chemical seepage model for the thermal period are greater than those predicted by the near-field chemistry model because the transport assumptions built into the two models differ. The near-field chemistry model approach is considered to be appropriate for TSPA because it allows for loss of CO_2 by gas-phase transport to cooler regions within the emplacement drifts.

Comparison to Drift Scale Test Gas Phase Data—The predicted near-field chemistry model pCO_2 range bounded the measured Drift Scale Test data well, especially during the cool-down period, after the cessation of drift-wall boiling. However, it was necessary to modify the model slightly, using a pCO_2 concentration of $10^{-3.42}$ bars (the level of CO_2 in the earth's atmosphere) for the non-condensable air in the drift, consistent with air movement from the ventilated drift, around the bulkhead, and into the heated drift during cooling. Samples from borehole BH-185, toward the end of the heated drift, were above the near-field chemistry predicted upper bound. However, that portion of the heated drift was lined with a cast-in-place concrete liner, 20 cm thick, which may have affected water compositions or gas-phase movement. A majority of the Drift Scale Test data corroborate the near-field chemistry model for the in-drift pCO_2 range.

Corroboration During Model Development—Two specific aspects of the near-field chemistry model are corroborated by results of calculations during model development or have been validated in other model reports.

- The plug flow implementation for pore-water transport is supported by the results of the FEHM calculations documented in Section 2.3.5.3.3.2.7. The FEHM results were used to optimize, or calibrate, the plug flow implementation, and hence cannot be used directly to corroborate the hydrologic model implemented, or transport times predicted, in the near-field chemistry model. However, the FEHM results vary little (less than 15%) relative to the uncalibrated plug flow calculations at all percolation fluxes from 1 mm/yr to 100 mm/yr. This provides corroboration for an important assumption required for the plug flow implementation, that matrix-fracture interactions are rapid relative to downward transport.

- The conduction-only heat transfer model for the thermal field is identical to that implemented in the in-drift condensation model (Section 2.3.5.4.2), and is also consistent with use in other project models. The multiscale thermal-hydrologic model (Section 2.3.5.4.1) also implements a conduction-only model, in part, and provides justification for this implementation.

2.3.5.3.4 TSPA Implementation of the Near-Field Chemistry Model

[NUREG-1804, Section 2.2.1.3.3.3: AC 3(1) to (4)]

The near-field chemistry model produces outputs that are used by the seepage evaporation abstraction (Section 2.3.5.5.4) and also outputs that are passed directly to TSPA.

Outputs Used by the Seepage Evaporation Abstraction—Outputs used by the seepage evaporation abstraction are the chemistry of potential seepage waters, which are provided in the form of output files from the thermodynamic solubility and speciation modeling program EQ3/6. Potential seepage water compositions are given parametrically, as functions of the 4 starting waters and 11 discrete water–rock interaction parameter values. Each file provides the seepage water composition as a function of temperature, from 23°C to 96°C. Two additional file sets have end-point temperatures of 30°C and 70°C. The end-point compositions of the three sets of files provide the starting waters for the EQ3/6 seepage evaporation simulations at 30°C, 70°C, and 100°C (SNL 2007b, Section 6.9.1). The near-field chemistry model also screens and groups the TSw pore-water analyses into four chemically similar groups. Discrete distributions of the chloride-nitrate ratios of the waters in each group are passed to the seepage evaporation abstraction, which incorporates the within-group variability in this ratio when calculating in-drift water compositions (SNL 2007b, Section 6.12.3).

Outputs Used Directly by TSPA—Near-field chemistry model outputs that are provided directly to the TSPA include the water–rock interaction parameter lookup table and the uncertainty in the water–rock interaction parameter value. The water–rock interaction parameter lookup table parametrically provides the value of the water–rock interaction parameter over the history of the repository (102 time steps from 50 years to 1 million years) for 336 locations representing different thermal histories and 20 sets of percolation flux values. The 336 sets of thermal histories (7 drifts, 16 locations per drift, 3 thermal conductivity values) cover the expected range of thermal histories in the repository. Each thermal history has a unique thermal measure, defined as the sum of the time when drift wall temperature drops below the boiling point of water, in years, and the maximum drift wall temperature, in degrees Celsius. For each waste package location examined, TSPA calculates the thermal measure from the multiscale thermal-hydrologic model (Section 2.3.5.4.1) outputs and selects the closest value from the water–rock interaction parameter map. For each thermal measure, twenty sets of time histories are given, each representing a different set of four percolation fluxes, corresponding to the three climate states (i.e., present-day, monsoonal, and glacial-transition), and the post-10,000-year period. The applicable water–rock interaction parameter value at any given time step is chosen by interpolating between the two percolation flux sets that most closely bound the percolation history at the waste package location of interest (SNL 2007b, Section 6.15.1).

Uncertainty in the Water–Rock Interaction Parameter—Uncertainty in the water–rock interaction parameter value is passed to TSPA as a beta distribution, the mean value of which is extracted from the water–rock interaction parameter lookup table. For each realization, TSPA extracts the water–rock interaction parameter value from the water–rock interaction parameter lookup table and uses the beta distribution parameters to generate a distribution of values. Then it implements the uncertainty in the water–rock interaction parameter with self-correlation; that is, after sampling the water–rock interaction parameter beta distribution for the first time step, it

samples the same probability value for the new distributions generated at each time step for the entire realization (SNL 2007b, Section 6.15.1).

The near-field chemistry model also provides TSPA with tables, derived from the composition of potential seepage waters, used to calculate the potential CO_2 range within the drift. The maximum pCO_2 in the drift is the value in equilibrium with the seepage water compositions (Section 2.3.5.3.3.2.11). These values are extracted from the EQ3/6 output files generated by the near-field chemistry model to represent potential seepage compositions (Section 2.3.5.3.4), and are provided to TSPA as four lookup tables, one for each starting water, with the maximum pCO_2 values given as functions of the water–rock interaction parameter value and the temperature of the evaporation front. After the boiling period, this corresponds to the temperature at which the vapor pressure of water in the drift (calculated from the waste package surface temperature and relative humidity) is equal to the saturation pressure. This rapidly converges to the drift wall temperature.

The minimum pCO_2 in the drift is calculated by assuming the noncondensable air in the drift has ambient CO_2 levels (10^{-3} bars, Section 2.3.5.3.2.2.1) and calculating the degree of dilution by water vapor released at the evaporation front. The CO_2 released by the evaporating water is also summed in; this is estimated from the total carbon (C_{total}) in solution in the potential seepage waters (Section 2.3.5.3.3.2.11). The value of C_{total} is extracted from the near-field chemistry model outputs and tabulated into four lookup tables, one for each starting water, with the C_{total} values given as functions of the water–rock interaction parameter value and the temperature of the evaporation front.

These two sets of lookup tables provide the basis for calculating the range of potential in-drift pCO_2 values. The TSPA implementation of this calculation is tied closely to the implementation of the seepage evaporation abstraction, and is documented in Section 2.3.5.5.4.3.

Implementation of Uncertainty in the Near-Field Chemistry Model—Uncertainty in the near-field chemistry model is propagated to the seepage evaporation abstraction and to TSPA in several ways. Four starting waters are used to capture the uncertainty in the pore-water compositions. In addition, the Cl^-/NO_3^- ratios for all waters that passed the screening analysis (Section 2.3.5.3.2.2.1), are passed to the seepage evaporation abstraction, which incorporates the within-group variability in this ratio when calculating in-drift water compositions (Section 2.3.5.5.4). Uncertainty in the in-drift pCO_2 is implemented by calculating upper and lower bounding values and then sampling within the range. Uncertainties in input parameters for calculating the water–rock interaction parameter value are propagated through the near-field chemistry model as described in Section 2.3.5.3.2.2.2. These are passed to TSPA as a beta distribution, the mean value of which is extracted from the water–rock interaction parameter lookup table. For each realization, TSPA extracts the water–rock interaction parameter value from the water–rock interaction parameter lookup table and uses the beta distribution parameters to generate a distribution of values. Then it implements the uncertainty in the water–rock interaction parameter with self-correlation; that is, after sampling the water–rock interaction parameter beta distribution for the first time step, it samples the same probability value for the new distributions generated at each time step for the entire realization (SNL 2007b, Section 6.15.1).

2.3.5.4 In-Drift Thermal-Hydrologic Environment

[NUREG-1804, Section 2.2.1.3.3.3: AC 1(1) to (10), AC 2(1) to (4), AC 3(1) to (4), AC 4(1) to (4), AC 5(1), (3)]

Temperature and relative humidity at different locations in the emplacement drifts, and the variation of these conditions with time and location in the repository, are important to repository performance because they help define the physical and chemical environment (Section 2.3.5) for degradation of the EBS (Section 2.3.6) and transport of radionuclides to the unsaturated zone (Section 2.3.7). Thermal-hydrologic models combine the responses of the host rock and the in-drift features to calculate these conditions in the emplacement drift environment. Figures 2.3.5-1 and 2.3.5-3 are flow charts of model architecture for the TSPA in-drift models and for the TSPA as a whole.

Thermal-hydrologic models are introduced in Section 2.3.3 with comparisons to the results from field thermal testing underground at Yucca Mountain and development of the thermal-hydrologic seepage model. The multiscale thermal-hydrologic model developed in Section 2.3.5.4.1 has the same conceptual basis as the thermal-hydrologic seepage model and is used to represent for TSPA the expected range of in-drift thermal-hydrologic conditions resulting from waste package heat output and parametric variability.

In-drift condensation is evaluated with the in-drift condensation model (Section 2.3.5.4.2 and Figures 2.3.5-1 and 2.3.5-3). This model provides the TSPA model with both the probability and magnitude of condensation on the drift wall during cooldown. The TSPA treats the flow of drift wall condensation as a source of liquid water to be added to the liquid water entering the drift as seepage. The TSPA uses this combined liquid-water source term in the EBS flow and chemical environment calculations.

The range of potential waste stream variability depends on the sequence of shipping waste to the repository, which is subject to future decisions by the waste producing organizations and the U.S. Department of Energy (DOE). In Section 2.3.5.4.3, the sensitivity of repository thermal response to the large-scale variability in the waste stream is discussed. The TSPA includes small-scale (40 m) variability, and the analyses in Section 2.3.5.4.3 show that the TSPA thermal goals (which flow from design requirements) for the drift wall and the mid-point of each pillar between the emplacement drifts can be met for large-scale and small-scale variability.

2.3.5.4.1 Multiscale Thermal-Hydrologic Model

[NUREG-1804, Section 2.2.1.3.3.3: AC 1(1) to (9), AC 2(1) to (4), AC 3(1) to (4), AC 4(1) to (4), AC 5(1), (3)]

The in-drift thermal-hydrologic conditions in the TSPA, particularly temperature and relative humidity, are provided by the multiscale thermal-hydrologic model (SNL 2008a, Section 1). The TSPA uses temperature and relative humidity, along with other parameters, at specific locations inside the emplacement drift, to determine the chemistry of water contacting various EBS features. The TSPA uses multiscale thermal-hydrologic model predictions of waste package temperature and relative humidity as inputs to the waste package corrosion model. The TSPA uses multiscale thermal-hydrologic model predictions of drift wall temperature, in-drift relative humidity, and invert liquid saturation to evaluate flow and transport in the EBS.

As described in this section, these TSPA inputs are the results of the following sequence of modeling products, starting with the evolution of process models and the generation of input parameters, and culminating in a comparison to field test data and model abstraction details for TSPA.

- **Development of Model Consistent with Data and Scientific Understanding**—Model development, including the determination of computational domain, initial and boundary conditions, assumptions, and approximations, is consistent with the scientific understanding of the natural barrier features and engineered systems that is based upon field and laboratory tests, modeling studies, natural analogues, and technical literature (Sections 2.3.5.4.1.2 and 2.3.5.4.1.3). The multiscale thermal-hydrologic model combines the results of submodels having various scales and different dimensionality to produce a final three-dimensional representation consistent with the three-dimensional character of the natural barriers and engineered systems. The multiscale thermal-hydrologic model represents heat flow at both the mountain scale (e.g., edge-cooling effects) and at the drift scale, including variability in waste package heat output. The mountain-scale computational domain reflects the natural barrier geometry obtained from site-characterization data and is the same as that used for modeling the unsaturated zone (Section 2.3.2), which is also the source of hydrologic properties and the percolation flux boundary condition and its uncertainty. The multiscale thermal-hydrologic model also incorporates important design aspects such as the thermal loading strategy, repository footprint, physical layout within the drift, and material selection.

  Limitations and uncertainties (Section 2.3.5.4.1.3) are evaluated and taken into account. The multiscale thermal-hydrologic model does not include axial transport of water vapor along the emplacement drifts (Section 2.3.5.4.1.3.1) and its effect on condensation (cold-trap effect). However, for a three-drift case, a comparison of results from the multiscale thermal-hydrologic model with results from a three-dimensional, mountain-scale, nested-grid, thermal-hydrologic model that does include axial vapor transport effects (Section 2.3.5.4.1.3.3) shows that the influence of axial vapor transport and associated condensation on calculated temperatures is minimal. For the TSPA, the multiscale thermal-hydrologic model results are used as well as results from the in-drift condensation model (Section 2.3.5.4.2), which includes axial transport. The use of these two models provides a sufficient representation of temperature and relative humidity in the emplacement drifts, as well as the onset conditions, location, and magnitude of in-drift condensation. Additional discussion of condensation processes as related to the multiscale thermal-hydrologic model is provided in Section 2.3.5.4.1.3.3.

- **Generation of Input Parameters**—Section 2.3.5.4.1.2 describes how data are used, interpreted, and synthesized into parameters for the multiscale thermal-hydrologic model. Parameter values and ranges, uncertainty distributions, and assumptions are based on site-specific field measurements, laboratory testing, process-level modeling studies, and scientific literature. Appropriate ranges of parameters are used. Input parameter uncertainty and variability in thermal properties, hydrologic properties, and percolation flux are also discussed.

- **Support of Model, Including Consideration of Alternative Modeling Approaches**—Several alternative approaches to modeling important FEPs were considered, including coupled processes captured by the multiscale thermal-hydrologic model. Section 2.3.5.4.1.3.3 presents three alternative approaches: an alternative three-dimensional mountain-scale model (SNL 2008a, Section 6.4), a three-dimensional nested-grid thermal-hydrologic model which is applied to a three-drift test case (SNL 2008a, Section 7.5), and a three-dimensional, pillar-scale, thermal-hydrologic simulation of a single repository drift (SNL 2008a, Section 6.3.18[a]). Additional model support activities include comparison with two site-specific thermal tests: the Large Block Test (SNL 2008a, Section 7.3) and the Drift Scale Test (SNL 2008a, Section 7.4[a]).

- **Creation, Execution, and Testing of Model Abstraction**—Section 2.3.5.4.1.4 presents the abstraction of the multiscale thermal-hydrologic model. The two steps to the abstraction process, binning into five percolation subregions and determining a typical waste package, provide the TSPA with inputs that appropriately represent the process model results. These results incorporate scientific understanding of processes such as capillarity and vaporization, both of which divert percolation away from the drifts (Section 2.3.3). As presented in Section 2.3.5.4.1.3.2, the multiscale thermal-hydrologic model propagates parametric uncertainty and variability in the sets of simulations supporting TSPA. This uncertainty and variability is reflected in the model abstraction.

2.3.5.4.1.1 Conceptual Description

[NUREG-1804, Section 2.2.1.3.3.3: AC 1(1), (6), AC 2(4)]

The following conceptual description first considers thermal-hydrologic processes as they vary according to location in the host rock and emplacement drifts. The natural and engineered features that influence thermal hydrology are included in the discussion. The section concludes with a time-based summary of thermal-hydrologic processes for three successive thermal regimes.

2.3.5.4.1.1.1 Thermal Hydrology in Repository Host Rock

Thermal-hydrologic behavior in the near-field host rock is dominated by the extent of boiling temperatures. Boiling of water occurs at approximately 96°C at the elevation of the Yucca Mountain repository, which is situated in an elevation range centered approximately 1,100 m above mean sea level. Although evaporation, water vapor flow away from the heat source, and condensation occur at below-boiling temperatures, significant rock dryout and relative humidity reduction does not occur unless the local temperature exceeds the boiling point of water (SNL 2008a, Section 6.1.3).

Waste package heat output is at a maximum during the preclosure period; however, because the majority of the heat is removed via ventilation air during the preclosure period, rock temperature at the emplacement drift wall does not reach the boiling temperature of water, for the thermal loading conditions represented in TSPA (SNL 2008a, Section 6.1.3). At closure, when forced ventilation stops, the rock temperature increases, and a dryout zone expands in the rock around each emplacement drift. As shown in Section 2.3.3, liquid flow is inhibited at this dryout zone, and capillary forces divert liquid flow around the emplacement drift opening, so that there is no seepage. At increased temperatures, there is a reduction in capillary pressure; however, this effect is incorporated within the uncertainty of the capillary-strength parameter (BSC 2005b, Section 5).

Capillary diversion continues to divert liquid flow around the emplacement drift opening after the emplacement drift wall temperature cools below the boiling point of water (Section 2.3.3).

Figure 2.3.3-33 represents the conceptual understanding of thermal-hydrologic processes occurring around two adjacent emplacement drifts, consistent with field testing at Yucca Mountain. During postclosure, much of the heat is transported away from the emplacement drifts by thermal conduction through the rock. A portion of the heat is transported as latent heat by water that vaporizes near the emplacement drift and condenses in cooler rock farther away (BSC 2005b, Sections 6.1.2 and 6.2.1.1.2). At the outer margin of the dryout zone, water vapor coexists with liquid condensate (BSC 2005b, Section 6.1.2; SNL 2008a, Section 6.1.4).

The repository design allows for liquid drainage of condensate through the rock pillars between emplacement drifts. The maximum lateral extent of the boiling zone is predicted to be approximately 11 m from the drift centerline (SNL 2008a, Table 6.3-51[a]). This distance is less than half the spacing between drifts (less than 40.5 m; Table 1.9-9, Parameter Number 01-13). The mid-pillar region of the host rock between emplacement drifts will therefore remain at temperatures below the boiling point of water so that condensate and percolation flux can drain between emplacement drifts (SNL 2008a, Sections 6.3.16[a] and 6.3.4[a]).

Condensation that drains away from the dryout zone can be removed from consideration as a source of potential seepage. However, some condensate may flow back toward the dryout zone, resulting in reflux. Reflux activity has been observed during thermal testing at Yucca Mountain, and occurs only when and where the rock temperature is near the boiling point of water (BSC 2005b, Section 7.4.3). The intensity of reflux activity is directly related to heat output, which will be strongest early in the thermal evolution when the dryout zone has its greatest extent. Reflux activity during the boiling period will be distant from the emplacement drift openings, will decrease with decreasing waste package heat output, and thus will not contribute to seepage into the emplacement drifts (Section 2.3.3).

In addition to radial temperature variation and dryout in the rock around the drift openings, there is axial temperature variation along the drifts. Nonuniformity in the extent and duration of boiling conditions along the drift axis results from variations in waste package heat output and from edge effects at the ends of the drifts (SNL 2008a, Section 6.1.5).

2.3.5.4.1.1.2 Thermal Hydrology in Drifts

The designs of the emplacement drifts and the EBS are summarized in Sections 1.3 and 1.5. Major features, particularly the waste package, drip shield, and invert, are represented explicitly in the multiscale thermal-hydrologic model, which directly feeds the TSPA (SNL 2008a, Section 6.1.4).

Thermal-hydrologic behavior in and around emplacement drifts is explained in terms of three processes (SNL 2008a, Section 6.1.4):

- **Heat Transport**—In the emplacement drift openings, heat is transferred from hotter to cooler surfaces primarily by thermal radiation. In the adjoining host rock, heat is transferred primarily by thermal conduction. The heat output of waste packages changes slowly, so the near-field rock temperatures change slowly, and the host-rock thermal

conductivity (rather than heat capacity or thermal diffusivity) is the key natural-system parameter that determines temperature changes in the host rock (SNL 2008a, Section 6.1.4).

- **Host-Rock Dryout**—This process occurs when pore water in the host rock evaporates, and the rock approaches complete dryout, at temperatures at or above the boiling point of water. Dryout lowers the liquid-phase saturation in the host rock, which lowers the partial pressure of water vapor (due to capillary forces), thereby lowering the relative humidity in the host rock and in the emplacement drifts. The extent of dryout is controlled mainly by the local heat output of the waste packages, thermal conductivity of the host rock, and the ambient percolation flux in the host rock (which has a cooling effect) (SNL 2008a, Section 6.1.4).

- **Host-Rock Rewetting**—As the waste packages in the emplacement drifts cool down, liquid eventually returns to the fractures and matrix of the host rock, principally from the ambient percolation flux. Once rock temperatures permit rewetting, the rate of rewetting is controlled by the ambient percolation flux, except in regions of very low percolation flux (less than approximately 0.1 mm/yr), where rewetting is predicted to occur primarily from capillary-driven imbibition in the matrix (SNL 2008a, Section 6.1.4).

Dryout results from the balance between evaporation and rewetting and is greatest where there is a combination of lower host-rock thermal conductivity and lower percolation flux. Dryout is least where there is higher host-rock thermal conductivity and greater percolation flux (SNL 2008a, Section 6.1.4).

Two important factors that influence the physical conditions in the emplacement drifts are the temperature and relative humidity at the emplacement drift wall. These conditions and the temperature differences between the waste packages and the emplacement drift wall, which depend on heat transfer between the engineered components (waste package and drip shield) and the rock, define the thermal-hydrologic conditions throughout the drift. The temperature at the emplacement drift wall is controlled by the temperature buildup in the host rock, which is controlled by the local heating conditions, host-rock thermal conductivity, and the local percolation flux. The relative humidity at the emplacement drift wall is related to the liquid-phase saturation of the rock, which is driven by temperature and by surrounding thermal conditions (SNL 2008a, Section 6.1.4).

The relative humidity at the emplacement drift wall controls the relative humidity in connected air spaces within the emplacement drift. Relative humidity in the emplacement drift must be less than at the wall because temperatures are greater in the emplacement drift. Larger temperature differences between the waste package and emplacement drift wall result in greater reduction of relative humidity on the waste package. Further, the drip shield, which is between the waste package and emplacement drift wall, functions as a thermal-radiation shield that increases the temperature difference between the waste package and the emplacement drift wall. This temperature difference is greatest shortly after closure and slowly decreases with time as the heat output of the waste packages decays (SNL 2008a, Section 6.1.4).

During the preclosure period (minimum of 50 years; Table 1.9-9, Parameter 06-01), when waste package heat output is at a maximum, the emplacement drifts are ventilated to remove most of the

heat (BSC 2004e, Sections 4.1.10 and 6.6). Waste package temperatures are elevated, and some packages may approach 100°C immediately after emplacement (subject to control by ventilation) (BSC 2004e, Section 6.6). The warming of ventilation air will ensure that preclosure conditions are dry (e.g., less than 20% relative humidity), especially where in-drift temperatures are greatest (BSC 2004e, Section 6.9.1).

At permanent closure, forced ventilation ceases, and the emplacement drift wall rock temperature increases sharply and peaks within approximately 50 years or sooner (SNL 2008a, Figure 6.3-76[a]). Waste package temperatures are as much as 28°C warmer than the emplacement drift wall at the time when waste package temperatures peak because of thermal resistance across the drip shield and the in-drift air spaces (SNL 2008a, Table 6.3-49[a]). This temperature difference decreases and approaches zero as the heat output declines over time. The maximum postclosure temperature of a waste package at any location is determined by the history of heat output, the resistance to dissipation of heat in the host rock, the rate of heat transfer from the waste package to the emplacement drift wall, and the relationship of the waste package to other nearby heat sources (SNL 2008a, Section 6.1.4).

After closure, when the near-field host rock temperature in the emplacement region is greater than the boiling point (96°C), water vapor produced by water boiling from the host rock will migrate into cooler regions of the rock, or into unheated parts of the drifts, where it will condense (SNL 2008a, Sections 6.1.2 and 6.3.18[a]). This process will continue throughout the thermal period, but is strongest in the first few hundred years after closure when the rock temperature is greatest, and the moisture that is initially present in the host rock is evaporated (SNL 2008a, Section 6.1.3).

After several hundred years of cooling, water vapor production from boiling is less important, and gas-phase transport within the emplacement drifts is driven by drift-scale and repository-scale in-drift natural convection, possibly supplemented by barometric pumping and repository-scale natural ventilation, as discussed with respect to the in-drift condensation model in Section 2.3.5.4.2.1. These transport processes have been investigated with regard to multiscale thermal-hydrologic modeling of in-drift environmental conditions using a three-dimensional, mountain-scale, nested-grid, thermal-hydrologic model and a three-dimensional, full-drift pillar-scale, thermal-hydrologic model (Section 2.3.5.4.1.3.3). Results indicate that the transport processes can produce condensation at cooler locations but move small amounts of heat relative to that produced by the waste, and have a small effect on the prediction of temperature and relative humidity in the emplacement area (SNL 2008a, Sections 7.5.2.7 and 7.5.3). The effect of condensation in cooler locations is addressed in Section 2.3.5.4.2.

Temperature and humidity conditions in the near-field host rock control the temperature and relative humidity within the emplacement drifts (SNL 2008a, Section 7.6). The multiscale thermal-hydrologic model represents this coupling on the scale of individual waste packages (drift scale) without considering the minor effects on the timing and magnitude of temperature and relative humidity changes due to the axial transport of water vapor along the emplacement drifts and the ensuing condensation at cooler waste package locations. When axial transport and condensation are included in three-dimensional, mountain-scale, nested-grid thermal-hydrologic simulations (Section 2.3.5.4.1.3.3), the results show that these processes remove additional water from the near-field host rock and contribute to greater total dryout over time, even at cooler waste package locations. The long-term effects of condensation at cooler waste package locations on the potential

for radionuclide transport are represented for TSPA by the in-drift condensation model (Section 2.3.5.4.2). In this manner, the in-drift condensation model plays a complementary role to the multiscale thermal-hydrologic model with regard to evaluating the in-drift thermal-hydrologic environment.

2.3.5.4.1.1.3 Time-Based Summary of Postclosure Thermal Regimes

The thermal evolution of the emplacement drifts can be sequenced into three regimes based on the emplacement drift wall and waste package surface temperatures:

- **Dryout: Emplacement Drift Wall Temperature Greater Than the Boiling Point of Water**—At the time of permanent closure, the emplacement drift wall rock will already be dried out by 50 years of forced ventilation, and the emplacement drifts are dry. After closure, emplacement drift wall temperatures increase to greater than the boiling point of water throughout much of the repository, relative humidity in the emplacement drifts remains low, and dryout of the near-field host rock proceeds. Waste package locations remain dry locally until the dryout zone disappears due to declining heat output and rewetting by the percolation flux. During the dryout period, the existence of aqueous conditions on the surfaces of the waste package and drip shield will be limited to the minor effects of deliquescence associated with dust constituents (Sections 2.3.5.5.1 and 2.2.1).

- **Transition: Emplacement Drift Wall Temperature At or Below the Boiling Point of Water and Waste Package Temperature At or Above the Boiling Point**—Seepage into the emplacement drifts becomes possible as the temperature of the emplacement drift wall drops below the boiling point of water (conservatively at 100°C in the thermal-hydrologic seepage model of Section 2.3.3). During this period, the waste package and drip shield surface temperatures will be greater than the emplacement drift wall temperature, so seepage water will tend to evaporate if it contacts drip shields or waste packages, causing evaporative concentration of salts on their surfaces (Section 2.3.5.5.1).

- **Low Temperature: Waste Package Temperature Less Than the Boiling Point of Water**—As the waste packages cool further, the in-drift relative humidity increases, so that evaporated solutions are not as concentrated. After hundreds to thousands of years (depending on local thermal conditions), waste package temperatures become sufficiently cool, and associated chemical conditions become sufficiently benign, that initiation of localized corrosion is unlikely in the repository environment (Section 2.3.6).

2.3.5.4.1.2 Data and Data Uncertainty

[NUREG-1804, Section 2.2.1.3.3.3: AC 1(2), (3), (8), (9), AC 2(1) to (4), AC 3(1) to (4)]

This section describes data sources used to develop the multiscale thermal-hydrologic model. Design and natural system information used to develop the multiscale thermal-hydrologic model are summarized, and the key uncertain parameter categories (thermal properties, hydrologic properties, and percolation flux) are reviewed. References to supporting studies are provided.

2.3.5.4.1.2.1 Data Sources

Data sources for in-drift thermal-hydrologic conditions include field thermal testing, the unsaturated zone flow model, preclosure ventilation modeling, and sources related to design features and waste characteristics.

Field Thermal Testing—The field thermal testing program included the Large Block Test, the Single Heater Test, and the Drift Scale Test, all of which are discussed in Section 2.3.3. The Drift Scale Test, which is the most important of the three tests, was designed to collect data on in situ coupled processes, including thermal-hydrology, for representative loading conditions (BSC 2004f, Section 5.4.5.3). The test area is located in one of the side alcoves of the ESF in the middle nonlithophysal tuff. Figure 2.3.3-34 shows a three-dimensional perspective of the Drift Scale Test, including heaters and many of the instrumented boreholes for monitoring thermal, hydrologic, mechanical, and chemical processes. The test area was heated from December 1997 until January 2002, followed by a 4-year cooldown period. Through continuous monitoring and periodic testing, the coupled thermal, mechanical, hydrologic, and chemical processes associated with the dryout and condensation zones as they change in time and space have been observed (BSC 2005b, Sections 7.2.1, 7.2.2, and 7.4; SNL 2007c, Section 7.1).

Unsaturated Zone Flow Model—The site-scale unsaturated zone flow model, herein called simply the unsaturated zone flow model, (Section 2.3.2; SNL 2007h) provides key input to the multiscale thermal-hydrologic model. These two models share a consistent gridding system, hydrologic properties, and flow fields resulting from various climate states and infiltration uncertainties (SNL 2008a, Section 6.2.2). The basis for, and development of, the unsaturated zone flow model is presented in Section 2.3.2. A brief description appears below.

The unsaturated zone flow model is a three-dimensional, site-scale, dual-permeability model modified from the general dual-permeability approach so that only a portion of connected fractures actively conduct liquid water (Section 2.3.2). Whether or not a fracture is active depends on the liquid-phase saturation in the fracture. The multiscale thermal-hydrologic model uses this same conceptualization of flow through unsaturated, fractured porous rock at Yucca Mountain (SNL 2008a, Section 6.2.2).

A three-dimensional description of hydrostratigraphic units developed for the unsaturated zone flow model includes the position of the water table and surface topography, thermal-hydrologic properties for these units, and model boundary conditions (Section 2.3.2). In all, there are 36 unsaturated zone model layers, each of which is considered to be homogeneous with respect to thermal and hydrologic properties (SNL 2008a, Section 6.2.2). Heterogeneity is captured by thermal and hydrologic properties that vary among the 36 unsaturated zone model layers. Hydrologic properties are determined through an inverse modeling approach constrained by site hydrologic data. Thermal properties are determined on the basis of laboratory and field measurements (SNL 2008a, Appendix IV).

The unsaturated zone flow model assumes steady-state flow conditions and generates 16 three-dimensional flow fields for four different infiltration boundary conditions scenarios using the nominal 10th, 30th, 50th, and 90th percentile infiltration maps for each of the three different climate states and the post-10,000-year percolation boundary condition. The three climate states are

the present-day climate for the first 600 years after waste emplacement, the monsoonal climate for the period 600 to 2,000 years after emplacement, and the glacial-transition climate for the period beyond 2,000 years after emplacement. The post-10,000-year percolation boundary condition within the period of geologic stability is developed by rescaling representative percolation maps selected from the pre-10,000 year climate states in a manner consistent with the proposed 10 CFR 63.342(c)(2) (SNL 2008a, Sections 6.2.6.6 and 6.2.12.4[a]).

The four different infiltration uncertainty cases represent epistemic uncertainty in unsaturated zone flow conditions. Climate change is modeled within the multiscale thermal-hydrologic model (consistent with the implementation in TSPA) by assuming a series of step changes in the boundary percolation flux values obtained from the unsaturated zone flow model. It is assumed that changes in percolation flux due to climate state apply instantaneously (SNL 2008b, Section 6.1.4.1; SNL 2008a, Sections 5.1.4[a] and 6.3.1).

Ventilation Model—The heat-removal efficiency for forced ventilation during the preclosure period (50 years for the multiscale thermal-hydrologic model) is calculated from a mechanistic model of ventilation performance (BSC 2004e, Section 6.6). This work shows that an integrated 50-year heat removal efficiency of approximately 80% to 90% is achievable. The multiscale thermal-hydrologic model uses a calculated result within this range, accounting for changes in heat removal efficiency with time and for variability along each ventilated emplacement drift (SNL 2008a, Section 6.3.12 and Table 4-1[a]). Section 1.3.5 describes the engineered system responsible for preclosure ventilation.

Design Sources—The multiscale thermal-hydrologic model simulates behavior in the emplacement drifts and, therefore, incorporates design information to represent important engineered features (Sections 1.3.1, 1.3.4, and 1.3.5; and SNL 2008a, Section 4.1[a]). Repository subsurface and waste package design information were obtained from controlled sources and is based on the current repository design (SNL 2008a, Section 4.1). During the thermal-hydrologic analysis for the license application, design evolution resulted in minor changes to the length of the codisposal waste packages and in a deeper invert. The waste package length changes and invert depth change were analyzed and found to be insignificant to thermal-hydrologic results (SNL 2008a, Table 6.2-6[a] and Section 6.3.19[a]). Design information used by the multiscale thermal-hydrologic model, and associated constraints placed on the design through implementation of this model in TSPA, are identified in Section 2.2.1.2 (Table 2.2-3).

2.3.5.4.1.2.2 Input Parameter Development

Input Parameter Description—The multiscale thermal-hydrologic model requires input of the following natural barrier and EBS information (Sections 1.3.1, 1.3.4, and 1.3.5; and SNL 2008a, Section 4.1):

- Design information and EBS properties
  - EBS materials and dimensions
  - Invert thermal and hydrologic properties
  - Waste package thermal properties
  - Drip shield thermal properties

  - Emplacement drift wall emissivity
  - Waste package heat-generation and ventilation heat-removal efficiency.

- Natural barrier information

  - Natural system geometry (i.e., the three-dimensional, site-scale, unsaturated zone model grid)

  - Hydrologic properties of the unsaturated zone model layers

  - Bulk thermal properties of the unsaturated zone model layers

  - Boundary conditions, mostly from the unsaturated zone flow model (e.g., temperatures and gas-phase pressures at the upper boundary, which is the ground surface, and temperatures at the lower boundary, which is the water table)

  - Percolation fluxes below the PTn unit from the unsaturated zone flow model, representing the range of climate and infiltration uncertainty (SNL 2008a, Table 4-1[a]; SNL 2008b, Section 6.1.4.1).

Input Parameter Uncertainty—The key uncertain input parameters for the multiscale thermal-hydrologic model fall into three categories, as follows (SNL 2008a, Section 6.3.2):

- **Thermal Properties**—The primary thermal properties of interest are heat capacity and thermal conductivity. Studies have shown that the sensitivity of multiscale thermal-hydrologic model results to host-rock heat capacity and invert thermal conductivity is low (SNL 2008a, Section 6.3.2). The host-rock thermal conductivity is the most important parameter for representing host-rock influence on the in-drift thermal environment. Uncertainty in host-rock thermal conductivity is propagated in the multiscale output that is used for TSPA (Section 2.3.5.4.1.3.2) (SNL 2008a, Sections 6.3.2[a] and 6.3.16[a]).

- **Hydrologic Properties**—The primary hydrologic properties of interest are the bulk permeability of the host rock, especially the permeability of the fracture continuum (SNL 2008a, Section 6.3.2), and the matrix capillary properties (i.e., permeability and van Genuchten parameters) that control imbibition of liquid water from the fractures into the rock matrix. A sensitivity study of host-rock bulk permeability shows the influence on in-drift conditions to be mainly limited to temperature. However, the effect of host-rock bulk permeability on temperatures is small compared to that associated with the uncertainty and variability of host-rock thermal conductivity, so further consideration of host-rock bulk permeability uncertainty is unnecessary. In addition, a sensitivity study over the range of host-rock hydrologic properties demonstrates that matrix capillary properties have a small or negligible effect on the extent or duration of dryout and on relative humidity in the host rock (SNL 2008a, Section 6.3.9).

- **Percolation Flux**—Percolation flux uncertainty at the repository horizon results from two primary sources. The first is the uncertain magnitude of percolation flux, which is

addressed by using the nominal 10th, 30th, 50th, and 90th percentile infiltration flux maps at the PTn/TSw interface for each climate state (and for the post-10,000-year percolation boundary condition) that represent propagation of infiltration uncertainty through the unsaturated zone flow model and into the multiscale thermal-hydrologic model. The multiple percolation flux maps result in a range of predicted percolation flux for any location within the repository. The second source of uncertainty is that of flow focusing associated with the spatial scale of flow in the fractured host rock. Large-scale estimates of percolation flux give the average behavior, while flow focusing describes the effects of concentrated flow in individual fractures at smaller scales. While flow focusing is not incorporated explicitly in the multiscale thermal-hydrologic model, which uses large-scale average flux values as boundary conditions, the impact of flux in general on the results is well understood, and a wide range of flux values is used in the calculations that support TSPA (SNL 2008a, Sections 6.3.2.1 and 6.3.2[a]).

2.3.5.4.1.3 Model and Model Uncertainty

[NUREG-1804, Section 2.2.1.3.3.3: AC 1(1) to (9), AC 2(2), (3), AC 3(1) to (3), AC 4(1) to (4), AC 5(1), (3)]

2.3.5.4.1.3.1 Model Description

The multiscale thermal-hydrologic model calculates temperature and relative humidity, as well as other thermal-hydrologic variables, at various in-drift locations. The model represents relevant features and processes that occur on scales from a few tens of centimeters around individual waste packages to the mountain scale (SNL 2008a, Section 8.1). Processes represented include the following:

- **Mountain-Scale Heat Flow**—Mountain-scale heat flow is represented using thermal conduction in a three-dimensional domain that extends from the ground surface to a depth that includes the entire unsaturated zone plus the upper 1,000 m of the saturated zone (SNL 2008a, Sections 6.2.1, 6.2.14[a], and 6.2.15[a]). Use of thermal conduction as the dominant mountain-scale heat transfer mechanism is justified as a modeling assumption (SNL 2008a, Section 5.2.1).

- **Drift-Scale Heat Flow in the Host Rock**—Heat flow in the host rock, both by conduction and convection, is represented in the model (SNL 2008a, Section 6.2.1).

- **Heat Flow within the Drift**—Variability in the heat output of the various waste package types as a function of their location along a drift is explicitly captured within the model (SNL 2008a, Sections 6.2.1 and 6.2.17[a]). Heat flow within the emplacement drift is dominated by thermal radiation; convective heat transfer also is included (SNL 2008a, Sections 5.2.2 and 6.2.1).

- **Percolation Flow in the Host Rock**—The effects from flow of liquid water that originates as net infiltration at the ground surface, temperature, and humidity in the repository are represented in the multiscale thermal-hydrologic model by percolation flux boundary conditions determined from the unsaturated zone flow model (Section 2.3.2; SNL 2008a, Section 6.1).

- **Host-Rock Dryout and Rewetting**—Heating and cooling of the host rock cause vaporization and water movement, which leads to a zone of rock around the drift that dries and eventually rewets (SNL 2008a, Section 6.2.1). Rewetting occurs by condensation and by capillary liquid flow such as the small wicking flux from the host rock into the invert.

The multiscale modeling approach rests on four submodels of varying dimensionality and scale. Figure 2.3.5-26 and Table 2.3.5-6 provide specific explanations of the naming conventions for the submodel acronyms as well as other information about the modeling approach.

The first submodel simulates three-dimensional mountain-scale heat flow to determine repository-scale variations in host-rock temperature (SMT). The second submodel simulates two-dimensional, drift-scale thermal-hydrologic conditions at selected locations, including dryout and rewetting of the host rock and relative humidity within the emplacement drift (two-dimensional, line-averaged-heat-source, drift-scale, thermal-hydrologic (LDTH)). The three-dimensional thermal effects from the first (SMT) model are incorporated into the second (LDTH) thermal-hydrologic model results through the use of a third (smeared-source, drift-scale, thermal-only (SDT)) thermal model that is one-dimensional (vertical). The LDTH and SDT models are run parametrically in lateral dimension perpendicular to the drift axis (which changes the effective areal mass loading, MTHM per acre), and, at each time step, the LDTH result used is the result with the lateral dimension in which the SDT and SMT results match at that location and time. The results are LDTH temperature and moisture histories at each selected location, with each history including the effects of three-dimensional mountain-scale heat flow. (SNL 2008a, Section 6.2.4[a]). The fourth submodel is a discrete-heat-source, drift-scale, thermal-conduction-radiation submodel (DDT) used to capture the effects from variability of waste package heat output along the drift. The first three submodels are used to generate an intermediate thermal-hydrologic model result (line-source, mountain-scale, thermal-hydrologic (LMTH)) and the final thermal-hydrologic model result (discrete-heat-source, mountain-scale, thermal-hydrologic (DMTH)) adds the results from the fourth submodel to the intermediate model results.

The calculational process results in an effective areal mass loading, or equivalently, an effective drift spacing that can be characterized as a mountain-scale heat-loss parameter (Figure 2.3.5-26). The effective drift spacing gradually increases in the calculation with time as the repository cools (SNL 2008a, Section 6.2.1), and is used in the corresponding two-dimensional submodel (LDTH) simulations at appropriate time steps to produce intermediate thermal-hydrologic results (LMTH) (SNL 2008a, Section 6.2.4).

The intermediate thermal-hydrologic model (LMTH) results would be applicable to a repository in which all waste packages have the same average heat output. However, variability in heat output of waste packages will lead to nonuniform heating along the emplacement drifts. To account for this variability in waste package heat output, the DDT submodel is used to calculate local differences in host-rock and in-drift temperatures. Temperature differences are presented as deviations, relative to the temperatures produced using a line-averaged heat source in the two-dimensional submodel (LDTH). These local temperature variations are added to the intermediate model temperatures (LMTH) to produce the final submodel temperatures (DMTH). Relative humidity values, corresponding to the final temperatures, are determined from the three-dimensional model (DMTH)

results by adjusting the effective drift spacing at each time step to account for local temperature deviations and mountain-scale heat flow (to obtain the appropriate drift wall saturation) (SNL 2008a, Section 6.2.4[a]). The drift wall temperatures and the relative humidity values calculated in this manner represent the overall results of the multiscale thermal-hydrologic model that are used in the TSPA.

Assumptions—The multiscale thermal-hydrologic model makes a variety of assumptions regarding boundary conditions, heat flow processes, material properties, waste package modeling, relative humidity in emplacement drifts, condensate drainage around emplacement drifts, gas- and liquid-phase flow in the longitudinal direction along emplacement drifts, and properties of host-rock rubble for the low-probability-seismic event scenario (SNL 2008a, Section 5[a]). The following key assumptions are made:

- **Mountain-Scale Heat Flow is Dominated by Thermal Conduction**—This assumption is equivalent to saying that convective heat transfer mechanisms (buoyant gas-phase convection and heat-pipe activity) have an insignificant influence on lateral mountain-scale heat flow at Yucca Mountain (SNL 2008a, Section 5.2.1). The assumption is justified because the bulk permeability of the host rock is less than the threshold at which buoyant gas-phase convection can significantly influence heat flow (Buscheck and Nitao 1994). Also, the assumption is corroborated by results from a three-dimensional mountain-scale thermal-hydrologic model that is similar in scale to the SMT submodel in the multi-scale thermal-hydrologic model (BSC 2005a, Section 6.3).

- **Selected Timing of Climate Change Adequately Represents Expected Behavior**—The transition from present-day to monsoonal climate is assumed to occur 600 years after emplacement and the transition from monsoonal to glacial transition climate is assumed to occur 2,000 years after emplacement (SNL 2008a, Section 5.1.4[a]). The transition to the post-10,000-year percolation boundary condition occurs 10,000 years after emplacement. As described in Section 2.3.1, the timing of transition to future climate states has been established along with the characteristics of those climate states. The unsaturated zone flow model (Section 2.3.2) generates flow fields associated with the present-day climate and each of the future climate states. These flow fields are used as inputs to the multiscale thermal-hydrologic model. The selection of these specific transition times is consistent with the TSPA model approach (Section 2.4).

- **Waste Package Emplacement Occurs at the Same Time**—The assumption is made that the entire waste package inventory of the repository is emplaced at the same time. The 50-year preclosure ventilation period is the minimum time that any waste package location in the repository will experience ventilation (SNL 2008a, Section 5.2.3).

- **Spatial Variability of In-Drift Temperatures is Controlled by Thermal Radiation**—Three-dimensional transfer of heat between waste packages, drip shields, the drift wall, and other drift surfaces can be represented using thermal radiation. Heat flow in the longitudinal direction in the host rock (both by conduction and convection) plays a much smaller role in attenuating waste package temperature variability than does thermal radiation in the drift (SNL 2008a, Section 5.2.2).

- **Single Waste Package Sequence Represents Waste Package–to–Waste Package Heat Output Variability throughout Repository**—The multiscale thermal-hydrologic model accounts for waste package–to–waste package variability in heat output by assuming a single sequence (or arrangement) of waste package types within each drift (SNL 2008a, Section 5.4.2[a]). The percentages of each of the respective waste package types in the assumed sequence are similar to the corresponding percentages in the repository inventory (SNL 2008a, Table 5.4-1[a]). Therefore, the waste package sequence assumed in the multiscale thermal-hydrologic model calculations is representative of the inventory of waste packages in the repository. Section 2.3.5.4.3 discusses the effects of other sequences of waste package types on thermal performance.

- **Absolute Humidity Is Radially Uniform in the Emplacement Drift and Is Equal to the Absolute Humidity at the Drift Wall**—To calculate relative humidity on the drip shield and on the waste package, the absolute humidity (the partial pressure of water vapor) in the drift is assumed to be radially uniform and the same as the absolute humidity at the drift wall for a given location (SNL 2008a, Section 5.5). A three-drift test case was simulated using both the multiscale thermal-hydrologic model and an equivalent three-dimensional, mountain-scale nested grid, thermal-hydrologic model that incorporates dispersive transport (Section 2.3.5.4.1.3.3). The comparison of the results of these two simulations justifies this assumption. Dispersive transport represents buoyant gas-phase convection and binary vapor diffusion of air and water vapor. These processes lead to vigorous mixing within the emplacement drift that attenuates compositional gradients. The invert allows equilibration of water vapor partial pressure between the underside and exterior of the drip shield. This was verified by an LDTH calculation that modeled the drip shield, waste package, and invert in more detail than the LDTH calculations within the full multiscale thermal-hydrologic model (SNL 2008a, Section 5.5[a]).

- **Temperature and Relative Humidity Are Not Influenced by Axial Vapor Transport Along the Drift**—Gas-phase transport in the axial (i.e., longitudinal) direction along the emplacement drifts is assumed to have an insignificant effect on temperature and relative humidity predicted by the multiscale thermal-hydrologic model (SNL 2008a, Section 5.7). For a three-drift test case, simulated temperatures, relative humidities, and liquid-phase saturations are compared between the multiscale thermal-hydrologic model and an equivalent three-dimensional, mountain-scale, nested-grid, thermal-hydrologic model that incorporates longitudinal vapor transport along the drift (Section 2.3.5.4.1.3.3). Because the model-to-model differences are less than the variability resulting from parametric uncertainty in the multiscale thermal-hydrologic model results, these differences are insignificant (SNL 2008a, Section 7.5.4). Therefore, the assumption that axial vapor transport along the drift need not be explicitly addressed in the multiscale thermal-hydrologic model is justified.

- **Open Air Spaces in the Emplacement Drift Can Be Represented as Porous Media with Appropriate Properties**—The assumption is that the air-filled gaps in the emplacement drift can be represented as a porous medium by assigning appropriate property values. Accordingly, porosity is 100% and permeability is sufficiently large to ensure unimpeded gas-phase flow. The effective thermal conductivity used to represent

conduction and thermally driven convection is assigned to avoid significant overestimation of the convective effect (SNL 2008a, Section 5.3.1.7).

Limitations—The primary limitations of the multiscale thermal-hydrologic model are two-fold. First, the model is not intended to predict the occurrence or magnitude of seepage. Section 2.3.3 discusses the models used to predict seepage. Second, the multiscale thermal-hydrologic model is not intended to predict condensation at cooler locations in the drifts because it does not include axial vapor transport along the drifts. As discussed above, this model simplification does not affect the use of temperature and relative humidity output from the multiscale thermal-hydrologic model (Section 2.3.5.4.1.3.3). In-drift condensation has been evaluated with the in-drift condensation model and the effects incorporated into TSPA (Section 2.3.5.4.2).

Parameter Outputs—The multiscale thermal-hydrologic model calculates the following thermal-hydrologic variables: temperature, relative humidity, liquid-phase saturation, evaporation rate, air-mass fraction, gas-phase pressure, capillary pressure, and liquid- and gas-phase fluxes (SNL 2008a, Table 1-1). These thermal-hydrologic variables are determined at 20-m intervals as a function of position for each emplacement drift in the repository and as a function of waste package type (SNL 2008a, Section 8.1). These variables are determined at defined locations within the emplacement drifts, including the waste package and drip shield surfaces and in the invert. They are also determined at defined locations in the host rock. The multiscale abstraction description (Section 2.3.5.4.1.4.2) outlines how these parameter outputs are implemented in the TSPA model.

Governing Equations—The equations that govern the multiscale thermal-hydrologic model calculations are based on accepted scientific methods (SNL 2008a, Sections 6.2.3 and 6.2.4[a]). For example, the thermal-hydrologic model solves the mass and energy balance equations for air and water components in mobile liquid and gas fluid phases in a nondeformable solid. All four submodels solve the energy-balance equation. To calculate the movement of fluids through the host rock, the thermal-hydrologic model utilizes a dual-permeability approach in which the fracture and matrix systems are treated as separate but fully overlapping continua. As with other Yucca Mountain models simulating flow in the unsaturated zone, the dual-permeability approach incorporates an active-fracture methodology (SNL 2008a, Section 6.2.3.5).

Radiative heat transfer is included for open spaces within the emplacement drifts. The surfaces of the emplacement drift wall and waste packages are subdivided into surface elements, each of which is mapped to a computational volume element. Radiative heat flux is calculated between each pair of surface elements, using temperatures from the corresponding volume elements (SNL 2008a, Section 6.2.3.3).

The Suite of Multiscale Thermal-Hydrologic Model Components—As seen in Table 2.3.5-6 and Figure 2.3.5-26, the multiscale thermal-hydrologic model uses four submodels that are solved at different spatial scales. Results from three of these submodels are used to produce intermediate model results. A combination of the intermediate model results and the fourth submodel results is then used to produce the final model results, which are the output of the multiscale thermal-hydrologic model (SNL 2008a, Figure 1-1 and Table 1-2).

- **SMT Submodel**—The three-dimensional SMT submodel is used to determine repository-scale variations in host-rock temperature that result from the heat output of the entire inventory of waste (SNL 2008a, Sections 6.2.5 and 6.2.14[a]).

  The SMT submodel includes the influence of mountain-scale stratigraphic variation of thermal-property distribution, the edge-cooling effect that results from lateral heat loss at the repository edges, and the overburden-thickness distribution. The vertical domain extends from the ground surface to 1,000 m below the present-day water table; the lateral (adiabatic) boundaries are far enough away from the repository that they do not affect repository temperatures (SNL 2008a, Section 6.2.5).

  The SMT submodel represents the 108 emplacement drifts within the overall domain with rows of heated gridblocks. Figure 2.3.5-27 shows the relationship of the SMT grid (which is aligned with the drifts in the repository footprint) and the unsaturated zone flow model grid. The repository footprint (Figure 2.3.5-28) for the TSPA base-case design consists of five panels designated P1 (central), P2 for panel 2 (south), P3W for panel 3 west (north-central panel in the footprint), P3E for panel 3 east (northeast), and P4 (northwest) Figure 2.3.5-28. The heated gridblocks are 20 m in length parallel to the drift axis, 81 m perpendicular to the drift axis, and 6 m in the vertical direction. In all, there are 3,264 heated gridblocks that allow the multiscale thermal-hydrologic model to provide thermal-hydrologic output for 3,264 repository locations (SNL 2008a, Sections 6.2.5.1, 6.2.12.1[a], and 6.2.14[a]).

- **LDTH Submodel**—LDTH submodel calculates temperature, relative humidity, and other thermal-hydrologic variables (SNL 2008a, Figure 1-1 and Table 1-3). To represent two-phase heat and fluid flow in the fractured porous rock, the LDTH submodel uses the dual-permeability method, consistent with the unsaturated zone flow model (Section 2.3.2) (SNL 2008a, Sections 6.2.6 and 6.2.16[a]).

  Constructed on the scale of the emplacement drift, the two-dimensional LDTH submodel domain incorporates the near-field host rock and the drift contents, which include (as modeled) the air space, lumped drip shield–waste package heat source (SNL 2008a, Sections 6.2.6.2 and 6.2.16[a]), and invert as seen in Figure 2.3.5-29. Note that the effects of this lumped approximation of the drip shield and waste package are modified downstream in the overall multiscale thermal-hydrologic model calculational sequence with the DDT submodel results, which rigorously account for the actual dimensions and relative positions of the drip shield and waste package (SNL 2008a, Sections 6.2.8 and 6.2.17[a]).

  The LDTH submodel is executed at 560 repository locations (SNL 2008a, Sections 6.2.6.7 and 6.2.12[a]).

- **SDT Submodel**—The one-dimensional SDT submodel functions as a link between the SMT and LDTH submodels. It effectively provides a means of imposing the influence of the three-dimensional, SMT submodel temperature for a particular LDTH submodel

location onto the two-dimensional, LDTH submodel results for that same location (SNL 2008a, Sections 6.2.4 and 6.2.12[a]).

Because of the inherent consistency requirements, the SDT submodel uses the same vertical discretization of gridblocks and natural system thermal properties as is used in the SMT submodel (SNL 2008a, Sections 6.2.7.2 and 6.2.15[a]). To be consistent with the LDTH submodel, the SDT submodel is run at the same 560 locations and for the same four parametric pillar half-widths, which are equivalent to parametric areal mass loadings using the same boundary conditions and the same heat-generation rate versus time (SNL 2008a, Sections 6.2.7 and 6.2.15[a]).

- **DDT Submodel**—The three-dimensional DDT submodel is used to determine waste package–specific deviations, relative to line-averaged-heat-source conditions of the LDTH submodel in temperatures in the emplacement drift and adjoining host rock (SNL 2008a, Sections 6.2.8 and 6.2.17[a]). The DDT submodel does so by explicitly accounting for waste-package-specific heat output and for thermal radiation between waste package and drift surfaces. The cross-sectional view of the model mesh is similar to that for the LDTH submodel mesh (Figure 2.3.5-29), except that the drip shield and waste package are not lumped (SNL 2008a, Section 6.2.8.2 and Figure 6.2-8).

  Seven waste packages (six full and two half packages at the ends of the repeating cell) are represented in the DDT submodel: three 21-PWR commercial spent nuclear fuel (SNF) waste packages, two 44-BWR commercial SNF waste packages, and two codisposal (DOE spent nuclear fuel and high level waste glass) waste packages (SNL 2008a, Section 6.2.17[a]). The heat generation rates of these waste packages cover a wide range, from low (the codisposal waste packages) to high (the 21-PWR commercial SNF waste packages) (SNL 2008a, Table 6.2-6[a]). The application of this waste package unit cell explicitly represents 93% of the total repository inventory (SNL 2008a, Table 5.4-1[a]). Moreover, the percentages of the respective waste package types in the model are similar to the corresponding percentages in the inventory (SNL 2008a, Table 5.4-1[a]).

  The DDT submodel is used to represent temperature variability among waste packages, which is controlled by heat transfer within the drift. The assumption that thermal radiation dominates heat transfer between the waste package, drip shield, drift wall, and other drift surfaces is used to simplify the DDT submodel. Thermal conduction and convection processes in the host rock have been determined to not significantly affect temperature differences between adjacent waste packages (SNL 2008a, Section 5.2.2), hence the multiscale thermal-hydrologic model calculation requires only one set of DDT submodel calculations for a single location in the repository. The selected location (g-9 in Figure 2.3.5-27) has the following attributes: it is in the middle of the Tptpll unit, which is the predominant host-rock type in the repository; the overburden thickness is close to the average for the repository; and the location is one of the 560 locations for which pairs of LDTH and SDT submodels are run (SNL 2008a, Sections 6.2.8 and 6.2.17[a]). Figure 2.3.5-30 shows the distribution of host-rock units within the repository footprint (SNL 2008a, Figure 6.2-18[a]).

To ensure the necessary consistency, the upper temperature boundary conditions for the DDT submodel correspond to that used for the SDT and LDTH submodels at that same location. The lower boundary condition is set to the initial temperature of the water table because the DDT submodel is only important at times earlier than the time for the water table temperature perturbation to be manifested (SNL 2008a, Section 5.1.5). The DDT submodel uses similar thermal loading and the same host-rock thermal properties that are used in the LDTH, SMT, and SDT submodels (SNL 2008a, Sections 6.2.4, 6.2.8, 6.2.12[a], and 6.2.17[a]).

LMTH Intermediate Model Results—The three-dimensional LMTH intermediate model results are created by using the SDT submodel results, in conjunction with the corresponding SMT submodel results, to modify LDTH submodel results. This step accounts for the influence of mountain-scale heat flow including edge effects. The LMTH intermediate model results are applicable to a repository that is uniformly heated with a repository-wide average thermal load per unit length (SNL 2008a, Section 6.2.4).

DMTH Final Model Results —The three-dimensional DMTH final model results are created using the LMTH intermediate model results, modified by DDT submodel temperature output (Figure 2.3.5-26), to account for waste-package-specific deviations from average waste package behavior (SNL 2008a, Section 6.2.4). These results are the multiscale thermal-hydrologic model output (SNL 2008a, Section 6.3[a]).

2.3.5.4.1.3.2 Model Results

Results summarized here include the effects of variability and uncertainty. The ranges of peak drift wall and waste package temperatures, predicted by the multiscale thermal-hydrologic model for all waste packages in the repository, are shown in Table 2.3.5-7 (SNL 2008a, Table 6.3-49[a]). The ranges for the time that boiling ceases at the drift wall are tabulated in Table 2.3.5-8 (SNL 2008a, Table 6.3-50[a]). The same information is shown as complementary cumulative distribution functions in Figures 2.3.5-31 and 2.3.5-32 (SNL 2008a, Figures 6.3-77[a] and 6.3-78[a]).

In Figures 2.3.5-33 and 2.3.5-34, the ranges for temperature and relative humidity histories at the drift wall and waste package are plotted for the eight waste packages in the unit cell at 3,264 locations across the repository footprint, and for all seven of the thermal conductivity-infiltration uncertainty cases modeled. Each range represents 182,784 histories (SNL 2008a, Figures 6.3-76[a] and 6.3-81[a]). Similarly, Figure 2.3.5-35 shows the range of liquid phase saturation at the drift wall and the invert (SNL 2008a, Figure 6.3-80[a]).

The maximum lateral extent of the dryout zone (defined as the distance from the drift center to the 96°C isotherm in the host rock) is tabulated in Table 2.3.5-9 and plotted as complementary cumulative distributions in Figure 2.3.5-36 (SNL 2008a, Figure 6.3-79[a]). Over all seven cases, the maximum lateral extent of boiling ranges from approximately 4.4 to 11.1 m with a median extent of 7.8 m. Thus, the lateral extent of boiling will always be smaller than the half-spacing between emplacement drifts (40.5 m; Table 1.9-9, Parameter Number 01-13). The majority of the host rock between emplacement drifts will remain at temperatures below the boiling point of water, thereby enabling condensate and percolation flux to drain between emplacement drifts. Because of this continuous drainage, the multiscale thermal-hydrologic model predicts that condensate will

drain between the drifts and not accumulate above the emplacement drifts (SNL 2008a, Section 8.2).

The multiscale thermal-hydrologic model was also used to calculate the effect of drift collapse on waste package temperatures (SNL 2008a, Section 6.3.17[a]). The model was run at a typical location (the g_9 location shown in Figure 2.3.5-27) for a drift that had collapsed and filled with rubble to a diameter of 11 m. The rubble was evaluated at high and low thermal conductivities. The result of the calculation is a set of time-dependent temperature and relative humidity changes for the drip shields and waste packages in the unit cell, and in the invert saturation and liquid flux, compared to the histories for the intact drift calculation. These changed histories are used to represent the thermal-hydrologic effects from drift collapse as discussed in Section 2.3.4.5.6.2. Figure 2.3.5-37 illustrates complementary cumulative distribution functions for the peak temperatures of both the commercial spent nuclear fuel and the codisposal waste packages, for high and low rubble thermal conductivity (SNL 2008a, Figure 6.3-87[a]).

Results of the multiscale thermal-hydrologic model demonstrate that a small number of parameters and factors are responsible for the majority of variability and uncertainty in simulated repository thermal-hydrologic conditions (SNL 2008a, Sections 6.1.4 and 6.3.1.2):

- Variability caused by the edge-cooling effect, which increases with proximity to the edges of the repository
- Variability in heat output among waste packages
- Variability and uncertainty in host-rock thermal conductivity
- Variability and uncertainty in percolation flux above the repository.

The multiscale thermal-hydrologic model simulations supporting TSPA address the influence of these four items. The first item is addressed explicitly by representing the repository-scale geometry of the heated repository footprint in the SMT submodel (SNL 2008a, Sections 6.2.5 and 6.2.17[a]), including each of the emplacement drifts in the repository layout (Figure 2.3.5-26). The multiscale thermal-hydrologic model addresses the second item with the DDT submodel by discretely representing the range of waste packages emplaced across the repository (SNL 2008a, Sections 6.2.8 and 6.2.17[a]), including pressurized water reactor (PWR) and boiling water reactor (BWR) commercial SNF waste packages and DOE SNF/high-level radioactive waste (HLW) (codisposal or DOE HLW) waste packages.

Variability and uncertainty in the host-rock thermal conductivity and the percolation flux, the third and fourth items, are addressed through the use of seven cases. Development of these seven cases considered the nominal 10th, 30th, 50th, and 90th percentile infiltration maps for present-day climate and their uncertainties. The unsaturated zone flow model (Section 2.3.2) calculates a percolation flux map at the top of the Topopah Spring rock unit for each time period (the three climate states and the post-10,000-year period) and infiltration uncertainty case, and these percolation maps were used by the multiscale thermal-hydrologic model. The infiltration maps were coupled with low (10th percentile), mean, and high (90th percentile) host-rock thermal conductivity for the four different rock units (Tptpul, Tptpmn, Tptpll, Tptpln) included in the

repository emplacement area (SNL 2008a, Section 6.2.12.2[a]). Although there are twelve possible combinations of infiltration uncertainty and thermal conductivity uncertainty, five were represented (for computational efficiency) using as a surrogate the most similar of the seven analyzed cases (SNL 2008a, Section 6.2.12.3[a]). This surrogate process is feasible because the temperatures increase for decreasing infiltration and for decreasing thermal conductivity, and the seven analyzed cases span the full ranges of both infiltration and thermal conductivity. The boiling duration was used as the metric to determine the most appropriate analyzed case to use for each surrogate case (SNL 2008a, Section 6.2.12.3[a]). The five cases using surrogates are low host-rock thermal conductivity coupled with nominal 30th, 50th, and 90th percentile infiltration estimates and the high host-rock thermal conductivity coupled with nominal 30th and 50th percentile infiltration estimates (SNL 2008a, Table 6.3-47[a]). The seven cases used to support TSPA are listed below (SNL 2008a, Tables 6.3-47[a] and 6.3.48[a]):

- Nominal 10th percentile infiltration flux with low (10th percentile) host-rock thermal conductivity
- Nominal 10th percentile infiltration flux with mean host-rock thermal conductivity
- Nominal 10th percentile infiltration flux with high (90th percentile) host-rock thermal conductivity
- Nominal 30th percentile infiltration flux with mean host-rock thermal conductivity
- Nominal 50th percentile infiltration flux with mean host-rock thermal conductivity
- Nominal 90th percentile infiltration flux with mean host-rock thermal conductivity
- Nominal 90th percentile infiltration flux with high host-rock thermal conductivity.

Propagation of parametric uncertainty in the multiscale thermal-hydrologic model involves two key natural system parameters: host-rock thermal conductivity and percolation flux (SNL 2008a, Section 8.2). Sensitivity studies show that hydrologic-property uncertainty does not need to be propagated in multiscale thermal-hydrologic model calculations of in-drift temperature and relative humidity because its impact is small compared to that of host-rock thermal-conductivity uncertainty (SNL 2008a, Sections 6.3.2.4 and 6.3.14[a]). The range of thermal-hydrologic conditions calculated by the multiscale thermal-hydrologic model across the repository is broad because it captures the major parameters and factors responsible for thermal-hydrologic variability and uncertainty, down to the scale of 20 m along each of the emplacement drifts.

2.3.5.4.1.3.3 Model Support and Uncertainty

Field Tests—The LDTH thermal-hydrologic submodel of the multiscale thermal-hydrologic model is supported by direct comparison between thermal-hydrologic simulations and results from field-scale thermal testing in welded tuff. Data and results from the Large Block Test, Drift Scale Test, and the Single Heater Test are summarized in *Thermal Testing Measurements Report* (SNL 2007g). The Single Heater Test was conducted in preparation for the Drift Scale Test and is

not discussed further here. The following discussion describes model–data comparisons that support use of the multiscale thermal-hydrologic model for TSPA:

Large Block Test—Using the same modeling approach as the two-dimensional LDTH submodel, a three-dimensional equivalent was used to simulate thermal-hydrologic behavior in the Large Block Test. The Large Block Test was constructed around an excavated block of tuff (3 m × 3 m × 4.5 m) at Fran Ridge, near Yucca Mountain (SNL 2007g, Section 6.1). The block was instrumented and subjected to heating and cooling. The thermal-hydrologic properties used to describe the test block in simulations are consistent with those used to describe the same rock unit in the multiscale thermal-hydrologic model, the unsaturated zone flow model, and other models supporting the performance assessment. A comparison of results shows agreement between the simulated and measured temperatures, demonstrating that the thermal-hydrologic model provides a valid representation of heat flow in partially saturated fractured porous rock. The thermal-hydrologic model was also able to qualitatively capture the dryout and rewetting behavior observed during the Large Block Test, although this agreement was not as good as that between the simulated and measured temperatures (SNL 2008a, Section 7.3).

Drift Scale Test—The three-dimensional LDTH submodel equivalent discussed above for the Large Block Test was also used to simulate the Drift Scale Test (SNL 2008a, Sections 7.4 and 7.4[a]). In this test, there are 28 boreholes instrumented with temperature sensors (Figure 2.3.3-34). As with the Large Block Test comparison, there is agreement between simulated and measured temperatures for the Drift Scale Test (SNL 2008a, Section 7.4.3). Some typical temperature histories of boreholes are given in Figure 2.3.5-38, which compares field measurements versus three simulated cases: a base case that represents gas leakage through the bulkhead; a sealed-bulkhead case that does not allow leakage in the calculation; and a high host-rock thermal conductivity case (noted "high *Kth*" in the figures) that is the same as the base case but has a host-rock thermal conductivity 1 standard deviation higher than the mean (SNL 2008a, Section 7.4.3). Figure 2.3.5-39 provides a typical spatial temperature profile using borehole 141, which is a vertical borehole below the drift. The heaters were turned off after 1,503 days. This figure compares field measurements to the prior simulation base case (SNL 2008a, Section 7.4.3) and to the new base case that uses updated thermal and hydrologic properties (SNL 2008a, Section 7.4.6[a]).

Typical of results from other boreholes, the field data for borehole 141 (Figure 2.3.5-39) exhibit a temperature plateau at 96°C that becomes more pronounced with time (most pronounced in the 730-day data shown in Figure 2.3.5-39). In contrast, most of the previous base case simulated profiles for boreholes do not have this plateau. It appears in only a few of the simulated profiles, and at later times compared to the field data (SNL 2008a, Section 7.4.3).

The temperature plateau does not develop in most of the previous simulated profiles because of the low value of matrix permeability (1.77×10^{-19} m^2, (SNL 2008a, Table IV-4, unit tswM4)) for the Tptpmn rock unit in those calculations, which caused a temporary gas-phase pressure buildup in the matrix (in the calculation). As a result, temperatures from the LDTH submodel equivalent were generally higher than the field-measured temperatures for values exceeding 96°C. The value of matrix permeability for the Tptpmn unit used in the current simulations (3.16×10^{-18} m^2 (SNL 2008a, Table IV-4[a], layer tsw34)) is the same as that used for repository predictions and results in better agreement with the Drift Scale Test measurements.

For temperatures less than about 80°C, the simulated and field-measured temperatures are in good agreement for all three cases considered in the previous calculations and for the current base case calculations, which use the same properties as the multiscale thermal-hydrologic model. Overall, the comparison of simulated and measured temperatures demonstrates that the LDTH submodel equivalent, and by extension the LDTH submodel, provides a valid representation of heat flow in the Drift Scale Test (SNL 2008a, Sections 7.4.5 and 7.4.6[a]).

Figure 2.3.5-40 provides liquid saturation profiles at various times as a function of distance from the borehole collar for borehole 80, which is parallel to the heated drift, but offset laterally and upward from the drift crown. This figure illustrates behavior common to other boreholes as well, in that the simulated rock dryout lags behind the dryout measured in the field, and that the calculations with the updated thermal and hydrologic properties greatly increase agreement with the Drift Scale Test measurements. The cause of the time lag in simulated dryout, which is more pronounced for the previous calculations, is the same as the cause for over-estimation of temperatures, illustrated in Figure 2.3.5-39. The low matrix permeability results in a gas-phase pressure buildup in the matrix, which delays the simulated dryout response compared to field data. However, this time lag is a transient effect in the model that dissipates as the gas-phase pressures drop, which is demonstrated in Figure 2.3.5-40 by the improved agreement over time between the simulated and field data. As seen in the two plots (1,510 and 1,917 days) for time periods following the end of the 1,503-day heating phase, the spatial extent of the simulated dryout zone approaches that of the observed dryout zone. Thus, despite the time lag, there is agreement between the maximum spatial extent of rock dryout simulated by the LDTH submodel equivalent and that measured in the Drift Scale Test (SNL 2008a, Sections 7.4.4, 7.4.5, and 7.4.7[a]).

In summary, the comparisons between the modeled and field-measured thermal-hydrologic behavior (e.g., Figures 2.3.5-38 to 2.3.5-40) show that the multiscale thermal-hydrologic model, together with the use of the thermal and hydrologic input parameters developed for TSPA, slightly overestimates temperature, liquid-phase saturation, and relative humidity. The differences are within, or comparable to, the parametric uncertainty of multiscale results.

Alternative Conceptual Models—Uncertainty in the multiscale thermal-hydrologic model is evaluated by considering alternative conceptual models or approaches. The first example presented is a comparison with an east–west, mountain-scale, thermal-hydrologic model. The second example is an alternative, three-dimensional, mountain-scale, nested-grid, thermal-hydrologic model representing a three-drift repository. The third example is an alternative, three-dimensional, pillar-scale, thermal-hydrologic model grid representing each waste package and drip shield in a single full-length drift, with lateral symmetry to adjacent drifts. These alternative model comparisons provide confidence in the predictive capability of the multiscale thermal-hydrologic model.

Comparison with an East–West, Mountain-Scale, Thermal-Hydrologic Model—One model used for comparison to the multiscale thermal-hydrologic model is an east–west, vertical cross-section, mountain-scale thermal-hydrologic model. Because this model does not simulate in-drift thermal-hydrologic conditions, the comparison is restricted by the respective modeling approaches to simulations of drift wall temperatures (SNL 2008a, Section 6.4).

During the period when temperatures in the rock and in the EBS are above boiling, the temperatures simulated by the respective modeling approaches are in agreement, as shown in Figure 2.3.5-41. During the early heat-up period, the coarse (lateral and axial) gridblock spacing in the east–west model does not capture the rapid drift wall temperature rise, which causes the east–west model to overpredict the temperature at both the drift wall and the mid-pillar locations and thereby prevent condensate from shedding between emplacement drifts. In contrast, the fine lateral gridblock spacing in the multiscale thermal-hydrologic model incorporates the influence that the lateral temperature gradient has on condensate shedding between emplacement drifts. Also, the line-averaged heat-source approximation used by the east–west model averages out differences in temperature between otherwise hot and cold waste package locations, while the multiscale thermal-hydrologic model calculates temperatures at individual waste packages; Figure 2.3.5-41 is at the location of an "average" 21-PWR, medium heat, commercial spent nuclear fuel waste package. Together, the underprediction of condensate shedding between emplacement drifts and overprediction of temperature at cold waste package locations causes the east–west model to build up more condensate above the repository horizon leading to heat-pipe behavior. This behavior is exhibited by temperature fluctuations in the east-west model at 400 years (SNL 2008a, Section 6.4).

Given the differences between the multiscale thermal-hydrologic model and the east–west cross-section mountain-scale model, the agreement in results between the two models provides confidence that the multiscale thermal-hydrologic model is suitable for predicting the evolution of thermal-hydrologic conditions in the repository emplacement drifts. The differences in predicted temperatures between the multiscale thermal-hydrologic model and the east–west model are within the range of temperature differences resulting from parametric uncertainty, indicating that the impact of conceptual-model uncertainty is no larger than that of parametric uncertainty (SNL 2008a, Section 6.4).

Comparison with a Three-Dimensional, Mountain-Scale, Nested-Grid, Thermal-Hydrologic Model for the Three-Drift Test Case—The validity of the multiscale thermal-hydrologic model approach was investigated by comparing its results with those of a three-dimensional, mountain-scale, nested-grid, thermal-hydrologic model for the three-drift test case shown in Figure 2.3.5-42. This large numerical model uses a nested grid that allows it to represent both mountain- and drift-scale thermal-hydrologic behavior (SNL 2008a, Section 7.5). The three-dimensional model is also used to evaluate condensation processes, as discussed below.

The test cases selected for multiscale thermal-hydrologic model validation are based on a simplified example of the repository system consisting of three 243-m-long emplacement drifts, areally uniform percolation flux, and a uniform overburden thickness (Figure 2.3.5-42) (SNL 2008a, Section 7.5.1) implemented using the NUFT code (SNL 2008a, Sections 3.1.1 and 3.1.2). The central emplacement drift uses a combination of a line-averaged heat source for most of the drift, four discrete sources (representing individual waste packages) at the center of the drift, and four discrete sources at the outer end of the drift (SNL 2008a, Figure 7.5-1). Three test cases were evaluated:

- Case 1—Includes no axial vapor (or gas) transport along the emplacement drifts. This corresponds to the multiscale thermal-hydrologic model, which does not include vapor transport along the drift axis (SNL 2008a, Sections 7.5.3 and 5.7[a]).

- Case 2—Includes axial vapor transport using a small value for the gas-phase dispersion coefficient to account for binary diffusion of water vapor but not for the influence of convective mixing. In addition, a bulkhead was located just beyond the outermost waste package at the end of each emplacement drift (SNL 2008a, Section 7.5.3).

- Case 3—Includes axial vapor transport using a high value of the gas-phase dispersion coefficient to account for the influence of turbulent convective mixing. The three-dimensional, mountain-scale, nested-grid, thermal-hydrologic model uses a dispersion coefficient that varies between 0.011 and 0.021 m^2/s (depending on temperature). The value for high dispersion used in the in-drift condensation model described in Section 2.3.5.4.2.3.1 is 0.008 m^2/s, which is slightly smaller than the lower range used in Case 3 (SNL 2008a, Section 7.5.2; SNL 2007e, Section 6.2.7). Case 3 has no bulkhead at the end of the emplacement drift and includes the unheated section of the emplacement drift beyond the outermost waste package. This case includes the effects of rock dryout during the ventilation period (SNL 2008a, Section 7.5.3).

Of the three cases, the third is most realistic and is emphasized in the discussion below. Differences in the simulated thermal-hydrologic conditions between Cases 1 and 3, for the emplacement drift and the adjoining host rock, are used as quantitative indicators of the importance of the cold-trap effect and moisture transport to the unheated part of each emplacement drift with respect to multiscale thermal-hydrologic model predictions (SNL 2008a, Section 7.5.3). Section 2.3.5.4.2 includes additional information about in-drift moisture flow.

For comparison, the multiscale thermal-hydrologic model was configured for this same three-drift configuration and associated boundary conditions. Therefore, the three-drift multiscale results are directly comparable to those of the corresponding three-dimensional, mountain-scale, nested-grid, thermal-hydrologic model. The locations selected for direct comparisons are at the center and edge of the simplified repository (SNL 2008a, Sections 7.5.3).

Temperature differences between the multiscale results and Cases 1 to 3 are dominated by how the multiscale methodology addresses three-dimensional heat losses (SNL 2008a, Section 7.5.3). For waste package locations more than 20 m from the repository edge, which represents approximately 97% of the Yucca Mountain repository area, overprediction of peak drip shield temperature by the multiscale thermal-hydrologic model is less than 7°C. At the edge, comparison of the multiscale results with Case 3 shows small differences (6.5°C to 17.1°C) in peak drip shield temperature (SNL 2008a, Figure 7.5-5). These differences are smaller than the overall effect of parametric uncertainty of host-rock thermal conductivity and percolation flux (SNL 2008a, Section 7.5.4). Temperature differences are greatest for the last two waste packages at the edge and are caused by the coarse spatial grid resolution of the mountain-scale thermal conduction submodel (SMT) used in the multiscale modeling framework (SNL 2008a, Section 7.5.3).

The small differences in temperatures between Cases 1 and 3 show the lack of influence of the cold-trap effect on temperatures for waste package locations at the repository edge. This result supports use of the multiscale thermal-hydrologic model for predicting thermal-hydrologic conditions in the emplacement drifts and the adjoining host rock, for waste package locations near the repository edge as well as for the center (SNL 2008a, Section 7.5.3).

For Case 3, which includes axial vapor transport and the resulting cold-trap effect, the simulated in-drift relative humidity and host-rock liquid saturation conditions (SNL 2008a, Figures 7.5-6 and 7.5-7) agree more closely with the multiscale thermal-hydrologic model results than the other cases (SNL 2008a, Section 7.5.3). The differences in predicted relative humidity and host-rock liquid saturation between the multiscale results and Case 3 are smaller than the overall effect of parametric uncertainty of host-rock thermal conductivity and percolation flux for the multiscale repository model (SNL 2008a, Section 7.5.4). Although the multiscale thermal-hydrologic model does not directly account for the influences of the cold-trap effect or of ventilation-driven rock dryout during the ventilation period, it shows agreement with Case 3, which includes both of these influences (SNL 2008a, Section 7.5.3). Therefore, it is unnecessary to incorporate axial vapor transport and the resulting cold-trap effect into the multiscale thermal-hydrologic model for TSPA. Because of two offsetting effects in the multiscale thermal-hydrologic model, Case 3 is a better match than Case 1 to the results from the multiscale thermal-hydrologic model. Case 1 has the same limitations on axial transport of vapor as does the multiscale thermal-hydrologic model. The first offsetting effect is an underprediction at early times of edge cooling of the waste packages at the drift ends. As discussed below for the alternative approach using a three-dimensional, pillar-scale, thermal-hydrologic model, the multiscale thermal-hydrologic model uses a temporally variable effective drift spacing in the LDTH and DDT submodels to incorporate the results of the SMT submodel, which includes edge effects explicitly. The variable effective drift spacing computational approach works well except at early times for the edge-most waste packages because later times or more centrally-located waste packages have the lateral heat sink (the mid-pillar at variable computational distance) a similar distance from the waste package as the actual repository edge (which is in the axial direction not included in the LDTH and DDT submodels). The second offsetting effect is the axial transport of vapor that is not included in the multiscale thermal-hydrologic model or in Case 1 and which tends to move latent heat axially toward the end of the drift. The first effect results in warmer waste packages at the drift ends at early times, and the second effect results in cooler waste packages at the drift ends, in the multiscale thermal-hydrologic model, which tend to compensate for each other. Case 3 does not include either of these two limitations and more correctly calculates edge cooling and axial vapor transport, whereas Case 1 correctly calculates edge cooling but does not include axial vapor transport.

The alternative model shows that the multiscale thermal-hydrologic model results for temperature and relative humidity, and their associated parameter-related uncertainties, envelope the results that would be obtained from the exercise of a more sophisticated multiscale thermal-hydrologic model that incorporates axial vapor transport (SNL 2008a, Section 7.5.4).

Alternative Approach Using a Three-Dimensional, Full-Length-Drift, Pillar-Scale, Thermal-Hydrologic Model with Individual Waste Packages and Drip Shields—As an alternative approach, an entire drift was modeled with individual waste packages and drip shields. An alternative model was constructed with 71 individual waste packages using the same unit cell as the multiscale thermal-hydrologic model. With lateral symmetry at the drift centerline and mid-pillar and with axial symmetry at one end of the set of waste packages, the alternative model accurately accounts for the thermal-hydrologic processes in a full-length, typical-location drift that is not near the north or south ends of the repository footprint. In addition to providing inputs to the in-drift condensation model (Section 2.3.5.4.2) (SNL 2008a, Section 6.3.18[a]), the alternative model was compared to the multiscale thermal-hydrologic model to evaluate the significance of

lateral and axial vapor transport in the drift, with respect to thermal-hydrologic conditions at center and edge locations for each of the eight waste packages in the unit cell (SNL 2008a, Section 7.8[a]).

Figure 2.3.5-43 plots the peak waste package temperature and time when boiling ceases on the waste package for all 71 waste packages in the pillar-scale test problem. A comparison of Case 1, which includes both axial and lateral vapor transport, and Case 2, which includes only lateral vapor transport, in Figure 2.3.5-43 shows the influence of vapor transport along the drift. Vapor is transported from the hotter repository center to the cooler repository edge, where it condenses, resulting in latent heat transport from center to edge. Consequently, latent heat transport causes peak waste package temperatures to be slightly lowered at the repository center and for most of the drift, while slightly increasing peak waste package temperatures for the outermost two waste packages. The same pattern is seen along the drift for the time when boiling ceases on the waste package. The influence of latent heat transport along the drift is stronger for the boiling duration than for peak temperature (SNL 2008a, Section 7.8[a]).

In Figure 2.3.5-43, the multiscale thermal-hydrologic model is in reasonable agreement with the alternative model for most of the drift, with the multiscale thermal-hydrologic model predicting higher temperatures for the outermost several waste packages (SNL 2008a, Section 7.8[a]). The cause of this overprediction of temperature at early times at the repository edge in the multiscale thermal-hydrologic model is the use of a wider effective drift spacing in the DDT submodel to account for the proximity of unheated rock to the waste packages at the end of the drift (SNL 2008a, Section 7.5).

For all eight waste packages in the unit cell, good agreement in temperature is obtained between the multiscale thermal-hydrologic model and the alternative model at the repository center. For the fourth or fifth waste package from the edge, the multiscale thermal-hydrologic model and the alternative model are in good agreement. For the outermost three to four waste packages, the multiscale thermal-hydrologic model predicts higher temperatures for early time (including when temperatures peak); however, the agreement improves with time, particularly after boiling ceases. From the fourth or fifth waste package from the edge, all the way to the repository center, the relative humidity and liquid-phase saturation histories predicted by the multiscale thermal-hydrologic model are in reasonable agreement with those of Case 2 (of the alternative model, which includes lateral but not axial vapor transport). However, Case 1 (of the alternative model, which includes both lateral and axial vapor transport) predicts drier conditions than the multiscale thermal-hydrologic model, which shows the influence of vapor transport and moisture loss from the heated portion of the emplacement drift. These results show that the assumption concerning axial vapor transport and condensation, which is discussed in *Multiscale Thermohydrologic Model* (SNL 2008a, Section 5.7), is justified with respect to temperature. However, vapor transport may result in drier conditions than those predicted by the multiscale thermal-hydrologic model (SNL 2008a, Section 7.8[a]).

2.3.5.4.1.4 Model Abstraction

[NUREG-1804, Section 2.2.1.3.3.3: AC 1(1) to (4), (7)]

This section explains how the multiscale thermal-hydrologic model is abstracted and how the abstraction is implemented in TSPA. The model produces files that are tables of time-dependent thermal-hydrologic variables (temperature and relative humidity at several locations within the drift

cross section, and invert saturation and water flux). Each table represents one location within the repository. These files are grouped into five bins representing subranges of the ambient percolation flux. In addition, for each percolation bin, the abstraction identifies the single commercial SNF waste package that is most representative of the ensemble of commercial SNF waste packages in that bin, and also the single codisposal waste package that is most representative of the ensemble of codisposal waste packages in that bin. As explained below, some components of the TSPA model use the full set of thermal-hydrologic histories and other components use ten representative waste package histories (two waste package types times five percolation bins) (SNL 2008a, Section 6.2.12.1[a]).

2.3.5.4.1.4.1 Abstraction Methodology

For each of the 16 unsaturated flow fields (three climate states plus the post-10,000-year percolation boundary condition, times four infiltration uncertainty cases) and eight waste packages simulated (in the unit cell), the multiscale thermal-hydrologic model calculates time-dependent thermal-hydrologic variables, temperature, and relative humidity at 3,264 locations. Before this information is passed to the TSPA, two sets of analyses are performed. First, the multiscale thermal-hydrologic model results and their associated locations are grouped into one of five repository subregions based on the percolation flux at the base of the PTn. The second set of analyses involves determining a single representative commercial SNF waste package and a single representative codisposal (DOE SNF and HLW) package, given a set of subdomain locations that define a percolation subregion (SNL 2008a, Sections 8.3 and 6.2.12.1[a]).

Binning into Percolation Subregions—For all 3,264 locations, bin indices are calculated based on the rank order of the percolation flux (nominal 10th percentile glacial transition climate flux map at the base of the PTn geologic unit) associated with the location (SNL 2008a, Sections 8.3 and 6.2.12.1[a]):

- Bin 1 includes locations with percolation fluxes below the 5th percentile.
- Bin 2 includes locations with percolation fluxes in the 5th to 30th percentile.
- Bin 3 includes locations with percolation fluxes in the 30th to 70th percentile.
- Bin 4 includes locations with percolation fluxes in the 70th to 95th percentile.
- Bin 5 includes locations with percolation fluxes above the 95th percentile.

Figure 2.3.5-44 shows the correlation of percolation flux bins with repository location (SNL 2008a, Figure VIII-1[a]). Output files (referred to as "WAPDEG binning files") are prepared with the output indexed by percolation subregion and location. A summary of the TSPA model components and submodels and use of the abstracted multiscale thermal-hydrologic results is included in the discussion on TSPA implementation in Section 2.4. The seepage, drip shield degradation, waste package degradation, and drift wall condensation components of the TSPA use the output files that are indexed by percolation bin, include all locations, include all eight waste packages simulated in the unit cell, and include all seven of the thermal conductivity-infiltration uncertainty cases that were analyzed. Parameters provided to TSPA in these output files include the temperature and relative humidity (versus time) for the waste package and for the drip shield and the temperature (versus time) for the drift wall (SNL 2008a, Sections 8.3 and 6.2.12.1[a]). These files also include the percolation fluxes that are input to the TSPA seepage model component and that were received from the unsaturated zone flow model for incorporation into the multiscale thermal-hydrologic

model files that are read by the TSPA model (SNL 2008a, Section 6.2.12.4[a]). Each of the five multiscale thermal-hydrologic model uncertainty cases that was not calculated is also provided to TSPA, using the appropriate percolation fluxes from the unsaturated zone model uncertainty case and the thermal-hydrologic parameters from the surrogate multiscale thermal-hydrologic model case (SNL 2008a, Sections 8.3, 6.2.12.1[a], and 6.3.15[a]).

Determination of Typical Waste Package—A typical waste package of each type (commercial SNF or codisposal), for each of the five percolation bins, was selected for use in representing that bin for the TSPA. The selected package was the one closest to the median of the packages with respect to both duration of boiling temperature at the waste package and peak waste package temperature (SNL 2008a, Section 6.2.12.1[a]). The approach was used for each of the seven cases calculated to represent uncertainty on thermal conductivity and infiltration flux (Section 2.3.5.4.1.3.2). For each uncertainty case, the selected thermal-hydrologic data (versus time) for temperature and relative humidity for each representative waste package and associated drip shield, average emplacement drift wall temperature, average invert temperature, average invert saturation, and average invert flux at each of the ten representative locations (two waste package types times five percolation bins), are stored in file set (termed "TSPA binning") that is subsequently accessed by the TSPA. These files are used as input to the EBS chemical environment, EBS flow, waste form degradation and mobilization, and EBS transport components of the TSPA model (SNL 2008a, Section 6.2.12.1[a]).

2.3.5.4.1.4.2 Abstraction Implementation in TSPA

The abstracted multiscale thermal-hydrologic model results are implemented by the EBS thermal-hydrologic environment submodel of the TSPA (Figure 2.3.5-1). This TSPA submodel provides the abstracted results to a number of TSPA model components and submodels (Figure 2.3.5-1) (SNL 2008b, Section 6.1.4.2):

- Drift seepage submodel (Section 2.3.3), which calculates seepage into the emplacement drifts from the unsaturated zone above the repository (uses percolation fluxes which were developed by the unsaturated zone flow process model and transmitted to the TSPA model within the multiscale thermal-hydrologic model output files; also uses drift wall temperature).

- Drift wall condensation submodel (Section 2.3.5.4.2), which uses multiscale model output tables that provide the time at which temperature falls below 96°C, for each waste package, and the average percolation flux over the entire length of the drift.

- Waste package and drip shield degradation model component (Section 2.3.6), which calculates drip shield and waste package breaches, including early package failures (uses the waste package temperature and relative humidity).

- EBS chemical environment submodel (Section 2.3.5.5), which implements the in-drift chemical environment abstractions (uses waste package temperature and relative humidity).

- Waste form degradation and mobilization model component (Section 2.3.7), which includes submodels for radionuclide inventory and related topics of in-package chemistry, cladding degradation, waste form degradation, dissolved radionuclide concentration limits, and waste form and EBS colloids (uses temperature and relative humidity).

- EBS flow and transport submodel (Section 2.3.7), which implements the EBS radionuclide transport abstraction (uses waste package temperature and relative humidity; invert temperature and saturation; and liquid phase wicking flux from the host rock into the invert that begins at the time of rewetting).

Details as to the specific parameters provided to each TSPA model component or submodel are given in Section 2.4.

In addition, the multiscale thermal-hydrologic model provides thermal-hydrologic conditions on the waste package surface, which are used as input to the localized corrosion initiation model for the waste package outer barrier (Section 2.3.6.4.3.1). The resultant localized corrosion initiation histories are then used by the TSPA waste package and drip shield degradation model component to include localized corrosion effects (SNL 2008b, Section 6.1.4.2).

2.3.5.4.2 In-Drift Condensation Model

[NUREG-1804, Section 2.2.1.3.3.3: AC 1(1), (2), (4) to (8), (10), AC 2(1), to (4), AC 3(1) to (4), AC 4(3), AC 5(1), (3)]

The in-drift condensation model complements the multiscale thermal-hydrologic model (Section 2.3.5.4.1) in terms of evaluating the in-drift thermal-hydrologic environment. The multiscale thermal-hydrologic model provides the TSPA model with the temperature and relative humidity at all waste package locations; however, the model simulations do not include axial transport of water vapor along the drifts. The in-drift condensation model was used to evaluate the hydrologic effects of axial transport of water vapor, and to describe drift wall condensation for use as input to the TSPA model. The in-drift condensation model provides the TSPA model with the potential for drift wall condensation at waste package locations, and, when condensation occurs, with the magnitude of condensation, which is correlated with percolation rate (SNL 2007e, Section 1). The TSPA adds drift wall condensation to the seepage flux (Section 2.3.7.12) for use in the EBS flow and chemistry model components. Condensation is another source of liquid water that can potentially contact the drip shield or waste package in EBS flow calculations (Section 2.3.7.12) (SNL 2007e, Section 6.3.1).

The inputs to TSPA from the in-drift condensation model are the outcome of a series of documented activities, from developing the model, to generating inputs, to abstracting the final results (SNL 2007e, Sections 6.3, 8.3, and 8[a]).

- **Development of the Model Consistent with Data and Scientific Understanding**—The model domain for the in-drift condensation model consists of the emplacement drift and the engineered features that it contains, with added influence from the near-field host rock. Expected ranges of environmental conditions within the model domain and their evolution with time are considered in model development. Observations in the unventilated portions of the ECRB Cross-Drift showed that evaporation and condensation

occur in response to small thermal gradients and, by inference, could be important processes in the repository (SNL 2007e, Section 6.3.1). A conceptual description of the natural and engineered systems is provided in Section 2.3.5.4.2.1. Model development, including computational domain, initial and boundary conditions, assumptions, limitations, and approximations, is discussed in Section 2.3.5.4.2.3.1. The in-drift condensation model also represents major design features such as thermal loading and the waste package, invert, and drip shield. Limitations and uncertainties (Sections 2.3.5.4.2.3.1 and 2.3.5.4.2.3.3) are taken into account to ensure appropriate representation of risk. Model support activities, described in Section 2.3.5.4.2.3.4, include comparisons of convection modeling results to literature as well as to scaled, three-dimensional laboratory tests of in-drift thermal convection (SNL 2007e, Sections 7.2 to 7.4 and 7[a]).

- **Generation of Input Parameters**—Section 2.3.5.4.2.2 describes the data that are synthesized into parameters for the in-drift condensation model. Input parameter uncertainty is dominated by percolation flux uncertainty. The in-drift condensation model propagates percolation flux uncertainty by using the 16 flow fields developed by the unsaturated zone flow model (Section 2.3.2). This input source is also used by other near-field and in-drift flow models, including the near field chemistry model (Section 2.3.5.3) and the multiscale thermal-hydrologic model (Section 2.3.5.4.1). Other input sources, including host rock thermal and hydrologic properties and waste package heat output, are also common to these models.

- **Creation, Execution, and Testing of Model Abstraction**—Observed processes, such as evaporation, convective transport, and condensation on the emplacement drift wall, are included in the in-drift condensation model (Sections 2.3.5.4.2.2 and 2.3.5.4.2.3.1) and reflected in its abstraction. Section 2.3.5.4.2.4 discusses the abstraction of the in-drift condensation model, which uses assumptions, technical bases, data, and models that are appropriate and consistent with other related abstractions and with process model simulations (Section 2.3.5.4.1.3.3).

2.3.5.4.2.1 Conceptual Description

[NUREG-1804, Section 2.2.1.3.3.3: AC 1(1), (6), AC 2(4)]

Within the emplacement drifts, water evaporated from the emplacement drift walls and invert is transported primarily by natural convection from warmer to cooler areas, where it condenses on cooler surfaces. The rates of evaporation and condensation, as well as the rate of water vapor transport in the emplacement drift, determine the extent of condensation.

Transport Mechanisms—There are several possible mechanisms for transport of air and water vapor in the emplacement drifts, including diffusion, convection, and convective mixing represented as dispersion. Convective transport may take the form of natural convection mixing within the drifts, barometric pumping driven by atmospheric pressure fluctuations, and repository-scale natural ventilation. Repository scale natural ventilation involves gas-phase circulation in the host rock that can result from temperature differences between the emplacement drifts, other connected openings, and the rock (SNL 2007e, Section 6.3.3.1).

The two most important transport mechanisms in the drifts are local scale (within a section of a drift) and drift scale (between a location in the drift and the unheated drift ends) (SNL 2007e, Section 6.3.3.1). The local scale occurs over distances of a few drift diameters or waste package lengths. Natural convection generates axial and radial convection cells in the drifts in response to differences in the temperature of adjacent waste packages, drip shields, and the host rock. Drift-scale natural convection also occurs within each emplacement drift in response to larger-scale variation of in-drift temperatures (i.e., over many waste package lengths) up to the length of the emplacement drift (SNL 2007e, Section 6.3.3.1).

Phase Behavior of Water in the Presence of Air and Transport of Water Vapor—The phase change of water from liquid to vapor or vapor to liquid depends on the temperature and the water vapor content in the air. These factors vary in both time and space in the repository (Section 2.3.5.4.1.3.2). When the air is saturated, it holds the maximum amount of water vapor given the local temperature.

When a state of phase equilibrium has been reached, the air is saturated, the relative humidity is 100%, and there is no net evaporation or condensation. If the conditions change and disturb that equilibrium, either evaporation or condensation will result. Evaporation occurs if the relative humidity drops below 100%. Condensation occurs upon cooling because the air can no longer contain all the water vapor. Various transport mechanisms in the repository will move water vapor away from the sites of evaporation. As air and water vapor move to locations at lower temperatures, the air will be less capable of holding water vapor, and condensation will occur (SNL 2007e, Section 6.3.3.1).

Cooling Stages—For the purpose of evaluating the potential for condensation within emplacement drifts, three conceptual stages have been defined to delineate the qualitatively distinct thermal conditions throughout an emplacement drift during the thermal evolution of the system. These three stages are based on the transitions within the drift that represent the range of variations of the relevant thermal-hydrologic processes occurring within the rock, including the evolution of the dryout zone (SNL 2007e, Section 6.3.3.1). The specific thermal environment of any location within a particular emplacement drift will vary based primarily on location relative to the edge of the repository, local rock thermal properties, local percolation flux, and thermal output of the waste package at that location. However, each location will evolve through these stages with the only difference being the duration of each stage. These stages are used as a conceptual framework for formulating and applying the in-drift condensation model to analyze the potential condensation in a range of emplacement drifts that represent the expected behavior of drifts throughout the repository.

- **Initial Cooling Stage**—The drift wall temperature is above the boiling point of water along the entire heated region of the emplacement drift where waste packages are emplaced. During preclosure ventilation, dryout of the host rock occurs throughout the emplacement drift because of evaporation associated with heating and forced ventilation (SNL 2008a, Section 6.1.4; SNL 2007e, Sections 6.3.3.1 and 6.3.5.2.5). After closure, above-boiling temperatures in the host rock cause dryout to extend further into the host rock (Sections 2.3.3 and 2.3.5.4.1). Any water vapor that flows from the host rock into the drift will be transported axially toward unheated regions at either end. The unheated regions are cooler so that condensation is possible (SNL 2007e, Section 6.3.3.1). This

stage corresponds to the first stage of evolution in the discussion of Section 2.3.5.1 and to the heat-up and initial cooldown stages discussed in Section 2.3.6.4.1.

- **Intermediate Cooling Stage**—The drift wall temperature is above the boiling point of water only in the central portion of the emplacement drift and below the boiling point of water in the outer portions near the repository edges, including the unheated regions and part of the drift in which waste is emplaced. Drift wall condensation continues in the unheated regions at either end of the emplacement drift but can also occur in the outer portions of the emplacement area where the temperature is below boiling if sufficient partial pressure of water vapor exists (SNL 2007e, Section 6.3.3.1). This stage corresponds approximately to the second, transition stage in the discussion of Section 2.3.5.1, recognizing that the intermediate stage defined here describes conditions over the entire length of an emplacement drift, as needed to describe the condensation process.

- **Final Cooling Stage**—The drift wall temperature is below the boiling point of water along the entire heated and unheated regions of the emplacement drift. The local partial pressure of water vapor varies depending on host-rock hydrologic conditions and axial transport in the drift. At the locations of cooler waste packages, especially in the outer portions of the drift, relative humidity may achieve 100% so that condensation occurs. At the hotter locations (central portion of the drift and hotter waste packages in the outer portions of the drift), the relative humidity remains below 100%, evaporation in the host rock continues, and condensation does not occur (SNL 2008a, Sections 6.1.3 and 6.1.4; SNL 2007e, Section 6.3.3.1). This stage combines aspects of the second, transition stage and the third, cooldown stage discussed in Section 2.3.5.1. For condensation modeling, this final stage includes locations where the drift wall has cooled below the boiling temperature of water, but the waste package has not yet cooled to this point.

These defined stages are used in the following sections that describe the development of the in-drift condensation model and its abstraction for TSPA. The in-drift condensation model is developed to describe condensation within the emplacement area for the final cooling stage and also is applied as an estimator of condensation during the intermediate stage.

2.3.5.4.2.2 Data and Data Uncertainty

[NUREG-1804, Section 2.2.1.3.3.3: AC 1(1), (2), AC 2(1), (2), AC 3(1) to (4)]

Four categories of data, listed below, are used in the convection–condensation analysis:

- Standard thermal-physical properties of common substances such as air, water, and water vapor (SNL 2007e, Section 4.1).

- Design dimensions for the emplacement drift features including the waste packages, invert, and drip shield; also, heat output from the waste package types represented (Sections 1.3.1, 1.3.4, and 1.5.1; SNL 2007e, Section 4.1; SNL 2007a, Table 7-5[a]). An uncertainty analysis for the in-drift condensation model concluded that percolation flux, dispersion coefficient, and thermal loading are more important to the conclusions of the model than are invert height, thermal conductivity, waste package diameter, drip shield

dimensions, or ventilation efficiency (SNL 2007e, Section 6.1.3[a]). Design information used by the in-drift condensation model, and associated constraints placed on the design through implementation of this model in TSPA, are identified in Section 2.2.1 (Table 2.2-3).

- Repository horizon thermal, physical, and hydrologic properties (SNL 2007e, Section 4.1). Matrix physical and hydrologic properties used to estimate capillary induction of moisture into the drift are taken from the properties developed for the unsaturated zone flow model. Matrix property uncertainty is not included in the in-drift condensation model because the uncertainty in water availability is dominated by the percolation rate (SNL 2007e, Section 6.3.5.1.4 and Appendix M). Drift wall temperature evolution with time for the in-drift condensation model is calculated using thermal properties for the lower lithophysal unit, which contains the majority of the repository. The effects of spatial property variability are qualitatively discussed in Section 2.3.5.4.2.3.

- Percolation rate at the repository horizon, which is handled in a manner consistent with the multiscale thermal-hydrologic model (Section 2.3.5.4.1). Sixteen three-dimensional flow fields are used to represent percolation in the host rock for four different infiltration uncertainty cases (Section 2.3.2) and three climate states plus the post-10,000-year percolation boundary condition (Section 2.3.1). The average percolation flux along each drift is calculated and used by the in-drift condensation model (SNL 2007e, Sections 6.3.5.1 and 6.1.1[a]).

The data uncertainties are handled in two ways. First, data uncertainties are included explicitly within the analyses conducted using the in-drift condensation model; specifically: (1) hydrologic uncertainties are incorporated using drift-specific percolation fluxes for each of the four infiltration uncertainty cases and for each of three climate states (present-day, monsoonal, glacial-transition) plus the post-10,000-year percolation boundary condition (SNL 2007e, Section 6.1.1[a]); (2) uncertainty of waste package thermal output is represented using the seven (six full and two half) waste package segment that includes a range from cool to hot waste packages (SNL 2007e, Section 6.1.1[a]); (3) uncertainty with respect to permeability of the interconnected drip shields is represented using the bounding cases of unequalized (impermeable drip shields) and equalized (water vapor pressure equilibrated across the drip shield thickness) gas mixing conditions, as described in Section 2.3.5.4.2.3.1; and (4) spatial variability of the drift location is represented using seven representative drifts that span the range of drift locations from repository center to edge (SNL 2007e, Figure 6-2[a]). Second, the remaining uncertainty is related to host-rock thermal conductivity, which is not explicitly included in the in-drift condensation model analyses. Rather, this uncertainty is addressed via the implementation of the condensation abstraction model within the TSPA. In the TSPA, the condensation abstraction model is linked with the thermal output from the multiscale thermal-hydrologic model (SNL 2008b, Section 6.3.3.2.2), which directly incorporates uncertainty in host-rock thermal conductivity (SNL 2008a, Sections 6.3.4 and 6.3.16[a]). Host-rock thermal conductivity has a dominant influence on temperature within the emplacement drifts. Therefore, the implementation of drift wall condensation in TSPA incorporates the effects from uncertainty associated with host rock thermal properties.

2.3.5.4.2.3 Model and Model Uncertainty

[NUREG-1804, Section 2.2.1.3.3.3: AC 1(1), (2), (4) to (8), (10), AC 2(3), (4), AC 3(1) to (4), AC 4(3), AC 5(1), (3)]

This section includes a description of the in-drift condensation model and reviews the assumptions used to develop the model. Limitations of the model are described, followed by a discussion of the results of the model for seven representative emplacement drifts. Model uncertainty is summarized and the information used to provide confidence in the model results is discussed.

2.3.5.4.2.3.1 Model Description and Limitations

The in-drift condensation model consists of a steady-state network condensation model that incorporates axial dispersion of water vapor in an emplacement drift and represents the waste packages, drip shields, invert, and emplacement drift wall as nodes. This model is supported by a three-dimensional computational fluid dynamics in-drift convection model (with associated two-dimensional studies) using the FLUENT software code. The convection model represents a drift segment and develops a dispersion coefficient for use in the in-drift condensation model (SNL 2007e, Section 6.3.3.1).

The in-drift condensation model represents all of the waste packages in each of several representative emplacement drifts, as well as the unheated exhaust standoff and access turnout sections located at the ends of the emplacement drift. These features are represented as nodes in a network, so the reported temperatures are lumped local averages. Line-source thermal conduction solutions are used to approximate the emplacement drift wall temperature variation for each emplacement drift, using the emplacement drift locations in the repository layout, and representing the contribution of every emplacement drift to mountain-scale heat transport. Heat transfer between the nodes (waste package to drip shield, drip shield to emplacement drift wall) is based on literature correlations for natural convection heat and mass transfer for the particular geometry. Thermal radiation is calculated based on surface-to-surface radiation. Only heat transfer in the radial direction is considered. The effect of axial heat transfer between waste packages is small because the circumferential surface area of the waste package, which radiates heat to the drip shield and invert, is much greater than the surface area of the ends of the waste package (SNL 2007e, Sections 6 and 6.3.1.1).

Temperatures for the surfaces of the waste package, drip shield, invert, and emplacement drift wall are calculated for each waste package location in the emplacement drift using the specific waste package heat output. Local evaporation and condensation rates are computed using heat and mass transfer correlations based on temperatures and water vapor content of the air. The water vapor content of the air is calculated as a function of axial position (SNL 2007e, Sections 6.3.5.1 and 6.1.1[a]).

The axial dispersion coefficient is determined from three-dimensional natural convection calculations using FLUENT for a unit cell in the emplacement drift that contains a repeated pattern of hot and cold waste packages (SNL 2007e, Section 6.2.7). The model grid represents a 71-m-long segment of emplacement drift containing 14 waste packages (SNL 2007e, Sections 6.2.5.2 and 6.2.7). Individual waste packages are modeled, including the drip shield and invert as well as 5 m of rock surrounding the emplacement drift. Individual waste package heat decay curves are used for

different waste package types. Natural convection is calculated based on implementation of the Navier-Stokes equations for transport phenomena (SNL 2007e, Section 6).

Once drift-scale and repository-scale natural convection cells are calculated by FLUENT, the dispersion coefficient needed by the in-drift condensation model is evaluated. A concentration difference of a neutrally buoyant tracer gas is applied at the axial ends of the unit cell, and the tracer gas mass flux is calculated by FLUENT. A reasonable lower bound for the dispersion coefficient (low-dispersion case) that does not include the effect of the axial temperature gradient on the flow in the unit cell is calculated. A reasonable upper value for the dispersion coefficient (high-dispersion case) is calculated by applying an axial temperature gradient to the unit cell. These two values bound the uncertainty of the axial dispersion coefficient (SNL 2007e, Section 6.2.7).

In the in-drift condensation model, the evaporation rates from the emplacement drift wall and invert surfaces are limited by the rate at which water is supplied from the rock by both capillary pumping and percolation flux. At each waste package location, the possible sources of water are at the emplacement drift wall and the invert. The rate of evaporation is based on the local saturated vapor pressure at the evaporating surface and the local water vapor partial pressure in the bulk air, and on the corresponding mass transfer correlation limited by water availability at the evaporating surface (SNL 2007e, Section 6.3.5).

The water availability rate is the sum of the calculated water supplied by capillary induction through the rock matrix plus the downward percolation through fractures in the host rock that is intercepted by the emplacement drift. Fracture percolation is the dominant term. The percolation fluxes corresponding to the nominal 10th, 30th, and 90th percentile values for the infiltration uncertainty cases (during each time period) are propagated through the model as uncertainty in the local evaporation limit (SNL 2007e, Sections 6.3.5 and 6.1.1[a]). The evaporation limit developed in this manner is a reasonable bound for the final cooling stage (SNL 2007e, Section 6.3.5.1.4) but is not intended to bound water availability for the intermediate stage. During the intermediate stage, boiling occurs in the host rock, and the mass flux of vapor into the drift may exceed the downward percolation flux that intersects the drift. This behavior depends on the rate of growth of the dryout zone (i.e., dewatering of the rock matrix) and on how much of the vapor produced in the host rock migrates toward the drift opening. These details are not addressed by the in-drift condensation model; however, the evaporation limit in the model is a reasonable estimate of water availability during the intermediate stage because the development of the dryout zone occurs primarily during preclosure ventilation and the initial stage of postclosure cooling. This approach is supported by comparison of the condensation rates predicted by the model, with similar results developed using a three-dimensional thermal-hydrologic model (Section 2.3.5.4.2.3.4).

Invert evaporation is important to the simulation of condensation under the drip shield. The invert surface temperature under the hotter pressurized water reactor waste packages is shown by the FLUENT calculations to be greater than the drip shield surface temperature overlying the adjacent cooler high-level radioactive waste packages. There are two reasons the partial pressure of water vapor at the invert surface may not be sufficient to cause condensation on the drip shield. First, evaporation from the invert may occur below the surface of the invert, where it is cooler, so that the partial pressure under the drip shield is lower. Second, the vapor pressure lowering effect of the capillary response of the unsaturated invert material is not included in the in-drift condensation

model; this effect causes reduction in the equilibrium partial pressure (SNL 2007e, Sections 6.3.3.2 and 6.3.7.2.4).

To address uncertainty in the invert response, two sets of cases were run in which the in-drift condensation model represented evaporation from the invert: evaporation at the upper surface of the invert (high-invert cases) and evaporation near the bottom of the invert (low-invert cases). These cases are implemented in the in-drift condensation model by holding the partial pressure at the invert surface equal to the vapor pressure at the simulated invert surface temperature (high) or at the temperature of the exposed emplacement drift wall (low) not covered by the invert. As discussed in Section 2.3.5.4.2.3.2, only the low-invert cases are used in TSPA because the high-invert cases do not include drainage of water from the invert or full treatment of invert heat transfer (SNL 2007e, Sections 6.3.3.2, 6.1.2[a], and 8.1[a]).

The joints where drip shield segments overlap will allow some mixing of gas underneath the drip shield with the gas outside the drip shield. In addition, the invert ballast material will allow some gas exchange. To examine the effects of gas exchange between the gas volume under the drip shield and the gas outside the drip shield, two sets of bounding cases were produced using the in-drift condensation model. These are the equalized (or mixed) cases in which the partial pressure of water vapor is equilibrated on both sides of the drip shield, and the unequalized cases in which there is no gaseous exchange (SNL 2007e, Sections 6.3.3.2 and 6.1[a]).

The in-drift condensation model is used to evaluate seven representative emplacement drifts in the repository layout (Figure 2.3.5-14). These emplacement drifts are chosen to span a range of behavior throughout the thermal evolution of the repository, corresponding to the final stage of cooling (Section 2.3.5.4.2.1). Locations 1 to 3 are collinear and lie near the northern edge of the repository. Edge effects from three-dimensional repository-scale heat conduction are pronounced at these locations. Locations 4 to 6 are also collinear and are near the middle of the repository layout, where the peak temperatures are greatest. Location 7 is in the southern part of the repository layout, where the emplacement drift lengths are longest. All seven emplacement drifts are analyzed for steady-state conditions at discrete times of 1,000, 3,000, 10,000, 30,000, 100,000, and 300,000 years (the temperatures are very uniform axially at 300,000 years; therefore, there was no calculation at 1 million years) (SNL 2007e, Section 6.1.1[a]).

The evaluation of these seven drifts is repeated for three infiltration uncertainty cases (i.e., nominal 10th, 30th, and 90th percentile) and is repeated for all combinations of the following parameters (SNL 2007e, Tables 6-2[a] and 6-3[a]):

- Low and high dispersion coefficients
- Equalized and unequalized drip shield (gas mixing) cases.

Assumptions—Key assumptions made in the in-drift condensation model include the following:

- Capillary lowering of water vapor partial pressure does not occur at source locations where evaporation occurs (e.g., at the invert surface). Water at these locations is in capillary tension or adsorbed to mineral surfaces, so that the local partial pressure of water vapor will be lower than used in the model (SNL 2007e, Section 6.3.3.2.2). This

will overestimate local evaporation rates and underestimate local condensation rates, which will result in the overestimation of condensation in other areas in the drift.

- The availability of percolation for evaporation in the emplacement drift is represented by how much percolation, on average, is intercepted by the footprint of the emplacement drift, plus water that can be inducted into the emplacement drift from the adjacent pillars. Capillary diversion of percolation flux around the emplacement drift, whether complete or partial (as when seepage occurs), is not considered, which is a bounding approach (SNL 2007e, Section 6.3.3.2.8).

- Condensation on the emplacement drift wall above the drip shield falls onto the drip shield or waste package. This assumption is used within the TSPA implementation of the condensation abstraction model to constrain the amount of condensation that may contact the EBS. The amount of condensation that drips is calculated based on the proportional area of drift wall above the drip shield, which provides a bounding result because (1) a portion of the condensation that forms on the drift wall above the drip shield may move laterally and flow down the sides of the drift, (2) at the point of condensation on the drift wall, capillary forces may imbibe a portion of the condensation into the rock where it could be drained away from the emplacement drift, and (3) movement of condensation from the drift wall to either the drip shield or waste package surface represents a movement to higher temperatures that would lead to evaporation of the water (see general discussion in Section 2.3.5.4.2.1). These processes can only reduce the volume of condensation considered in the TSPA, and have not been included in the abstraction, for simplification (SNL 2007e, Section 6.3.3.2.9).

- The effects of barometric pumping and repository-scale natural convection and ventilation on the axial dispersivity are not included. As noted above (Section 2.3.5.4.2.1), these effects would tend to increase the axial dispersion, decreasing the magnitude and extent of condensation in the emplacement area. This is consistent with the bounding nature of the in-drift condensation model, although the magnitude of these effects has not been estimated (SNL 2007e, Section 6.3.3.2.4).

- Inter-package radiative heat transfer is neglected as a model simplification. This is justified because the circumferential area of the waste package is much greater than the area of the ends and because it serves to overstate temperature differences between adjacent waste packages and drip shields, thus maximizing condensation rates in the vicinity of the coolest waste packages (SNL 2007e, Section 6.3.3.2.5).

Limitations—The following limitations of the in-drift condensation model are identified:

- The emplacement drift wall temperature profiles are estimated using a spatially uniform line source that does not account for the axial redistribution of energy that will be associated with the latent heat of axial vapor transport and condensation. Accounting for latent heat transport would decrease temperature differences and may decrease the amount of condensation (SNL 2007e, Section 6.3.3.2.6).

- The in-drift condensation model is formulated for an areally uniform (but temporally varying) average percolation rate in each selected emplacement drift (SNL 2007e, Section 6.3.5.1). Local-scale variability in the percolation flux can produce faster or slower cooling and affect the time needed for the near-field host rock to rewet (Section 2.3.5.4.1). However, these local-scale variations combine to produce the average percolation flux. Therefore, the in-drift condensation model does not include the effects of such local-scale variability in evaporation and in-drift condensation in the emplacement drifts. This simplification in the model provides an appropriate constraint on the availability of water for evaporation during the final cooling stage (SNL 2007e, Sections 6 and 6.1.1[a]). For the intermediate cooling stage, this simplification is consistent with a reasonable approximation of the availability of water for evaporation as discussed above (SNL 2007e, Section 6.2.1[a]).

2.3.5.4.2.3.2 Model Results

For the low-invert cases used in TSPA, condensation is calculated to occur only on the drift wall but not on the drip shield or waste package, and only at the 1,000-year calculation time (SNL 2007e, Tables 6-2[a] and 6-3[a]), which is applied up to 2,000 years (Section 2.3.5.4.2.4). After 2,000 years, no drift wall condensation is predicted to occur. The occurrence of condensation for only the 1,000-year calculation time is independent of whether the drip shield is ventilated or not (i.e., whether the gas is well mixed between the underside and the upperside of the drip shield); however, the probability of drift wall condensation and the rate of drift wall condensation are different for the four situations (combinations of drip shield ventilation and dispersivity) (SNL 2007e, Tables A-2[a] and B-2[a]). The high-invert cases are not used in TSPA (SNL 2007e, Section 6.1.2[a]). The reason for this decision is twofold. First, the high-invert cases do not include the possibility of invert drainage, which would reduce the water source at the top of the invert, and the source of water during the intermediate cooling stage is limited due to the extent of dryout at that time. Second, the in-drift condensation model does not include heat transfer by thermal conduction within the invert, and additional heat transfer would reduce the invert surface temperature, which is the driver for invert evaporation that supplies water vapor for condensation elsewhere (SNL 2007e, Section 6.1.2[a]).

Figure 2.3.5-45 is an example of model results for drift wall condensation at 1,000 years and at Drift Location #7, for low-invert transport, high-dispersion coefficient and well-ventilated drip shield conditions. The unheated regions at each end of the drift (indicated by vertical lines) are the access turnout and the exhaust standoff. The top portion of Figure 2.3.5-45 shows the vapor mass fraction in the gas phase (dashed line) and the equilibrium vapor mass fraction (i.e., the maximum vapor mass fraction for saturated air) at the emplacement drift wall (solid line) based on the emplacement drift wall temperature. Axial transport near the midpoint of the emplacement drift causes the partial pressure of water vapor to be lower than the equilibrium vapor pressure at the emplacement drift wall, resulting in evaporation of water (SNL 2007e, Section 6.1.2[a]).

Progressing from the midpoint of the emplacement drift toward the ends, the partial pressure reaches a point where it is slightly higher than the equilibrium vapor pressure at the emplacement drift wall near the ends of the drift. A portion of the axially transported water vapor condenses on the emplacement drift wall in these two regions as shown in the lower portion of Figure 2.3.5-45. The rate of condensation on the emplacement drift wall in these regions is determined by the vapor

mass fraction difference between the gas and the wall, and by the thickness of the gas boundary layer. Beyond the two condensation zones to the ends of the emplacement drifts, evaporation occurs at the wall because the vapor mass fraction in the gas again dips below the equilibrium mass fraction at the wall (note that temperature influences the gas flow and vapor pressures, but the vapor pressure is not strictly proportional to the temperature because of mass transport that is occurring). Water vapor also condenses in the unheated regions outside the ends of the emplacement drifts (SNL 2007e, Section 6.3.7.2.2).

Figure 2.3.5-46 is an example of model results for drift wall condensation at 3,000 years and 10,000 years, both at Drift Location #7 for high percolation rate, low invert transport, low dispersion coefficient, and well-ventilated drip shield conditions. The data in Figure 2.3.5-46 reflect a later time than that in Figure 2.3.5-45 and have no condensation because the axial temperature gradient at the drift wall is smaller, resulting in only minor axial vapor transport, and in the vapor mass fraction being slightly lower than the equilibrium vapor mass fraction (SNL 2007e, Section 6.1.2[a]).

General results from the final-stage in-drift condensation model are summarized as follows (SNL 2007e, Section 6.1.2[a]):

- Higher axial dispersion coefficients place more of the evaporated water in the unheated sections of the emplacement drift and thereby decrease condensation in the emplacement area.

- Condensation under the drip shield does not occur when evaporation takes place at the bottom of the invert.

Because of model simplifications and the bounding approach used, the in-drift condensation model is likely to overpredict the magnitude and extent of condensation (SNL 2007e, Section 6.3.7.3). For the intermediate stage (when part of the drift wall is above boiling, and part is below boiling), a bounding approach was taken. The three-dimensional, pillar-scale, thermal-hydrologic model discussed in Section 2.3.5.4.1.3.3 was used to calculate vapor transport down the drift for a range of percolation and dispersivity values. Of the five combinations of percolation flux and dispersivity considered, and for the eight waste packages in the last unit cell at the drift end, condensation was calculated to occur at only the two codisposal waste packages (DOE SNF and HLW glass) and only for the low percolation-low dispersivity and high percolation-low dispersivity cases. The highest of the four calculated condensation rates was taken to apply to all codisposal waste packages for the situations of early-failed drip shields, early failed waste packages, and seismic mechanical damage to waste packages under intact drip shields. In each of these cases, the condensation can result in advective transport through the invert, and the bounding value of 100 kg/m/year is used (SNL 2007e, Section 6.2.2[a]).

2.3.5.4.2.3.3 Model Uncertainty

The following discussion summarizes some important uncertainties associated with the in-drift condensation model.

Uncertainty Associated with the Axial Dispersion Coefficient—The axial dispersion coefficient is determined from the local-scale and drift-scale natural convection calculations. The principal factors contributing to natural convection are the arrangement of hot and cold waste packages (drift scale) and the axial temperature profile along the emplacement drift (repository scale). To capture uncertainty associated with the determination of the axial dispersion coefficient, the in-drift condensation model implements two bounding cases: the low-dispersion case and the high-dispersion case (SNL 2007e, Sections 6.3.7.3 and 6.1.3[a]).

The low-dispersion case is based upon the drift-scale convection pattern and represents a true physical lower bound on the range of possible values. The high-dispersion case approximates the influence of drift-scale gradients in the host-rock temperature, which tend to elongate the natural circulation cells established by the arrangement of hotter and cooler waste packages, and thereby increase axial transport. While the high-dispersion case bounds the impact of local-scale and drift-scale natural convection, it is not a true upper bound on possible axial dispersion coefficient values. Other phenomena, such as barometric pumping, repository-scale natural convection, and transient flow oscillations not captured in the steady-state computational fluid dynamics calculations, could increase axial transport and result in an increased axial dispersion coefficient. However, an increased dispersion coefficient decreases the likelihood of condensation within the emplacement region. Thus, the use of the low- and high-dispersion cases by the TSPA provides reasonable bounds on the magnitude and extent of condensation (SNL 2007e, Sections 6.3.7.3 and 6.1.3[a]).

Uncertainty Due to Computed Drift Wall Temperature Profiles—Temperature histories are computed for the emplacement drift wall along each selected emplacement drift using a finite line-source thermal conduction solution with average lineal heat output and homogenous thermal properties in the host rock. This simplification corresponds with the overall approach to the in-drift condensation model, which produces approximate bounding estimates for the distribution and rate of condensation. Variability of waste package temperature is represented explicitly in the model through the coupling of waste package heat output to the drift wall temperature. The use of an averaged thermal line-source with homogeneous rock thermal properties to calculate drift wall temperature in the in-drift condensation model does not, however, capture the full range of package-to-package variability in drift wall temperature. However, the simplified approach does ensure that a thermal gradient is maintained in the model along the drift to drive water vapor migration to potential condensation zones (SNL 2007e, Section 6.3.7.3).

The simplified approach is sufficient for abstraction in TSPA because it represents the range of thermal conditions present in the drifts (Section 2.3.5.4.1.4). Package-to-package variability in drift wall temperature from the multiscale thermal-hydrologic model output, which includes the full range of uncertainty in host-rock thermal conductivity and percolation flux, is incorporated in TSPA and combined with the in-drift condensation model.

Uncertainty Due to Invert Vapor Pressure and Water Partitioning—Setting the partial pressure of water vapor at the invert surface to correspond to the saturation vapor pressure at the invert surface temperature (high-invert transport) produces a physical upper bound on the potential invert evaporation rate, and the process model calculated the results of that bounding case. However, because the high-invert case does not model invert drainage or the full scope of invert heat transfer, those process model results were not abstracted for the TSPA model

(SNL 2007e, Section 6.1.2[a]). Setting the partial pressure at the invert surface to correspond to the saturation vapor pressure at the exposed wall temperature (low-invert transport) is not a lower bound. The emplacement drift wall beneath the invert will actually be cooler than the exposed emplacement drift wall (SNL 2007e, Section 6.3.7.3). TSPA uses only the results of the low-invert transport cases, which are the most realistic of the potential cases (the high-invert transport cases are known to overpredict water availability at the invert top.

2.3.5.4.2.3.4 Model Support

The in-drift condensation model calculations are supported by comparison to literature for small-scale natural convection in horizontal concentric cylinders, a layout that is geometrically similar to the emplacement drift arrangement. The overall heat transfer from the horizontal concentric cylinder geometry simulated using FLUENT compares closely with the literature over a wide range of Rayleigh numbers, including laminar and turbulent flow conditions (SNL 2007e, Sections 7.2.1 and 7.3).

The convection model calculations are also supported by comparison to experimental data from the 25% and 44% scale Yucca Mountain Natural Convection Tests conducted in Las Vegas. Simulated component temperatures closely match the experimental data, while simulated fluid velocities are qualitatively similar (SNL 2007e, Section 7.4.4). The in-drift condensation model was designed to explicitly represent the final cooling stage (Section 2.3.5.4.2.1) when the entire drift has drift wall temperatures below the boiling point of water (SNL 2007e, Section 6.3.7.2.2). The model is then supplemented with a bounding approach to the intermediate stage of cooling (SNL 2007e, Section 6.2[a]). The bounding approach for the intermediate stage of cooling uses results from the three-dimensional, full-length-drift, pillar-scale, thermal-hydrologic model presented in Section 2.3.5.4.1.3.3.

2.3.5.4.2.4 Model Abstraction and Implementation in the TSPA

[NUREG-1804, Section 2.2.1.3.3.3: AC 1(4)]

Model Abstraction—As discussed in Section 2.3.5.4.2.3.2, only the low-invert cases are used in TSPA, for which condensation is calculated to occur only on the drift wall, and only at the 1,000-year calculation time (SNL 2007e, Tables 6-2[a] and 6-3[a]).

The in-drift condensation model generated 72 sets of results for each of the seven drifts, corresponding to the combinations of the following: 2 dispersion coefficients × 2 drip shield ventilation values × 6 simulation times × 3 percolation cases. The abstraction process used linear regression over the three percolation cases to establish the statistical relationship between the percolation flux and the magnitude of drift wall condensation. This step resulted in 24 possible regressions (2 dispersion coefficients × 2 drip shield ventilation values × 6 simulation times) of which only the ones at early time (1,000 yr) predict drift wall condensation to occur (Section 2.3.5.4.2.3.2). Drift wall condensation results for discrete simulation times are applied to the postclosure period, starting with the onset of drift wall temperature at or below the boiling point of water (SNL 2007e, Section 8.3.1). Drift wall condensation results calculated for 1,000 years are applied until 2,000 years (the mid-point between simulations for 1,000 and 3,000 years), after which the rate of drift wall condensation is zero. The percolation rate tends to change when the climate change is simulated at 2,000 years, which was taken into account in development of this

discretization scheme (SNL 2007e, Section 8.3.1.2). The output parameters, which are used by the drift wall condensation submodel of the TSPA (SNL 2008b, Section 6.3.3.2; SNL 2007e, Section 8.1[a]), are the slopes and y-intercepts resulting from the linear regressions (against percolation flux) for the fraction of waste package locations where drift wall condensation occurs and the magnitude of the condensation rate conditioned on that occurrence. The associated uncertainties are also provided to TSPA in the form of standard deviations on the regression parameters.

Implementation in TSPA—Waste package locations are binned into five percolation subregions in the TSPA according to the local host-rock percolation flux (Section 2.3.5.4.1.4.1). The TSPA applies the drift wall condensation submodel to each bin to evaluate the occurrence and magnitude of condensation for the representative waste packages within each bin. The edge-cooling effect, variability of waste package thermal output, and variability in host-rock thermal conductivity are modeled through the use of temperature histories for each waste package as calculated by the multiscale thermal-hydrologic model. The regressions for the occurrence and rate of drift wall condensation combine different waste package types and locations within the drifts simulated, so that drift wall condensation is applied randomly to the representative waste packages within each bin (SNL 2008b, Sections 6.3.2 and 6.3.3.2).

For each realization and percolation subregion in TSPA, two waste package types are considered: a representative codisposal (HLW) package and a representative commercial SNF package. The drift wall condensation submodel is configured to evaluate the occurrence of condensation at the drift wall for each of the four dispersion coefficient–drip shield ventilation cases (SNL 2007e, Sections 8.3.1.1 and 8.1[a]). The four cases represent uncertainty in the conditions controlling condensation processes, and one is selected for use for the entire realization. Each case is treated as equally likely in order to represent epistemic uncertainty (SNL 2008b, Section 6.1.4.3; SNL 2007e, Section 8.1[a]). Once a case is selected, the occurrence of drift wall condensation is determined by sampling the regression for occurrence, as a function of percolation flux; then the rate of condensation on the wall is calculated as a function of the percolation rate. The appropriate uncertainties from the statistics of the regressions are also sampled and applied in the TSPA (SNL 2007e, Section 8.1[a]).

Drift wall condensation is treated in the TSPA in a manner similar to seepage (i.e., as a source of liquid water flow in the emplacement drift). The effect of drift wall condensation on potential advective transport of radionuclides is thus included in the TSPA (SNL 2008b, Section 6.3.6). To determine the chemical composition of drift wall condensation, the TSPA uses the seepage evaporation tables; this assumes that a small amount of pore water in the wall rock diffusively or advectively mixes with the condensate, which then evaporatively concentrates on the waste package surface. (Section 2.3.5.5.4.2.1).

2.3.5.4.3 Near-Field Response to the Range of Design Thermal Loadings

[NUREG-1804, Section 2.2.1.3.1.3: AC 1(1) to (5), (7); Section 2.2.1.3.2.3: AC 1(1), (2), (4), (5); Section 2.2.1.3.3.3 AC 1(1) to (8), (10), AC 2(2), AC 3(1)]

This section describes an assessment of the hydrogeologic, geomechanical, and geochemical responses to the anticipated range of thermal loading. The range of thermal loading is represented by an operational simulation of repository waste receipt, handling, and emplacement. The resulting

as-emplaced sequences of individual waste packages of different types, are used in a postclosure thermal assessment. The assessment shows that for uncollapsed emplacement drifts, only minor changes are needed to represent the anticipated range of thermal loading in the TSPA model feeds, and that designation of FEPs as included or excluded (Section 2.2.1) does not change. For seismically-induced drift collapse, several processes are identified that are thermally sensitive; however, the risk from EBS temperatures exceeding 300°C because of seismically-induced drift collapse during the peak thermal period immediately after repository closure is so small that this sensitivity to extreme temperatures is excluded from TSPA (SNL 2008c, Section 6.5). The assessment described in this section supports the thermal management strategy described in Section 1.3.1.2.5, which gives the preclosure and postclosure constraints on loading of waste packages in the underground repository. As part of the thermal management strategy (Section 1.3.1.2.5) each repository drift will be analyzed before emplacement when the particular characteristics of the waste forms that will be emplaced in a drift are known.

Postclosure Temperature Limits—Established temperature limits (Section 1.3.1.2.5) will be met by the repository given the anticipated range of thermal loadings, in a manner that is consistent with the inclusion or exclusion of FEPs (Section 2.2.1). The bases for these limits (Tables 1.9-9 and 2.2-3) are summarized as:

- Mid-pillar temperature limit of 96°C has been determined to facilitate drainage of percolation water and condensate between emplacement drifts, and through the repository horizon, thereby limiting the amount of such water that can enter the repository (DOE 2006, Section 4.6.5).

- Peak postclosure drift wall temperature limit of 200°C will limit thermal-mechanical degradation of rock quality by differential thermal expansion (micro-cracking) and other processes, and thereby limit impacts on drift opening stability.

- Waste package outer wall temperature limit of 300°C for 500 years, followed by 200°C for 9,500 years, will limit degradation of Alloy 22 due to phase ingrowth (Table 2.2-5, FEP 2.1.11.06.0A, Thermal sensitization of waste packages).

These temperature limits have been used in the repository design basis (Section 1.3.1.2.5, which includes additional thermal limits for emplacement of naval SNF waste packages), and in developing screening designations for FEPs (Section 2.2.1).

Estimated Limiting Waste Stream—The anticipated range of thermal loading is represented using an estimated limiting waste stream, consisting of a sequence of waste packages of different types as they are likely to be received at the Yucca Mountain repository. This sequence was developed using output from a preclosure operational simulation (SNL 2008c), Section 6.1. This simulation takes into account such variables as commercial SNF selection at the nuclear utilities, age and thermal requirements for transport, and throughput of repository facilities. The simulation case adopted as the estimated limiting waste stream assumes that approximately 90% of commercial SNF will be packaged at the nuclear utilities in transportation, aging, and disposal (TAD) canisters (Section 1.3.1.2.5) and constrains the commercial SNF part of the waste stream to be not less than 5 years old (out of reactor) and thermal output to be not more than 22 kW per canister at receipt (Section 1.3.1.2.5).

Importantly, the overall average thermal line load for the estimated limiting waste stream is slightly cooler than the postclosure thermal reference case used to represent thermal loading for TSPA (SNL 2008c, Section 6.1) (Figure 2.3.5-47). The postclosure reference case defines a unit-cell arrangement of eight different waste packages averaging 1.45 kW/meter at emplacement, for which the hottest waste package has output of 12.66 kW at emplacement (SNL 2008a, Table 6.2-6[a]). This similarity means that the far-field thermal effects associated with the anticipated range of thermal loading will be closely comparable to the far-field effects considered in the thermal modeling basis (Sections 2.3.3 and 2.3.5) and FEP screening (Section 2.2.1) for TSPA (SNL 2008c, Section 6.4.2).

Simulate the Sequence of Waste Packages Emplaced Underground—Emplacement of waste packages underground, as discussed in Section 1.3.1.2.5, was simulated by processing the sequence of waste packages of different types constituting the estimated limiting waste stream, while observing the receipt schedule, and following the set of loading rules discussed in Section 1.3.1.2.5:

- Maximum waste package thermal output at emplacement: 18.0 kW
- Maximum seven-package running average of waste package heat output at emplacement: 2.0 kW/m
- Maximum seven-package running average of the calculated thermal energy density for each waste package (SNL 2008c, Section 6.1.3) constrained to a value that controls the peak postclosure mid-pillar temperature.

The seven-package running average scheme was selected because the overall length of seven waste packages is similar to the distance from each drift to the nearest mid-pillar location, thus limiting the local influence of hotter waste packages on the peak mid-pillar temperature (SNL 2008c, Section 6.1.3). Also, axial heat sharing from hotter packages to adjacent cooler ones limits peak postclosure drift wall temperature (SNL 2008c, Section 6.3).

A measure of thermal energy density is used for each waste package, representing its capability to influence the controlling postclosure temperature limit, which is the peak mid-pillar temperature. The measure is equivalent to the peak postclosure mid-pillar temperature if the repository were loaded exclusively with identical waste packages. The thermal energy density for each waste package takes into account the effects on the local peak mid-pillar temperature of the individual thermal decay history, calendar year of origin, emplacement year, and ventilation history (SNL 2008c, Sections 6.1.3 and 6.1.7). The mid-pillar temperature history calculated in the same manner as the waste package thermal energy density, using the estimated limiting waste stream average line load, is shown in Figure 2.3.5-48 as an example. The calculated values of this measure for adjacent waste packages in a given location or drift segment, are then averaged to obtain an estimate for the ensemble influence on the local peak mid-pillar temperature. Because the mid-pillar temperature history is slowly changing, or flat, near the peak, it is not necessary to account for differences in timing of peak mid-pillar temperature for different types of waste packages.

Waste packages will be selected for emplacement, from among those available in surface aging facilities, to optimize the local emplacement sequence to achieve a specified limit (e.g., 96°C) for

the seven-package running average of the mid-pillar thermal energy density. This is an appropriate strategy because the mid-pillar temperature is the limiting constraint among the postclosure temperature limits listed above (SNL 2008c, Section 7.1).

In the as-emplaced sequences, cooler codisposal (DOE SNF and HLW) waste packages are interspersed with hotter commercial SNF waste packages to control local thermal loading, and are assumed to be available on demand during the operation period (SNL 2008c, Section 6.1). Emplacement sequences were constructed by selecting commercial SNF waste packages arriving at the repository or from surface aging, or selecting codisposal waste packages, to achieve local thermal loading that resulted in the estimated local average mid-pillar postclosure peak temperature as close as possible to the target value while meeting the loading rules given above. This process has yielded two bounding (for the estimated limiting waste stream) emplacement sequences which show how the thermal management strategy functions (Section 1.3.1.2.5; SNL 2008c, Section 6.1):

- **96/2 Sequence**—Optimized the emplacement sequence to achieve a 96°C target mid-pillar temperature, which represents the hottest condition consistent with the postclosure temperature limits. This case uses an initial condition (i.e., prior to the start of emplacement) whereby repository surface storage inventory contains approximately 2 years of commercial SNF receipts.

- **85/4 Sequence**—Optimized the emplacement sequence to achieve an 85°C target mid-pillar temperature, which represents the coolest condition that could be obtained with the estimated limiting waste stream. This case uses an initial condition (i.e., prior to the start of emplacement) whereby repository surface storage inventory contains approximately 4 years of commercial SNF receipts.

The 96/2 sequence demonstrated that the mid-pillar temperature limit of 96°C could be achieved with the estimated limiting waste stream. Whereas these sequences were developed using thermal measures based on the mean thermal conductivity for the lithophysal host rock, sensitivity analysis (SNL 2008c, Section 6.2) shows that there is margin in the analysis, principally the influence of hydrology, which compensates for the uncertainty and spatial variability in host-rock thermal conductivity. Thus, although the thermal energy density is calculated using a mean thermal conductivity for typical lithophysal host rock, the hydrologic effects on the mid-pillar temperature compensate for the potentially higher temperature that would be associated with lower values of thermal conductivity such as the 10th percentile values used in the multiscale thermal-hydrologic model for TSPA (Section 2.3.5.4.1.3).

Select Local Hottest Segments for Near-Field Sensitivity Analyses—The 85/4 and 96/2 emplacement sequences were searched to find the hottest and coolest segments and the locations of maximum heterogeneity (or difference in thermal output between adjacent packages). A drift wall thermal energy density criterion, similar to the mid-pillar energy density criterion, is used to quantify waste package heat output in a manner suited for selecting the hottest segments (SNL 2008c, Sections 6.1.4 and 7.1). Hottest segments were selected on the basis of the hottest seven-package running average, and the hottest three-package running average, of the drift-wall thermal energy density (SNL 2008c, Table 6.1-2). The seven-package and three-package averages were selected as a range, to evaluate the influence of axial heat sharing on peak temperatures at the

hottest locations. Both segments were found in the 96/2 emplacement sequence, and both were emplaced near the end of the 50-year operational period. The seven-package segment selected represents the most likely hottest local average thermal loading condition. By comparison, the three-package segment contains the hottest overall waste package, flanked by cooler packages. Finite-element calculations, that explicitly simulate the seven-package and three-package segments, confirm the extent of postclosure axial heat sharing (SNL 2008c, Section 6.3). These hottest segments were used to assess the responses of the geomechanical, hydrogeologic, and geochemical systems to the anticipated local extremes of thermal loading.

Geomechanical Impact Evaluation Summary—Thermal-mechanical analyses were performed using a distinct element (UDEC) approach (BSC 2004g). This modeling approach has been used to assess the impacts of seismic ground motion, and the effects from variability in rock quality on rockfall and drift collapse, for use in FEP disposition and in TSPA (SNL 2007i; see Section 2.3.4). The principal focus of this analysis was to determine if higher rock temperatures possible with the range of thermal loading, represented by average thermal line loads for the selected hottest segments, significantly change the likelihood of drift collapse or the amount of rockfall. The results (SNL 2008c, Section 6.4.1) show that the strength-to-stiffness ratios for the host rock units are large enough that the higher temperatures will not significantly increase the amount of rockfall, even considering the lowest quality of lithophysal rock (Category 1; see Section 2.3.4). Significant drift collapse is not predicted as a consequence of thermal loading. Seismic ground motion would therefore remain the principal cause of drift collapse, possibly augmented by time dependent degradation of rock strength properties (BSC 2004g; also Section 2.2.1, Table 2.2-5, excluded FEPs 2.1.07.01.0A, Rockfall, and 2.1.07.02.0A, Drift collapse).

Hydrogeologic Impact Evaluation Summary—A series of two-dimensional and three-dimensional thermal-hydrologic analyses were used to evaluate hydrogeologic impacts (SNL 2008c, Section 6.4.2). These same modeling approaches were used for the multiscale thermal-hydrologic model (SNL 2008a; see Section 2.3.5.4.1). Both the seven-package and three-package segments were simulated three-dimensionally, using various combinations of rock properties and percolation flux boundary conditions. The resulting postclosure peak temperatures (i.e., waste package, drift wall, and mid-pillar) comply with the temperature limits described above. Examination of package–package variability shows that rewetting behavior (i.e., percolation flux in the host rock at the transition from dryout to post-thermal conditions) is temperature controlled rather than driven by "cold trap" effects at cooler waste packages near the hottest ones (SNL 2008c, Section 6.4.2). Thermal-hydrologic processes occur coherently among the different waste package types, with at most moderate differences in the timing of cooling and rewetting.

Using a two-dimensional modeling approach, far-field thermal-hydrologic effects were examined for the average line load for the postclosure reference case, and for the average line load corresponding to the estimated limiting waste stream. Far-field effects from these two thermal loading conditions are very similar, which is expected from the similarity of the line loads and the tendency for far field conditions to respond to average thermal loading rather than smaller-scale variation among waste packages. The three-dimensional simulations of the hottest segments were repeated in a configuration representing complete drift-collapse, using the same worst-case reasonable-bound values for rubble thermal conductivity, host rock thermal conductivity, and percolation flux that are used for TSPA (SNL 2008c, Section 6.4.2). The resulting waste package

temperature histories show that temperatures approaching 400°C could be reached for a few waste packages, for these worst-case conditions (SNL 2008c, Figure 6.4.2-29). The probability and consequences of these high temperatures are discussed below in relation to FEPs.

Geochemical Impact Evaluation Summary—The near-field chemistry model (Section 2.3.5.3; SNL 2007b) was used to evaluate potential changes in composition of seepage water that could result from the anticipated range of thermal loading. This model includes the effects from variability and uncertainty in host-rock thermal properties, percolation flux, repository edge-cooling effects, in situ geochemical properties, and kinetics of water–rock interaction (SNL 2008c, Section 6.4.3). A representative average line load was extracted from the hottest seven-package segment and used as input to the near-field chemistry model. The resulting seepage water compositions exhibit slightly more water–rock interaction, and thus higher pH, and less calcium and magnesium compared to sodium and potassium. These aspects are generally favorable to corrosion resistance of Alloy 22 (Section 2.3.6). The model results used in this analysis are within the range of uncertainty that is incorporated in the near-field chemistry model abstraction used in TSPA (within the range of water–rock interaction provided in the TSPA abstraction). Potential effects from other coupled thermal-hydrologic-chemical processes are insignificant, as discussed in Section 2.3.5.2.3.

FEP Impact Evaluation Summary—An evaluation of FEPs was conducted to identify and analyze those FEPs that are thermally sensitive and might be affected by higher temperatures associated with the anticipated range of thermal loading (SNL 2008c, Section 6.5). Of 374 FEPs overall, 79 were evaluated to determine whether: (1) the screening justification used for inclusion/exclusion applies to the anticipated range of thermal loading; and (2) the modeling basis used for included FEPs in TSPA has the capability to represent the range of thermal loading. The results show that for the nominal scenario class (uncollapsed drifts), all the FEP screening justifications can be applied and that the TSPA modeling basis is adequate.

For collapsed-drift conditions, seven FEPs were identified (SNL 2008c, Section 6.5) that describe thermally sensitive engineered-barrier degradation processes, for which the screening justifications used for TSPA depend on peak waste package temperatures lower than the extreme temperatures predicted for the anticipated range of thermal loading. In addition, six additional FEPs that pertain to commercial SNF cladding are not important to commercial SNF because no performance credit is taken for commercial SNF cladding integrity in TSPA (Section 2.3.7). All of these FEPs, including aspects pertaining to naval SNF, have been evaluated for peak waste temperatures up to 300°C to produce the screening results summarized in Section 2.2.1. An additional exclusion justification (SNL 2008c, Section 6.5.1; SNL 2007i, Section 6.7.1) supports determination that the risk from such extreme waste package temperatures is insignificant, considering the probability of a seismic event sufficient to cause drift collapse during the 90 years immediately after repository closure.

Excluding peak temperatures greater than 300°C due to drift collapse immediately after repository closure is supported by additional information (SNL 2008c, Section 6.5.1). Firstly, the multiscale thermal-hydrologic model (Section 2.3.5.4.1) and simulations for the anticipated range of thermal loading (SNL 2008c, Section 6.4.2) are based on a porous-medium modeling approach that does not include heat transfer by gas-phase natural convection in rubble. Secondly, there is a qualitative relationship between the rubble volume sufficient for complete collapse, and the characteristics of

the rubble produced. Finally, calculations of peak temperature for the range of thermal loading (SNL 2008c, Section 6.4.2) are based on bounding values for waste package heat output, rubble thermal conductivity, host-rock thermal conductivity, and percolation flux. Together these three factors provide support to a probability of less than 10^{-4} that the hottest waste package will exceed 300°C (SNL 2008c, Section 6.5.1).

Conclusions—The anticipated range of thermal loading has been evaluated using operational simulation of waste handling, aging, and emplacement. The hydrogeologic, geomechanical, and geochemical responses to the anticipated range of thermal loading have been evaluated, and for the nominal scenario class (which includes uncollapsed drifts), the TSPA modeling basis is directly applicable to assessing dose consequences for the anticipated range of thermal loading, and FEP screening is unaffected (Section 2.2.1).

For seismically induced drift collapse a number of FEPs are thermally sensitive, and the screening designations summarized in Section 2.2.1 depend on peak waste package temperatures lower than the extreme temperatures predicted for the anticipated range of thermal loading. However, the risk associated with the peak temperature of any waste package exceeding 300°C is insignificant, considering the probability of a seismic event sufficient to cause drift collapse during the 90 years immediately after repository closure (SNL 2008c, Section 6.5.1). These results demonstrate the feasibility of the postclosure aspects of the thermal management strategy described in Section 1.3.1.2.5.

2.3.5.5 In-Drift Chemical Environment Models

[NUREG-1804, Section 2.2.1.3.3.3: AC 1(1) to (8), (10), AC 2(1), (2), (4), AC 3(1) to (4), AC 4(1) to (4), AC 5]

The in-drift chemical environment affects the corrosion environment for engineered barrier features and the transport of radionuclides within the EBS. This section discusses models and analyses used to characterize the in-drift chemical environment outside of the waste package for the nominal, early waste package failure, and seismic scenario classes. Potential changes in seepage water chemistry due to interaction with an igneous intrusion under the igneous scenario class are described in Section 2.3.11.

The in-drift precipitates/salts model (Section 2.3.5.5.3) is a process-level geochemical model designed to evaluate evaporation, condensation, exchange of gases with the atmosphere, and precipitation and dissolution of salts. With this model, seepage evaporation analyses were conducted and used to generate the seepage dilution/evaporation abstraction, hereafter referred to as the seepage evaporation abstraction (Section 2.3.5.5.4.2). The seepage evaporation abstraction provides the TSPA with the compositional range of waters that could contact the outer barrier of the waste package and the invert. The concentration of CO_2 within the drifts is provided to the TSPA by the near-field chemistry model (Section 2.3.5.3.4). As is discussed in Section 2.3.5.3, the boundary conditions for gas and water compositions are the potential seepage water compositions determined by the near-field chemistry model. The models that are used to predict the in-drift chemical environment and their feeds and outputs are summarized in Figure 2.3.5-1. Design information used by the in-drift chemical environment models, and associated constraints placed on the design through implementation of this model in TSPA, are identified in Section 1.9.2.

In the event of a waste package failure, the near-field chemistry model (Section 2.3.5.3.4) provides pCO_2 for the evaluation of in-package chemistry, which is addressed in Section 2.3.7. Section 2.3.7 also discusses the quantity of water contacting engineered barrier features, the chemistry of water contacting waste forms, and radionuclide release from the EBS.

The in-drift chemical environment abstractions are the outcomes of a series of documented activities, including the following:

- **Model Development Consistent with Data and Scientific Understanding**—Development of the in-drift precipitates/salts model is consistent with scientific understanding based on field and laboratory tests, literature describing high salinity conditions at elevated temperatures, near-field chemistry modeling, and natural analogues of evaporation. A conceptual description of seepage evaporation and its impact on in-drift water chemistry is provided in Section 2.3.5.5.1. Inputs from the near-field chemistry model incorporate important design features and properties. The in-drift precipitates/salts model simulations, which provide parameters important to waste package corrosion including pH, chloride (Cl^-) concentration, nitrate (NO_3^-) concentration, and nitrate-chloride molar ratio (NO_3^-/Cl^-), are consistent with the description of temperature and relative humidity conditions output from the multiscale thermal-hydrologic model. Limitations and uncertainties (Section 2.3.5.5.3.3) are evaluated and taken into account. For example, one limitation of the seepage evaporation abstraction is the fact that it is a single mixing cell that does not accommodate the process of localized salt separation. To address this limitation, an approach representing salt separation is incorporated within the seepage evaporation abstraction (Section 2.3.5.5.4.2.1).

- **Development of Input Parameters**—Section 2.3.5.5.2 describes how data are used, interpreted, and synthesized into parameters for the seepage evaporation analyses. Parameter values, assumed ranges, uncertainty distributions, and bounding assumptions are based on site-specific field measurements, laboratory experiments, natural analogue research, process-level modeling studies, and scientific literature. For example, the initial gas and water compositions are based on the near-field chemistry model results. As described in Sections 2.3.5.5.2, 2.3.5.5.3.3, and 2.3.5.5.4.3, uncertainties in the in-drift precipitates/salts model and the seepage evaporation abstraction are propagated to the TSPA model.

- **Model and Abstraction Support**—Section 2.3.5.5.3.3.1 describes various confidence-building activities completed to support the in-drift precipitates/salts model including comparison of model output with independent data sets representing laboratory and field data, natural analogues, and published literature. In addition, abstractions have been tested against process model results to ensure the abstractions appropriately capture the process model results (Sections 2.3.5.5.4.1 and 2.3.5.5.4.2.2).

2.3.5.5.1 Conceptual Description

[NUREG-1804, Section 2.2.1.3.3.3: AC 1(1), (3), (4), (8), (10)]

The composition of water within the drift affects the corrosion environment for engineered barrier features and the potential transport of radionuclides within the EBS. The evolution of in-drift water

chemistry depends primarily on the incoming seepage composition, temperature, relative humidity, and CO_2 gas partial pressure (SNL 2007b, Section 6.9.1). Section 2.3.5.3 presents the evaluation of seepage composition; information regarding temperature and relative humidity in the drift is provided in Section 2.3.5.4.1. Chemical processes expected to occur within the drifts include gas-water interactions, seepage evaporation, precipitation and dissolution of salts, salt separation, and deliquescence.

Gas-Water Interactions—The gas-phase species with the greatest influence on in-drift water chemistries is carbon dioxide. Changes in the pCO_2 can affect pH as well as the types of solids that precipitate on evaporation. Analyses discussed in Section 2.3.5.5.4.1.1 show that oxygen will exist in amounts great enough to maintain oxidizing conditions. As a result, reactions involving oxygen will not significantly affect the bulk chemical environment (SNL 2007b, Section 6.7).

Seepage Evaporation, Precipitation and Dissolution, and Salt Separation—Early in the postclosure period, drift wall temperatures higher than the boiling point of water will prevent seepage from occurring (Section 2.3.3.3.4). After drift wall temperatures fall below the boiling point of water enabling the rewetting process to begin, seepage may occur depending on local hydrologic conditions. However, waste package surface temperatures will still be elevated, so seepage water falling on waste package and drip shield surfaces will evaporate and concentrate. As waste package temperatures continue to decrease, relative humidity will increase to the point that wet conditions persist. Further increases in relative humidity with time will result in progressively more dilute aqueous solutions (SNL 2007b, Section 6.9).

When conditions favor seepage evaporation, minerals will begin to precipitate and the most soluble components will concentrate in the remaining brine. With precipitation, the relative concentrations of dissolved components will change as a result of chemical divides (SNL 2007b, Section 6.3.3.1). A useful description of chemical divides is given by *The Geochemistry of Natural Waters, Surface and Groundwater Environments* (Drever 1997a, pp. 329 to 330):

> Whenever a binary salt is precipitated during evaporation, and the effective ratio of the two ions in the salt is different from the ratio of these ions in solution, further evaporation will result in an increase in the concentration of the ion present in greater relative concentration in solution and a decrease in the concentration of the ion present in lower relative concentration.

The major geochemical divides for natural lakes are shown in Figure 2.3.5-49. These geochemical divides largely control the types of waters that can develop by evaporation. In general, natural waters fall into three groups on the basis of the chemical divides encountered as they evaporate. At relatively low degrees of evaporation, saturation with respect to calcite is achieved, and depending upon the relative concentrations of bicarbonate and Ca^{2+}, the waters can evolve toward calcium-poor, carbonate-rich brines or calcium-rich, carbonate-poor brines. The carbonate-rich brines are one of the three common natural brine types. Sodium and potassium bicarbonates/carbonates have generally lower solubility than sodium and potassium chlorides/nitrates. Hence, at high degrees of evaporation, carbonate waters are chloride or nitrate-rich, although still containing a significant component of carbonate.

Waters that evolve toward calcium-rich compositions intersect the calcium sulfate (gypsum or anhydrite) chemical divide. Depending upon the relative concentrations of sulfate and Ca^{2+}, the waters can evolve toward calcium-poor, sulfate-rich brines, or calcium-rich, sulfate-poor brines. The calcium-rich brines are the second common natural brine type; the dominant anions are chloride and/or nitrate. The sulfate-rich brines are the third common brine type. As with the carbonate waters, because sodium and potassium sulfates have generally lower solubility than sodium and potassium chlorides/nitrates, high degrees of evaporation result in waters that are chloride or nitrate-rich although still containing a significant component of sulfate.

As shown in Figure 2.3.5-49, it is also possible for sulfate-rich brines to develop from magnesium-rich solutions, although this is relatively rare in nature because the abundance of silica generally limits magnesium concentrations through precipitation of sepiolite.

The three brine types expected to occur within drifts due to evaporative concentration of seepage are similar to the brines that form given the same process occurring for natural waters at the earth's surface: calcium chloride brine, carbonate brine, and sulfate brine. However, one major difference is expected; nitrate is a significant component of in situ pore waters, and will comprise a large component of the more concentrated brines because of the high solubility of nitrate minerals. With respect to the water types described above, nitrate behaves similarly to chloride (SNL 2007b, Section 6.13.5.3).

When seepage water drips onto the drip shield or waste package surfaces, it may flow downward over the metal surface. When water is moving and significant evaporation occurs, spatial separation of components is possible, with transport of the more soluble aqueous components leaving behind less soluble precipitates. This process may affect the relative concentrations of NO_3^- and Cl^-, as halite (NaCl) may precipitate while more soluble nitrate salts remain mobile (SNL 2007b, Section 6.13.6). This is conceptually shown in Figure 2.3.5-50. When seepage (X) drips onto the waste package, it evaporates to equilibrium with the local relative humidity. If this is below the relative humidity at which salt precipitation occurs (X1), then salt precipitates on the waste package. In the case of the seepage evaporation abstraction, this salt is commonly halite. The composition of the remaining solution moves down the liquidus until equilibrium with the local relative humidity is achieved. At some point (X2) along this pathway, physical separation of the precipitated salts and the solution could occur (e.g., the solution could advectively flow off of the side of the waste package, leaving the salts behind). The bulk composition of the brine-salt mixture remaining on the waste package surface changes; it becomes more chloride-rich as nitrate-rich brine is lost and chloride-containing salts are retained. The remaining brine is still in equilibrium with the deposited salts and remains on the liquidus. As the repository cools and the relative humidity in the drift rises, the brine composition moves back up the liquidus. However, because the bulk composition of the brine-salt system has changed (a fraction of the brine was lost), it moves further up the liquidus before departing from it (X3). As the amount of brine lost is uncertain, the actual point of departure from the liquidus is not predicted. Hence, the composition of the brine is not readily predicted once the relative humidity has increased beyond the initial point of salt precipitation (X1), and a chloride-rich solution is conservatively assumed to form. The TSPA implementation of this is discussed in Section 2.3.5.5.4.3.

Deliquescence—Another possible source of aqueous conditions on the drip shield or waste package surfaces is the deliquescence of minerals in deposited dusts. In the process of

deliquescence, very soluble minerals, generally salts, condense liquid directly from water vapor in response to appropriate conditions of relative humidity. The mineral/salt will dissolve into this solution to form a brine composition in equilibrium with the relative humidity. Tunnel dusts and atmospheric aerosols will accumulate during the preclosure period when temperatures are lower, but active ventilation keeps the relative humidity low. After closure, higher temperatures develop with associated decreases in relative humidity, followed by cooling and increasing relative humidity, which may promote deliquescence behavior of salts present in dust (SNL 2007j, Section 6).

Although deliquescence can occur on drip shield surfaces, the drip shields are not subject to localized corrosion (Section 2.3.6). In contrast, the Alloy 22 waste package outer barrier may be subject to localized corrosion. The potential effects of dust deliquescence on localized corrosion of the waste package outer barrier were evaluated in a screening analysis (SNL 2007j), and have been excluded from consideration in the TSPA (Table 2.2-5, excluded FEP 2.1.09.28.0A, Localized corrosion on waste package outer surface due to deliquescence).

2.3.5.5.2 Data and Data Uncertainty

[NUREG-1804, Section 2.2.1.3.3.3: AC 1(3), (5), (6), (8), AC 2(1), (2), (4), AC 3(1) to (4)]

The following is a summary of data and related uncertainties used to predict the in-drift chemical environment. Propagation of associated uncertainty is discussed in Sections 2.3.5.5.3 and 2.3.5.5.4.2.1.

Thermodynamic Database with Pitzer Parameters—In order to simulate the behavior of aqueous systems at high salinity conditions, the in-drift precipitates/salts model uses a thermodynamic database called the Pitzer database (SNL 2007k, Appendix I). The Pitzer parameters in the database support implementation of the Pitzer activity coefficient model, which is a component of the in-drift precipitates/salts model. Data used to build this database were obtained from a variety of sources in the scientific literature and synthesized into an internally consistent data set. The principal temperature-dependent Pitzer parameters in the synthesized data set were individually evaluated for their ability to reproduce the original source information (SNL 2007k, Appendix I).

As described above, the Pitzer database is used specifically to evaluate aqueous systems at high concentrations (i.e., brines), generally above 1 mol/kg, but can also be applied to dilute systems. Geochemical modeling of aqueous solutions below about 1 mol/kg is more commonly achieved using simpler models for activity coefficients (than the Pitzer approach), which allows synthesis of a thermal-chemical database encompassing a more comprehensive chemical system. Although such a database can only be applied to a more limited range of aqueous solution concentrations (up to approximately 1 mol/kg), a wider variety of chemical systems can be evaluated. The qualified Yucca Mountain Project database that is used for geochemical simulation of more dilute systems is called data0.ymp.R5 (SNL 2007l). Where appropriate, the same equilibrium constants for reactions among aqueous, solid, and gaseous species are used in the Pitzer and dilute solution databases (SNL 2007k, Appendix I). This ensures consistency of analyses for systems that can be evaluated using either database. In addition, the Pitzer database contains equilibrium constants for selected solid salts that were estimated using thermodynamic data and solubility measurements from the

scientific literature. Where solubility measurements were limited, the thermodynamic data were used to develop initial estimates of the equilibrium constants. The initial estimates were then modified by fitting the values to the solubility data using the Pitzer activity coefficient model. Using this method to develop equilibrium constants ensures that the Pitzer activity coefficient model and the equilibrium constant are consistent when calculating saturation concentrations for the relevant salt (SNL 2007k, Appendix I).

Several chemical data sets are used for model support and to evaluate uncertainties of the in-drift precipitates/salts model:

- Laboratory data for evaporation of waters relevant to Yucca Mountain (SNL 2007k, Sections 7.2.1 to 7.2.4)
- Natural analogue data (McCaffrey et al. 1987; SNL 2007k, Section 7.2.5)
- Saturation points of binary and ternary solutions from handbook and published sources (SNL 2007k, Section 7.1).

Section 2.3.5.5.3.3 presents comparisons of these data sets with results from the in-drift precipitates/salts model. The section also describes how uncertainties associated with the model and parameters in the database are propagated to TSPA.

Near-Field Chemistry Model Data—The near-field chemistry model (Section 2.3.5.3) provides boundary conditions for the emplacement drift, which are used to generate the gas and seepage evaporation abstractions (Section 2.3.5.5.4). The near-field chemistry model represents the compositional range of potential seepage and invert imbibition waters. Specifically, the near-field chemistry model parametrically generates potential seepage water compositions for drift wall temperatures from 23°C to 96°C, at 11 discrete water–rock interaction parameter values (amounts of feldspar dissolved), for each of the 4 starting waters, representing four chemically distinct pore-water groups (Section 2.3.5.3.2.2.1). Results representing temperatures of 30°C, 70°C, and 96°C are used in the seepage evaporation abstraction (SNL 2007b, Section 6.9.1).

Uncertainty in the pore-water compositions is propagated to the in-drift seepage evaporation abstraction through use of four starting waters in the near-field chemistry model. In addition, because of the importance of the chloride-nitrate ratio with respect to corrosion of the waste package outer barrier, the chloride-nitrate ratios for all 34 of the TSw pore waters that passed the screening analysis discussed in Section 2.3.5.3.2.2.1 are used in the seepage evaporation abstraction (Section 2.3.5.5.4.3).

Input Values of Temperature, Relative Humidity, pCO_2, and pO_2—The seepage evaporation analyses were performed at discrete temperature, relative humidity, and pCO_2 values. As explained in Section 2.3.5.5.4.2.1, the three temperatures used were 30°C, 70°C, and 100°C (SNL 2007b, Section 6.9.1). The temperature values were chosen to cover the temperature range of interest while minimizing interpolation errors. The lower value, 30°C, is slightly higher than ambient temperatures at the repository level (approximately 23.5°C). The upper value of 100°C is based on the boiling point of water at the repository elevation including uncertainty; slightly higher temperatures may be predicted on the waste package surface. Predicted water chemistries

at 30°C and 100°C can be used to represent water chemistries at temperatures down to ambient and above 100°C, respectively, because this does not result in significant differences in the seepage model results (SNL 2007b, Section 6.7.2). The relative humidity generally ranges from approximately 100% to the dryout point for each water composition, with a discretization interval of, nominally, 2% (SNL 2007b, Section 6.13.2). The discrete pCO_2 values were selected based on results from the near-field chemistry model (Section 2.3.5.3.4). The majority of predicted pCO_2 values fall between 10^{-4} and 10^{-2} bar, with a few values outside of this range. Accordingly, the three values selected for use are 10^{-2}, 10^{-3}, and 10^{-4} bar (SNL 2007b, Section 6.9.1). The oxygen partial pressure (pO_2) is set equal to the atmospheric value to represent oxidizing conditions in the drift. This value is consistent with the estimates of oxygen levels within the drift (Section 2.3.5.5.4.1.1).

2.3.5.5.3 Model and Model Uncertainty

[NUREG-1804, Section 2.2.1.3.3.3: AC 1(1), (5), (7), (8), (10), AC 3(1) to (4), AC 4(1) to (4), AC 5(1), (3)]

This section describes the in-drift precipitates/salts model and its use in conducting the seepage evaporation analyses. Also described are the results of the seepage evaporation analyses and the evaluation of uncertainty associated with the in-drift precipitates/salts model.

2.3.5.5.3.1 Model Description

The purpose of the in-drift precipitates/salts model is to estimate the effects of evaporation or dilution for given environmental conditions on solution composition. The model is used to conduct 11 seepage evaporation analyses. The analysis results form the basis for the seepage evaporation abstraction, which enables TSPA to calculate the following parameters and their uncertainties for given environmental conditions: pH, ionic strength; Cl^- and NO_3^- concentrations, and the NO_3^-/Cl^- ratio (SNL 2007b, Sections 6.12.3 and 6.15.1). A description of the in-drift precipitates/salts model, including the assumptions, appears below.

The in-drift precipitates/salts model uses a geochemical software package for speciation and reaction-path simulations called EQ3/6. The EQ3/6 package consists of two principal codes: EQ3NR and EQ6. EQ3NR is a speciation-solubility code designed to calculate equilibrium aqueous species concentrations and mineral solubilities, and to compute the degree of solution equilibrium/disequilibrium with respect to mineral phases (SNL 2007k, Section 6.6.1). EQ3NR is useful in evaluating many different conceptual geochemical systems, which are defined by the contents of the supporting thermodynamic database and by other user-defined inputs and constraints in the EQ3NR input file. The supporting thermodynamic database provides not only parameter values, but also the identities of components and chemical species represented in the geochemical system (SNL 2007b, Section 6.2.1.1). EQ6 is a reaction mass-transfer code that starts with the resulting solution speciation from EQ3NR and performs reaction-path calculations, evaluating changes in solution composition due to evaporation, mineral precipitation, and mineral dissolution (SNL 2007k, Section 6.6.1).

The in-drift precipitates/salts model calculates the evolution of a given water composition undergoing evaporation at a given temperature and pCO_2. Once seepage enters an assigned control volume, there is no further flow of liquid water in or out for the simulation time step. The amount

of liquid water decreases due to evaporation. Water is incrementally removed from the solution while the remaining solution is maintained at equilibrium. Depending on mineral saturation indices and interaction with the gas phase, removal of water causes the dissolved ions to concentrate, to precipitate as minerals, or to exsolve as gas species (SNL 2007k, Section 6.6.3.2). With increasing degrees of evaporation, seepage water either evaporates completely or forms a brine which is stable at the relative humidity being considered. The higher ionic strength of such brines (~1 mol/kg or higher) requires that the Pitzer activity coefficient model be used (SNL 2007k, Section 6.6).

The in-drift precipitates/salts model is a quasi-equilibrium model (SNL 2007k, Section 1). While most reactions proceed to equilibrium, some mineral precipitation reactions are suppressed to account for minerals not expected to form under repository conditions. A set of six criteria are used to determine if a particular mineral should be suppressed in the model. The first three criteria relate to the defined chemical system, the kinetic controls, and any related analytical or natural analogue information. The last three criteria relate to model sensitivity to a given mineral suppression and are useful for evaluating modeling uncertainties due to the chosen suppressions (SNL 2007b, Section 6.2.4.1).

The mineral suppression framework only needs to be applied to phases that achieve saturation in the solutions that are evaluated. The Pitzer database includes more than 220 minerals. For the water compositions calculated to evolve within the drift, a majority of the minerals in the database never reach saturation in the solutions. In fact, fewer than 40 of the 220 minerals in the database become saturated in the in-drift precipitates/salts model simulations of in-drift seepage evaporation. Therefore, the criteria for mineral suppression were only applied to approximately 40 minerals to determine whether or not they should be suppressed (SNL 2007b, Section 6.2.4.1).

Assumptions—The assumptions pertinent to the application of the in-drift precipitates/salts model to the in-drift chemical environment include the following:

- **Aqueous and Gas Constituents and Most Mineral Phases Are in Local Equilibrium**—The assumption that all aqueous and gas constituents achieve and maintain local equilibrium, and most mineral phases achieve and maintain local equilibrium upon saturation, is implicit in the in-drift precipitates/salts model. The technical basis is that most chemical reactions occur rapidly compared to the modeling timeframe. Certain mineral reactions that are not expected to occur fast enough in the in-drift environment are suppressed as a means of reflecting their slow reaction rates. Highly soluble nitrate and chloride salts rapidly dissolve and precipitate when solubility limits are exceeded and, therefore, are well approximated by equilibrium modeling (SNL 2007k, Section 5.2; SNL 2007b, Section 5.1.2).

- **Inputs from Near-Field Chemistry Model Apply to Entire Repository**—Another key assumption is that the gas and water compositions from the near-field chemistry model are applicable across the entire repository at locations with different host-rock lithologies. The technical bases for this assumption are that (1) the repository horizon within the Topopah Spring Tuff (which includes the Tptpll, Tptpul, Tptpmn, and Tptpln units) is nearly uniform in composition, based on an analysis of bulk rock compositions throughout the unit (Peterman and Cloke 2002); and (2) the four starting waters used in the near-field chemistry model simulations were chosen to represent the entire range of

available pore-water compositions (Section 2.3.5.3.2.2.1) and include pore waters from three of the four repository-level lithologic units (SNL 2007b, Section 5.2.1.).

2.3.5.5.3.2 Seepage Evaporation Analyses and Results

For each of the four starting waters, at each of eleven water–rock interaction parameter values, the seepage evaporation analyses evaluate the effects of evaporation and dilution for a given combination of temperature and pCO_2. There are nine combinations based on the three input temperatures (30°C, 70°C, and 100°C) and the three input pCO_2 values (10^{-2}, 10^{-3}, and 10^{-4} bar) discussed in Section 2.3.5.5.2. The in-drift precipitates/salts model, which implements the EQ3/6 geochemical software package, is the primary tool used for conducting the seepage evaporation analyses (SNL 2007b, Section 6.9).

Results from the seepage evaporation analyses include the following:

- **Abstraction-Related Result**s—This category includes information directly or indirectly related to the seepage evaporation abstraction: pH, activity of water, ionic strength, mass of solvent water remaining, total concentrations of each element, concentrations of select aqueous species that potentially contribute to acid-neutralizing capacity, and amounts of solids precipitating (SNL 2007k, Section 6.6.3.5).

- **Supplemental Calculation Results—**The supplemental calculations provide the concentration factor or dilution factor at equilibrium for each step of evaporation or dilution. The concentration factor describes the extent to which a conservative ion (i.e., an ion that does not precipitate) concentrates due to evaporation. Because no ions are conservative for the entire simulation range of the seepage evaporation analyses, the concentration factor is estimated by the relative amount of solvent water remaining at each stage of evaporation. If dilution is occurring, the dilution factor is based on the solvent water accumulating at each stage of dilution (SNL 2007k, Section 6.6.2.5).

Figures 2.3.5-51 and 2.3.5-52 provide examples of results from the seepage evaporation analyses for the combination of 70°C and pCO_2 of 10^{-3} bar. The figures depict the total elemental aqueous species and precipitating minerals for the evaporative evolution of the Group 1 representative water—the group representing the greatest number of measured pore-water analyses (Section 2.3.5.3.2.2.1)—at degrees of water–rock interaction corresponding to no feldspar dissolved and to a relatively high amount of feldspar dissolved.

Predicted compositions are most sensitive to the degree of water–rock interaction and the pCO_2, with the temperature having comparatively less effect. This is illustrated in Figures 2.3.5-53 and 2.3.5-54, which show how pH varies with water group, degree of water–rock interaction, temperature, and pCO_2. The degree of water–rock interaction has the largest effect on the pH; Group 1 waters always evaporatively evolve to higher pH, but the other water groups evaporate to lower pH solutions at low degrees of water–rock interaction and to higher pH solutions at higher degrees of water–rock interaction. The change in the evaporative pathway of the waters with the degree of water–rock interaction is due to changes in the brine type. For low amounts of feldspar dissolved, Group 1 waters form carbonate brines, Group 4 waters form sulfate brines, and Groups 2 and 3 waters form calcium chloride brines. With increasing amounts of feldspar dissolved, all the

waters evolve into the carbonate-type brines. This is because feldspar dissolution and secondary mineral precipitation consume calcium and magnesium and raise the pH and bicarbonate concentration (Section 2.3.5.3.3.3).

As seepage evaporates, chloride and nitrate concentrate in solution. Because chloride and nitrate salts are highly soluble, these two species vary linearly with the degree of concentration and the relative humidity until a salt containing chloride or nitrate precipitates, generally between 60% and 75% relative humidity. At the point of salt precipitation, chloride concentrations vary from about 2 to about 8 molal. At higher degrees of evaporation, concentrations can increase to as high as 11 molal. The chloride-nitrate ratio of the evaporating solution remains constant until a chloride-containing or nitrate-containing salt precipitates. Chloride salts (halite or sylvite) nearly always precipitate first and the chloride:nitrate ratio decreases. In a few cases, a nitrate salt precipitates first and the chloride:nitrate ratio increases slightly; however, a chloride salt soon begins to precipitate, and the ratio drops. At the highest degrees of evaporation, the chloride-nitrate ratio can increase again. The change in the chloride-nitrate ratio for the Group 1 waters is shown in Figure 2.3.5-55.

As discussed in Section 2.3.5.5.1, three types of brines typically form in nature, from the evaporative concentration of dilute natural waters at the earth's surface: calcium chloride brine, alkaline carbonate brine, and high-sulfate brine. In general, the brines expected to occur in the repository from evaporative concentration of seepage fall within these three types because they are produced by processes that are similar to those that occur at the earth's surface. However, one major difference is expected; nitrate is a significant component of in situ pore waters, and will comprise a large component of the brines because of the high solubility of nitrate minerals. With respect to the water types described above, nitrate behaves similarly to chloride. In Table 2.3.5-10, the end-point brine composition and classification are given for each of the four starting waters, at three different water–rock interaction parameter values, corresponding to low, moderate, and high amounts of feldspar dissolved. In terms of the three stated natural brine types, the waters are classified dominantly as carbonate-type. The composition of each group water is a function of the water–rock interaction parameter value, temperature, pCO_2, and relative humidity. As noted previously, the water–rock interaction parameter value, the amount of feldspar dissolved, is a dominant control on the brine type. At low amounts of water–rock interaction, Group 1 waters form carbonate brines, Group 4 waters form sulfate brines, and Group 2 and Group 3 waters form calcium chloride brines. With higher degrees of water–rock interaction, all brines evolve into carbonate brines. Table 2.3.5-10 shows the brine types expected to be produced by seepage evaporation are well represented among the solutions used for corrosion testing of Alloy 22 and titanium materials (Section 2.3.6.1.2) (SNL 2007b, Section 6.13.5.2). The classification of the corrosion test solutions with respect to brine type is as follows:

Calcium Chloride Brines—Naturally occurring brines of this type may have acidic to near-neutral pH and no significant bicarbonate, carbonate, fluoride, or sulfate content. These brines may contain other cations such as Na^+, K^+, and Mg^{2+}, and other anions such as NO_3^-. The endpoint of the evaporative concentration of this type of brine would contain Ca-Cl-NO_3 or a mixture of Ca-Mg-Cl-NO_3. Corrosion test solutions (Table 2.3.6-1) corresponding to calcium chloride-type brines include: calcium chloride, calcium chloride plus calcium nitrate, simulated saturated water, and sodium chloride solutions. The simulated saturated water and sodium chloride test solutions represent the moderate relative humidity scenario where calcium is a minor

component in the aqueous solution. Numerous electrochemical studies were performed in these test solutions. Thin film studies were also performed using these types of solutions on coupons of Alloy 22 using an environmental thermal-gravimetric analyzer.

Carbonate Brines—These brines are alkaline and do not contain significant calcium or magnesium. In the early stages of the evaporative concentration, calcium precipitates as carbonate minerals (calcite or aragonite). Magnesium precipitates as magnesium silicate. As shown in Table 2.3.5-10, carbonate-type brines are expected to comprise the largest fraction of those produced by seepage evaporation. Corrosion test solutions (Table 2.3.6-1) corresponding to carbonate-type brines include: simulated dilute water, simulated concentrated water, basic saturated water, and under certain circumstances, simulated saturated water and NaCl aqueous test solutions. The simulated dilute water test solution is a dilute alkaline solution; solutions in this concentration range could be expected to form for high relative humidity (greater than 99%). The simulated concentrated water test solution is a moderately concentrated alkaline solution; solutions in this concentration range could be expected to form for relative humidity in the range of 90% to 95%. The basic saturated water test solution is a highly concentrated alkaline solution and could be expected under repository conditions where temperatures could be at its measured boiling point of nominally 112°C to 113°C, or where the relative humidity is nominally 70% to 75%. Under conditions of low relative humidity, carbonate-type brines can be rich in Cl^- and NO_3^- with low carbonate content. The simulated saturated water and NaCl test solutions have characteristics of this type of brine.

Sulfate Brines—These have near-neutral pH and no significant carbonate or calcium content. Calcium precipitates as carbonates and possibly sulfates. In addition, the brines typically have only a small amount of magnesium, though some surface brines have been observed to have high magnesium (Drever 1997b, Table 15-1, p. 333, brines 1 through 3). As with the other brine types, the dominant ions in sulfate brines vary with relative humidity. At low relative humidity, the solutions will be dominated by Cl^- and NO_3^- anions, with NO_3^- ions dominating at the lowest relative humidity. At moderate relative humidity (greater than 70%), Cl^- ions may dominate. However, unlike the carbonate brines, sulfate brines are expected to have near-neutral to slightly acidic pH. Significant amounts of dissolved carbonate and Ca^{2+} are not predicted until the relative humidity is greater than 85%. The corrosion test solutions (Table 2.3.6-1) corresponding to sulfate-type brines include simulated acidified water, simulated saturated water, and sodium chloride. The simulated saturated water has characteristics of water at low relative humidity, where sulfate is not a major brine component. Sodium chloride test solutions simulate the scenario where Cl^- is the dominant anion under moderate relative humidity conditions. The simulated acidified water test solutions have characteristics of solutions in equilibrium with nominally 90% relative humidity.

2.3.5.5.3.3 Model Support and Uncertainty

Results from the in-drift precipitates/salts model have been compared with a variety of independent data sets. These model–data comparisons build confidence in the model's ability to simulate the combined effects of temperature and relative humidity on water compositions as well as complex multicomponent systems. They also provide insight into the uncertainty in model results. The following discussion addresses the model–data comparisons and the associated uncertainties in parameters important to the seepage evaporation abstraction.

2.3.5.5.3.3.1 Model Support

The independent data sets used for comparison to in-drift precipitates/salts model results include the following: (1) data derived from independent laboratory experiments specifically designed to investigate the effects of evaporation on the chemical evolution of water compositions and environmental conditions relevant to the repository; (2) a natural analogue for evaporative concentration; and (3) compilations of salt solubility measurements (SNL 2007k, Section 7). The laboratory experiments with site-specific data and the natural analogue comparison support model calculations for degrees of evaporation less than the point at which salt minerals start to precipitate. Higher degrees of evaporation are supported by comparisons with published saturation points of single, binary, and ternary salt systems.

Comparison with Site-Specific Data from Independent Laboratory Experiments—Several sources of evaporation data were compared to the in-drift precipitates/salts model results, including the following experiments involving evaporation of (SNL 2007k, Section 7.2):

- Synthetic J-13 well water at 85°C (Rosenberg et al. 1999a)
- Synthetic Topopah Spring Tuff pore water at 95°C (Alai et al. 2005)
- Synthetic Topopah Spring Tuff pore water at 75°C (Rosenberg et al. 1999b)
- One hundred times concentrated synthetic J-13 well water at 90°C and 85% relative humidity (SNL 2007k, Section 7.2.2).

Rosenberg et al. (1999a) evaporated synthetic J-13 well water in a beaker that was open to the atmosphere and maintained at a constant elevated temperature of 85°C. In the experiment, synthetic average J-13 well water was evaporated without contact with tuff or other rock material. Water samples were collected after the original 30 L of synthetic J-13 well water had been evaporated to approximately 30 mL. The solids that accumulated by this stage were identified by X-ray diffraction to be amorphous silica, aragonite, and calcite. Analysis of solids after complete evaporation indicated the additional presence of halite, niter, thermonatrite, and possibly gypsum, anhydrite, and hectorite (SNL 2007k, Section 7.2.1).

For comparison purposes, the in-drift precipitates/salts model simulated the experimental conditions. Figure 2.3.5-56 shows the comparison between measured data and results from the in-drift precipitates/salts model. The modeled evaporation results approximate the aqueous sodium, potassium, chlorine, nitrogen, carbon, sulfur, fluorine, and silicon concentrations within a factor of 10 or better when compared to the laboratory measurements. Calcium and magnesium predictions are within a factor of 100 of the measurements. The discrepancies between the predicted and measured silicon, calcium, and magnesium concentrations and pH may be due to errors or uncertainty in the Pitzer thermodynamic database, kinetic limitations of precipitation reactions, and/or analytical errors such as incomplete removal of small particles of minerals containing these elements from the aqueous samples (SNL 2007k, Section 7.2.1). The discrepancies in measured and predicted calcium and magnesium are greatest when these components are present only in trace quantities (Figure 2.3.5-56).

Alai et al. (2005) evaporated synthetic Topopah Spring pore water at 95°C in four successive legs, each leg using the synthetic brine corresponding to the final composition of the previous leg as a starting composition. In each leg, a concentration factor of 9 to 15 was achieved. In-drift precipitates/salts model simulations predicted most dissolved salt concentrations to within a factor of 10 for each leg except for silicon concentrations in leg 4 (SNL 2007k, Section 7.2.4). Most dissolved salt concentrations are predicted within a factor of two. Predicted ionic strength is always within 50% of experimentally estimated values and usually within 10%. The largest differences (near 50%) are observed in leg 4 when the ionic strength exceeds 5 molal.

In a third experiment, synthetic Topopah Spring Tuff pore water was evaporated (Rosenberg et al. 1999b) using similar procedures to the experiment described above for J-13 water evaporated at 85°C except that the temperature was maintained at 75°C instead. (Rosenberg et al. 1999a). The final solution was reported to have an approximate concentration factor of $1243 \pm 10\%$. Figure 2.3.5-57 shows that the modeled results closely approximate the measured sodium, magnesium, calcium, chlorine, and potassium concentrations. At a concentration factor of 690, modeled results underestimate the measured sulfate and silicon concentrations by approximately 0.5 order of magnitude (SNL 2007k, Section 7.2.3).

In the fourth evaporation experiment, synthetic 100-times-concentrated average J-13 well water was dripped through a column of heated tuff into a beaker. The beaker was open to the atmosphere and maintained at a constant temperature of 90°C and relative humidity of 85%. The solution was then allowed to evaporate to approximately 5% of the original volume, based on the concentration factors reported (SNL 2007k, Section 7.2.2). Figure 2.3.5-58 compares measured values and model predictions for the experiment. The predictions closely approximate the sodium, fluorine, chlorine, potassium, nitrate, bicarbonate, and sulfate concentrations when compared to the laboratory measurements. Calcium and magnesium predictions can be off by up to two orders of magnitude though, presumably due to kinetic factors.

Comparison with Natural Analogues—Results with the in-drift precipitates/salts model were compared with data from a natural analogue for concentration by evaporation of seawater at the Morton Bahamas solar salt production facility on Great Inagua Island in the Bahamas.

The Morton Bahamas solar salt production facility on Great Inagua Island in the Bahamas provides an example of the evaporative chemical evolution of a natural multicomponent water. At this plant, seawater is concentrated through evaporation in a sequence of reservoirs to precipitate halite. The final brine in this production process has a concentration factor near 40 with respect to seawater. One of the advantages of this data set compared to those from saline lakes is the absence of mixing effects from streams and rivers. In addition, the reservoirs are shallow and open to the atmosphere, facilitating equilibrium conditions with respect to atmospheric partial pressures of carbon dioxide and oxygen. Thus, the major processes affecting the evolution of seawater at the plant are the same processes incorporated in the in-drift precipitates/salts model (SNL 2007k, Section 7.2.5).

McCaffrey et al. (1987) sampled and analyzed the chemical compositions of the evolving seawater at the plant. Three of the most concentrated samples were evaporated further in the laboratory. These laboratory evaporation experiments resulted in samples with degrees of evaporative concentration greater than 40 times the starting concentration. These experiments were closed to the

atmosphere, and as such, reflect different boundary conditions than the samples evolved at the plant and the simulated results discussed below (SNL 2007k, Section 7.2.5).

The measured data show agreement with results from in-drift precipitates/salts model simulations of the seawater evaporation at the plant. Figure 2.3.5-59 provides an example of the model–data comparisons for Br^-, Cl^-, and SO_4^{2-} concentrations. Halite precipitation begins to control the concentration of Cl^- at a degree of evaporation around 10. The largest difference between model results and measured data shown by this figure is for the SO_4^{2-} concentration, which is underestimated by a factor of about 2.2 at a degree of evaporation of 69.2. The marked decrease in measured SO_4^{2-} concentration above this degree of evaporation is due to the precipitation of one or more magnesium sulfates (McCaffrey et al. 1987, p. 935). One factor contributing to differences between modeled and measured values at higher concentrations may be the difference in boundary conditions between the laboratory evaporation experiments and the simulations. Carbonate/bicarbonate concentrations were not measured; the calculated values shown in Figure 2.3.5-59 are based on equilibrium with atmospheric levels of CO_2 (SNL 2007k, Section 7.2.5).

Comparison with Compilations of Salt Solubility Measurements—Saturation points for solutions of many binary and ternary salt systems were calculated with the in-drift precipitates/salts model for comparison with measurements reported in handbooks and the scientific literature (SNL 2007k, Section 7.1). Results of the model–data comparisons for binary salt systems at 25°C and 100°C are provided in Figures 2.3.5-60 and 2.3.5-61. These two figures show that the model compares well with the measured values over a range of about 5 orders of magnitude. Comparisons for solutions from binary and ternary salt systems were performed over a range of temperatures and in most cases agreement is within an order of magnitude or better. For many of the binary salt systems, model results are within 20% (SNL 2007k, Section 7.1.1.1). This level of agreement is reasonable given that some species concentrations can change by several orders of magnitude as dilute waters experience evaporative concentration (SNL 2007k, Section 7).

2.3.5.5.3.3.2 Model Uncertainty

Uncertainty in the in-drift precipitates/salts model was evaluated using the model–data comparisons discussed in the previous section as well as various sensitivity studies. This section addresses the model uncertainty evaluations with respect to the following: pH, ionic strength, concentrations of Cl^- and NO_3^-, NO_3^-/Cl^- ratio, deliquescence relative humidity, and the limited availability of mineral thermodynamic data. The sensitivity studies are also discussed.

pH Uncertainty—Uncertainty in the in-drift precipitates/salts model is evaluated by use of model-data comparisons. However, comparing model-data pH values is generally not an accurate method of evaluating uncertainty for this parameter, for two reasons. First, the form of pH provided by the in-drift precipitates/salts model and used by downstream models is not consistent with the measured data. Measured pH data are determined using an electrode that is calibrated against a standard solution, the pH value of which is assigned by the National Bureau of Standards. This "National Bureau of Standards pH" value does not represent the true activity of the hydrogen ion, but rather what the activity would be if a simplified activity coefficient model were used, and if the only ion interactions occurring are H^+–Cl^-. However, the in-drift

precipitates/salts model and all downstream models are parameterized using the "Pitzer pH" values, representing the predicted activity of the hydrogen ion in solutions using the Pitzer model for activity coefficients, which is a more accurate representation of the ion activities in concentrated solutions. The Pitzer and National Bureau of Standards pH values differ increasingly with increasing ionic strength. Second, there is significant experimental error in the process of measuring pH, especially in concentrated brines, where the development of an electrical potential across the electrode junction results in pH values which are increasingly erroneous as the ionic strength increases. Standard pH electrodes are also temperature-sensitive, and the appropriate corrections may not have been applied when the measurements were made. Because Pitzer pH and measured pH values are not equivalent, and because of likely measurement errors in the experimentally-determined pH, comparing them significantly overestimates the uncertainty in the predicted Pitzer pH values.

However, most geochemical systems have pH-sensitive components present, which can be used to either more accurately constrain the pH or to constrain the possible pH range (SNL 2007k). In systems of relevance to the in-drift chemical environment models, one pH-sensitive solution parameter that is always present is total inorganic carbon concentration (TIC, or C_{total}). Using this parameter to quantify the uncertainty in pH requires determining the sensitivity of the component used, C_{total}, to pH. This was done for several solutions, from dilute solutions representing pore waters from the TSw to brines with an activity of water of 0.75, just above the point of halite saturation. Over the near-neutral pH range (approximately 6 to 8), $\log C_{total}$ varies 1:1 with pH-that is, uncertainty in the value of $\log C_{total}$ corresponds to the same uncertainty in pH, which is also a log-transformed value. The pH should exhibit the largest relative uncertainty in the near-neutral range because at these values it does not contribute significantly to the charge balance of the solution and is only loosely constrained by this requirement. At higher and lower pH values, the pH is "mass buffered" and relative uncertainty is less; the concentration of pH-buffering species is so large that mass balance constraints limit the uncertainty in pH. Hence, examination of C_{total} uncertainty at neutral pH should provide a maximum, bounding uncertainty for all conditions.

To evaluate the uncertainty in C_{total}, data from eleven geochemical studies were examined, including four evaporation experiments and seven equilibrium measurements of calcite or CO_2 solubility. Ten of these were determined to be applicable, and were used to evaluate pH uncertainty (138 data points). These experimental systems ranged in concentration from very dilute to ionic strengths of approximately 6 molal, corresponding to an activity of water of about 0.75. The measured values and model results for C_{total} generally matched to within 0.1 log units, except at low C_{total} concentrations, where the mismatches for some samples are as large as 0.4 log units. Over the ranges examined, the differences between modeled and measured C_{total} did not correlate significantly with temperature, value of pH, or the ionic strength. The lack of a systematic change with ionic strength indicates that the errors are not associated with the thermodynamic database, as the Pitzer activity coefficient model plays a large role in concentrated brines, but reduces to a simpler activity model (Debye-Hückel) in dilute systems. Hence, the uncertainty in C_{total} is largely due to errors in the description of the experimental conditions, or measurement errors.

The uncertainty in $\log C_{total}$, and by inference, pH, is represented probabilistically. The entire data set consisting of the differences in $\log C_{total}$ ($\log C_{total}$ measured – $\log C_{total}$ modeled) from the experiments described above, is plotted as a histogram and a discrete distribution in Figure 2.3.5-62. The majority of the data (approximately 80%) fall within 0.1 log units of zero. The

uncertainty is provided to TSPA as the discrete distribution of 138 values shown in Figure 2.3.5-62. The experimental studies used to define this distribution do not attain activities of water below approximately 0.75, so for more concentrated solutions the estimates of uncertainty are based on comparisons to measured pH data. As noted previously, such measurements probably greatly overestimate the pH uncertainty, but provide an upper bound. In each of the simulations used for direct comparison with experimental systems, modeled Pitzer and measured National Bureau of Standards pH values correspond to within 0.79 pH units or less. For relative humidity below 75%, the estimated model uncertainty for pH is ±1 pH unit, increasing to ±2 pH units for relative humidity less than 65% (SNL 2007k, Table 7-10).

Ionic Strength Uncertainty—In each of the multicomponent evaporation simulations evaluated, ionic strength is predicted within a factor of 2 or better (SNL 2007k, Section 7.5.2). As shown in Table 2.3.5-11, the maximum observed ionic strength difference is 50%. However, the largest differences reported in Table 2.3.5-11 for ionic strength are from the 95°C TSw pore water evaporation experiment, for which "measured" ionic strength values were calculated from individual component concentrations, an approach which inherently has a greater uncertainty than that of directly measured ionic strength values (SNL 2007k, Section 7.2.4). The maximum difference between measured and simulated ionic strength in the seawater samples and in the other laboratory evaporation experiments is approximately 15%. Considering the accuracy in the predicted ionic strength for these experiments, the estimated model uncertainty in ionic strength of ±0.1 log units, or approximately 30%, at RH values of 100% to 85% is supported and justified (Table 2.3.5-12) (SNL 2007k, Section 7.5.2). Uncertainty in ionic strength was not evaluated at lower relative humidity values, because a quantitative estimate of ionic strength at lower relative humidities is not utilized by TSPA.

Cl^- and NO_3^- Uncertainties—The maximum differences between simulations and measurements for Cl^- and NO_3^- in each of the evaporation data sets are summarized in Table 2.3.5-11. The J-13 and 75°C TSw pore-water evaporation experiments did not produce results beyond a water activity of about 0.91; halite does not precipitate until the activity of water falls to approximately 0.7 or lower in these solutions. Given that no Cl^- or NO_3^- precipitated in these experiments, the Cl^- and NO_3^- concentrations should have increased in direct proportion to the concentration factor, and the model results and measurements should be identical. Thus, the differences for these experiments (Table 2.3.5-11) cannot be attributed to model uncertainty. Instead, the differences are attributed to experimental uncertainty (SNL 2007k, Sections 7.2.1 and 7.2.3).

The seawater evaporation and the 95°C TSw pore-water evaporation experiments attained lower activities of water than the J-13 and 75°C TSw pore-water evaporation experiments (SNL 2007k, Sections 7.2.4 and 7.2.5). Thus, Cl^- did not concentrate conservatively in these experiments, except during the early stages. Once the activity of water decreased to approximately 0.7, halite began to precipitate as indicated by the plateau of the Cl^- concentration curve in Figure 2.3.5-59. The maximum difference between measured and simulated Cl^- in the seawater and 95°C TSw pore-water evaporation experiments is approximately 12%, except for an outlier at the highest degree of evaporation, possibly due to the technical challenge involved in making measurements at such high ionic strengths. The largest error in NO_3^- in the 95°C TSw pore-water evaporation experiment was 20%; NO_3^- was not measured in the seawater study (SNL 2007k, Section 7.2.5).

The estimated model uncertainties for Cl^- and NO_3^- are presented in Table 2.3.5-12 as functions of relative humidity. Above 85% relative humidity, Cl^- and NO_3^- minerals will not precipitate, as implied in Figure 2.3.5-63 by the absence of data points at relative humidity greater than 85%. Instead, Cl^- and NO_3^- simply concentrate (or dilute) conservatively as water evaporates (or condenses). Thus, the model uncertainty in Cl^- and NO_3^- predictions is set at 0 for relative humidity between 100% and 85% (SNL 2007k, Section 7.5.4).

As relative humidity decreases below 85%, the uncertainty in Cl^- and NO_3^- concentrations increases (SNL 2007k, Section 7.5.4). Between 85% and 60% relative humidity, the concentrations of these anions can be controlled by the solubilities of Na^+ and K^+ salts of Cl^- and NO_3^-. The estimated model uncertainties in Cl^- and NO_3^- in this relative humidity range consider effects of other dissolved components, such as SO_4^{2-}, CO_3^{2-}, and the effects of ternary systems involving both Cl^- and NO_3^-, as compared in Figure 2.3.5-63 (SNL 2007k, Section 7.5.4).

Below 60% relative humidity, model uncertainties in Cl^- and NO_3^- increase markedly (Table 2.3.5-12). In this low relative humidity range, Cl^- and NO_3^- concentrations can be controlled by the solubilities of Ca^{2+} and Mg^{2+} salts. In addition, when temperatures are above approximately 90°C in this relative humidity range, NO_3^- concentrations can be controlled by the solubility of KNO_3. The larger differences between simulated and measured solubilities shown in Figure 2.3.5-63 justify the higher estimated model uncertainties in Cl^- and NO_3^- at these low relative humidity values (Table 2.3.5-12). The model uncertainty estimates in Cl^- and NO_3^- in this relative humidity range are based on simulations of binary and ternary salt systems containing Cl^-, KCl, and NO_3^- (SNL 2007k, Section 7.5.4).

NO_3^-/Cl^- Ratio Uncertainty—The NO_3^-/Cl^- ratio is an important parameter in evaluating the potential for localized corrosion of the waste package outer barrier. Consequently, uncertainty in NO_3^-/Cl^- due to in-drift precipitates/salts model uncertainty was directly estimated for propagation in the TSPA. The estimated uncertainties in NO_3^-/Cl^- are presented in Table 2.3.5-12 as a function of relative humidity; these uncertainty estimates consider the effects of ternary systems involving both NO_3^- and Cl^- (Figure 2.3.5-63) (SNL 2007k, Section 7.5.7).

Much of the model uncertainty discussion in this section for Cl^- and NO_3^- applies to the NO_3^-/Cl^- ratio predictions as well. The model uncertainty in the NO_3^-/Cl^- ratio is zero for relative humidity values above that of salt saturation, although, as discussed in Section 2.3.5.5.4.3, uncertainty associated with using a single water to represent each pore water group is captured by sampling a distribution of the ratios for each group. Saturation and precipitation of salts occurs at relative humidities between 60% and 72%, with chloride salts commonly precipitating prior to nitrate salts. At lower relative humidity values, all seepage water compositions exhibit increasing NO_3^-/Cl^- values (corresponding to decreasing Cl^-/NO_3^- values) with further evaporative concentration (Figure 2.3.5-55). At relative humidities between salt saturation and 65%, the model uncertainty is ±0.2. At lower relative humidities, estimated model uncertainty in NO_3^-/Cl^- increases markedly, a reflection of the increased differences between simulations and measurements (Figure 2.3.5-63) (SNL 2007k, Section 7.5.4).

Deliquescence Relative Humidity Uncertainty—Each salt mineral has a characteristic deliquescence relative humidity, which is a function of temperature. The deliquescence relative humidities of salt mixtures are lower than those of any of the contained individual salts or subset

mixtures (SNL 2007j, Appendix E.1). Results from the in-drift precipitates/salts model were compared to reported values of deliquescence relative humidity from literature data (Kracek 1928; Greenspan 1977; Dingemans and Dijkgraaf 1948) and from handbook sources (Dean 1992, p. 11.6; Weast and Astle 1981, p. E-44). In the comparisons using literature data, the differences between simulated and measured values of deliquescence relative humidity for relevant salt systems are less than 10% expressed as a difference in relative humidity, for most salts. Comparisons using handbook sources are shown in Table 2.3.5-13. These simulated values agree with the measured values, to within a 5% difference in relative humidity. These two sets of comparisons support the application of the computational method to predict dryout behavior in the seepage evaporation abstraction (SNL 2007k, Section 7.5.3).

Although the in-drift precipitates/salts model results for deliquescence relative humidity are well supported for most simple single salt systems, within a reasonable range of relative humidity, for $Mg(NO_3)_2$ at all temperatures above 25°C and for KF at 25°C, the model does not adequately represent dryout (SNL 2007k, Section 7.5.3). Deliquescence relative humidity data are sparse for more complex salt systems, and in experimental studies using three- and four-salt assemblages anticipated to form by seepage evaporation, dryout was not observed at temperatures up to 190°C (SNL 2007j, Section 6.1.2.2). For these reasons, once seepage onto a waste package occurs, an aqueous solution is assumed to be present thereafter, for all possible temperature or relative humidity conditions (SNL 2007b, Section 1.3).

Model Uncertainty Due to Limited Mineral Thermal-Chemical Data—The in-drift precipitates/salts model simulates aqueous evolution and reasonably predicts the general compositions of precipitated minerals. Because geochemical models use idealized mineral phases and do not include solid solutions, in some cases the minerals predicted to occur are more representative of the bulk mineral composition rather than the exact minerals observed to precipitate in laboratory evaporation experiments. However, the minerals predicted by the model to precipitate are adequate for estimating the evaporative evolution of the major components of the aqueous phase and the evolution of the aqueous phase as minerals/salts dissolve or deliquesce (SNL 2007k, Section 7.5.6).

Sensitivity Analysis—A process-level sensitivity analysis was conducted to examine the effect of interactions with introduced materials, such as components of the ground support system and invert and their corrosion products, on in-drift water chemistry. The results indicated that interactions with steel ground support materials will not have a significant effect on the predicted chemistry of aqueous solutions in the drift (SNL 2007b, Section 6.8). Metal ion solubilities are low under oxidizing conditions, and the corrosion of steel to oxides/oxyhydroxides had no effect on pH, ionic strength, or other compositional parameters. The potential for reduction of nitrate in seepage water by interactions with metal in the drift was also evaluated. However, metal oxidation reactions greatly favor free oxygen, and this selectivity, as well as the greater abundance of oxygen relative to nitrate in the drift environment, will inhibit reduction of nitrate in seepage water.

Summary of In-Drift Precipitates/Salts Model Uncertainty—Uncertainty in the in-drift precipitates/salts model was evaluated through sensitivity studies and model–data comparisons using site-specific data from independent laboratory experiments, natural analogues, and literature compilations of salt solubility measurements. The maximum differences in the model–data

comparisons (Table 2.3.5-11) are the basis for the uncertainty ranges applied to the compositional parameters generated for TSPA by the seepage evaporation abstraction. TSPA implementation of these uncertainty ranges is discussed in Section 2.3.5.5.4.3.

2.3.5.5.4 Abstraction and TSPA Implementation

[NUREG-1804, Section 2.2.1.3.3.3: AC 1 (1) to (8), (10), AC 2(1), AC 3(1) to (3), AC 5]

The seepage evaporation abstraction, along with the range of in-drift CO_2 concentrations predicted by the near-field chemistry model, describes the in-drift chemical environment. This section describes the seepage evaporation abstraction and also summarizes how TSPA implements it.

2.3.5.5.4.1 Gas Phase Composition

Important parameters for the seepage evaporation abstraction are the gas phase oxygen and CO_2 concentrations. The effects of oxygen and carbon dioxide gases are included indirectly or directly, respectively, in all the water chemistries. Bounds on the oxygen content define the equilibrium oxidation state of the in-drift system. Carbon dioxide concentration in the emplacement drifts is modeled because of its influence on pH and other compositional factors in brines that form by seepage evaporation (SNL 2007b, Section 6.13.3).

2.3.5.5.4.1.1 Oxygen Concentrations

Within the seepage evaporation abstraction, the in-drift pO_2 is set equal to the atmospheric level, which is 21% of the total pressure, as a means of representing oxidizing conditions in the drift. For this value to be representative, the pO_2 must be great enough to ensure that the model results are not significantly affected by redox reactions. Values for pO_2 associated with the equivalence points for the NO_2^-/NO_3^- and Fe^{2+}/Fe^{3+} redox couples are on the order of 10^{-28} bar or less (SNL 2007b, Section 6.7.1.6). The equivalence point is the point at which the activity of the reduced species (e.g., NO_2^-) is equal to that for the species that occurs at oxidizing conditions (e.g., NO_3^-). However, the pO_2 values based upon equivalence points are much smaller than the lower limit on pO_2 of 10^{-9} bar established for use of the in-drift precipitates/salts model (SNL 2007k, Section 4.1.2). As a result, the higher value of 10^{-9} bar is used for comparison purposes in the evaluations described below.

Following repository closure, oxygen will be depleted in the emplacement drifts as steel in the invert (Table 1.9-9), Parameter 02-08) corrodes and is replaced continuously by convective gas flux from the host rock. The reduction in oxygen fugacity, or partial pressure, depends on the flux of incoming air and on the environmental conditions favoring rapid corrosion of the steel. To evaluate the pO_2 in the drift through time, the flux of incoming air is estimated using output from two-dimensional thermal-hydrologic-chemical seepage model simulations (Section 2.3.5.2.3), one representing the repository center (81-m drift spacing) and one for repository-edge conditions (162 m). This estimate is for incoming air from the host rock, and does not take into account axial transport in the emplacement drifts. The results show that oxygen fugacity may decrease by several orders of magnitude compared to atmospheric air, as low as 10^{-9} bars. This is jointly caused by steel corrosion and displacement of air from the drifts by steam during the boiling period. These results represent lower-bound estimates of oxygen fugacity, because the thermal-hydrologic-chemical seepage

model simulations do not include gas-phase axial transport in the drifts. Axial transport effects such as barometric pumping (SNL 2007e, Section 6.3.7) can potentially increase the availability of oxygen in the emplacement drifts (SNL 2007b, Section 6.7.1).

An additional analysis was performed to evaluate the effect on oxygen consumption of an accumulated layer of corrosion products (rust) on the invert steel. The results show that a layer of corrosion products will hinder corrosion and decrease the impact of ongoing corrosion on in-drift oxygen fugacity while extending the duration of the effect. This is further support that the estimates described above are lower bounds on O_2 fugacity and that the actual fugacity is likely to be much greater than 10^{-9} bars (SNL 2007b, Section 6.7.1).

2.3.5.5.4.1.2 Carbon Dioxide Concentrations

The near-field chemistry model provides the potential range of CO_2 partial pressures within the repository drifts (Section 2.3.5.3.3.2.11). Predicted pCO_2 values range from approximately 2×10^{-2} bars to approximately 10^{-5} bars (SNL 2007b, Section 6.7.2). Three discrete CO_2 concentrations—10^{-2}, 10^{-3}, and 10^{-4} bars—are implemented in the seepage evaporation abstraction; when higher or lower CO_2 concentrations are predicted, water compositions are predicted by extrapolation (Section 2.3.5.5.4.2.2).

2.3.5.5.4.2 Seepage Evaporation Abstraction

The seepage evaporation abstraction enables the TSPA to determine the composition of seepage on the waste package or in the invert for a given set of temperature, relative humidity, and pCO_2 conditions. What follows is a description of the abstraction lookup tables, the related uncertainties, and the TSPA implementation.

2.3.5.5.4.2.1 Seepage Evaporation Abstraction Description

The seepage evaporation abstraction includes multiple sets of lookup tables representing possible in-drift crown and invert water compositions due to evaporation or dilution of seepage or imbibed water and the associated model uncertainties (SNL 2007b, Section 6.9). TSPA implementation of the lookup tables is discussed in Section 2.3.5.5.4.3.

As described in Section 2.3.5.5.3.2, the near-field chemistry model provides the potential seepage water compositions that are the inputs to the seepage evaporation analyses. The near-field chemistry model inputs consist of the four representative group waters, modified by the addition of 11 discrete amounts of alkali feldspar (water–rock interaction parameter values) to generate 44 water compositions, and brought to equilibrium at three discrete temperatures at the evaporation front (30°C, 70°C, and 96°C). The 44 waters at each temperature provide feeds to in-drift seepage evaporation simulations at corresponding temperatures of 30°C, 70°C, and 100°C (the near-field chemistry model does not predict water compositions at temperatures above the boiling point of water, so 96°C near-field chemistry water compositions are used as the feed for the 100°C seepage evaporation simulations). At each temperature, the waters are evaporated at three different pCO_2 values (10^{-2}, 10^{-3}, and 10^{-4}) bars; in a second set of EQ3/6 simulations, the waters were diluted by a factor of 100. The results of the evaporation and dilution simulations for each water, at each combination of temperature and pCO_2, were combined), resulting in 396 lookup tables (4 pore

waters × 11 water–rock interaction parameter values × 3 temperatures × 3 pCO_2 values). These lookup tables represent the range of chemical compositions potentially generated by evaporation or dilution of crown seepage or condensation, or waters imbibed into the invert. Dilution is implemented when the in-drift relative humidity at the waste package surface exceeds the equilibrium relative humidity of the seepage input water from the near-field chemistry model (SNL 2007b, Section 6.9.1).

Conceptually, the set of lookup tables for a particular starting water describes the compositional behavior of that water over ranges of extent of water–rock interaction (water–rock interaction parameter values), temperatures, relative humidities, and pCO_2 values. The output for pH, ionic strength, and chemical species in each of the tables represents the continuous evaporative concentration or dilution of each of the waters under the specified conditions of temperature and pCO_2 (SNL 2007b, Section 6.9.2).

TSPA determines which set of lookup tables to use for the water composition in the drift using four inputs: the starting water identity (Groups 1 through 4); the water–rock interaction parameter parameter derived from the near-field chemistry model; the pCO_2, derived from the near-field chemistry model; and the waste package surface temperature, derived from the multiscale thermal-hydrologic model. The actual water composition in the table is selected as a function of the relative humidity at the waste package surface, derived from the multiscale thermal-hydrologic model (Section 2.3.5.4.1). For water–rock interaction parameter values, temperatures, and pCO_2 conditions between those reported in the lookup tables, chemical parameters are derived by interpolation between the values in adjacent tables (SNL 2007b, Section 6.15.1).

Salt Separation Effect—Separation of salts may occur on the surfaces of any waste packages exposed to seepage from the emplacement drift crown. When the emplacement drift crown temperature cools to 100°C, the waste package surface temperatures are approximately 5°C warmer, and the relative humidity may be significantly less than 100%. For waste package relative humidity less than that at which chloride minerals precipitate, evaporation may cause precipitation of halite, and the remaining nitrate-rich aqueous phase can migrate, leaving behind the chloride-rich halite. When relative humidity subsequently increases above that at which salt separation occurred, this halite can deliquesce to form a chloride-rich brine with little or no nitrate. This salt separation effect is included to represent potential effects of transport processes on fluid compositions in the drift (SNL 2007b, Section 6.13.6). Section 2.3.5.5.4.3 provides a description of how salt separation is implemented in the TSPA.

Maximum Relative Humidity Constraint on Invert Pore-Water Composition—In general, implementation of the seepage evaporation abstraction is similar both on the waste package and in the invert. However, there is one exception. The hydrologic properties of the invert and host rock allow relative humidity to approach unity (e.g., greater than 99.99%) during cool down, whereas constraints on the chemistry of aqueous solutions would require high degrees of dilution to achieve such high relative humidity. To prevent unrealistic over-dilution of the solution compositions in response to high relative humidity values generated by the multiscale thermal-hydrologic model (Section 2.3.5.4.1), an upper boundary for the relative humidity is calculated. The rationale for this boundary is: (1) the unsaturated zone contains limited water available for dilution, and (2) even the most dilute waters present in the repository near field will have some concentration of total dissolved solids due to dissolution of calcite and silica polymorphs in the invert, and due to

equilibrium with CO_2 in the gas phase; these components in solution will lower the water activity (i.e., equilibrium relative humidity) slightly from 100%. The relative humidity boundary is calculated as a function of temperature by assuming equilibrium with the in-drift pCO_2, calcite, and amorphous silica, and is provided to TSPA as a lookup table.

Condensation on the Drift Walls—Drift wall condensation occurs when the air becomes saturated and can no longer contain the amount of moisture within it (Section 2.3.5.4.2). The chemical composition of drift wall condensation is assumed to be the same as seepage (SNL 2007b, Table 6.15-1). Condensation that forms under the drip shield or on the waste package surface under an intact drip shield, is assumed to have benign composition with respect to waste package corrosion because it is dilute (Table 2.2-5, excluded FEP 2.1.08.14.0A, Condensation on underside of drip shield). Drift wall condensation that penetrates a failed drip shield and contacts the waste package surface, is conservatively assumed to have the same composition as seepage originating from the host rock (SNL 2007b, Section 6.15.2).

2.3.5.5.4.2.2 Seepage Evaporation Abstraction Support and Uncertainty

The seepage evaporation lookup tables at discrete temperature and pCO_2 values represent an abstraction of the continuous range of conditions that will occur in the drift. Support for the abstraction approach is provided by demonstrating that results derived by interpolation between lookup tables are within the stated model uncertainties for in-drift precipitates/salts model simulations at the actual temperature and pCO_2 conditions tested (SNL 2007b, Section 7.2.1).

For the evaporation/dilution lookup tables, the TSPA uses the relative humidity value in the table nearest to the value calculated by the multiscale thermal-hydrologic model. For interpolation of water compositional parameters with respect to pCO_2 and temperature values, it is useful to imagine a grid describing possible water composition parameters with lines for each of the pCO_2 (10^{-4}, 10^{-3}, and 10^{-2}) and temperature (100°C, 70°C, and 30°C) values. The grid has nine nodes associated with line intersections; each node is associated with a lookup table. The compositional parameters for any point inside the grid are determined by interpolating between the four nearest nodes (SNL 2007b, Section 7.2.1).

Using the Group 1 representative water with a median amount of feldspar added as an example, interpolated results are compared to explicitly calculated results at a temperature of 56°C, at 98% relative humidity, and with a pCO_2 of $10^{-3.2}$ bar. In the supporting comparison, values for pH, ionic strength, Cl^-, and NO_3^- were first interpolated with respect to pCO_2 at 40°C and 70°C, the two nearest temperatures in the set of lookup tables. Interpolation for $10^{-3.2}$ bar of pCO_2 is accomplished by linearly interpolating between the logarithms of 10^{-4} bar and 10^{-3} bar. The interpolated parameter values are then plotted (Figure 2.3.5-64) at 40°C and 70°C and connected by a straight line to determine the final interpolated value at 56°C and $10^{-3.2}$ bar of pCO_2 (SNL 2007b, Section 7.2.1).

Results from the in-drift precipitates/salts model, when compared to the interpolation results, indicate that the interpolated values fall within the model uncertainty and are almost identical to the actual model results. This similarity of model results and interpolation results indicates that the interpolation method is a well-supported means of implementing the lookup table results (SNL 2007b, Section 7.2.1).

For the independent variable pCO_2, limited linear extrapolation of the dependent variables—ionic strength, Cl^- concentration, NO_3^- concentration, and pH—is supported within the modeling uncertainty (SNL 2007b, Section 7.2.2). The most significant effect on pH is about 0.08 pH units at $pCO_2 = 2 \times 10^{-2}$ bar, which is the highest pCO_2 found in the lookup tables (SNL 2007b, Section 6.7.2).

Uncertainty introduced through the use of the in-drift precipitates/salts model is described in Section 2.3.5.5.3.3 and summarized for key parameters in Table 2.3.5-12. This uncertainty is propagated to TSPA as described in the following section.

2.3.5.5.4.3 TSPA Implementation of the Seepage Evaporation Abstraction

The near-field chemistry model provides the CO_2 partial pressures (Section 2.3.5.3.4) needed to implement the seepage evaporation abstraction. The seepage evaporation abstraction provides the information used by the TSPA chemical environment submodel to determine the composition of water on the waste package surfaces and in the invert (SNL 2007b, Section 6.3.3). The solution composition parameters selected to represent the corrosion environment for the waste package surfaces and for radionuclide transport in the invert in the TSPA are pH, ionic strength, Cl^- concentration, NO_3^- concentration, and the NO_3^-/Cl^- ratio (SNL 2007b, Section 1.1). Implementation of the seepage evaporation abstraction within the TSPA chemical environment submodel is the same for the nominal, early waste package or drip shield failure, and seismic scenario classes and is described below.

A general rule that applies to the seepage scenario discussed in the following subsection is that once a starting water is selected (i.e., Gp1, Gp2, Gp3, Gp4), and a water–rock interaction parameter identified that include the, these two values must be used within TSPA to identify and select both the lookup tables required to calculate the range of pCO_2 gas (partial pressure of carbon dioxide) and the appropriate seepage dilution/evaporation lookup table. These lookup tables must be selected using the same starting water and water–rock interaction parameter value.

The appropriate water–rock interaction parameter value is selected from the water–rock interaction parameter lookup table, output of the near-field chemistry model, by TSPA (Section 2.3.5.3). The water–rock interaction parameter values are tabulated as a function of the thermal measure (a location-specific measure of the thermal history, generated by summing the time when drift wall drops below boiling in years and the maximum drift wall temperature in degrees Celsius), the percolation flux, and time.

Determining Seepage Compositions—TSPA implements the lookup tables for chemistry on the waste package surface when seepage is directly dripping onto the drip shields and waste packages. Two parameters are used to select both the lookup tables used by TSPA to calculate the range of appropriate pCO_2 values and the set of diluted/evaporated water chemistry lookup tables. These are the starting water type and the water–rock interaction parameter. For each TSPA realization, the starting water (Gp1, Gp2, Gp3, Gp4) is randomly selected. All four of these waters have an equal probability of selection (25%) for any given realization. The water–rock interaction parameter value is determined at each time step as described in Section 2.3.5.3.4, using parameters such as temperature and relative humidity available from the multiscale thermal-hydrologic model for waste package locations within the drift.

In addition to the starting water, a second parameter, ΔpCO_2, is also determined at the beginning of each TSPA realization (SNL 2008b, Section 6.3.4.2). This parameter is sampled uniformly between -1 and 1. The near-field chemistry process model provides a range of possible pCO_2 values, from a maximum to a minimum, which asymmetrically encompass the ambient value of 10^{-3} bars. The ΔpCO_2 value represents the relative offset from the ambient value within that range. If the offset is positive, then it is carried through time as a constant fraction of the difference between the predicted maximum pCO_2 value at each time step and the ambient value. This preserves the pCO_2 trend (i.e., the offset curve will track similarly to the maximum pCO_2 trend). Similarly, if the ΔpCO_2 is negative, then the offset is propagated through time as a constant fraction of the difference between the predicted minimum pCO_2 value at each time step and the ambient value, in order to preserve the pCO_2 behavior over time. The ΔpCO_2 is treated as a stochastic (epistemic) uncertainty and sampled only once per realization.

The starting water identity and water–rock interaction parameter value are used to select the lookup tables used to calculate the possible pCO_2 range within the drift. The maximum pCO_2 is the partial pressure of CO_2 in equilibrium with predicted seepage compositions obtained from the near-field chemistry model. These values are provided to the TSPA in lookup tables for each starting water (Section 2.3.5.3.4). The minimum pCO_2 in the drift is calculated from the vapor pressure of water in the drift assuming that the gas phase in the rock is at ambient pCO_2 (10^{-3} bars), and that this gas phase diffuses into the drift and is diluted by water vapor released by boiling or evaporation of water at the evaporation front. The CO_2 released as the water evaporates is also summed in. It is calculated from the total carbon in the seepage water, which is provided to TSPA in lookup tables for each starting water, as a function of the water–rock interaction parameter value and the temperature of the evaporation front (Section 2.3.5.3.4). Once the possible pCO_2 range has been determined, the actual value is selected by applying the offset, ΔpCO_2, to that range. In addition to the starting water, the water–rock interaction parameter value, and the pCO_2, the final parameter required to select the relevant seepage dilution/evaporation lookup tables is the temperature at the waste package surface, which is derived from the multiscale thermal-hydrologic model.

The relative humidity at the waste package surface is used to access the appropriate row of the combined dilution/evaporation lookup tables to retrieve the chemical parameters of interest (pH, ionic strength, $[Cl^-]$, $[NO_3^-]$). The TSPA uses the total molal chlorine, [Cl], and total molal nitrogen, [N], to represent chloride and nitrate. This is consistent with the use of these parameters in the process model for evaluating corrosion of the outer barrier of the waste package.

The independent variable in the lookup tables is relative humidity. To select the appropriate chemistry from a selected lookup table, TSPA interpolates between rows representing relative humidities that bound the waste package surface relative humidity. When selecting chemical parameters that fall between lookup tables, the parameters are estimated using linear interpolation on temperature and on the water–rock interaction parameter value, and log linear interpolation for pCO_2 (SNL 2008b, Section 6.3.4.3.1). Chemistry values are extrapolated linearly on log (pCO_2) for pH, ionic strength, Cl^-, and NO_3^- in those rare cases when the pCO_2 exceeds the range of 10^{-4} to 10^{-2} bars; sensitivity analyses have established that this yields an acceptable result for the observed range of pCO_2 values, which vary from approximately 10^{-5} to 2×10^{-2} bars. For temperatures above 100°C and below 30°C, extrapolation is not performed; instead, the lookup table values at 100°C or 30°C are used, respectively.

Maximum Relative Humidity Constraint on Invert Pore-Water Composition—For all invert conditions, the relative humidity from the multiscale thermal-hydrologic model is compared to the relative humidity boundary corresponding to the local temperature and pCO_2. As with seepage compositions, TSPA uses linear interpolation on temperature and then on log pCO_2 to calculate the relative humidity boundary associated with the local conditions. If the relative humidity boundary value is smaller than the extant relative humidity, then relative humidity boundary value is used to enter the seepage evaporation lookup tables; otherwise, the extant value from the multiscale thermal-hydrologic model is used (SNL 2007b, Section 6.15.2)

Implementation at or Below the Lowest Relative Humidity Point Provided in the Lookup Table—Although the in-drift precipitates/salts model predicts dryout conditions for simple, single-salt systems, deliquescence relative humidity data are sparse for more complex salt systems. Also, in experimental studies using the three- and four-salt assemblages anticipated to form by seepage evaporation, dryout was not observed up to 190°C (SNL 2007j, Section 6.1.2.2). For these reasons, once seepage onto a waste package is predicted to occur, aqueous conditions are assumed to be present regardless of relative humidity (SNL 2007b, Section 6.15.1.2).

Applying Uncertainty to the Compositional Parameters—Once the compositional parameters are determined for water on the waste packages and in the invert, the TSPA accounts for uncertainty in the in-drift precipitates/salts model (Section 2.3.5.5.3.3), and then the uncertainty in chloride-nitrate associated with use of a single pore water to represent each of the compositionally distinct pore-water groups. For each parameter used by TSPA (pH, log ionic strength, log Cl^-, and log of the Cl^-/NO_3^- ratio) the uncertainties are incorporated in the following manner:

In-drift precipitates/salts model uncertainties for individual seepage water chemical parameters ($[Cl^-]$, $[NO_3^-]$, Cl^-/NO_3^- ratio, ionic strength, and pH) are applied by first selecting the nominal value for the parameter from the seepage evaporation lookup tables and then sampling within the uncertainty range predicted for that parameter. The in-drift precipitates/salts model uncertainties are implemented as triangular distributions. The in-drift precipitates/salts model uncertainties in NO_3^-, Cl^-, and the NO_3^-/Cl^- ratio are modified to incorporate the additional variability observed within each of the four pore-water groups, and in-drift precipitates/salts uncertainties in pH are reduced for the predicted seepage compositions, as described below.

Because of the importance of NO_3^- and Cl^- concentrations and the NO_3^-/Cl^- ratio in evaluating the occurrence of localized corrosion, the variability in these values that is observed in each of the four pore-water groups is propagated as an uncertainty through the seepage evaporation abstraction. This is accomplished after NO_3^- and Cl^- values are interpolated from the seepage evaporation lookup tables, which are based on the representative water for each group. A NO_3^-/Cl^- ratio value is selected from a discrete distribution of the values for the relevant pore-water group (Section 2.3.5.3.2.2.1). The summed ($NO_3^- + Cl^-$) value is then partitioned back into NO_3^- and Cl^- concentrations, in accordance with the selected ratio. The NO_3^-/Cl^- ratio can be modified *a postieri* because chloride and nitrate are chemically similar in solution (e.g., nonreactive), and the actual ratio of chloride to nitrate has almost no effect on other solution components. However, it can only be applied at relative humidity values higher than the value at which chloride/nitrate salt precipitation occurs. At lower values, the NO_3^- and Cl^- concentrations, and the NO_3^-/Cl^- ratio are sampled from the seepage evaporation lookup tables, and the in-drift precipitates/salts uncertainties in these parameters are applied directly (SNL 2007b, Section 6.12.3) to the TSPA values.

Once a nominal pH value has been extracted from the seepage abstraction lookup tables, uncertainty is applied to it. If the relative humidity is above the relative humidity at which salt separation occurs, then the uncertainty in pH is determined by sampling the discrete distribution of values from the model-data comparison described in Section 2.3.5.5.3.3.2 and shown in Figure 2.3.5-62. Because these data are based on experimental systems in which highly soluble chloride and nitrate salts have not precipitated, this discrete distribution is only used for relative humidity conditions above the halite divide; for more concentrated solutions, the in-drift precipitates/salts uncertainties of ±1 to 2 pH units (as a function of relative humidity) are used.

Determining Whether to Implement Salt Separation—The TSPA implements the salt separation effect (Section 2.3.5.5.1) only if (1) the local relative humidity at the waste package surface is below the predicted relative humidity of chloride or nitrate salt precipitation for the relevant lookup table and (2) seepage occurs and is not diverted by the drip shield. When salt separation is implemented, the TSPA flags the affected waste package, and when the relative humidity at that location increases above the value at which salt separation occurred, a chloride-rich brine is assumed to have formed, and localized corrosion on the waste package is initiated (SNL 2007b, Section 6.15.1.3; SNL 2008b, Section 6.3.5.2.2).

Incorporating Condensation on the Drift Walls—When the drift wall relative humidity is high enough to cause condensation on the drift wall to occur (Section 2.3.5.4.2), TSPA uses seepage evaporation abstraction lookup tables to calculate the composition of the water used to represent the condensate fluid chemistry, whether or not seepage occurs at the same location (SNL 2007b, Table 6.15-1). The chemical composition of drift wall condensation is assumed to be the same as seepage because the evaporative evolution of the aqueous solution is controlled by the relative humidity; the same solution composition will be predicted by the seepage evaporation abstraction, regardless of whether the initial solution is seepage or condensation plus some small component of seepage. The condensation serves merely to dilute the initial aqueous solution. Condensation that occurs under the drip shield or on the waste package under an intact drip shield is expected to have benign composition with respect to waste package corrosion (Table 2.2-5, excluded FEP 2.1.08.14.0A, Condensation on underside of drip shield). Drift wall condensation that penetrates a failed drip shield and contacts the waste package surface, is conservatively assumed to have the same composition as seepage originating from the host rock (SNL 2007b, Section 6.15.2).

Passing Compositional Parameters from the TSPA Chemical Environment Submodel—The information flow to and from the TSPA chemical environment submodel is illustrated in Figures 2.3.5-3 and 2.3.5-1. The TSPA chemical environment submodel provides the compositional parameters described above to the following:

- The localized corrosion initiation analysis (Section 2.3.6.4.3.1). This analysis uses the compositional parameters for water on waste package surfaces to generate localized corrosion initiation histories that are used by the TSPA waste package and drip shield degradation model component (Section 2.4.1).

- The TSPA waste form degradation and mobilization submodel (Section 2.4.1). This TSPA submodel uses the compositional parameters for water in the invert generated by the in-drift seepage evaporation abstraction in the case of diffusive releases from the

waste package (SNL 2007b, Section 6.15.2.1). In the case of advective flow through the waste package, the in-package chemistry model (Section 2.3.7) supplies the composition of water in the invert.

2.3.5.6 Conclusions

The models developed in Section 2.3.5 are used to represent the physical and chemical features and processes in the repository emplacement drifts and the manner in which the features of the EBS work together to complement the natural barriers. As described in Section 2.1, the EBS features prevent or substantially reduce the release of radionuclides from the waste and prevent or substantially reduce the rate of movement of radionuclides from the repository to the accessible environment. Integration of results from models for thermal, hydrologic, and chemical processes in the emplacement drifts shows that the occurrence of potentially aggressive conditions on the waste package and drip shield is limited, both in duration and in predicted frequency of occurrence.

Features and processes that comprise the unsaturated zone component of the Upper Natural Barrier impact the chemical and physical environment that develops in the repository drifts. Some of the key included processes that affect the emplacement drift environment in this way are evaluated in Section 2.3.5:

- **Heat Generation in the EBS**—Heat produced from radioactive decay affects the thermal-hydrologic-mechanical-chemical environment in the emplacement drifts. Models described in Section 2.3.5 represent thermal-hydrologic effects on in-drift temperature, humidity, and condensation; thermal-hydrologic-chemical effects on seepage; and evaporative evolution of water in the in-drift chemical environment. These processes affect the quantity and chemistry of water that may be mobilized due to heat generated by the emplaced waste, and may enter the emplacement drifts and contact the drip shields, waste packages, and waste forms.

- **Geosphere Dryout Due to Waste Heat (EBS and Host Rock)**—Heat from radioactive decay produces dryout in the geosphere around the emplacement drifts. Although this process is transient, it is important when the drift wall temperatures exceed the boiling point of water. Boiling and transport of water vapor to cooler regions within the host rock redistributes moisture and limits the water available to enter the repository. Coupled processes involved in geosphere dryout are described in Section 2.3.5.2. Diversion of unsaturated flow in the host rock during the dryout period is described in Section 2.3.3.3.

- **Thermal Effects on Flow in the EBS**—Thermal effects on hydrologic processes are included in models of in-drift thermal hydrology in Section 2.3.5.4, and seepage models in Section 2.3.3. These models determine the amount and distribution of moisture (both liquid and vapor) in the drift and on waste packages. The rates of diffusion and advection predicted to occur through the EBS are determined by the thermal-hydrologic and seepage conditions in the emplacement drift.

Within the emplacement drift feature of the EBS, a number of key processes are associated with characteristics that are important to barrier capability. These include heat generation in the EBS,

discussed above. In addition, the following key processes, related to the in-drift physical and chemical environment and important to barrier capability, are evaluated in Section 2.3.5:

- **Chemistry of Water Flowing into the Drift**—The chemistry of seepage water is evaluated in the near-field chemistry model described in Section 2.3.5.3. The chemistry of the water in the emplacement drift determines the potential for localized corrosion of the waste package outer barrier and, in the event of waste package failure, can affect the chemical environment inside the waste package and control the stability of radionuclide-bearing colloids and radionuclide solubility in the invert.

- **Chemical Characteristics of Water in Drifts**—The chemical characteristics of water in the drift are affected by seepage, condensation, capillary flow from the host rock, evaporation, and other thermal-chemical processes in the drift that are functions of the thermal-hydrologic environment. Models for evaluating the evolution of the in-drift chemical environment, representing effects of these processes, are presented in Section 2.3.5.5.

- **Unsaturated Flow in the EBS**—Unsaturated flow occurs in the emplacement drift due to seepage or condensation processes. The nature of this flow has been included in the abstractions for flow and transport through the EBS features. Unsaturated flow limits advective transport of radionuclides and other chemical species (for example under intact drip shields), facilitates isolation of water from the waste packages and waste forms, and is therefore important to barrier capability.

- **Thermal Effects on Chemistry and Microbial Activity in the EBS**—The in-drift temperature substantially affects the evolution of in-drift chemistry and is important to the capability of the engineered barrier. The effect of temperature on microbial activity in the drift does not significantly impact barrier capability because microbial activity will be limited by environmental factors. The potential for microbially influenced corrosion of the waste package outer barrier is included, although it does not significantly impact barrier capability.

- **Localized Corrosion on Waste Package Outer Surface Due to Deliquescence**—Although deliquescence of salts on the waste package surface is expected to occur, this process has been excluded from TSPA (Section 2.2.1) because the effects of such deliquescence have been determined to be insignificant to performance (Section 2.3.5.5.1). The physical-chemical characteristics of brines produced through deliquescence of minerals in deposited dusts are not expected to initiate localized corrosion or support significant propagation for Alloy 22 waste packages. In addition, at elevated temperatures (greater than 120°C), only small quantities of brine will form from the available dust, and brine volume will limit the extent of localized corrosion damage should it initiate.

Evolution of the in-drift physical and chemical environment will take place in three stages: dryout, transition, and low-temperature (Section 2.3.5.4). Dryout begins during preclosure and continues during the period when host-rock temperatures are above the boiling point of water. For most of the waste packages, dryout will remove the water in a zone of up to 5 to 10 m around the emplacement

drift openings, and no seepage will occur. The transition stage occurs as the host-rock temperatures cool to below 100°C, waste package surface temperatures are near 100°C, and localized corrosion is possible under certain conditions. Seepage will not resume until rewetting of the rock occurs. The final low-temperature stage is when the rock temperature and the temperature on the waste package surface are well below 100°C, reducing the potential for localized corrosion (Section 2.3.6). Capillary diversion remains effective and relative humidity within the drift increases to approximately 70% or greater, with many waste package locations approaching 100% relative humidity. Condensation may occur on the emplacement drift walls. Increasingly dilute and benign conditions develop on the waste package and drip shield surfaces as humidity increases and temperature decreases.

Evolution of water and gas compositions in the near-field host rock due to coupled thermal, hydrologic, and chemical processes influences the composition of potential seepage water and the associated gas-phase composition in the emplacement drifts. Thermal-hydrologic-chemical seepage model results (Section 2.3.5.2.3) show that during the transition stage (described above) when rewetting of the near-field host rock occurs, concentrations of some dissolved species increase temporarily, but liquid saturations are too low for flow to occur. After the drift crown temperature decreases to be below the boiling point of water, potential seepage waters are relatively dilute. The gas-phase carbon dioxide concentration decreases during the boiling period because of dilution by water vapor and then increases during the cooling phase as carbonate precipitates are redissolved. Evolution of seepage chemistry after the drift wall temperature cools to below 100°C, and the corresponding carbon dioxide pressure, are represented for TSPA by the near-field chemistry model (Section 2.3.5.3).

The multiscale thermal-hydrologic model predicts above-boiling conditions in the host rock for up to approximately 1,345 years. Peak waste package temperatures are predicted to be approximately 107°C to 211°C depending on waste package thermal output and location within the repository. Thermally driven natural convection and condensation will cause axial and radial convection cells to develop in the emplacement drifts. Water vapor transport from hotter to cooler parts of the drifts will cause condensation to occur. Condensation is shown to be correlated with waste packages having lower heat output, and with high percolation flux in the host rock, which promotes lower temperatures.

The chemistry of seepage water is modified by evaporation (Section 2.3.5.5), as represented by the in-drift precipitates/salts model. Conditions for evaporation are determined by the temperature and relative humidity calculated by the multiscale thermal-hydrologic model (Section 2.3.5.4.1). The in-drift precipitates/salts model is also applied to represent the chemistry of invert pore-water and drift-wall condensation.

The anticipated range of repository thermal loading has been evaluated using operational simulation of waste handling, aging, and emplacement. The hydrogeologic, geomechanical, and geochemical responses to this range have been evaluated, and for the nominal scenario class (which includes uncollapsed drifts), the TSPA modeling basis is directly applicable to assessing dose consequences for the anticipated range of thermal loading, and FEP screening is unaffected (Section 2.2.1). For seismically-induced drift collapse, a number of FEPs are thermally sensitive, but the likelihood for the peak temperature of any waste package to exceed 300°C is insignificant, considering the probability of a seismic event sufficient to cause drift collapse during the 90 years immediately after

repository closure (SNL 2008c, Section 6.5.1). These results demonstrate the feasibility of the postclosure aspects of the thermal management strategy described in Section 1.3.1.2.5.

Uncertainties Associated with In-Drift Physical and Chemical Environment Models and Analyses—Uncertainties in input parameters, numerical methods, and approximations used in developing these models were evaluated. Key uncertainties are propagated through the model using several methods: (1) by using ranges of percolation flux and host rock thermal conductivity for calculating in-drift temperature and humidity in the multiscale thermal-hydrologic model; (2) by using four starting waters to represent possible pore-water compositions in the near-field chemistry model; (3) by sampling an uncertainty range for the water–rock interaction parameter in the near-field chemistry model, which includes uncertainties associated with the feldspar dissolution rate, and the water–rock ratio; (4) by propagating the observed uncertain range of the nitrate-chloride ratio for pore waters; (5) by using an uncertainty distribution to describe the in-drift carbon dioxide pressure; and (6) by applying the model uncertainty characterization developed for the in-drift precipitates/salts model. The effects from uncertainty in percolation flux and rock thermal properties on model results are evaluated explicitly in the near-field chemistry model, and uncertainties in these values are implemented by the TSPA, by sampling a range of values (Section 2.3.5.3.3.4).

Sensitivity studies show that input parameter uncertainty for the multiscale thermal-hydrologic model is dominated by uncertainty in the host rock thermal conductivity and percolation flux. Uncertainties in these parameters are propagated to the TSPA through the use of seven modeling cases using parameter combinations that span the expected ranges of values. Input parameter uncertainty for the in-drift condensation model is incorporated in the TSPA through four modeling cases implementing different dispersion coefficient values and drift shield ventilation conditions. In addition, calculated uncertainties in the associated condensation rates are propagated to the TSPA.

Uncertainty related to the composition of seepage water is propagated to TSPA using the near-field chemistry model. Model development includes justification for selection of four pore waters representing the range of observed compositions from the host rock. The range of variability in the nitrate-chloride ratio from an extended set of observed pore water compositions is propagated to TSPA. The near-field chemistry model also provides uncertainty distributions for key parameters describing water–rock interaction, including host rock percolation flux and thermal conductivity, and the in-drift carbon dioxide pressure.

Uncertainty related to the in-drift precipitates/salts model was evaluated through sensitivity analyses and through comparison of model results with site-specific data from independent laboratory experiments, natural analogues, and compilations of salt solubility measurements (Section 2.3.5.5.3). The maximum differences in the model–data comparisons are the basis for the model uncertainty ranges propagated to the TSPA. Section 2.3.5.5.4 discussed how TSPA implements uncertainty to modify the compositional parameters determined with the seepage evaporation abstraction lookup tables.

Conservatisms in the In-Drift Physical and Chemical Environment Models and Analyses—Although a number of conservatisms exist in the models and analyses described in Section 2.3.5, only those with the potential to influence TSPA results are noted. In some cases, the conservatism

is related to the manner in which the model or model results are incorporated into the TSPA. The following paragraphs discuss the model-specific conservatisms.

- **Multiscale Thermal-Hydrologic Model**—Heat loss at the repository edges through convection is not included and results in less movement of water vapor into the host rock and away from the emplacement drifts. Earlier rise in relative humidity and higher relative humidity values are predicted than if convective heat loss were included.

- **In-Drift Condensation Model**—The TSPA approach to implementing this model uses zero as the lower bound on condensation rates, and the upper value is determined by the sampled uncertainty. This simplification slightly over-estimates condensation rates in the TSPA abstraction, which impacts the transport of radionuclides from the waste package to the host rock.

- **In-Drift Chemical Environment Models and Analyses**—Seepage waters on the waste package surface are assumed to reach equilibrium with the relative humidity on the surface of the waste package. Under most conditions, the waste package surface is hotter than its surroundings, resulting in a lower relative humidity, and the prediction that seepage will evaporate and concentrate on the waste package surface. This prediction is conservative because evaporation will result in a higher predicted chloride concentration, resulting in a less benign water composition with respect to localized corrosion.

Summary of Consistency between TSPA Abstractions and Process Models—The multiscale thermal-hydrologic model does not consider the process of axial flow of water vapor along the emplacement drifts. The in-drift condensation model includes this process. However, this difference has been evaluated using three-dimensional process modeling and shown to have a small effect on the primary model predictions of temperature and relative humidity, with the major effect being that the multiscale thermal-hydrologic model generates slightly higher temperatures and hastens the return of humidity to the emplacement drifts (Section 2.3.5.4).

The near-field chemistry model (Section 2.3.5.3) incorporates a range of host rock thermal conductivity values and percolation flux conditions as uncertain inputs, thus conforming with the treatment of these uncertainties in the multiscale thermal-hydrologic model (Section 2.3.5.4.1).

Summary of Key Input Parameters Provided to TSPA—The key inputs to TSPA from the multiscale thermal-hydrologic model are the following:

- Temperature and relative humidity in the emplacement drift and the host rock, grouped into five repository subregions based on the percolation flux at the base of the PTn for five different waste package types and all waste package locations

- Representative commercial SNF waste packages and representative codisposal (HLW and DOE SNF) waste package, and for each packages, histories of:

  – Temperature and relative humidity
  – Average drift wall temperature
  – Average invert temperature

– Average invert saturation
– Average invert flux.

The key inputs to TSPA from the in-drift condensation model are the following:

- Occurrence and magnitude of drift wall condensation at waste package locations for seven representative emplacement drifts for two dispersion coefficients, two drip shield ventilation conditions, and for time periods when drift wall condensation is predicted to occur.

The key inputs to TSPA from the near-field chemistry model are the following:

- The composition of potential seepage waters at the drift wall, as a function of the drift wall temperature and degree of water–rock interaction, which is in turn a function of the percolation flux and thermal history at the location of interest

- The range of carbon dioxide pressures within the drift, as a function of the degree of water–rock interaction and the drift wall temperature.

The key inputs to TSPA from the seepage evaporation abstraction are the following:

- Composition of seepage water, as affected by percolation flux and thermal evolution of the host rock

- Composition of seepage and drift wall condensation on the waste package surface, after drip shield failure, due to evaporative equilibrium with in-drift conditions

- Water compositions in the invert.

This section has described the coupled processes that could affect the in-drift physical and chemical environment, including insights gained from fully coupled simulations of thermal-hydrologic-mechanical and thermal-hydrologic-chemical processes. Appropriate abstractions of these processes, including thermal-hydrology and condensation, seepage chemistry, and evaporative evolution, are developed to represent the environment in TSPA. Key uncertainties are identified and propagated into the abstractions. Conservatisms in the modeling framework are also identified. The resulting description is appropriate, in its level of detail and technical support, for representing the in-drift physical and chemical environment in TSPA.

2.3.5.7 General References

Alai, M.; Sutton, M.; and Carroll, S. 2005. “Evaporative Evolution of a $Na–Cl–NO_3–K–Ca–SO_4–Mg–Si$ Brine at 95°C: Experiments and Modeling Relevant to Yucca Mountain, Nevada.” *Geochemical Transactions, 6* (2), 31–45. Melville, New York: American Institute of Physics. TIC: 258272.

Altman, W.D.; Donnelly, J.P.; and Kennedy, J.E. 1988. *Qualification of Existing Data for High-Level Nuclear Waste Repositories: Generic Technical Position.* NUREG-1298. Washington, D.C.: U.S. Nuclear Regulatory Commission. TIC: 200652.

Bish, D.L. and Vaniman, D.T. 1985. *Mineralogic Summary of Yucca Mountain, Nevada.* LA-10543-MS. Los Alamos, New Mexico: Los Alamos National Laboratory. ACC: MOL.19950412.0041.

Bish, D.L.; Vaniman, D.T.; Chipera, S.J.; and Carey, J.W. 2003. "The Distribution of Zeolites and their Effects on the Performance of a Nuclear Waste Repository at Yucca Mountain, Nevada, U.S.A." *American Mineralogist, 88* (11-12, Part 2), 1889–1902. Washington, D.C.: Mineralogical Society of America. TIC: 255986.

BSC (Bechtel SAIC Company) 2004a. *Drift Scale THM Model.* MDL-NBS-HS-000017 REV 01. Las Vegas, Nevada: Bechtel SAIC Company. ACC: DOC.20041012.0001.

BSC 2004b. *Heat Capacity Analysis Report.* ANL-NBS-GS-000013 REV 01. Las Vegas, Nevada: Bechtel SAIC Company. ACC: DOC.20041101.0003.

BSC 2004c. *Mineralogic Model (MM3.0) Report.* MDL-NBS-GS-000003 REV 01. Las Vegas, Nevada: Bechtel SAIC Company. ACC: DOC.20040908.0006.

BSC 2004d. *Geologic Framework Model (GFM2000).* MDL-NBS-GS-000002 REV 02. Las Vegas, Nevada: Bechtel SAIC Company. ACC: DOC.20040827.0008.

BSC 2004e. *Ventilation Model and Analysis Report.* ANL-EBS-MD-000030 REV 04. Las Vegas, Nevada: Bechtel SAIC Company. ACC: DOC.20041025.0002.

BSC 2004f. *Yucca Mountain Site Description.* TDR-CRW-GS-000001 REV 02 ICN 01. Two volumes. Las Vegas, Nevada: Bechtel SAIC Company. ACC: DOC.20040504.0008.

BSC 2004g. *Drift Degradation Analysis.* ANL-EBS-MD-000027 REV 03. Las Vegas, Nevada: Bechtel SAIC Company. ACC: DOC.20040915.0010.

BSC 2005a. *Mountain-Scale Coupled Processes (TH/THC/THM) Models.* MDL-NBS-HS-000007 REV 03. Las Vegas, Nevada: Bechtel SAIC Company. ACC: DOC.20050825.0007.

BSC 2005b. *Drift-Scale Coupled Processes (DST and TH Seepage) Models.* MDL-NBS-HS-000015 REV 02. Las Vegas, Nevada: Bechtel SAIC Company. ACC: DOC.20050114.0004.

Buscheck, T.A. and Nitao, J.J. 1994. *The Impact of Buoyant, Gas-Phase Flow and Heterogeneity on Thermo-Hydrological Behavior at Yucca Mountain.* UCRL-JC-115351. Livermore, California: Lawrence Livermore National Laboratory. ACC: NNA.19940524.0012.

Carnahan, C.L. 1987. *Effects of Coupled Thermal, Hydrological and Chemical Processes on Nuclide Transport.* LBL-23186. Berkeley, California: Lawrence Berkeley National Laboratory. TIC: 232514.

Carslaw, H.S. and Jaeger, J.C. 1959. *Conduction of Heat in Solids*. 2nd Edition. Oxford, Great Britain: Oxford University Press. TIC: 206085.

Chipera, S.J.; Vaniman, D.T.; Carlos, B.A.; and Bish, D.L. 1995. *Mineralogic Variation in Drill Core UE-25 UZ#16, Yucca Mountain, Nevada.* LA-12810-MS. Los Alamos, New Mexico: Los Alamos National Laboratory. ACC: NNA.19940427.0099.

CRWMS M&O (Civilian Radioactive Waste Management Systems Management and Operating Contractor) 1998. *Drift Scale Test As-Built Report*. BAB000000-01717-5700-00003 REV 01. Las Vegas, Nevada: CRWMS M&O. ACC: MOL.19990107.0223.

Dean, J.A. 1992. *Lange's Handbook of Chemistry.* 14th Edition. New York, New York: McGraw-Hill. TIC: 240690.

Dingemans, P. and Dijkgraaf, L.L. 1948. "The Vapour Pressure of Saturated Solutions of Sodium Nitrate in Water." *Recueil des Travaux Chimiques des Pays-Bas, 67,* 231-234. Leyden, The Netherlands: Société Chimique Neerlandaise. TIC: 255168.

DOE (U.S. Department of Energy) 2006. *Yucca Mountain Project Conceptual Design Report*. TDR-MGR-MD-000014, Rev. 05. Las Vegas, Nevada: U.S. Department of Energy, Office of Repository Development. ACC: ENG.20060505.0003.

Drever, J.I. 1997a. *The Geochemistry of Natural Waters, Surface and Groundwater Environments.* 3rd Edition. Upper Saddle River, New Jersey: Prentice Hall. TIC: 246732.

Drever, J.I. 1997b. "Evaporation and Saline Waters." Chapter 15 of *The Geochemistry of Natural Waters: Surface and Groundwater Environments.* 3rd Edition. Upper Saddle River, New Jersey: Prentice Hall. TIC: 246732.

Evans, N.J.; Wilson, N.S.F.; Cline, J.S.; McInnes, B.I.A.; and Byrne. J. 2005. "Fluorite (U-Th)/He Thermochronology: Constraints on the Low Temperature History of Yucca Mountain, Nevada." *Applied Geochemistry, 20,* 1099-1105. New York, New York: Elsevier. TIC: 259246.

Gascoyne, M.; Miller, N.H.; and Neymark, L.A. 2002. "Uranium-Series Disequilibrium in Tuffs from Yucca Mountain, Nevada, as Evidence of Pore-Fluid Flow Over the Last Million Years." *Applied Geochemistry*, *17* (6), 781–792. New York, New York: Elsevier. TIC: 251901.

Greenspan, L. 1977. "Humidity Fixed Points of Binary Saturated Aqueous Solutions." *Journal of Research of the National Bureau of Standards, 81A* (1), 89–96. Washington, D.C.: U.S. Department of Commerce. TIC: 241138.

Harr, M.E. 1987. *Reliability-Based Design in Civil Engineering*. New York, New York: McGraw-Hill. TIC: 240687.

Haukwa, C.; Wu, Y.S.; Hinds, J.J.; Zhang, W.; Ritcey, A.C.; Pan, L.H.; Simmons, A.M.; and Bodvarsson, G.S. 1998. *Results of Sensitivity Studies of Thermo-Hydrologic Behavior Conducted on Hydrologic Parameter Sets*. Milestone SP3CK5M4. Berkeley, California: Lawrence Berkeley National Laboratory. ACC: MOL.19980918.0001.

Helgeson, H.C.; Murphy, W.M.; and Aagaard, P. 1984. "Thermodynamic and Kinetic Constraints on Reaction Rates Among Minerals and Aqueous Solutions, II. Rate Constants, Effective Surface Area, and the Hydrolysis of Feldspar." *Geochimica et Cosmochimica Acta, 48,* 2405-2432. New York, New York: Pergamon Press. TIC:220177.

Johnson, T.M. and DePaolo, D.J. 1994. "Interpretation of Isotopic Data in Groundwater–Rock Systems: Model Development and Application to Sr Isotope Data from Yucca Mountain." *Water Resources Research, 30* (5), 1571-1587. Washington, D.C.: American Geophysical Union. TIC: 252320.

Kracek, F.C. 1928. "P-T-X Relations for Systems of Two or More Components and Containing Two or More Phases (L-V, L^{I}-L^{II}-V and S-L-V Systems)." *International Critical Tables of Numerical Data, Physics, Chemistry and Technology.* Washburn, E.W., ed. Volume III. New York, New York: McGraw-Hill. TIC: 243268.

Langmuir, D. 1997. *Aqueous Environmental Geochemistry.* Upper Saddle River, New Jersey: Prentice Hall. TIC: 237107.

Lasaga, A.C.; Soler, J.M.; Ganor, J.; Burch, T.E.; and Nagy, K.L. 1994. "Chemical Weathering Rate Laws and Global Geochemical Cycles." *Geochimica et Cosmochimica Acta, 58* (10), 2361–2386. New York, New York: Pergamon. TIC:237441.

Levy, S.S. and O'Neil, J.R. 1989. "Moderate-Temperature Zeolitic Alteration in a Cooling Pyroclastic Deposit." *Chemical Geology, 76* (3/4), 321–326. Amsterdam, The Netherlands: Elsevier. TIC: 237819.

Lide, D.R., ed. 2000. *CRC Handbook of Chemistry and Physics*. 81st Edition. Boca Raton, Florida: CRC Press. TIC: 253056.

Manteufel, R.D.; Ahola, M.P.; Turner, D.R.; and Chowdhury, A.H. 1993. *A Literature Review of Coupled Thermal-Hydrologic-Mechanical-Chemical Processes Pertinent to the Proposed High-Level Nuclear Waste Repository at Yucca Mountain.* NUREG/CR-6021. Washington, D.C.: U.S. Nuclear Regulatory Commission. TIC: 207771.

Marshall, B.D. and Futa, K. 2001. "Strontium Isotope Evolution of Pore Water and Calcite in the Topopah Spring Tuff, Yucca Mountain, Nevada." "Back to the Future—Managing the Back End of the Nuclear Fuel Cycle to Create a More Secure Energy Future," *Proceedings of the 9th International High-Level Radioactive Waste Management Conference (IHLRWM), Las Vegas, Nevada, April 29-May 3, 2001.* La Grange Park, Illinois: American Nuclear Society. TIC: 247873.

McCaffrey, M.A.; Lazar, B.; and Holland, H.D. 1987. "The Evaporation Path of Seawater and the Coprecipitation of Br^- and K^+ with Halite." *Journal of Sedimentary Petrology, 57* (5), 928–937. Tulsa, Oklahoma: Society of Economic Paleontologists and Mineralogists. TIC: 254627.

Paces, J.B. and Neymark, L.A. 2004. "U-Series Evidence of Water–Rock Interaction at Yucca Mountain, Nevada, USA." *Water–Rock Interaction: Proceedings of the Eleventh International Symposium on Water–Rock Interaction.* Wanty, R.B. and Seal, R.R., II, eds. 475–479. New York, Leiden, The Netherlands: Balkema Publishers. TIC: 257516.

Paces, J.B.; Neymark, L.A.; Marshall, B.D.; Whelan, J.F.; and Peterman, Z.E. 2001. *Ages and Origins of Calcite and Opal in the Exploratory Studies Facility Tunnel, Yucca Mountain, Nevada.* Water-Resources Investigations Report 01-4049. Denver, Colorado: U.S. Geological Survey. TIC: 251284.

Palandri, J.L. and Reed, M.H. 2001. "Reconstruction of In Situ Composition of Sedimentary Formation Waters." *Geochimica et Cosmochimica Acta, 65* (11), 1741–1767. New York, New York: Pergamon. TIC:259444.

Peterman, Z.E. and Cloke, P.L. 2002. "Geochemistry of Rock Units at the Potential Repository Level, Yucca Mountain, Nevada." *Applied Geochemistry, 17* (6, 7), 683–698, 955–958 (errata). New York, New York: Pergamon. TIC: 252516; 252517; 254046.

Pruess, K.; Wang, J.S.Y.; and Tsang, Y.W. 1990. "On Thermohydrologic Conditions Near High-Level Nuclear Wastes Emplaced in Partially Saturated Fractured Tuff, 2. Effective Continuum Approximation." *Water Resources Research*, *26* (6), 1249–1261. Washington, D.C.: American Geophysical Union. TIC: 224854.

Rosenberg, N.D.; Knauss, K.G.; and Dibley, M.J. 1999a. *Evaporation of J13 Water: Laboratory Experiments and Geochemical Modeling.* UCRL-ID-134852. Livermore, California: Lawrence Livermore National Laboratory. TIC: 246322.

Rosenberg, N.D.; Knauss, K.G.; and Dibley, M.J. 1999b. *Evaporation of Topopah Spring Tuff Pore Water.* UCRL-ID-135765. Livermore, California: Lawrence Livermore National Laboratory. TIC: 246231

Sawyer, D.A.; Fleck, R.J.; Lanphere, M.A.; Warren, R.G.; Broxton, D.E.; and Hudson, M.R. 1994. "Episodic Caldera Volcanism in the Miocene Southwestern Nevada Volcanic Field: Revised Stratigraphic Framework, $^{40}Ar/^{39}Ar$ Geochronology, and Implications for Magmatism and Extension." *Geological Society of America Bulletin, 106* (10), 1304–1318. Boulder, Colorado: Geological Society of America. TIC: 222523.

SNL (Sandia National Laboratories) 2007a. *Initial Radionuclide Inventories.* ANL-WIS-MD-000020 REV 01 ADD 01. Las Vegas, Nevada: Sandia National Laboratories. ACC: DOC.20070801.0001.

SNL 2007b. *Engineered Barrier System: Physical and Chemical Environment.* ANL-EBS-MD-000033 REV 06. Las Vegas, Nevada: Sandia National Laboratories. ACC: DOC.20070907.0003.

SNL 2007c. *Drift-Scale THC Seepage Model.* MDL-NBS-HS-000001 REV 05. Las Vegas, Nevada: Sandia National Laboratories. ACC: DOC.20071010.0004.

SNL 2007d. *THC Sensitivity Study of Heterogeneous Permeability and Capillarity Effects.* ANL-NBS-HS-000047 REV 01. Las Vegas, Nevada: Sandia National Laboratories. ACC: DOC.20070807.0006.

SNL 2007e. *In-Drift Natural Convection and Condensation.* MDL-EBS-MD-000001 REV 00, ADD 01. Las Vegas, Nevada: Sandia National Laboratories. ACC: DOC.20070907.0004.

SNL 2007f. *General Corrosion and Localized Corrosion of Waste Package Outer Barrier.* ANL-EBS-MD-000003 REV 03. Las Vegas, Nevada: Sandia National Laboratories. ACC: DOC.20070730.0003.

SNL 2007g. *Thermal Testing Measurements Report.* TDR-MGR-HS-000002 REV 01. Las Vegas, Nevada: Sandia National Laboratories. ACC: DOC.20070307.0010.

SNL 2007h. *UZ Flow Models and Submodels*. MDL-NBS-HS-000006, REV 03 ADD 01. Las Vegas, Nevada: Sandia National Laboratories. ACC: DOC.20080108.0003.

SNL 2007i. *Seismic Consequence Abstraction.* MDL-WIS-PA-000003 REV 03. Las Vegas, Nevada: Sandia National Laboratories. ACC: DOC.20070928.0011.

SNL 2007j. *Analysis of Dust Deliquescence for FEP Screening.* ANL-EBS-MD-000074 REV 01 ADD 01. Las Vegas, Nevada: Sandia National Laboratories. ACC: DOC.20070911.0004.

SNL 2007k. *In-Drift Precipitates/Salts Model.* ANL-EBS-MD-000045 REV 03. Las Vegas, Nevada: Sandia National Laboratories. ACC: DOC.20070306.0037.

SNL 2007l. *Qualification of Thermodynamic Data for Geochemical Modeling of Mineral-Water Interactions in Dilute Systems.* ANL-WIS-GS-000003 REV 01. Las Vegas, Nevada: Sandia National Laboratories. ACC: DOC.20070619.0007.

SNL 2008a. *Multiscale Thermohydrologic Model.* ANL-EBS-MD-000049 REV 03 ADD 02. Las Vegas, Nevada: Sandia National Laboratories. ACC: DOC.20080201.0003.

SNL 2008b. *Total System Performance Assessment Model /Analysis for the License Application.* MDL-WIS-PA-000005 REV 00 ADD 01. Las Vegas, Nevada: Sandia National Laboratories. ACC: DOC.20080312.0001.

SNL 2008c. *Postclosure Analysis of the Range of Design Thermal Loadings.* ANL-NBS-HS-000057 REV 00. Las Vegas, Nevada: Sandia National Laboratories. ACC: DOC.20080121.0002.

Stefansson, A. and Arnorsson, S. 2000. "Feldspar Saturation State in Natural Waters." *Geochimica et Cosmochimica Acta, 64* (15), 2567-2584. New York, New York: Elsevier. TIC: 249336.

Stumm, W. and Morgan, J.J. 1996. *Aquatic Chemistry, Chemical Equilibria and Rates in Natural Waters.* 3rd Edition. New York, New York: John Wiley & Sons. TIC: 246296.

Thorstenson, D.C.; Weeks, E.P.; Haas, H.; and Woodward, J.C. 1990. "Physical and Chemical Characteristics of Topographically Affected Airflow in an Open Borehole at Yucca Mountain, Nevada." *Proceedings of the Topical Meeting on Nuclear Waste Isolation in the Unsaturated Zone, Focus '89, September 17-21, 1989, Las Vegas, Nevada.* Pages 256–270. La Grange Park, Illinois: American Nuclear Society. TIC: 212738.

Vaniman, D.T.; Bish, D.L.; Chipera, S.J.; Carlos, B.A.; and Guthrie, G.D., Jr. 1996. *Chemistry and Mineralogy of the Transport Environment at Yucca Mountain.* Volume I of *Summary and Synthesis Report on Mineralogy and Petrology Studies for the Yucca Mountain Site Characterization Project.* Milestone 3665. Los Alamos, New Mexico: Los Alamos National Laboratory. ACC: MOL.19961230.0037.

Vaniman, D.T.; Chipera, S.J.; Bish, D.L.; Carey, J.W.; and Levy, S.S. 2001. "Quantification of Unsaturated-Zone Alteration and Cation Exchange in Zeolitized Tuffs at Yucca Mountain, Nevada, USA." *Geochimica et Cosmochimica Acta, 65* (20), 3409–3433. New York, New York: Elsevier. TIC: 251574.

Weast, R.C. and Astle, M.J., eds. 1981. *CRC Handbook of Chemistry and Physics.* 62nd Edition. Boca Raton, Florida: CRC Press. TIC: 240722.

Whelan, J.F.; Neymark, L.A.; Moscati, R.J.; Marshall, B.D.; and Roedder, E. 2006. *Thermal History of the Unsaturated Zone at Yucca Mountain, Nevada, USA.* Denver, Colorado: U.S. Geological Survey. ACC: MOL.20070508.0200.

White, A.F. 1995. "Chemical Weathering Rates of Silicate Minerals in Soils." Chapter 9 of *Chemical Weathering Rates of Silicate Minerals.* White, A.F. and Brantley, S.L., eds. Reviews in Mineralogy Volume 31. Washington, D.C.: Mineralogical Society of America. TIC: 222496.

Wilson, N.S.F.; Cline, J.S.; and Amelin, Y.V. 2003. "Origin, Timing, and Temperature of Secondary Calcite-Silica Mineral Formation at Yucca Mountain, Nevada." *Geochimica et Cosmochimica Acta, 67* (6), 1145–1176. New York, New York: Pergamon. TIC: 254369.

Yang, I.C. 2002. "Percolation Flux and Transport Velocity in the Unsaturated Zone, Yucca Mountain, Nevada." *Applied Geochemistry, 17* (6), 807–817. New York, New York: Elsevier. TIC: 253605.

Yang, I.C.; Rattray, G.W.; and Yu, P. 1996. *Interpretation of Chemical and Isotopic Data from Boreholes in the Unsaturated Zone at Yucca Mountain, Nevada.* Water-Resources Investigations Report 96-4058. Denver, Colorado: U.S. Geological Survey. ACC: MOL.19980528.0216.

Table 2.3.5-1. Features, Events, and Processes Relevant to the Near-Field Chemistry Model and Included into TSPA

FEP Number and FEP Name	FEP Description	Summary of Technical Basis/Approach for FEP Inclusion
1.1.02.02.0A Preclosure ventilation	The duration of preclosure ventilation acts together with waste package spacing (as per design) to control the extent of the boiling front (zone of reduced water content).	Preclosure ventilation in drifts will remove much of the heat output from the waste packages. For the postclosure thermal reference case, the ventilation period following emplacement is 50 years, during which a large fraction of the heat energy supplied to the rock by the waste is removed from the drifts by ventilation. This heat removal effect is explicitly simulated with the thermal-hydrologic seepage model (Section 2.3.3.3) and the near-field chemistry model by using time-dependent boundary conditions for the thermal load. Initial rock drying in the drift vicinity as a result of evaporation effects due to ventilation is not explicitly addressed, which overestimates the quantity of water available for flow in the near-field host rock, early in the postclosure period.
1.3.01.00.0A Climate change	Climate change may affect the long-term performance of the repository. This includes the effects of long-term change in global climate (e.g., glacial/interglacial cycles) and shorter-term change in regional and local climate. Climate is typically characterized by temporal variations in precipitation and temperature.	Global climate change is addressed in TSPA using a climate analysis (Section 2.3.1) based on the record of climate changes in the past. This record is used to predict the expected changes in climate for the future. Climate modeling is incorporated into TSPA through the unsaturated zone flow fields (Section 2.3.2), which have different infiltration boundary conditions for future climates. These climates are referred to as present-day for 0 to 600 years, followed by monsoonal for the next 1,400 years, followed by glacial-transition from 2,000 to 10,000 years after closure. Finally, there is a 10,000 to 1-million-year period for which percolation conditions are defined, but no explicit climate is defined.
1.4.01.01.0A Climate modification increases recharge	Climate modification causes an increase in recharge in the Yucca Mountain region. Increased recharge might lead to increased flux through the repository, perched water, or water table rise.	The effects of climate change (Section 2.3.1) on unsaturated zone flux through the repository are incorporated through explicit simulations of future unsaturated zone flow fields (Section 2.3.2). These flow fields correspond to the nominal 10th, 30th, 50th, and 90th percentile infiltration cases for the present-day, monsoonal, and glacial-transition climates, and the 10,000 to 1 million year period. The flow fields are used directly by the TSPA and are also used to develop flux boundary conditions for other models including the near-field chemistry model (Section 2.3.5.3) and the multiscale thermal-hydrologic model (Section 2.3.5.4.1).

Table 2.3.5-1. Features, Events, and Processes Relevant to the Near-Field Chemistry Model and Included into TSPA (Continued)

FEP Number and FEP Name	FEP Description	Summary of Technical Basis/Approach for FEP Inclusion
2.1.11.01.0A Heat generation in EBS	Temperature in the waste and EBS will vary through time. Heat from radioactive decay will be the primary cause of temperature change, but other factors to be considered in determining the temperature history include the in situ geothermal gradient, thermal properties of the rock, EBS, and waste materials, hydrologic effects, and the possibility of exothermic reactions. Considerations of the heat generated by radioactive decay should take different properties of different waste types, including DOE SNF, into account.	The temperature history in the EBS is calculated by the multiscale thermal-hydrologic model (Section 2.3.5.4.1) and used by the TSPA. Consistent representation of heat generation is used in the thermal-hydrologic seepage model (Section 2.3.3.3), the near-field chemistry model (Section 2.3.5.3), and the in-drift condensation model (Section 2.3.5.4.2). The calculated temperatures are influenced not only by the heat of radionuclide decay, but also by the geothermal gradient from the ground surface to the water table and the thermal-physical properties of the rock and significant EBS features. The thermal effects from having different types of waste forms, including DOE SNF, is reflected in the multiscale thermal-hydrologic model output. Exothermic reactions (FEP 2.1.11.03.0A) produce insignificant amounts of heat and are not included in TSPA.
2.2.03.01.0A Stratigraphy	Stratigraphic information is necessary information for the performance assessment. This information should include identification of the relevant rock units, soils and alluvium, and their thickness, lateral extents, and relationships to each other. Major discontinuities should be identified.	Stratigraphy is included in the unsaturated zone flow model (Section 2.3.2) using grids developed with information from the geologic framework model. Because the assignment of unit hydrologic properties is associated with the grid used for the unsaturated zone flow model, the stratigraphy information is embedded in the TSPA through the output flow fields. In addition, other models use the flow fields, hydrologic properties, and other information from the unsaturated zone flow model. The near-field chemistry model (Section 2.3.5.3) uses a generalized stratigraphy for the model domain, with percolation flux conditions based on the unsaturated zone flow model flow fields.
2.2.03.02.0A Rock properties of host rock and other units	Physical properties such as porosity and permeability of the relevant rock units, soils, and alluvium are necessary for the performance assessment. Possible heterogeneities in these properties should be considered. Questions concerning events and processes that may cause these physical properties to change over time are considered in other FEPs.	Rock characteristics are defined for the stratigraphic units/layers classified in the geologic framework model, and further used to develop hydrologic properties for the unsaturated zone flow model layers (Section 2.3.2). Heterogeneity is modeled in terms of the sequence of hydrogeologic units and discrete faults. Therefore, rock properties are embedded in the TSPA through the output flow fields, with site-scale layering and faults explicitly taken into account. Intermediate-scale heterogeneity in flow properties is included in the form of flow-focusing relationships used to represent seepage (Section 2.3.3.4). At the drift scale, the effects of rock heterogeneity on seepage are explicitly modeled in seepage process models (Section 2.3.3) through the use of data from seepage tests, and field measurements of permeability. A sensitivity study using the thermal-hydrologic-chemical seepage model shows that the effect of heterogeneity in hydrologic properties on predicted gas and water compositions is insignificant at the drift scale (Section 2.3.5.2.3), so such heterogeneity is not included in the near-field chemistry model (Section 2.3.5.3).

Table 2.3.5-1. Features, Events, and Processes Relevant to the Near-Field Chemistry Model and Included into TSPA (Continued)

FEP Number and FEP Name	FEP Description	Summary of Technical Basis/Approach for FEP Inclusion
2.2.07.02.0A Unsaturated groundwater flow in the geosphere	Groundwater flow occurs in unsaturated rocks in most locations above the water table at Yucca Mountain, including at the location of the repository. See related FEPs for discussions of specific issues related to unsaturated flow.	This FEP is included in the unsaturated zone flow model (Section 2.3.2). The unsaturated zone flow model describes three-dimensional, steady flow in a heterogeneous dual-permeability system that includes discrete fault zones and produces a realistic description of flow pathways in the unsaturated zone. The flow fields generated by the unsaturated zone flow model are used directly by the TSPA and are also included in the TSPA as input to other models, including the near-field chemistry model (Section 2.3.5.3) and the multiscale thermal-hydrologic model (Section 2.3.5.4.1).
2.2.07.08.0A Fracture flow in the UZ	Fractures or other analogous channels may act as conduits for fluids to move into the subsurface to interact with the repository and as conduits for fluids to leave the vicinity of the repository and be conducted to the saturated zone. Water may flow through only a portion of the fracture network, including flow through a restricted portion of a given fracture plane.	The unsaturated zone flow model (Section 2.3.2) is based on the dual-permeability concept, with the fractures represented by a continuum. The fracture continuum represents the spatially averaged flow through discrete fractures. The fracture continuum interacts with the matrix continuum, which represents matrix blocks separated by fractures. Fracture-continuum properties are developed for each unsaturated zone model layer and include effects from flow channeling. Fracture permeability and other properties are further calibrated using inverse modeling, based on measured air permeability, matrix saturation, and moisture potential. The fracture-continuum properties are used as inputs to the unsaturated zone flow model, and their effects are incorporated into the output flow fields developed for use in TSPA. This dual-permeability concept is also applied in the near-field coupled process models (the thermal-hydrologic seepage model, the near-field chemistry model through calibration of a simpler plug flow transport model, and the multiscale thermal-hydrologic model), which provide input for TSPA (Sections 2.3.3.3, 2.3.5.3, and 2.3.5.4.1, respectively). In addition, the role of host-rock fractures in transport is addressed in the partitioning of released radionuclides from the EBS to the unsaturated zone (Section 2.3.7.12).
2.2.08.01.0B Chemical characteristics of groundwater in the UZ	Chemistry and other characteristics of groundwater in the unsaturated zone may affect groundwater flow and radionuclide transport of dissolved and colloidal species. Groundwater chemistry and other characteristics, including temperature, pH, Eh, ionic strength, and major ionic concentrations, may vary spatially throughout the system as a result of different rock mineralogy.	The near-field chemistry model simulations (Section 2.3.5.3) feeding the in-drift chemical environment abstractions (Section 2.3.5.5) were run using four different input water compositions spanning the range of compositions in the repository units. The four input water compositions, and the full range of observed nitrate-chloride ratios for a larger set of pore waters, are propagated to the TSPA through the chemistry lookup tables created using results from the near-field chemistry model.

Table 2.3.5-1. Features, Events, and Processes Relevant to the Near-Field Chemistry Model and Included into TSPA (Continued)

FEP Number and FEP Name	FEP Description	Summary of Technical Basis/Approach for FEP Inclusion
2.2.08.12.0A Chemistry of water flowing into the drift	Inflowing water chemistry may be used in analysis or modeling that requires initial water chemistry in the drift. Chemistry of water flowing into the drift is affected by initial water chemistry in the rock, mineral and gas composition in the rock, and thermal-hydrologic-chemical processes in the rock.	This FEP is explicitly included in the near-field chemistry model (Section 2.3.5.3). The initial water, mineral, and gas composition in the rock are reflected in the inputs to the near-field chemistry model. The model captures significant thermal-hydrologic-chemical processes in the rock, such as the evolution of the thermal field through time, pore-water percolation, fracture-matrix interaction, and mineral dissolution and precipitation. These effects are propagated through the model results, which are used as a boundary condition for the development of the in-drift chemical environment abstractions (Section 2.3.5.5) implemented in the TSPA.
2.2.10.12.0A Geosphere dry-out due to waste heat	Repository heat evaporates water from the unsaturated zone rocks near the drifts as the temperature exceeds the vaporization temperature. This zone of reduced water content (reduced saturation) migrates outward during the heating phase (about the first 1,000 years) and then migrates back to the waste packages as heat diffuses throughout the mountain and the radioactive sources decay. This FEP addresses the effects of dryout within the rocks.	The coupled processes of vaporization, dryout, and resaturation are included in the multiscale thermal-hydrologic model (Section 2.3.5.4.1). The near-field chemistry model (Section 2.3.5.3) tracks the location of the boiling front through time using a similar thermal conduction-only modeling approach. Dryout is also included in coupled process models (Section 2.3.5.2) that provide indirect support to TSPA.
2.3.11.03.0A Infiltration and recharge	Infiltration into the subsurface provides a boundary condition for groundwater flow in the unsaturated zone. The amount and location of the infiltration influences the amount of seepage entering the drifts; and the amount and location of recharge influences the height of the water table, the hydraulic gradient, and therefore specific discharge. Different sources of infiltration could change the composition of groundwater passing through the repository. Mixing of these waters with other groundwaters could result in mineral precipitation, dissolution, and altered chemical gradients in the subsurface.	The hydrologic effects of infiltration and recharge are included in the infiltration model (Section 2.3.1). The time dependence of infiltration results is linked to the timing of climate change (Section 2.3.1). This is incorporated in TSPA through the unsaturated zone flow fields. The unsaturated zone flow fields are sampled to develop maps of percolation flux at the upper boundary of the repository host rock, at the contact with the overlying PTn nonwelded unit. These percolation maps are used as upper flux boundary conditions for thermal hydrologic modeling and other coupled process modeling discussed in Section 2.3.5. TSPA includes three distinct climate regimes: present-day (0 to 600 years), monsoonal (600 to 2,000 years), and glacial-transition (2,000 to 10,000 years). There is also a 10,000 to 1-million-year period for which percolation conditions are defined. The transition times for these regimes are constrained by climate information discussed in Section 2.3.1. Each climate regime is characterized using four selected infiltration maps (nominal 10th, 30th, 50th, and 90th percentiles). The weights applied to these maps in TSPA are determined as part of the unsaturated zone model calibration activities described in Section 2.3.2.

Table 2.3.5-2. Features, Events, and Processes Relevant to the In-Drift Thermal-Hydrologic Models and Included into TSPA

FEP Number and FEP Name	FEP Description	Summary of Technical Basis/Approach for FEP Inclusion
1.1.02.02.0A Preclosure ventilation	The duration of preclosure ventilation acts together with waste package spacing (as per design) to control the extent of the boiling front (zone of reduced water content).	Preclosure ventilation in drifts will remove much of the heat output from the waste packages. For the postclosure thermal reference case, the ventilation period following emplacement is 50 years, during which a large fraction of the heat energy supplied to the rock by the waste is removed from the drifts by ventilation. This heat removal effect is explicitly simulated with the multiscale thermal-hydrologic model (Section 2.3.5.4.1), and the in-drift condensation model (Section 2.3.5.4.2), by using time-dependent boundary conditions for the thermal load. Initial rock drying in the drift vicinity as a result of evaporation effects due to ventilation is not explicitly addressed, which overestimates the quantity of water available for flow in the near-field host rock, early in the postclosure period.
1.2.02.01.0A Fractures	Groundwater flow in the Yucca Mountain region and transport of any released radionuclides may take place along fractures. The rate of flow and the extent of transport in fractures are influenced by characteristics such as orientation, aperture, asperity, fracture length, connectivity, and the nature of any linings or infills.	Fractures are included in the unsaturated zone flow model using the dual-permeability concept, with fractures represented by a continuum (Section 2.3.5.4.2). The fracture continuum represents spatially averaged flow through discrete fractures. It interacts with the matrix continuum representing rock blocks separated by fractures (Section 2.3.2.4.1). Fracture continuum properties are based on observed rock characteristics, and some properties are calibrated using inverse modeling (Section 2.3.2). Hydrologic properties of the fracture continuum are used in the dual-permeability formulation of coupled process models, including the multiscale thermal-hydrologic model (Section 2.3.5.4.1), and coupled process models that indirectly support TSPA (Section 2.3.5.2).
1.3.01.00.0A Climate change	Climate change may affect the long-term performance of the repository. This includes the effects of long-term change in global climate (e.g., glacial/interglacial cycles) and shorter-term change in regional and local climate. Climate is typically characterized by temporal variations in precipitation and temperature.	Global climate change is addressed in TSPA using a climate analysis (Section 2.3.1) based on the record of climate changes in the past. This record is used to predict the expected changes in climate for the future. Climate modeling is incorporated into TSPA through the unsaturated zone flow fields (Section 2.3.2), which have different infiltration boundary conditions for future climates. These climates are referred to as present-day for 0 to 600 years, followed by monsoonal for the next 1,400 years, followed by glacial-transition from 2,000 to 10,000 years after closure. Finally, there is a 10,000 to 1-million-year period for which percolation conditions are defined, but no explicit climate is defined.

Table 2.3.5-2. Features, Events, and Processes Relevant to the In-Drift Thermal-Hydrologic Models and Included into TSPA (Continued)

FEP Number and FEP Name	FEP Description	Summary of Technical Basis/Approach for FEP Inclusion
1.4.01.01.0A Climate modification increases recharge	Climate modification causes an increase in recharge in the Yucca Mountain region. Increased recharge might lead to increased flux through the repository, perched water, or water table rise.	The effects of climate change (Section 2.3.1) on unsaturated zone flux through the repository are incorporated through explicit simulations of future unsaturated zone flow fields (Section 2.3.2). These flow fields correspond to the nominal 10th, 30th, 50th, and 90th percentile infiltration cases for the present-day, monsoonal, and glacial-transition climates, and the 10,000 to 1 million year period. The flow fields are used directly by the TSPA and are also used to develop flux boundary conditions for other models including the near-field chemistry model (Section 2.3.5.3) and the multiscale thermal-hydrologic model (Section 2.3.5.4.1).
2.1.03.11.0A Physical form of waste package and drip shield	The specific forms of the various drip shields, waste packages, and internal waste containers that are proposed for the Yucca Mountain repository can affect long-term performance. Waste package form may affect container strength through the shape and dimensions of the waste package and affect heat dissipation through waste package volume and surface area. Waste package and drip shield materials may affect physical and chemical behavior of the disposal area environment. Waste package and drip shield integrity will affect the releases of radionuclides from the disposal system. Waste packages may have both local effects and repository-scale effects. All types of waste packages and containers, including commercial SNF, DOE SNF, and DOE HLW, should be considered.	Several waste package configurations are considered in Sections 2.3.6 and 2.3.7.4, and three nominal waste package configurations are selected for use in TSPA to represent those containing commercial SNF, codisposed HLW and DOE SNF (long and short waste packages), and naval SNF (long and short waste packages). These cover the potential ranges of waste package length and diameter, and outer barrier thickness, accounting for the majority of waste packages (Section 2.3.6.3.4). Environmental conditions imposed by the form and relative positioning of the waste packages and drip shields are taken into account in modeling of in-drift thermal hydrologic conditions (Section 2.3.5.4.1), and modeling of the chemistry of contacting waters (Section 2.3.5.5).

Table 2.3.5-2. Features, Events, and Processes Relevant to the In-Drift Thermal-Hydrologic Models and Included into TSPA (Continued)

FEP Number and FEP Name	FEP Description	Summary of Technical Basis/Approach for FEP Inclusion
2.1.06.06.0A Effects of drip shield on flow	The drip shield will affect the amount of water reaching the waste package. Effects of the drip shield on the disposal region environment (for example, changes in relative humidity and temperature below the shield) should be considered for both intact and degraded conditions.	The in-drift thermal-hydrologic environment, including the effect of the drip shield, is simulated by the multiscale thermal-hydrologic model (Section 2.3.5.4.1) and the in-drift condensation model (Section 2.3.5.4.2). The multiscale model predicts temperature of the in-drift environment both outside and under the intact drip shield. It then calculates relative humidities by assuming a well-mixed gas phase. The multiscale model also provides temperature and relative humidity in the drift for the seismic scenario class, which includes a breached drip shield. The abstracted output from the multiscale thermal-hydrologic model is an input to the TSPA. The in-drift condensation model considers ventilated and unventilated drip shield conditions, corresponding to the range of possible gas-phase mixing (Section 2.3.5.4.2.3.2).
2.1.08.01.0A Water influx at the repository	An increase in the unsaturated water flux at the repository may affect thermal, hydrologic, chemical, and mechanical behavior of the system. Increases in flux could result from climate change, but the cause of the increase is not an essential part of the FEP.	Increases in water influx are included in the TSPA through the flow fields developed with the unsaturated zone model (Section 2.3.2) in response to climate and infiltration changes. The ambient and thermally-driven coupled-process models (Sections 2.3.3, 2.3.5.3, and 2.3.5.4) that evaluate seepage and in-drift environmental conditions use these flow fields. The thermal-hydrologic-mechanical model (Section 2.3.5.2.2) and the thermal-hydrologic-chemical seepage model (Section 2.3.5.2.3) also use boundary conditions based on these flow fields. Changes to water influx due to flow focusing are also included in the abstraction of drift seepage (Section 2.3.3.4).
2.1.08.03.0A Repository dry-out due to waste heat	Repository heat evaporates water from the unsaturated zone rocks near the drifts, as the temperature exceeds the vaporization temperature. This zone of reduced water content (reduced saturation) could migrate outward during the heating phase and then migrate back to the waste package as heat diffuses throughout the mountain and the radioactive heat sources decay. This FEP addresses the effects of dryout within the repository drifts.	This FEP is included through the multiscale thermal-hydrologic model (Section 2.3.5.4.1), which is a direct feed to the TSPA. The multiscale thermal-hydrologic model captures repository dryout during the heating phase and rewetting during the cooling phase. These processes are reflected in the model output variables describing in-drift temperature, humidity, and liquid-phase flux in the near-field host rock.

Table 2.3.5-2. Features, Events, and Processes Relevant to the In-Drift Thermal-Hydrologic Models and Included into TSPA (Continued)

FEP Number and FEP Name	FEP Description	Summary of Technical Basis/Approach for FEP Inclusion
2.1.08.04.0A Condensation forms on roofs of drifts (drift-scale cold traps)	Emplacement of waste in drifts creates thermal gradients within the repository. Such thermal gradients can lead to drift-scale cold traps characterized by latent heat transfer from warmer to cooler locations. This mechanism can result in condensation forming on the roof or other parts of the drifts, leading to enhanced dripping on the drip shields, waste packages, or exposed waste material.	The in-drift condensation model (Section 2.3.5.4.2) is used to represent condensation and evaporation along the entire length of seven selected drifts at different times. The model output is used to represent the location and rate of condensation on the drift walls for TSPA. The predicted condensation on drift walls is implemented in TSPA as an addition to the seepage flux (Section 2.3.7.12). This approach acknowledges the presence of condensation, even where there is no seepage, and provides a reasonable bound for the quantity of water available for EBS flow and transport.
2.1.08.04.0B Condensation Forms at Repository Edges (Repository-Scale Cold Traps)	Emplacement of waste in drifts creates thermal gradients within the repository. Such thermal gradients can lead to repository-scale cold traps characterized by latent heat transfer from warmer to cooler locations. This mechanism can result in condensation forming at repository edges or elsewhere in the EBS, leading to enhanced dripping on the drip shields, waste packages, or exposed waste material.	Condensation at the repository edges is included in the TSPA through application of the in-drift condensation model, which provides correlation functions representing the probability of condensation on the drift wall, and the magnitude of condensation where it occurs (Section 2.3.5.4.2). This abstraction is used in conjunction with the abstracted output from the multiscale thermal-hydrologic model, which describes the temperature evolution at waste package locations (Section 2.3.5.4.1). Condensation can occur only where the drift wall temperature has cooled through the local boiling temperature (96°C), which happens first near the repository edges. The condensation rate is generally greater on cooler waste packages, and the effect of repository edge cooling on drift wall temperature is represented in the in-drift condensation model. The implementation in TSPA uses repository-wide condensation frequency and magnitude distributions, which are not specific to waste package location, applied to representative waste packages based on correlation with percolation flux. The effect of repository-scale edge cooling on condensation is thus included in TSPA, in order to represent the potential effects on radionuclide transport in the invert and transport coupling to the unsaturated zone.

Table 2.3.5-2. Features, Events, and Processes Relevant to the In-Drift Thermal-Hydrologic Models and Included into TSPA (Continued)

FEP Number and FEP Name	FEP Description	Summary of Technical Basis/Approach for FEP Inclusion
2.1.08.05.0A Flow through invert	The invert, a porous material consisting of crushed tuff, separates the waste package from the bottom of the drift. Flow and transport through and around the invert can influence radionuclide release to the unsaturated zone.	Flow through the invert is included in the TSPA through the use of two models: the radionuclide transport abstraction (Section 2.3.7.12) and the multiscale thermal-hydrologic model (Section 2.3.5.4.1). The radionuclide transport abstraction is implemented directly within the TSPA to simulate the flow pathways through the EBS. Flow through the invert consists of the flux diverted by the drip shield and by the waste package, and the flux through the waste package, and is reduced by any evaporation from the invert. Water saturation in the invert, for the case of no drift seepage or condensation, is provided to TSPA by the multiscale thermal-hydrologic model, which includes the processes of capillary condensation and unsaturated flow (wicking) from the host rock.
2.1.08.06.0A Capillary effects (wicking) in EBS	Capillary rise, or wicking, is a potential mechanism for water to move through the waste and EBS.	The multiscale thermal-hydrologic model (Section 2.3.5.4.1) includes wicking from the host rock to the invert. Multiscale thermal-hydrologic model results feed the TSPA both directly and indirectly, including through the radionuclide transport abstraction (Section 2.3.7.12), which is implemented directly in TSPA to evaluate the fluxes along flow pathways. The seepage evaporation abstraction (Section 2.3.5.5.4.2) also includes evaluation of pore-water chemistry in the invert, which is affected by wicking in the invert. This abstraction has two lookup tables: one for water entering the drift by crown seepage and the other for water entering the invert by wicking.
2.1.08.07.0A Unsaturated flow in the EBS	Unsaturated flow may occur along preferential pathways in the waste and EBS. Physical and chemical properties of the EBS and waste form, in both intact and degraded states, should be considered in evaluating pathways.	Unsaturated flow occurs in the emplacement drift due to seepage or condensation processes (Section 2.3.5.4.1). The nature of this flow has been included in the abstractions for flow and transport through the EBS features (Section 2.3.7). Unsaturated flow limits advective transport of radionuclides and other chemical species, for example under intact drip shields, and facilitates isolation of water from the waste packages and waste forms.
2.1.08.11.0A Repository resaturation due to waste cooling	Following the peak thermal period, water in the condensation cap may flow downward, resaturating the geosphere dry-out zone and flowing into the drifts. This may lead to an increase in water content and/or resaturation in the repository.	The multiscale thermal-hydrologic model (Section 2.3.5.4.1) and the thermal-hydrologic seepage model (Section 2.3.3.3) include dryout of the repository followed by resaturation as the waste packages cool. Each of these models provides either direct or indirect input to the TSPA. Dryout and resaturation effects are captured by both of these models, particularly the multiscale thermal-hydrologic model, which predicts the near-field temperatures and humidity conditions used in the TSPA.

Table 2.3.5-2. Features, Events, and Processes Relevant to the In-Drift Thermal-Hydrologic Models and Included into TSPA (Continued)

FEP Number and FEP Name	FEP Description	Summary of Technical Basis/Approach for FEP Inclusion
2.1.11.01.0A Heat generation in EBS	Temperature in the waste and EBS will vary through time. Heat from radioactive decay will be the primary cause of temperature change, but other factors to be considered in determining the temperature history include the in situ geothermal gradient, thermal properties of the rock, EBS, and waste materials, hydrologic effects, and the possibility of exothermic reactions. Considerations of the heat generated by radioactive decay should take different properties of different waste types, including DOE SNF, into account.	The temperature history in the EBS is calculated by the multiscale thermal-hydrologic model (Section 2.3.5.4.1) and used by the TSPA. Consistent representation of heat generation is used in the thermal-hydrologic seepage model (Section 2.3.3.3), the near-field chemistry model (Section 2.3.5.3), and the in-drift condensation model (Section 2.3.5.4.2). The calculated temperatures are influenced not only by the heat of radionuclide decay, but also by the geothermal gradient from the ground surface to the water table and the thermal-physical properties of the rock and significant EBS features. The thermal effects from having different types of waste forms, including DOE SNF, is reflected in the multiscale thermal-hydrologic model output. Exothermic reactions (FEP 2.1.11.03.0A) produce insignificant amounts of heat and are not included in TSPA.
2.1.11.02.0A Nonuniform heat distribution in EBS	Uneven heating and cooling at edges of the repository may lead to nonuniform thermal effects during both the thermal peak and the cool-down period.	The multiscale thermal-hydrologic model (Section 2.3.5.4.1) predicts the repository thermal-hydrologic environment, including thermal gradients from the repository center to the edges and corners of the repository. The spatial distribution of repository heating is also represented in the near-field chemistry model (Section 2.3.5.3) and the in-drift condensation model (Section 2.3.5.4.2). Thus, the impact of uneven heating and cooling during both the thermal peak and the cooldown period is captured in the model outputs (e.g., temperature, relative humidity, and condensation rates) used by the TSPA.

Table 2.3.5-2. Features, Events, and Processes Relevant to the In-Drift Thermal-Hydrologic Models and Included into TSPA (Continued)

FEP Number and FEP Name	FEP Description	Summary of Technical Basis/Approach for FEP Inclusion
2.1.11.09.0A Thermal effects on flow in the EBS	High temperatures in the EBS may influence seepage into, and flow within, the waste and EBS. Thermally induced changes to fluid saturation and/or relative humidity could influence in-package chemistry. Thermal gradients in the repository could lead to localized accumulation of moisture. Wet zones could form below the areas of moisture accumulation.	The TSPA EBS flow submodel (Section 2.4), which implements part of the radionuclide transport abstraction (Section 2.3.7.12), calculates flow within the drift. It incorporates the thermal effects on seepage and flow in the EBS through inputs from the multiscale thermal-hydrologic model (Section 2.3.5.4.1) and the TSPA drift seepage and drift wall condensation submodels (Section 2.4). The multiscale thermal-hydrologic model simulates near-field and in-drift thermal-hydrologic conditions that result from the system response to the heat generation of the waste packages. This model provides inputs to the TSPA EBS flow submodel, including relative humidity as well as the invert liquid saturations and flow rates. The TSPA drift seepage and drift wall condensation submodels (Section 2.4) also use inputs to incorporate the thermal effects on flow. The multiscale thermal-hydrologic model provides percolation flux and temperatures as inputs for the probabilistic calculations of the amount and distribution of seepage into the drift. The in-drift condensation model (Section 2.3.5.4.2) provides the probability and magnitude of condensation on the drift wall. The TSPA EBS flow submodel treats condensation on the drift wall like seepage (e.g., it is another source of liquid water flow within the drift).
2.1.11.09.0C Thermally driven flow (convection) in drifts	Temperature differentials may result in convective flow in the EBS. Convective flow within the drifts could influence in-drift chemistry.	The in-drift condensation model (Section 2.3.5.4.2), which provides direct input to TSPA, uses dispersion parameters based on fluid-dynamics simulation of natural convection in the drifts. The multiscale thermal-hydrologic model (Section 2.3.5.4.1), which also provides direct input to TSPA, uses an average equivalent (in-drift) thermal conductivity correlation that is also based on convection analyses.
2.2.03.01.0A Stratigraphy	Stratigraphic information is necessary information for the performance assessment. This information should include identification of the relevant rock units, soils and alluvium, and their thickness, lateral extents, and relationships to each other. Major discontinuities should be identified.	Stratigraphy is included in the unsaturated zone flow model (Section 2.3.2) using grids developed with information from the geologic framework model. Because the assignment of unit hydrologic properties is associated with the grid used for the unsaturated zone flow model, the stratigraphy information is embedded in the TSPA through the output flow fields. In addition, other models, such as the multiscale thermal-hydrologic model (Section 2.3.5.4.1), use the flow fields, hydrologic properties, and other information from the unsaturated zone flow model.

Table 2.3.5-2. Features, Events, and Processes Relevant to the In-Drift Thermal-Hydrologic Models and Included into TSPA (Continued)

FEP Number and FEP Name	FEP Description	Summary of Technical Basis/Approach for FEP Inclusion
2.2.03.02.0A Rock properties of host rock and other units	Physical properties such as porosity and permeability of the relevant rock units, soils, and alluvium are necessary for the performance assessment. Possible heterogeneities in these properties should be considered. Questions concerning events and processes that may cause these physical properties to change over time are considered in other FEPs.	Rock characteristics are defined for stratigraphic units/layers classified in the geologic framework model, and further used to develop hydrologic properties for the unsaturated zone flow model layers (Section 2.3.2). Heterogeneity is modeled in terms of the sequence of hydrogeologic units and discrete faults. Therefore, rock properties are embedded in the TSPA through the output flow fields, with site-scale layering and faults explicitly taken into account. Intermediate-scale heterogeneity in flow properties is included in the form of flow-focusing relationships used to represent seepage (Section 2.3.3.4). At the drift scale, the effects of rock heterogeneity on seepage are explicitly modeled in seepage process models (Section 2.3.3) through the use of data from seepage tests, and field measurements of permeability. The effects of drift-scale heterogeneity in fracture permeability are considered in the seepage calculations for TSPA, through inputs derived from modeling of ambient seepage (Section 2.3.3.2). Calibrated hydrologic properties for the host rock (Section 2.3.2) are evaluated and used in the multiscale model (Section 2.3.5.4.1.2). Physical and thermal properties for the host rock units are obtained from site characterization data and used in the multiscale model and the in-drift condensation model. Uncertainty on host-rock thermal conductivity is quantified for the multiscale model and propagated to TSPA (Section 2.3.5.4.1.2).
2.2.07.02.0A Unsaturated groundwater flow in the geosphere	Groundwater flow occurs in unsaturated rocks in most locations above the water table at Yucca Mountain, including at the location of the repository. See related FEPs for discussions of specific issues related to unsaturated flow.	This FEP is included in the unsaturated zone flow model (Section 2.3.2). The unsaturated zone flow model describes three-dimensional, steady flow in a heterogeneous dual-permeability system that includes discrete fault zones and produces a realistic description of flow pathways in the unsaturated zone. The flow fields generated by the unsaturated zone flow model are used directly by the TSPA and are also included in the TSPA as input to other models, including the near-field chemistry model (Section 2.3.5.3) and the multiscale thermal-hydrologic model (Section 2.3.5.4.1).

Table 2.3.5-2. Features, Events, and Processes Relevant to the In-Drift Thermal-Hydrologic Models and Included into TSPA (Continued)

FEP Number and FEP Name	FEP Description	Summary of Technical Basis/Approach for FEP Inclusion
2.2.07.08.0A Fracture flow in the UZ	Fractures or other analogous channels may act as conduits for fluids to move into the subsurface to interact with the repository and as conduits for fluids to leave the vicinity of the repository and be conducted to the saturated zone. Water may flow through only a portion of the fracture network, including flow through a restricted portion of a given fracture plane.	The unsaturated zone flow model (Section 2.3.2) is based on the dual-permeability concept, with the fractures represented by a continuum. The fracture continuum represents the spatially averaged flow through discrete fractures. The fracture continuum interacts with the matrix continuum, which represents matrix blocks separated by fractures. Fracture-continuum properties are developed for each unsaturated zone model layer and include effects from flow channeling. Fracture permeability and other properties are further calibrated using inverse modeling (Section 2.3.2) based on measured air permeability, matrix saturation, and moisture potential. The fracture-continuum properties are used as inputs to the unsaturated zone flow model, and their effects are incorporated into the output flow fields developed for use in TSPA. This dual-permeability concept is also applied in the near-field coupled process models (the thermal-hydrologic seepage model, the near-field chemistry model through calibration of a simpler plug flow transport model, and the multiscale thermal-hydrologic model), which provide input for TSPA (Sections 2.3.3.3, 2.3.5.3, and 2.3.5.4.1, respectively). In addition, the role of host-rock fractures in transport is addressed in the partitioning of released radionuclides from the EBS to the unsaturated zone (Section 2.3.7.12).
2.2.07.09.0A Matrix imbibition in the UZ	Water flowing in fractures or other channels in the unsaturated zone may be imbibed into the surrounding rock matrix. This may occur during steady flow, episodic flow, or into matrix pores that have been dried out during the thermal period.	Matrix imbibition refers to the movement of water into the matrix as a result of capillary forces. This process affects the distribution of flow between fractures and matrix in a dual-permeability flow model for fractured rock. Matrix imbibition is included in the process model for unsaturated zone flow at the mountain scale (Section 2.3.2). The effect of imbibition is incorporated in the output flow fields used in the TSPA. Imbibition is also represented in the near-field chemistry model (Section 2.3.5.3) through calibration to a dual-permeability transport model, and in the multiscale thermal-hydrologic model (Section 2.3.5.4.1) which simulates the transient response to heating.

Table 2.3.5-2. Features, Events, and Processes Relevant to the In-Drift Thermal-Hydrologic Models and Included into TSPA (Continued)

FEP Number and FEP Name	FEP Description	Summary of Technical Basis/Approach for FEP Inclusion
2.2.07.10.0A Condensation zone forms around drifts	Condensation of the two-phase flow generated by repository heat may form in the rock where the temperature drops below the local vaporization temperature. Waste package emplacement geometry and thermal loading may affect the scale at which condensation caps form (over waste packages, over panels, or over the entire repository), and the extent to which “shedding” will occur as water flows from the region above one drift to the region above another drift or into the rock between drifts.	Formation of a condensation cap in the fractured rock above the drifts and shedding between the drifts is simulated with coupled-processes models, including the thermal-hydrologic seepage model (Section 2.3.3.3), and the multiscale thermal-hydrologic model (Section 2.3.5.4.1). These two models are used in creating abstractions for TSPA.
2.2.07.11.0A Resaturation of geosphere dry-out zone	Following the peak thermal period, water in the condensation cap may flow downward into the drifts. Influx of cooler water from above, such as might occur from episodic flow, may accelerate return flow from the condensation cap by lowering temperatures below the condensation point. Percolating groundwater will also contribute to resaturation of the dryout zone. Vapor flow, as distinct from liquid flow by capillary processes, may also contribute.	The multiscale model (Section 2.3.5.4.1) simulates evaporation and condensation in the host rock, the drainage of condensate around and between drift openings, and resaturation of the host rock as the rock cools. It provides direct input to TSPA as histories of in-drift temperature and relative humidity conditions. The effects from variation of in-drift temperature and relative humidity on the evaporative chemical evolution of waters in the EBS are described in Section 2.3.5.5.
2.2.07.20.0A Flow diversion around repository drifts	Flow in unsaturated rock tends to be diverted by openings such as waste emplacement drifts due to the effects of capillary forces. The resulting diversion of flow could have an effect on seepage into the repository. Flow diversion around the drift openings could also lead to the development of a zone of lower flow rates and low saturation beneath the drift, known as the drift shadow.	The impact of flow diversion around the drifts and its relevance for seepage are explicitly captured in the seepage process model used for the seepage abstraction (Section 2.3.3.4). From these model simulations, seepage predictions are available in the form of lookup tables, which are used in TSPA to calculate ambient seepage by sampling parameter cases of seepage-relevant parameters from uncertainty distributions. The abstraction of drift seepage also captures the effects of drift collapse in terms of the larger drift profile that results. Capillary diversion of flow around the drifts is also captured in the multiscale thermal-hydrologic model (Section 2.3.5.4.1), both of which are used to provide input to TSPA.

Table 2.3.5-2. Features, Events, and Processes Relevant to the In-Drift Thermal-Hydrologic Models and Included into TSPA (Continued)

FEP Number and FEP Name	FEP Description	Summary of Technical Basis/Approach for FEP Inclusion
2.2.10.03.0B Natural geothermal effects on flow in the UZ	The existing geothermal gradient, and spatial or temporal variability in that gradient, may affect groundwater flow in the unsaturated zone.	Natural geothermal effects, observed as the ambient temperature profile in the unsaturated zone, are included in the unsaturated zone flow model calibration (Section 2.3.2). The temperature profile in the unsaturated zone is primarily determined by the ground surface temperature, the water table temperature, water flux through the unsaturated zone, and the thermal conductivity from layer to layer. These conditions are included in coupled process models, including the multiscale thermal-hydrologic model (Section 2.3.5.4.1), and coupled process models that indirectly support TSPA (Section 2.3.5.2).
2.2.10.10.0A Two-phase buoyant flow/heat pipes	Heat from waste can generate two-phase buoyant flow. The vapor phase (water vapor) could escape from the mountain. A heat pipe consists of a system for transferring energy between a hot and a cold region (source and sink respectively) using the heat of vaporization and movement of the vapor as the transfer mechanism. Two-phase circulation continues until the heat source is too weak to provide the thermal gradients required to drive it. Alteration of the rock adjacent to the drift may include dissolution that maintains the permeability necessary to support the circulation (as inferred for some geothermal systems).	The coupled processes causing heat-pipe behavior are explicitly simulated with the thermal-hydrologic seepage model (Section 2.3.3.3), and the multiscale thermal-hydrologic model (Section 2.3.5.4.1). These two models are used in the development of abstractions for TSPA.
2.2.10.12.0A Geosphere dry-out due to waste heat	Repository heat evaporates water from the unsaturated zone rocks near the drifts as the temperature exceeds the vaporization temperature. This zone of reduced water content (reduced saturation) migrates outward during the heating phase (about the first 1,000 years) and then migrates back to the waste packages as heat diffuses throughout the mountain and the radioactive sources decay. This FEP addresses the effects of dryout within the rocks.	The coupled processes of vaporization, dryout, and resaturation are included in the multiscale thermal-hydrologic model (Section 2.3.5.4.1). The near-field chemistry model (Section 2.3.5.3) tracks the location of the boiling front through time using a similar thermal conduction-only modeling approach. Dryout is also included in coupled process models (Section 2.3.5.2) that provide indirect support to TSPA.

Table 2.3.5-2. Features, Events, and Processes Relevant to the In-Drift Thermal-Hydrologic Models and Included into TSPA (Continued)

FEP Number and FEP Name	FEP Description	Summary of Technical Basis/Approach for FEP Inclusion
2.3.11.03.0A Infiltration and recharge	Infiltration into the subsurface provides a boundary condition for groundwater flow in the unsaturated zone. The amount and location of the infiltration influences the amount of seepage entering the drifts; and the amount and location of recharge influences the height of the water table, the hydraulic gradient, and therefore specific discharge. Different sources of infiltration could change the composition of groundwater passing through the repository. Mixing of these waters with other groundwaters could result in mineral precipitation, dissolution, and altered chemical gradients in the subsurface.	The hydrologic effects of infiltration and recharge are included in the infiltration model (Section 2.3.1). The time dependence of infiltration results is linked to the timing of climate change (Section 2.3.1). This is incorporated in TSPA through the unsaturated zone flow fields. The unsaturated zone flow fields are sampled to develop maps of percolation flux at the upper boundary of the repository host rock, at the contact with the overlying PTn nonwelded unit. These percolation maps are used as upper flux boundary conditions for thermal hydrologic modeling and other coupled process modeling discussed in Section 2.3.5. TSPA includes three distinct climate regimes: present-day (0 to 600 years), monsoonal (600 to 2,000 years), and glacial-transition (2,000 to 10,000 years). There is also a 10,000 to 1-million-year period for which percolation conditions are defined. The transition times for these regimes are constrained by climate information discussed in Section 2.3.1. Each climate regime is characterized using four selected infiltration maps (nominal 10th, 30th, 50th, and 90th percentiles). The weights applied to these maps in TSPA are determined as part of the unsaturated zone model calibration activities described in Section 2.3.2.

Table 2.3.5-3. Features, Events, and Processes Relevant to the In-Drift Chemical Environment Models and Included into TSPA

FEP Number and FEP Name	FEP Description	Summary of Technical Basis/Approach for FEP Inclusion
2.1.03.11.0A Physical form of Waste Package and Drip Shield	The specific forms of the various drip shields, waste packages, and internal waste containers that are proposed for the Yucca Mountain repository can affect long-term performance. Waste package form may affect container strength through the shape and dimensions of the waste package and affect heat dissipation through waste package volume and surface area. Waste package and drip shield materials may affect physical and chemical behavior of the disposal area environment. Waste package and drip shield integrity will affect the releases of radionuclides from the disposal system. Waste packages may have both local effects and repository-scale effects. All types of waste packages and containers, including commercial SNF, DOE SNF, and DOE HLW, should be considered.	Several waste package configurations are considered in Sections 2.3.6 and 2.3.7.4, and three nominal waste package configurations are selected for use in TSPA to represent those containing commercial SNF, codisposed HLW and DOE SNF (long and short waste packages), and Naval SNF (long and short waste packages). These cover the potential ranges of waste package length and diameter, and outer barrier thickness, accounting for the majority of waste packages (Section 2.3.6.3.4). Environmental conditions imposed by the form and relative positioning of the waste packages and drip shields are taken into account in modeling of in-drift thermal hydrologic conditions (Section 2.3.5.4.1), and modeling of the chemistry of contacting waters (Section 2.3.5.5).
2.1.08.06.0A Capillary effects (wicking) in EBS	Capillary rise, or wicking, is a potential mechanism for water to move through the waste and EBS.	The multiscale thermal-hydrologic model (Section 2.3.5.4.1) includes wicking from the host rock to the invert. Multiscale thermal-hydrologic model results feed the TSPA both directly and indirectly, including through the radionuclide transport abstraction (Section 2.3.7.12), which is implemented directly in TSPA to evaluate the fluxes along flow pathways. The seepage evaporation abstraction (Section 2.3.5.5.4.2) also includes evaluation of pore-water chemistry in the invert, which is affected by wicking in the invert. This abstraction has two lookup tables: one for water entering the drift by crown seepage and the other for water entering the invert by wicking.
2.1.08.11.0A Repository resaturation due to waste cooling	Following the peak thermal period, water in the condensation cap may flow downward, resaturating the geosphere dry-out zone and flowing into the drifts. This may lead to an increase in water content and/or resaturation in the repository.	The multiscale thermal-hydrologic model (Section 2.3.5.4.1) and the thermal-hydrologic seepage model (Section 2.3.3.3) include dryout of the repository followed by resaturation as the waste packages cool. Each of these models provides either direct or indirect input to the TSPA. Dryout and resaturation effects are captured by both of these models, particularly the multiscale thermal-hydrologic model, which predicts variation of in-drift temperatures and humidity conditions used in the TSPA. The effects from variation of in-drift temperature and relative humidity on the evaporative chemical evolution of waters in the EBS are described in Section 2.3.5.5.

Table 2.3.5-3. Features, Events, and Processes Relevant to the In-Drift Chemical Environment Models and Included into TSPA (Continued)

FEP Number and FEP Name	FEP Description	Summary of Technical Basis/Approach for FEP Inclusion
2.1.09.01.0A Chemical characteristics of water in drifts	When flow in the drifts is re-established following the peak thermal period, water may have chemical characteristics influenced by the near-field host rock and EBS. Specifically, the water chemistry (pH and dissolved species in the groundwater) may be affected by interactions with cementitious materials or steel used in the disposal region. These point source contaminated waters may coalesce to form a larger volume of contaminated water. This altered groundwater is referred to as the carrier plume because dissolution and transport will occur in this altered chemical environment as contaminants move through the EBS, and down into the unsaturated zone. (Note: There is no defining limit as to what volume of contaminated water constitutes a plume.)	The composition of water entering the drift by wicking in the invert or by crown seepage is determined in the TSPA through implementation of the seepage evaporation abstraction (Section 2.3.5.5.4.2). Potential carrier plume effects are considered in the evaluation of seepage water interaction with stainless steel and carbon steel structural materials. Cementitious materials are not included because they are not part of the design for the emplacement drifts. Chemical effects from EBS material degradation products in the drift are considered (FEP 2.1.09.02.0A).
2.1.09.06.0B Reduction-oxidation potential in drifts	The redox potential in the EBS influences the oxidation of the in-drift materials and the in-drift solubility of radionuclide species. Local variations in the in-drift redox potential can occur.	The reduction-oxidation potential in the drifts is included in the in-drift chemical environment abstractions (Section 2.3.5.5), which are implemented directly in the TSPA. Oxidizing conditions are predicted to occur indefinitely in the in-drift environment (Section 2.3.5.5.4.1), based on corrosion of carbon steel (which is rate-limited by oxygen supply) as the principal representative cause of oxygen consumption.
2.1.09.07.0B Reaction kinetics in drifts	Chemical reactions, such as radionuclide dissolution/precipitation reactions and reactions controlling the reduction-oxidation state, may not be at equilibrium in the drifts.	In-drift chemical kinetics are implicitly included through suppression of individual mineral phases in the seepage evaporation abstraction (Section 2.3.5.5.3). Individual mineral phases are suppressed if those phases are kinetically inhibited from forming under repository conditions. In addition, the kinetics of corrosion for committed materials are examined with respect to the effect on in-drift water and gas compositions (FEP 2.1.06.01.0A, Chemical effects of rock reinforcement and cementitious materials in EBS; Section 2.2.1).

Table 2.3.5-3. Features, Events, and Processes Relevant to the In-Drift Chemical Environment Models and Included into TSPA (Continued)

FEP Number and FEP Name	FEP Description	Summary of Technical Basis/Approach for FEP Inclusion
2.1.11.08.0A Thermal effects on chemistry and microbial activity in the EBS	Temperature changes may affect chemical and microbial processes in the waste and EBS.	This FEP is included in the TSPA through inputs and models that are affected by temperature. The near-field chemistry model (Section 2.3.5.3) captures the impact of temperature on the evolution of potential seepage chemistries. The effects of temperature on mineral stabilities and chemical reaction rates are also included in the geochemical modeling used to create the seepage evaporation abstraction (Section 2.3.5.5.4.2). Temperature is one of the parameters required as input to implement this abstraction in the TSPA. The thermal effects on microbial activity have been evaluated and found to be insignificant. Thermal and humidity effects on microbial activity are included in the use of the microbially influenced corrosion-modified corrosion rate for Alloy 22 (Section 2.3.6).
2.1.11.09.0C Thermally driven flow (convection) in drifts	Temperature differentials may result in convective flow in the EBS. Convective flow within the drifts could influence in-drift chemistry.	The in-drift condensation model (Section 2.3.5.4.2), which provides direct input to TSPA, uses dispersion parameters based on fluid-dynamics simulation of natural convection in the drifts. The multiscale thermal-hydrologic model (Section 2.3.5.4.1), which also provides direct input to TSPA, uses an average equivalent (in-drift) thermal conductivity correlation that is based on convection analyses. The multiscale model predicts variation of in-drift temperatures and humidity conditions used in the TSPA. The effects from variation of in-drift temperature and relative humidity on the evaporative chemical evolution of waters in the EBS are described in Section 2.3.5.5.
2.2.07.11.0A Resaturation of Geosphere Dry-Out Zone	Following the peak thermal period, water in the condensation cap may flow downward into the drifts. Influx of cooler water from above, such as might occur from episodic flow, may accelerate return flow from the condensation cap by lowering temperatures below the condensation point. Percolating groundwater will also contribute to resaturation of the dryout zone. Vapor flow, as distinct from liquid flow by capillary processes, may also contribute.	The multiscale model (Section 2.3.5.4.1) simulates evaporation and condensation in the host rock, the drainage of condensate around and between drift openings, and resaturation of the host rock as the rock cools. It provides direct input to TSPA as histories of in-drift temperature and relative humidity conditions. The effects from variation of in-drift temperature and relative humidity on the evaporative chemical evolution of waters in the EBS are described in Section 2.3.5.5.

Table 2.3.5-4. Direct and Indirect Onsager Processes Driven by Temperature, Pressure, Chemical Potential, and Electrical Potential Gradients

	Gradient			
Flux	**Temperature**	**Pressure**	**Chemical Potential**	**Electrical Potential**
Heat Flux	**Fourier's Law– heat flow in a temperature gradient**	Thermal filtration– heat flow in a pressure gradient	Dufour effect– heat flow in a density gradient	Peltier effect– heat flow in a voltage gradient
Volume Flux	Thermal osmosis– volume flow in a temperature gradient	**Darcy's Law– volume flow in a pressure gradient**	Chemical osmosis– volume flow in a concentration gradient	Electro-osmosis– volume flow in a voltage gradient
Mass Flux	Soret effect–particle flow in a temperature gradient	Reverse osmosis– mass flow in a pressure gradient, ultrafiltration	**Fick's Law– Mass flow in a concentration gradient**	Electrophoresis– mass flow in a voltage gradient
Electrical Flux	Seebeck effect– electrical current in a temperature gradient	Streaming current– electrical current in a pressure gradient	Sedimentation current– electrical current in a density gradient	**Ohm's Law– Current flow in a voltage gradient**

NOTE: Direct Onsager processes are along the main diagonal in bold type. The indirect Onsager processes (off-diagonal) are typically dominated by the direct processes, and the direct processes may be dominated by advection.

Source: Carnahan 1987, Table 1; SNL 2007b, Table 6.4-1.

Table 2.3.5-5. Representative Pore-Water Compositions for the Four Groups, Used as Inputs for the Near-Field Chemistry Model

Sample ID		**SD-9/ 1184.7-1184.8/UC**	**ESF-THERMALK-017/ 26.5-26.9/UC**	**ESF-HD-PERM-3/ 34.8-35.1/Alcove 5**	**HD-PERM-3/ 56.7-57.1/UC**
Lithostratigraphic Unit		**Tptpll**	**Tptpul**	**Tptpmn**	**Tptpmn**
Water designation		**Gp1**	**Gp2**	**Gp3**	**Gp4**
Members in Group		**21**	**7**	**3**	**3**
Parameter	**Units**	**Values**			
pH (meas.)	pH	8.2	7.7	8.31	—
Na^+	mg/L	59	45	62	123
K^+	mg/L	4.8	14.4	9	13.8
Mg^{2+}	mg/L	0.7	7.9	17.4	16.7
Ca^{2+}	mg/L	19	62	97	59.9
Cl^-	mg/L	23	67	123	146
SO_4^{2-}	mg/L	16	82	120	126
HCO_3^-	mg/L	142	126	—	149
NO_3^-	mg/L	16	44	10	57.4
F^-	mg/L	2.2	1.4	0.76	1.3
SiO_2(aq)	mg/L	42	52	75	—

Source: SNL 2007b, Tables 4.1-3, 6.6-3.

Table 2.3.5-6. Suite of Submodels and Intermediate and Final Results for the Multiscale Thermal-Hydrologic Model

Name	Description	Spatial Dimensionality	Function	Modeling Details
SMT	Smeared-heat-source, mountain-scale, thermal-only submodel	3	To determine repository-scale variations in host-rock temperature resulting from heat output of entire waste inventory.	3,264 output locations 1 areal mass loading profile consistent with entire repository 1 submodel execution
LDTH	Line-averaged-heat-source, drift-scale, thermal-hydrologic submodel	2	To simulate thermal-hydrologic processes at drift scale and to calculate temperature, relative humidity, and other thermal-hydrologic variables. Considers line-averaged-heat-source conditions (e.g., waste package and drip shield are a lumped heat source).	560 execution locations 4 areal mass loading profiles 7 infiltration-flux/thermal- conductivity cases 15,680 submodel executions
SDT	Smeared-heat-source, drift-scale, thermal-only submodel	1	To link SMT and LDTH submodels by imposing the influence of three-dimensional, SMT-calculated temperature for a particular LDTH location onto two-dimensional LDTH results for same location.	560 execution locations 4 areal mass loading profiles 2,240 submodel executions
LMTH	Line-average-heat-source, mountain-scale, thermal-hydrologic intermediate results	3	To use the SDT and SMT submodels to modify LDTH submodel results, in preparation for applying the DDT submodel to represent waste package variability.	3,264 locations 7 infiltration-flux/thermal-conductivity cases 4 areal mass loading profiles
DDT	Discrete-heat-source, drift-scale, thermal-only submodel	3	To determine waste package–specific deviations (relative to line-averaged-heat-source conditions used by LDTH) in host rock and in-drift temperatures. Explicitly accounts for waste package–specific heat output and for thermal radiation between all waste package and drift surfaces.	1 execution location 4 areal mass loading profiles 4 submodel executions
DMTH	Discrete-heat-source, mountain-scale, thermal-hydrologic final model results	3	The DMTH final model results are the multiscale thermal-hydrologic model output that considers the topography, stratigraphy, repository footprint and layout, and thermal variability among waste packages.	3,264 output locations 7 infiltration-flux/thermal-conductivity cases 8 distinct waste packages in the unit cell

NOTE: Collapsed drifts have been simulated using the LDTH and DDT submodels with high and low thermal conductivity of the rubble. The result is a time-dependent set of changes in the temperature at the waste package, drip shield, and invert; in the relative humidity at the waste package, drip shield, and invert; in the saturation of the invert; and in the liquid flux of the inner and outer invert, all compared to the values for an intact drift.

Source: SNL 2008a, Sections 6.2.4 to 6.2.9, 6.2.10[a] to 6.2.19[a], and Appendix IX.

Table 2.3.5-7. Peak Drift Wall and Waste Package Temperatures Over All Waste Packages Summarized for Seven Uncertainty Cases

Infiltration Flux, Host-Rock Thermal Conductivity Case	Peak Drift Wall Temperature (°C)			Peak Waste Package Temperature (°C)		
	Coolest	Median	Hottest	Coolest	Median	Hottest
P10L (low K_{th})	120.5	152.0	184.3	131.6	172.8	211.0
P10 (mean K_{th})	111.3	138.0	161.2	122.3	158.7	188.1
P10H (high K_{th})	102.7	126.6	149.5	113.5	147.2	176.5
P30 (mean K_{th})	109.2	136.4	160.5	120.1	157.0	187.3
P50 (mean K_{th})	107.8	135.3	159.6	118.8	156.0	186.4
P90 (mean K_{th})	103.8	131.0	159.6	114.6	152.1	186.4
P90H (high K_{th})	96.9	120.9	147.4	107.4	141.8	174.7
Ensemble	96.9	137.0	184.3	107.4	157.4	211.0

NOTE: These cases cover the range of infiltration-flux and host-rock thermal-conductivity uncertainty addressed. This table is based on data plotted in Figure 2.3.5-31.

Source: SNL 2008a, Table 6.3-49[b].

Table 2.3.5-8. Duration of Drift Wall Temperatures At or Above Boiling Summarized for Seven Uncertainty Cases

Infiltration-Flux, Host-Rock Thermal Conductivity Case	Time When Boiling at the Drift Wall Ceases (years after emplacement)						
	Shortest	10th Percentile	30th Percentile	Median	70th Percentile	90th Percentile	Longest
P10L (low K_{th})	189.2	423.9	680.2	848.9	962.9	1,088.8	1,345.1
P10 (mean K_{th})	148.5	295.7	516.6	672.6	784.7	890.0	1,153.3
P10H (high K_{th})	115.2	214.4	363.8	514.5	624.1	727.5	968.9
P30 (mean K_{th})	139.0	277.2	471.8	621.5	718.0	824.5	1,129.3
P50 (mean K_{th})	134.0	265.3	444.7	594.1	683.7	799.6	1,114.4
P90 (mean K_{th})	116.3	224.9	348.9	464.3	559.0	648.3	1,030.7
P90H (high K_{th})	87.3	169.3	243.6	319.1	405.0	560.6	900.8
Ensemble	87.3	263.4	453.2	610.3	741.9	930.0	1,345.1

NOTE: These cases cover the range of infiltration-flux and host-rock thermal conductivity uncertainty addressed. This table is based on data plotted in Figure 2.3.5-32 (panel “a”).

Source: SNL 2008a, Table 6.3-50[b].

Table 2.3.5-9. Maximum Lateral Extent of the Boiling-Point Isotherm (96°C), Summarized for Seven Uncertainty Cases

Infiltration-Flux, Host-Rock Thermal Conductivity Case	Maximum Lateral Extent of Boiling (T > 96°C) (m)						
	Least	Nominal 10th Percentile	30th Percentile	Median	70th Percentile	90th Percentile	Greatest
P10L (low K_{th})	6.62	8.19	9.25	9.89	10.27	10.57	11.12
P10 (mean K_{th})	5.86	7.24	7.84	8.06	8.20	8.43	9.21
P10H (high K_{th})	5.00	6.06	6.68	7.03	7.24	7.45	7.83
P30 (mean K_{th})	5.64	6.97	7.65	7.91	8.04	8.18	9.18
P50 (mean K_{th})	5.46	6.75	7.51	7.78	7.95	8.12	8.94
P90 (mean K_{th})	4.97	6.22	6.59	6.95	7.36	7.82	8.66
P90H (high K_{th})	4.38	5.34	5.92	6.09	6.19	6.38	7.69
Ensemble	4.38	6.39	7.23	7.82	8.19	10.01	11.12

NOTE: The lateral extent of the boiling-point isotherm is measured from the center of the emplacement drift. These cases cover the range of infiltration-flux and host-rock thermal-conductivity uncertainty addressed. This table is based on data plotted in Figure 2.3.5-32.

Source: SNL 2008a, Table 6.3-51[a].

Table 2.3.5-10. Relationship of Evaporated Seepage Water to Brine Types and Corrosion Test Solutions

Group Water	Dominant Constituents in Endpoint Brines	Brine Type	Corresponding Corrosion Test Solution
Group 1, low water–rock interaction parameter	Na-K-NO_3-Cl	Carbonate	SDW, SCW, BSW, SSW, NaCl
Group 1, moderate water–rock interaction parameter	Na-K-Cl-NO_3	Carbonate	SDW, SCW, BSW, SSW, NaCl
Group 1, high water–rock interaction parameter	K-Na-NO_3-CO_3-Cl	Carbonate	SDW, SCW, BSW, SSW, NaCl
Group 2, low water–rock interaction parameter	Ca-K-Na-NO_3-Cl	Calcium Chloride	$CaCl_2$; $CaCl_2 + Ca(NO_3)_2$, SSW, NaCl
Group 2, moderate water–rock interaction parameter	Na-K-NO_3-Cl	Sulfate	SAW, SSW, NaCl
Group 2, high water–rock interaction parameter	K-Na-NO_3-CO_3-Cl	Carbonate	SDW, SCW, BSW, SSW, NaCl
Group 3, low water–rock interaction parameter	Ca-Mg-Cl-NO_3	Calcium chloride	$CaCl_2$; $CaCl_2 + Ca(NO_3)_2$, SSW, NaCl
Group 3, moderate water–rock interaction parameter	Mg-K-Na-Cl-NO_3	Carbonate	SDW, SCW, BSW, SSW, NaCl
Group 3, high water–rock interaction parameter	K-Na-NO_3-Cl-CO_3	Carbonate	SDW, SCW, BSW, SSW, NaCl
Group 4, low water–rock interaction parameter	Na-K-NO_3-Cl	Sulfate	SAW, SSW, NaCl
Group 4, moderate water–rock interaction parameter	Na-K-NO_3-Cl	Sulfate	SAW, SSW, NaCl
Group 4, high water–rock interaction parameter	K-Na-Cl-NO_3-CO_3	Carbonate	SDW, SCW, BSW, SSW, NaCl

NOTE: Cations, then anions, are listed in descending order of concentration.
BSW = basis saturated water; SAW = simulated acidified water; SCW = simulated concentrated water; SDW = simulated dilute water; SSW = simulated saturated water

Source: SNL 2007b, Table 6.13-7.

Table 2.3.5-11. Maximum Differences Between Predictions and Measurements for pH, Ionic Strength, Chlorine, Fluorine, NO_3, and the Cl/NO_3 Ratio

Evaporation Simulation	pH[a] (pH units)	Ionic Strength (RPD)	Cl (RPD)	NO_3 (RPD)	Cl/NO_3 Ratio (RPD)
J-13 Evaporation Experiment (SNL 2007k, Section 7.2.1)	–0.79	–12%	26%	18%	16%
100x J-13 Evaporation Experiment (SNL 2007k, Section7.2.2)	Not measured	Not estimated[b]	5%	8%	–3%
Topopah Spring Tuff Pore-Water Evaporation (SNL 2007k, Section 7.2.3) Experiment at 75°C	0.17	–2%	–9%	Not measured	Not measured
Topopah Spring Tuff Pore-Water Evaporation Experiments at 95°C (SNL 2007k, Section 7.2.4)	–0.68	50%	–12%	20%	9%
Seawater Evaporation (SNL 2007k, Section 7.2.5)	–0.79	15%[b]	10%[c]	Not measured	Not measured

NOTE: [a]The difference between measured pH and modeled (Pitzer) pH provides a maximum value for pH uncertainty (Section 2.3.5.5.3.3.2).
[b]Not estimated. pH needed for estimate.
[c]Based on two data points.
RPD (relative percent difference) = 100% * ([predicted concentration] – [measured concentration]) / [measured concentration].

Source: SNL 2007k, Table 7-9.

Table 2.3.5-12. Estimated In-Drift Precipitates/Salts Model Uncertainties for Temperatures between 20°C and 140°C

Parameter[a]	Units	*RH* Range				
		100% to 85%	**85% to 65%**	**65% to 40%**	**40% to 20%**	**20% to 0%**
Cl^-	log molal	±0.0	±0.1	±0.4	±0.5	±0.7
NO_3^-	log molal	±0.0	±0.2	±0.4	±0.5	±0.9
$Cl^- + NO_3^-$[b]	log molal	±0.0	±0.22	±0.57	NA	NA
Ionic Strength	log molal	±0.1	NA[c]			
Cl^-/NO_3^-	log mole ratio	Discrete dist. to 60%-72%[d]	±0.2	±0.5	±0.5	±1.4
pH	pH units	Discrete dist. to 75%[e]	±1	±2	±2	±2
F^-	log molal	±0.5[f]	±0.5	±0.5	±0.5	±0.5

NOTE: [a]Unless specifically stated otherwise, the uncertainties of these parameters can be described with a triangular distribution with the most likely uncertainty defined as ±0% and the maximum and minimum uncertainties defined by the values in this table. The uncertainties for pH represent uncertainties in the evaporative evolution of pH in unbuffered systems. The uncertainty in pH may be reduced by considering pH buffering reactions in specific systems.
[b]Uncertainties calculated assuming linear combinations of independent variables.
[c]Not applicable to TSPA. Prediction of ionic strength is for colloids model. At *RH* below 85%, ionic strength is greater than 1 molal, which is far above the critical ionic strength where colloids are unstable.
[d]Above the relative humidity at which salt precipitation occurs (between 72% and 60%), discrete distributions of chloride:nitrate ratios for each of the four water groups are sampled. No model uncertainty is added to the sampled value.
[e]Above a relative humidity of 75%, a discrete distribution of pH uncertainties, based on model-data comparisons, is sampled.
[f]The exception for this estimated uncertainty is for a model simulation of a solution saturated with respect to sellaite (MgF_2). The model simulation underestimates the total soluble fluorine, probably because there is experimental uncertainty in the solubility of MgF_2 given by Lide (2000).
Consistent with use in project corrosion models, NO_3^-, Cl^-, and F^- in this table represent total N, total Cl, and total fluorine in solution, respectively.

Source: SNL 2007k, Table 7-10; SNL 2007b, Section 6.12.3, Tables 6.12-1 and 6.12-2.

Table 2.3.5-13. Model Predictions of Equilibrium Relative Humidity for Saturated Aqueous Solutions in Contact with an Excess of Solid-Phase Salts

Salt	Predicted Equilibrium Relative Humidity (or Deliquescence Point) (%)	Temperature (°C)	Difference Compared to Handbook Values[a] (%)	Precipitating Mineral
NaCl	74.7	80	–1.7	Halite
KCl	77.0	80	–2.5	Sylvite
$MgCl_2 \cdot 6H_2O$	37.0	25	4.0	Bischofite
$Na_2CO_3 \cdot 10H_2O$	90.0	24.5	3.0	Natron
$K_2CO_3 \cdot 2H_2O$	37.8	40	–4.2	$K_2CO_3 \cdot 1.5H_2O$
NaF	96.1	100	–0.5	Villiaumite
KF	28.0	100	5.1	Carobbite
$Na_2SO_4 \cdot 10H_2O$	95.6	20	2.6	Mirabilite
K_2SO_4	96.4	60	0.4	Arcanite
$NaNO_3$	61.6	80	–3.9	Soda niter
KNO_3	77.9	60	–4.1	Niter

NOTE: [a]Handbook values are from Dean 1992.

Source: SNL 2007k, Table 7-4.

INTENTIONALLY LEFT BLANK

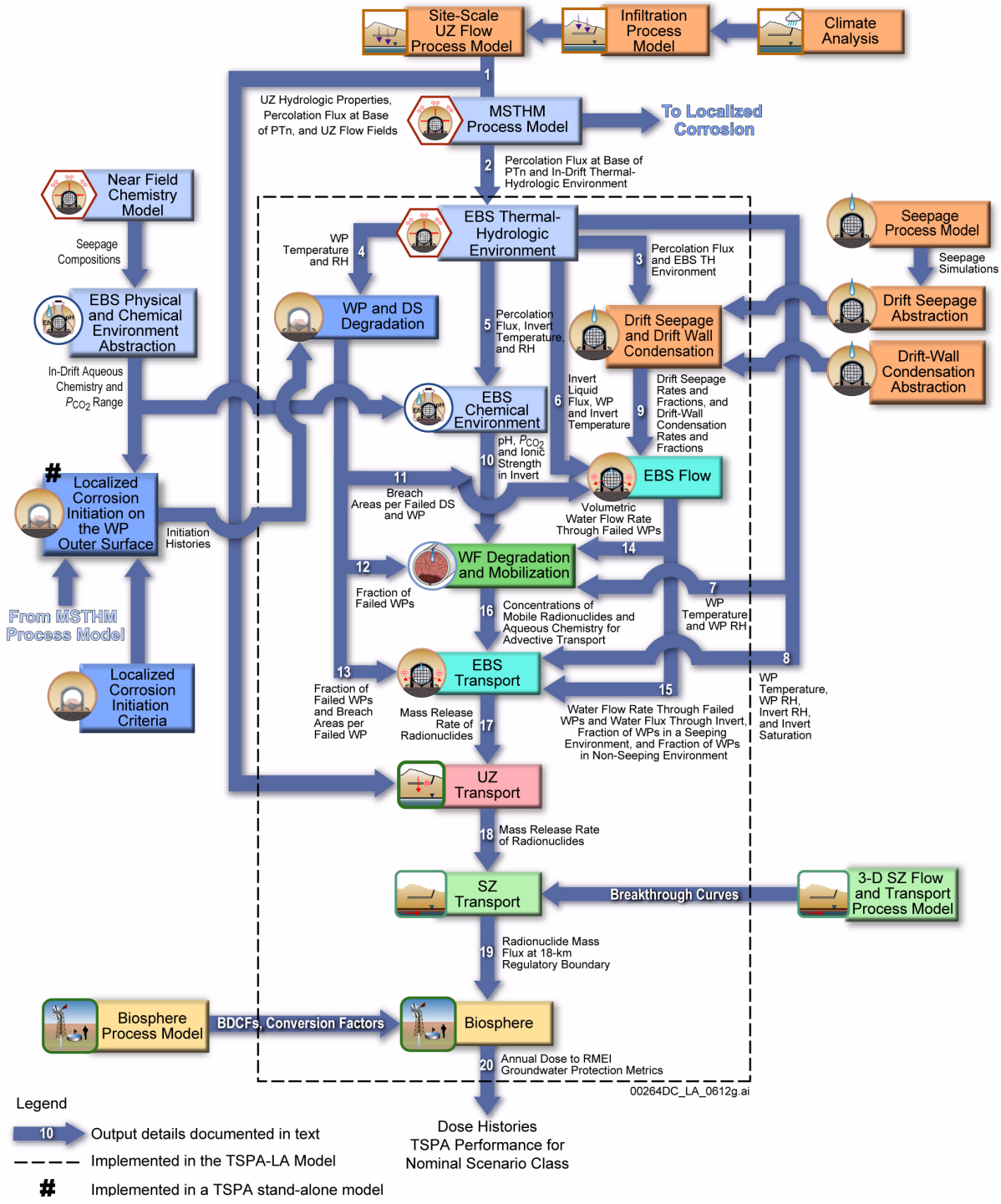

Figure 2.3.5-1. Information Transfer Among the Principal Model Components of the TSPA Nominal Scenario Class Model

NOTE: For details about outputs and information transfer shown on this figure, see Section 2.4.2.3.2.1.
DS = drip shield; LC = localized corrosion; PA = performance assessment; RH = relative humidity; SZ = saturated zone; TH = thermal-hydrologic; THC = thermal-hydrologic-chemical; UZ = unsaturated zone; WF = waste form; WP = waste package.

Source: SNL 2008b.

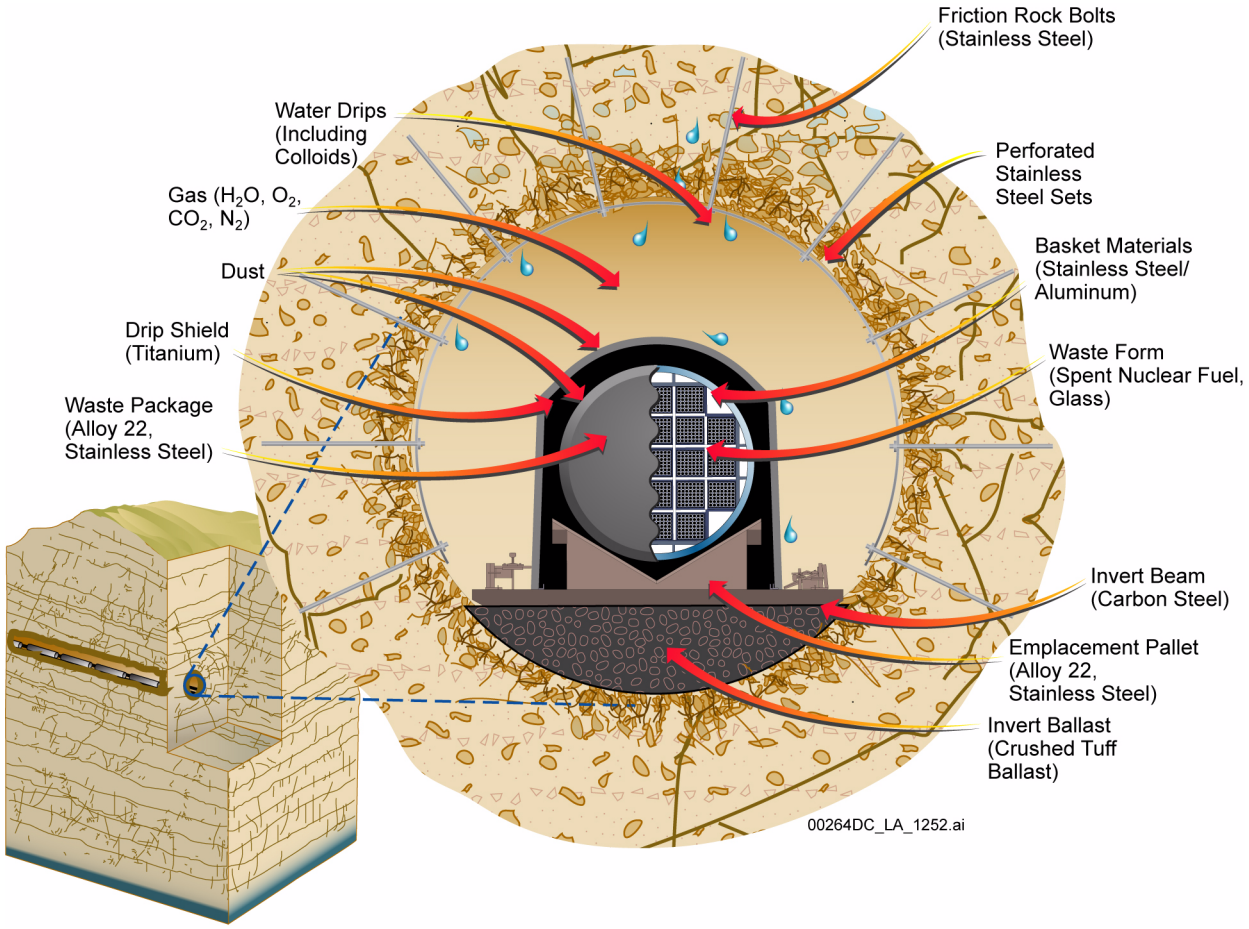

Figure 2.3.5-2. General Locations of Engineered Barrier System Features and Materials

Source: SNL 2007b, Figure 6.5-1.

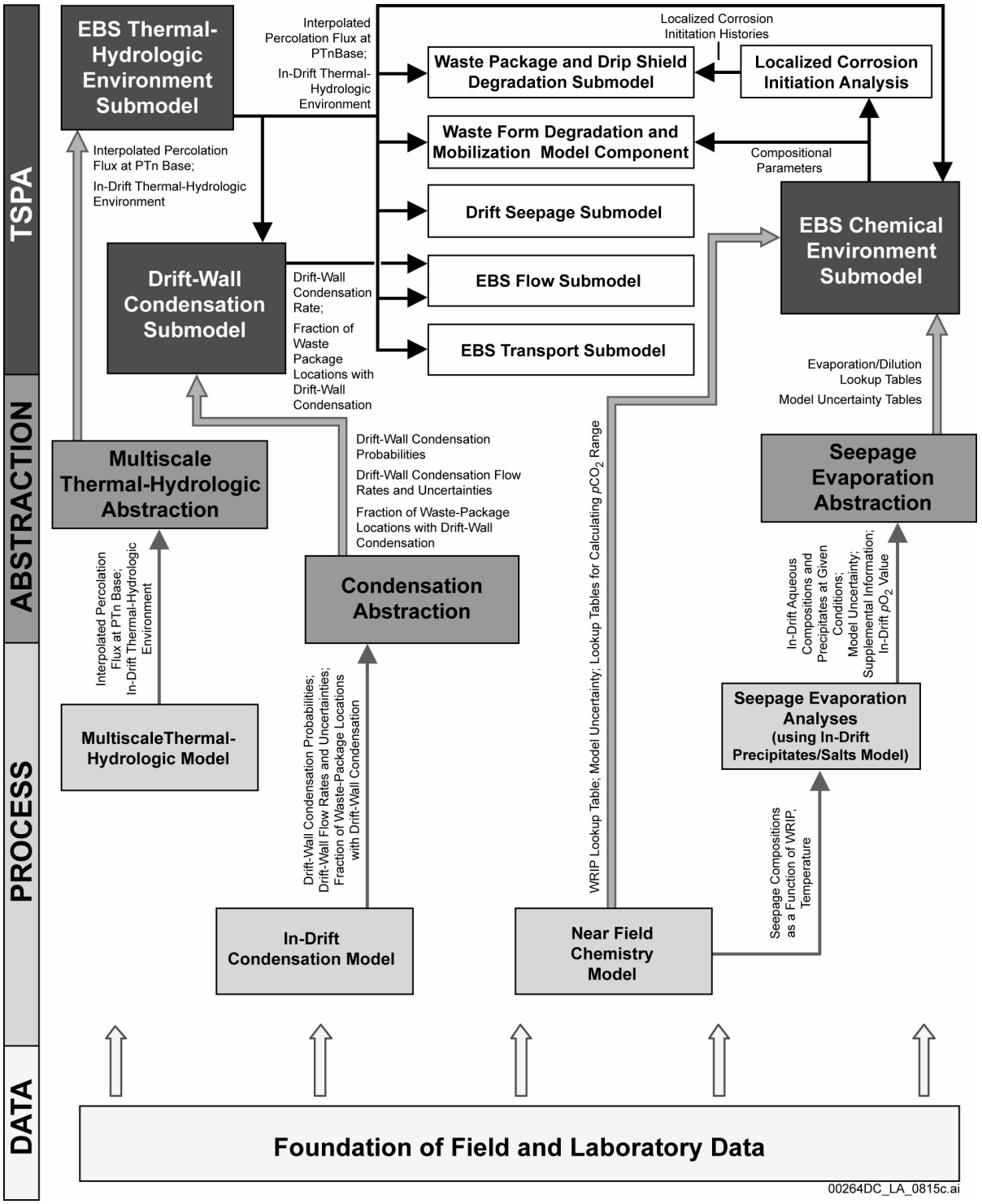

Figure 2.3.5-3. Information Flow Supporting TSPA for the In-Drift Physical and Chemical Environment Models and Analyses at the Data, Process, Abstraction, and Total System Performance Assessment Levels

NOTE: WRIP = water-rock interaction parameter.

Source: SNL 2008b.

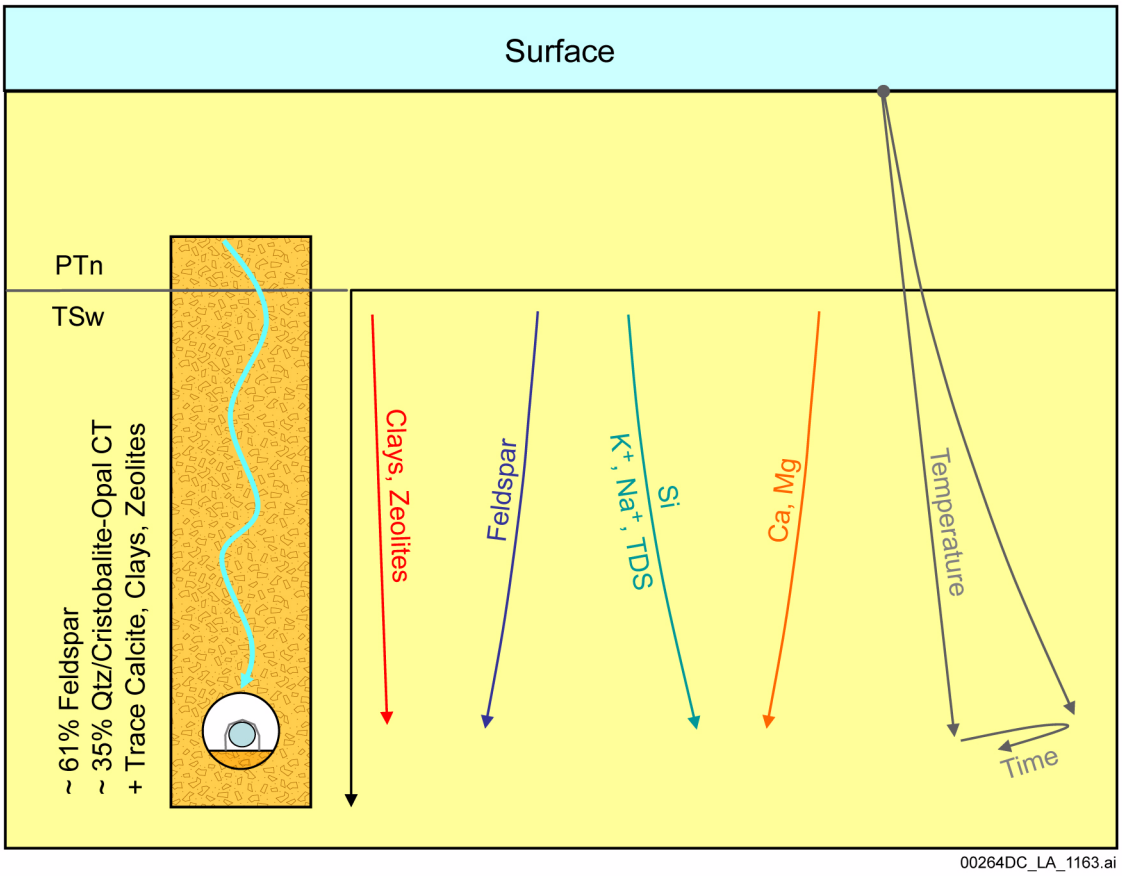

Figure 2.3.5-4. Generalized Processes Incorporated into the Near-Field Chemistry Model

NOTE: As water percolates down through the evolving thermal field above the drift, feldspar and silica phases dissolve, releasing Na^{+}, K^{+}, and dissolved silica, while secondary minerals (clays and zeolites) precipitate, reducing Ca^{+2} and Mg^{+2} in solution.

Source: SNL 2007b, Figure 6.3-1.

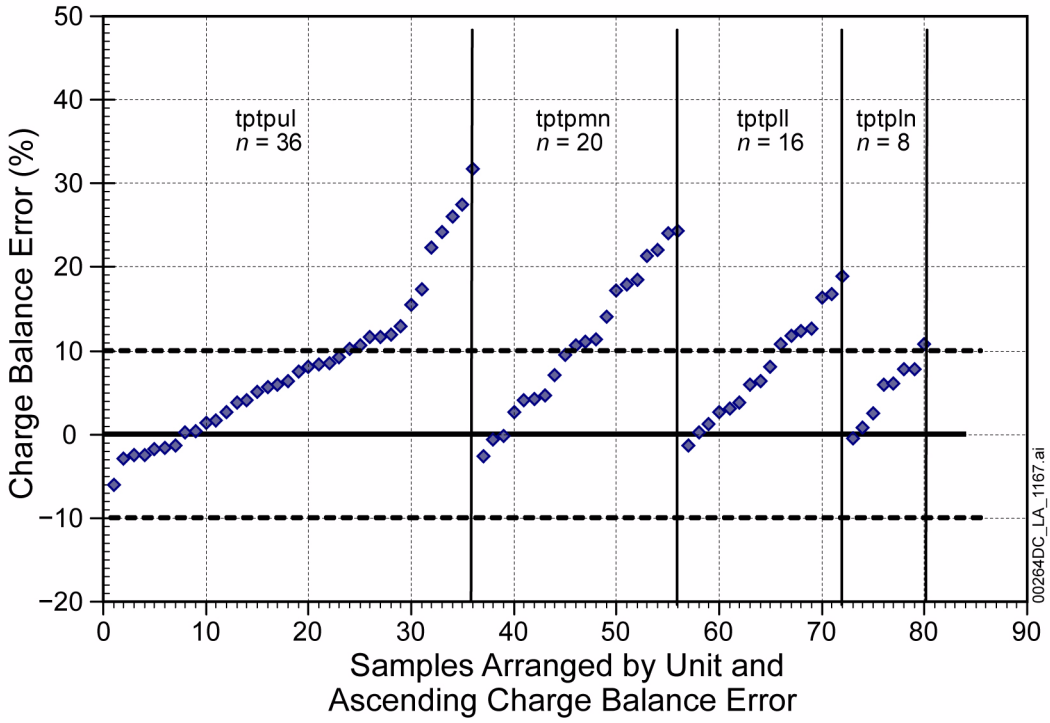

Figure 2.3.5-5. Calculated Charge Balance Error for TSw Pore-Water Analyses

NOTE: Charge balance = $(Equiv_{cations} - Equiv_{anions}) / (Equiv_{cations} + Equiv_{anions})$. Dotted lines indicate ±10% error in charge balance, corresponding to the acceptable range. Ten analyses missing bicarbonate are not shown.

Source: SNL 2007b, Figure 6.6-2.

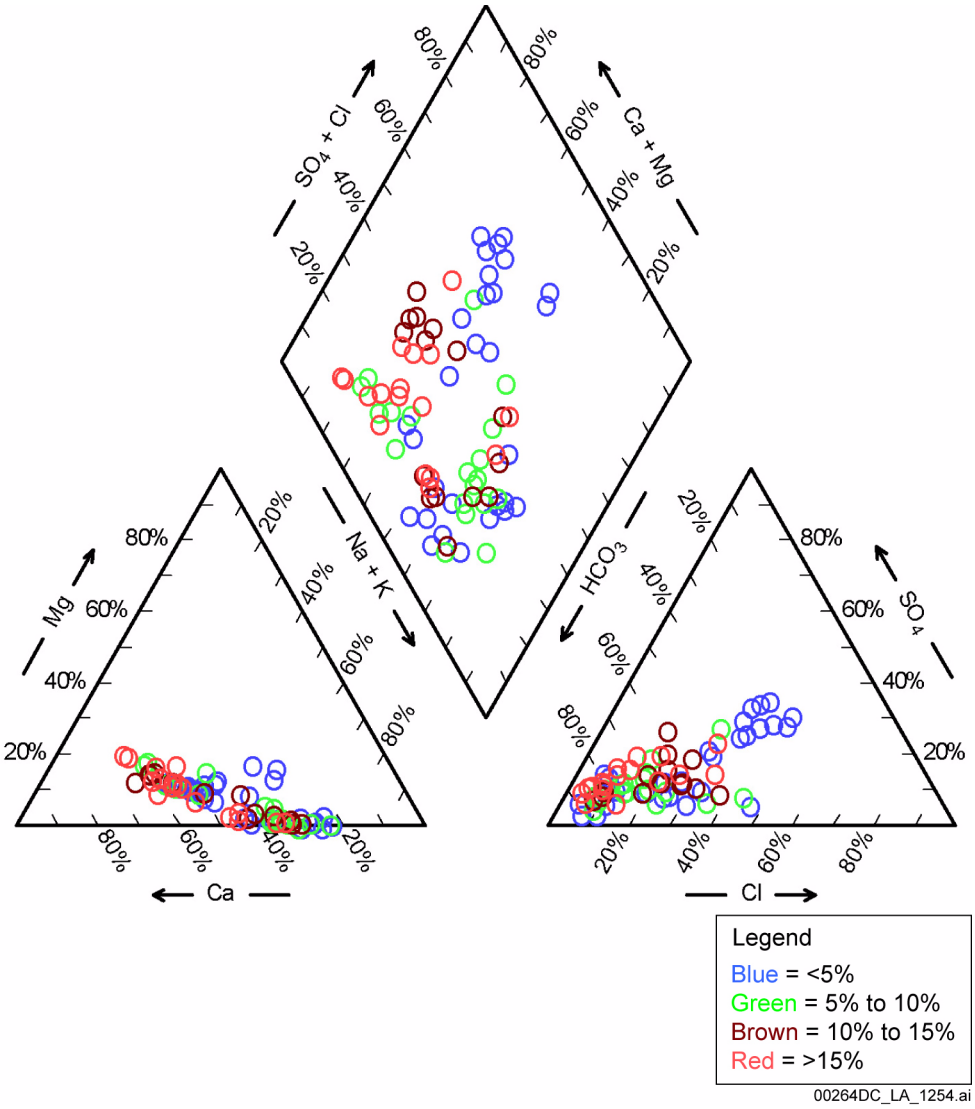

Figure 2.3.5-6. Piper Plot of 80 TSw Pore Waters, Color-Coded to Show the Magnitude of the Charge Balance Error

NOTE: Samples for which bicarbonate was not analyzed are not plotted.

Source: SNL 2007b, Figure 6.6-3.

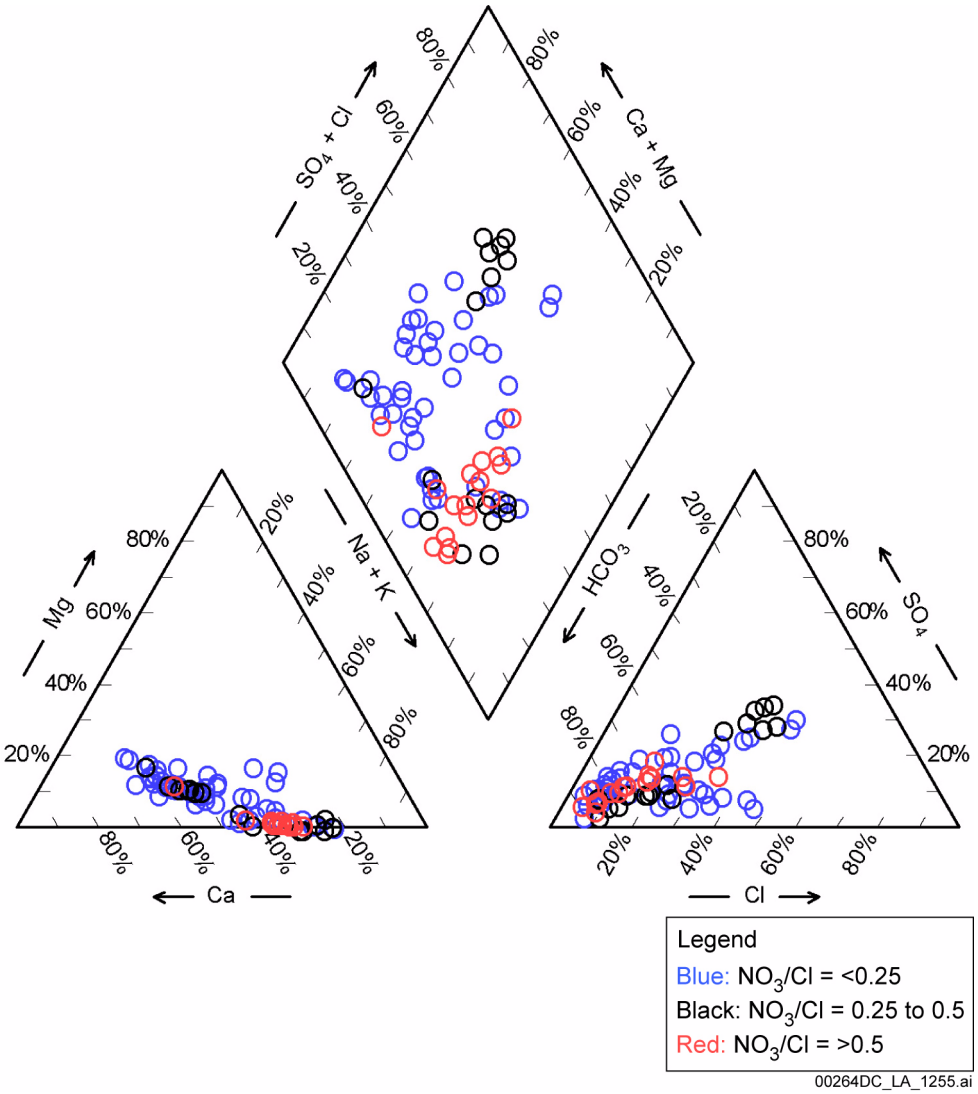

Figure 2.3.5-7. Piper Plot of 80 TSw Pore Waters, Color-Coded to Show the Magnitude of the NO_3/Cl Ratio

NOTE: Samples for which bicarbonate was not analyzed are not plotted.

Source: SNL 2007b, Figure 6.6-4.

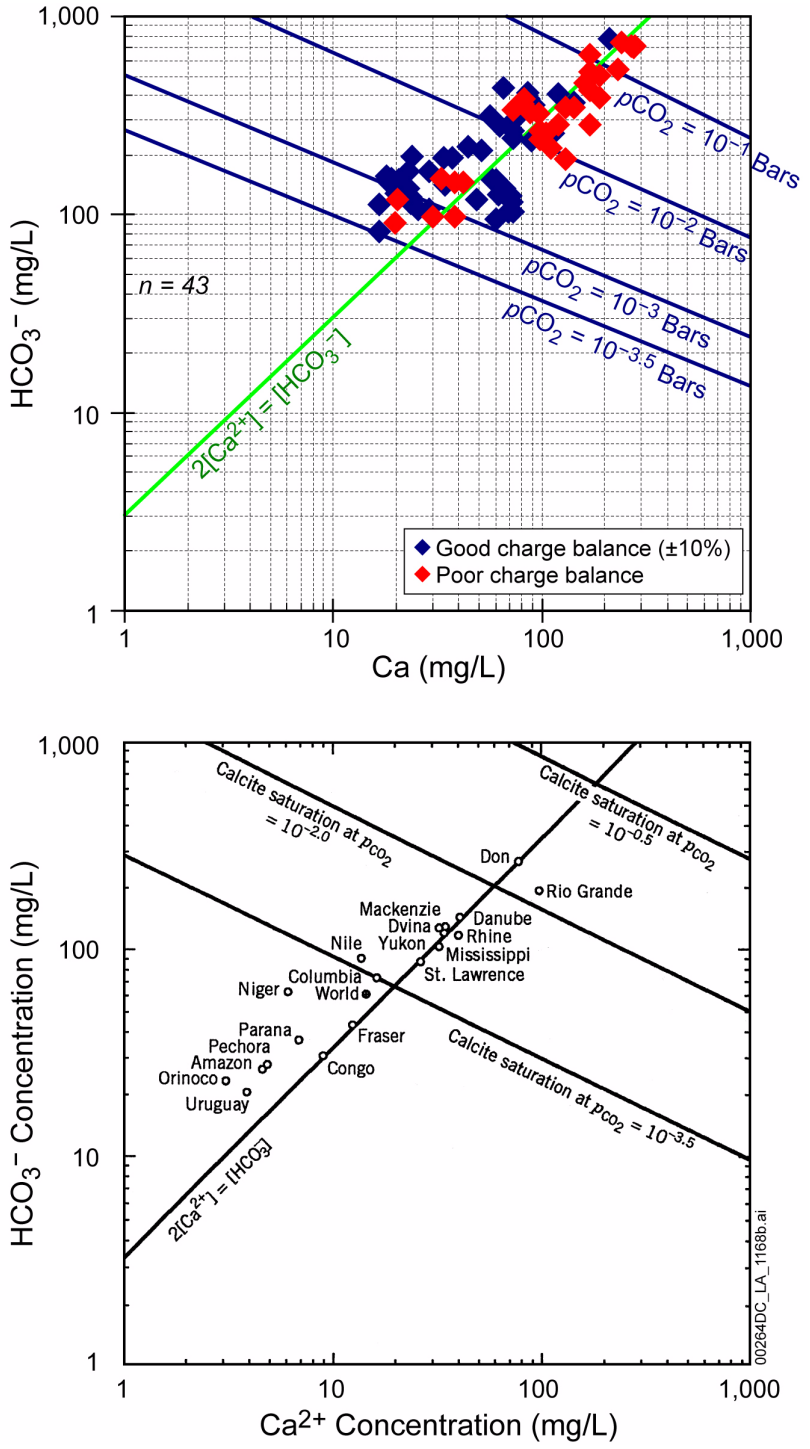

Figure 2.3.5-8. TSw Pore Waters (Upper) are in Equilibrium with pCO_2 Values Greater than 10^{-3} bars, the Ambient Gas-Phase Concentration in the Rock; Elevated pCO_2 Values Observed in Surface Waters (Lower) are Commonly Attributed to Microbial Activity

NOTE: Blue lines represent calcite saturation at the stated pCO_2 for the Ca-CO_2-H_2O system.

Source: Upper: SNL 2007b, Figure 6.6-8. Lower: Stumm and Morgan 1996, Figure 4.15.

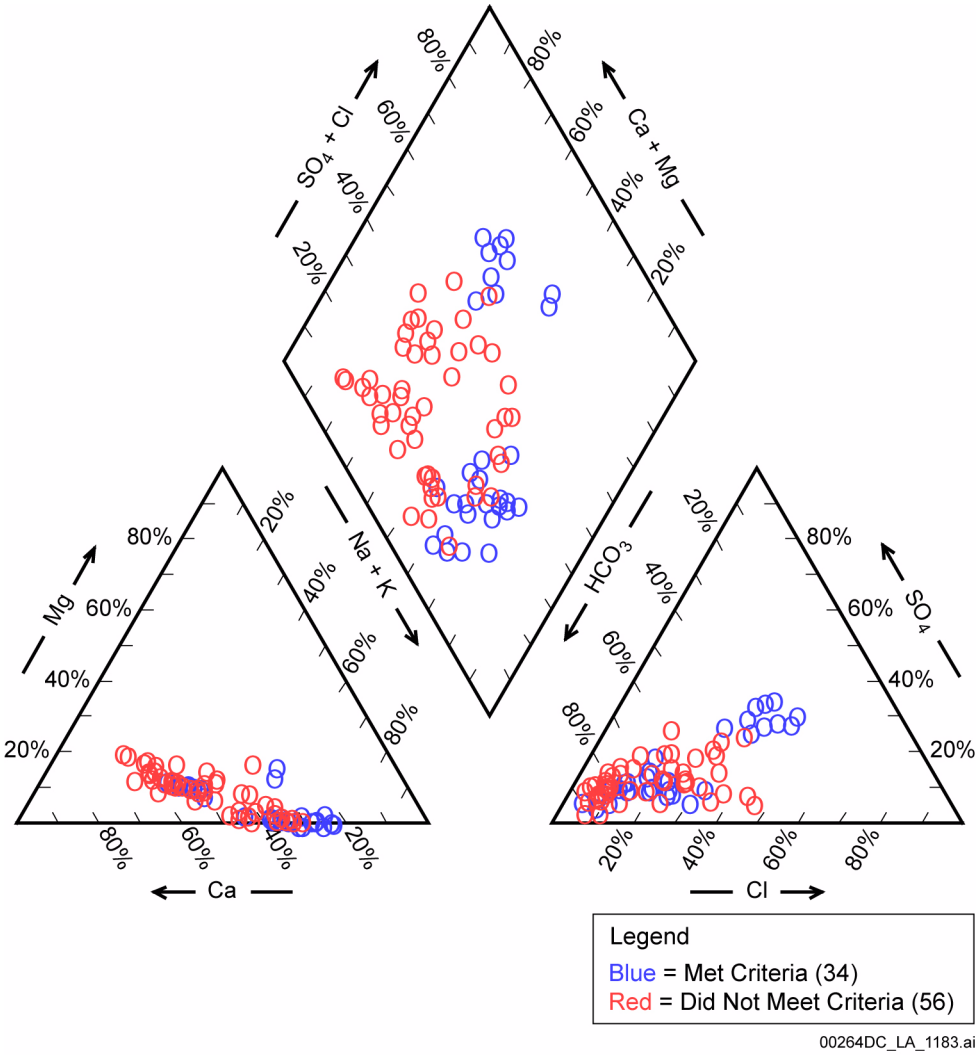

Figure 2.3.5-9. Piper Diagram Showing Pore Waters That Passed and Failed the Quality Screening Criteria

NOTE: Samples for which bicarbonate was not analyzed are not plotted, but are included in the totals.

Source: SNL 2007b, Figure 6.6-12.

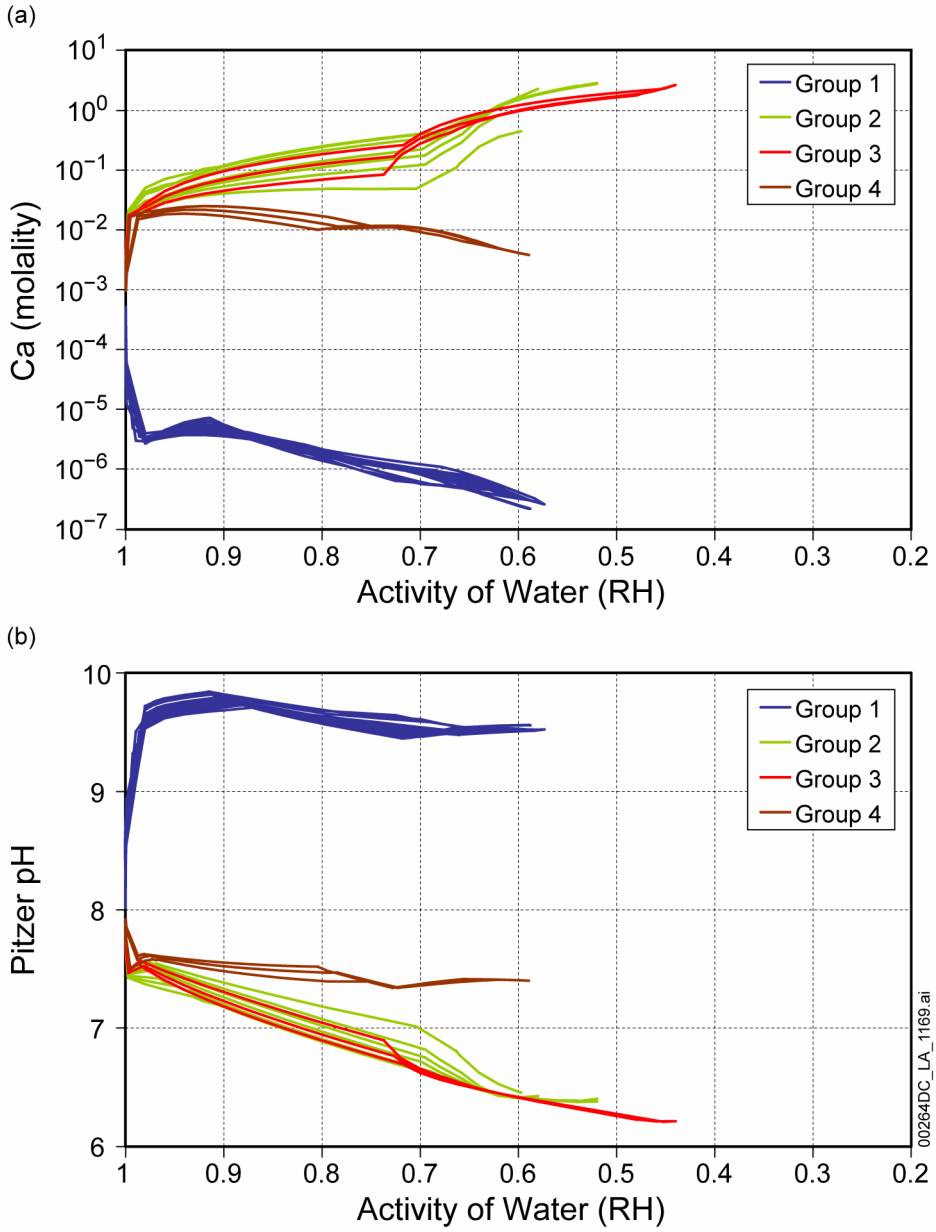

Figure 2.3.5-10. Evaporative Evolution of the 34 TSw Pore Waters That Meet the Screening Criteria; Calcium Concentration (upper) and pH (lower)

NOTE: The colors indicate the four groups determined by principal component analysis.

Source: SNL 2007b, Figure 6.6-17.

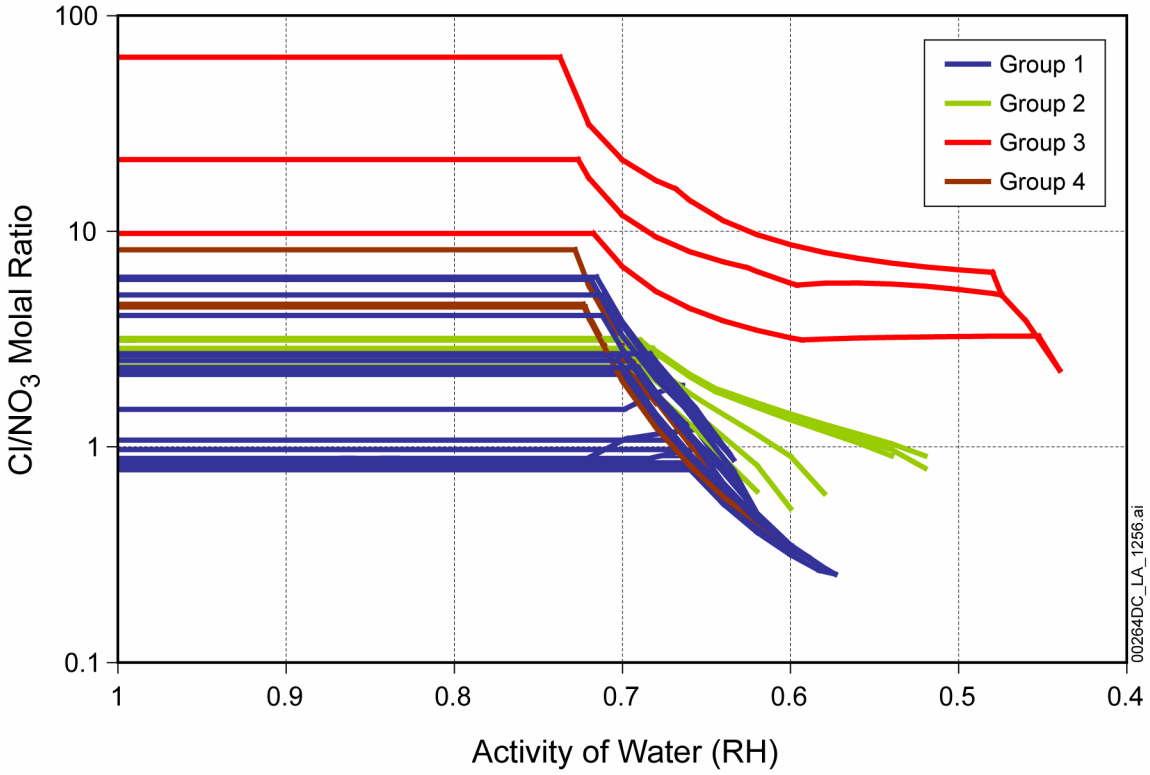

Figure 2.3.5-11. Change in Chloride-Nitrate Molal Ratio with Evaporation

NOTE: The colors indicate the four groups determined by principal component analysis.

Source: SNL 2007b, Figure 6.6-18.

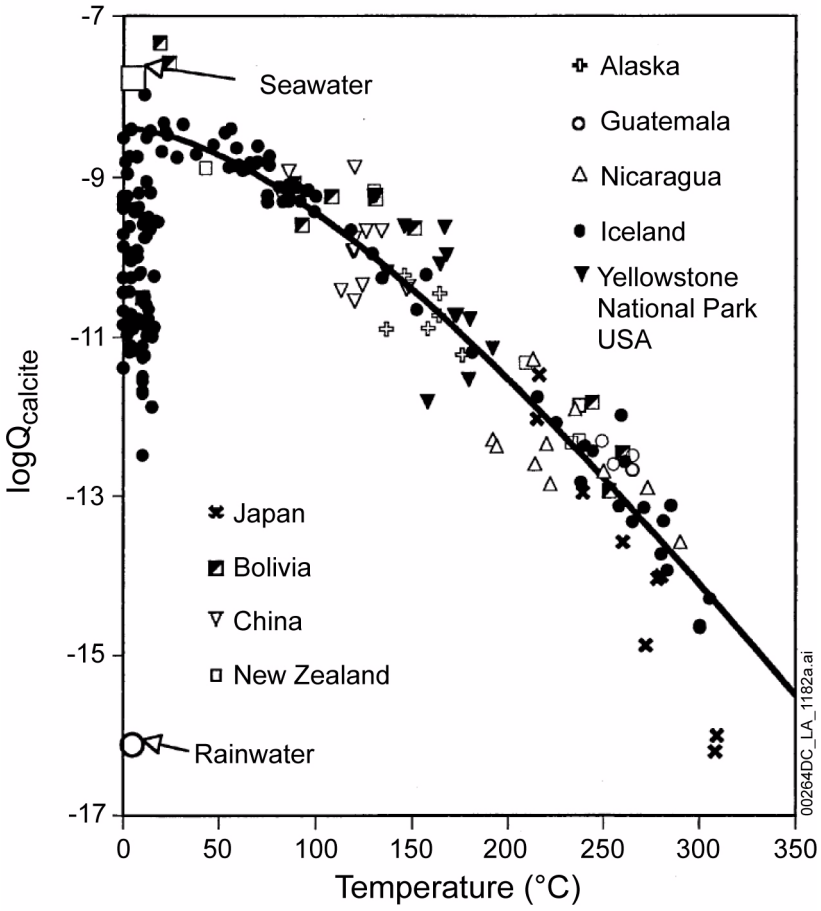

Figure 2.3.5-12. Comparison of Predicted Calcite Solubility Curves with Water Compositional Data from Several Geothermal Fields

Source: Stefansson and Amorsson 2000, Figure 4a.

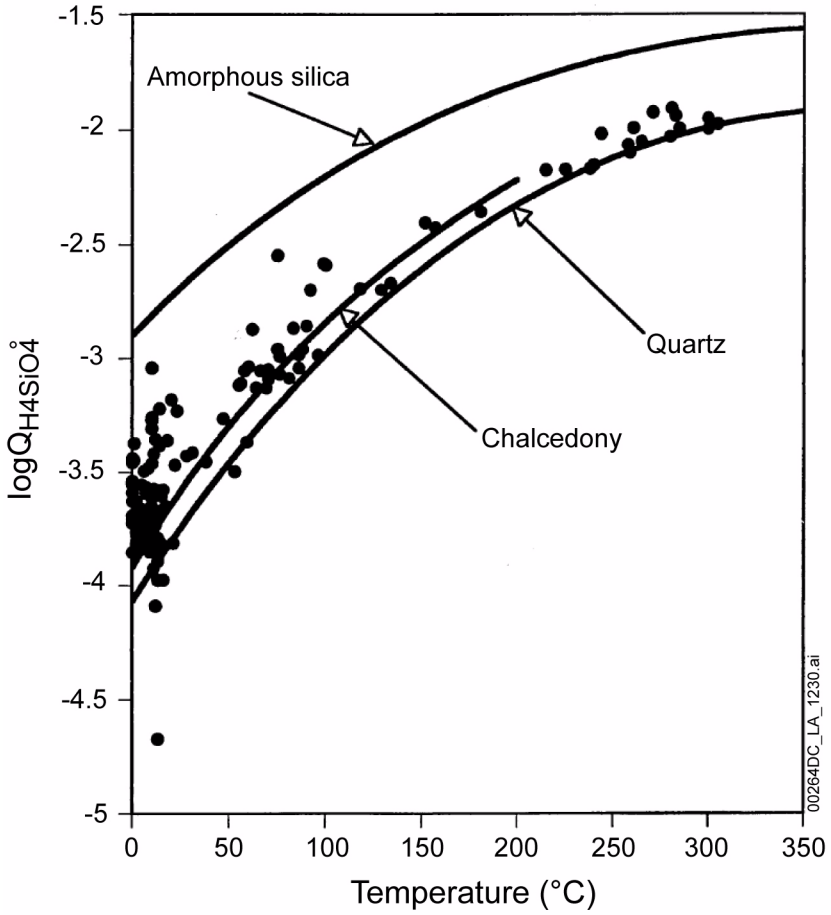

Figure 2.3.5-13. Comparison of Predicted Silica Polymorph Solubility Curves with Water Compositional Data from Several Geothermal Fields

Source: Stefansson and Arnorsson 2000, Figure 4b.

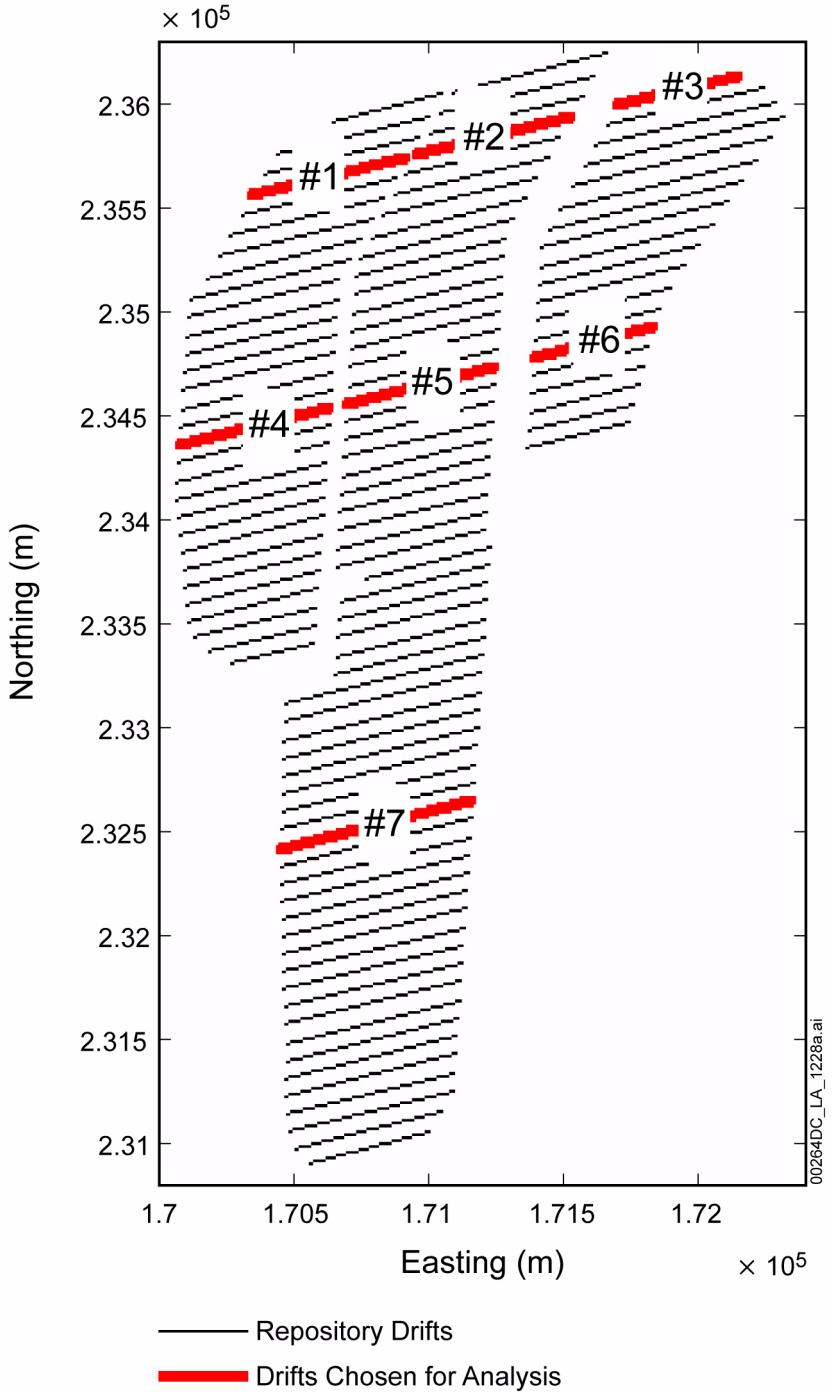

Figure 2.3.5-14. Location of Drifts Along Which Thermal Profiles to the Land Surface Were Generated

Source: SNL 2007e, Figure 6-2[a].

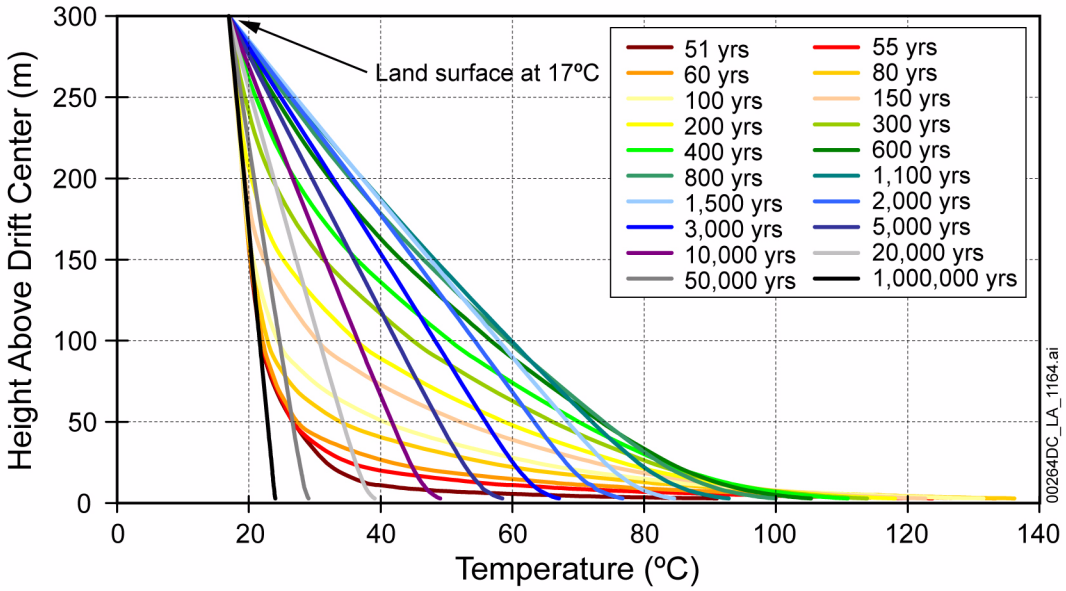

Figure 2.3.5-15. Thermal Profiles Above the Drift, Through Time

NOTE: Values in legend are “years since loading and beginning of ventilation” (i.e., repository closure is at 50 years). In this simulation, the maximum drift wall temperature was 137°C at 70 years after loading (20 years after cessation of ventilation and closure), and the drift wall remained above boiling for 900 to 1,000 years. The land surface is 17°C at a distance of 300 m above the drift. These thermal profiles are for a location near the center of Drift choice 4 (Figure 2.3.5-14), using the mean rock thermal conductivities.

Source: SNL 2007b, Figure 6.3-6.

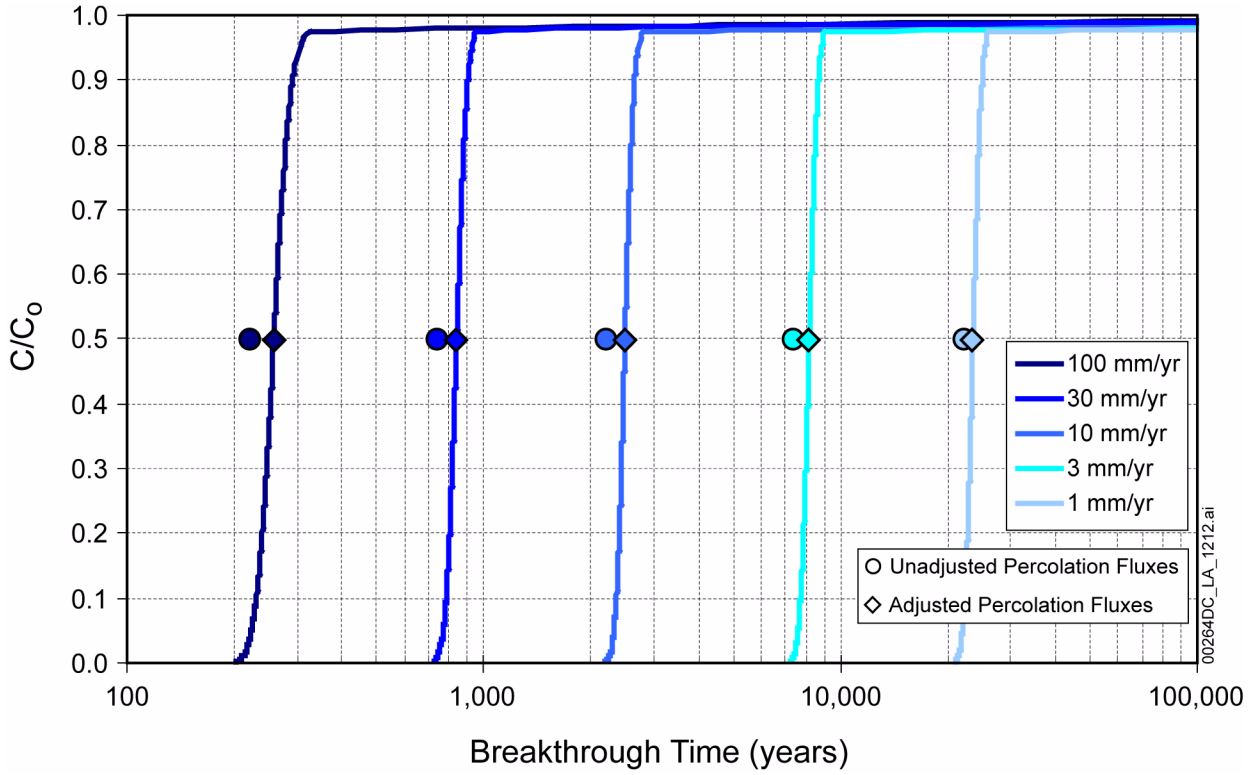

Figure 2.3.5-16. Breakthrough Curves Generated by FEHM Modeling of Transport Through the TSw at Five Different Percolation Fluxes, Using the Particle Tracking Option

NOTE: Also shown are the predicted transport times for the same percolation fluxes using a plug flow assumption (filled circles) and also transport times for "adjusted" percolation fluxes (filled diamonds).

Source: SNL 2007b, Figure 6.3-7.

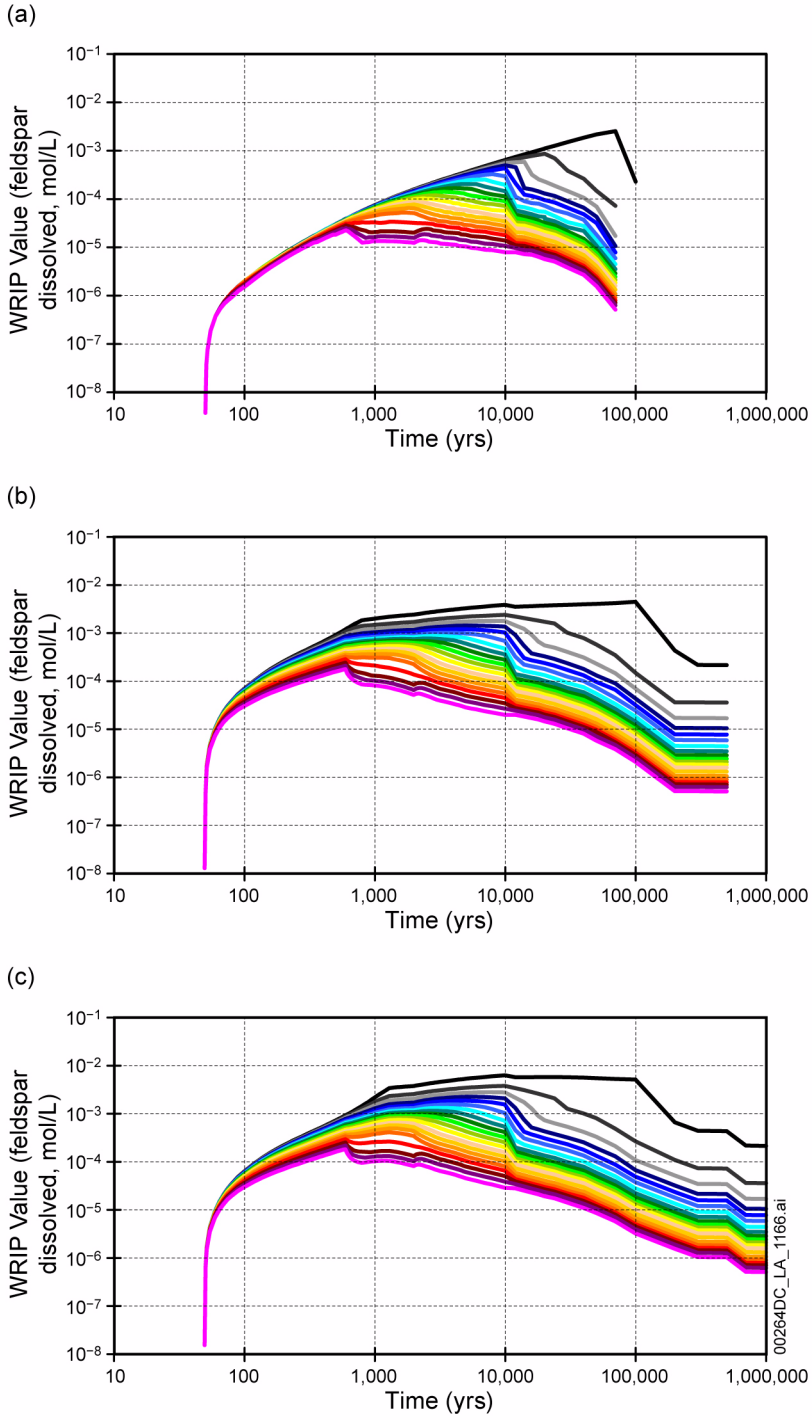

Figure 2.3.5-17. Calculated Water-Rock Interaction Parameters Values (Moles Feldspar Dissolved) for Three Different Locations within the Drift: (a) the Coolest Location Evaluated (Thermal Measure = 37.8); (b) a Median Thermal Measure Value (Thermal Measure = 859); and (c) the Hottest Location Evaluated (Thermal Measure = 1,546)

NOTE: The twenty profiles in each case represent the twenty sets of percolation flux sets implemented in the near-field chemistry model with the flux rates increasing from black to red.

Source: SNL 2007b, Figure 6.3-8.

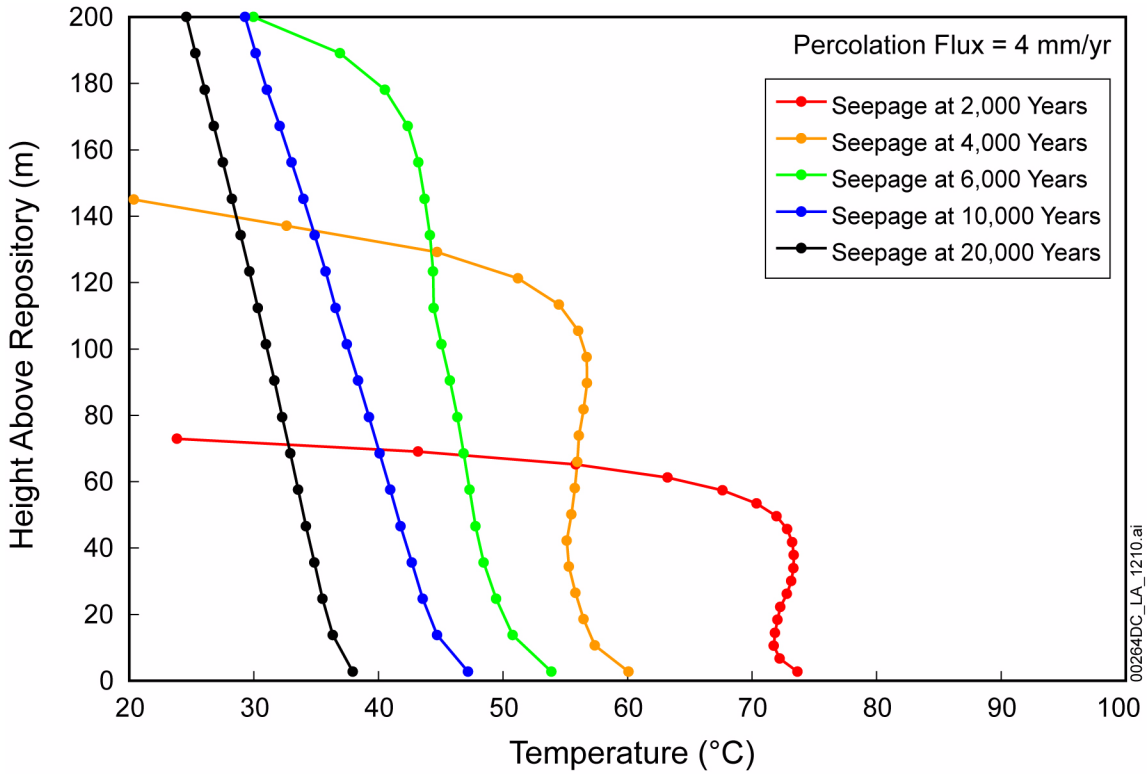

Figure 2.3.5-18. Temperature-Flow Paths Followed by Percolating Waters Representing Five Different Seepage Times

NOTE: For a 4-mm/year flux rate, the water reaching the repository at 2,000 and 4,000 years starts at an elevation below the top of the near-field chemistry model section (200 m).

Source: SNL 2007b, Figure 6.3-9.

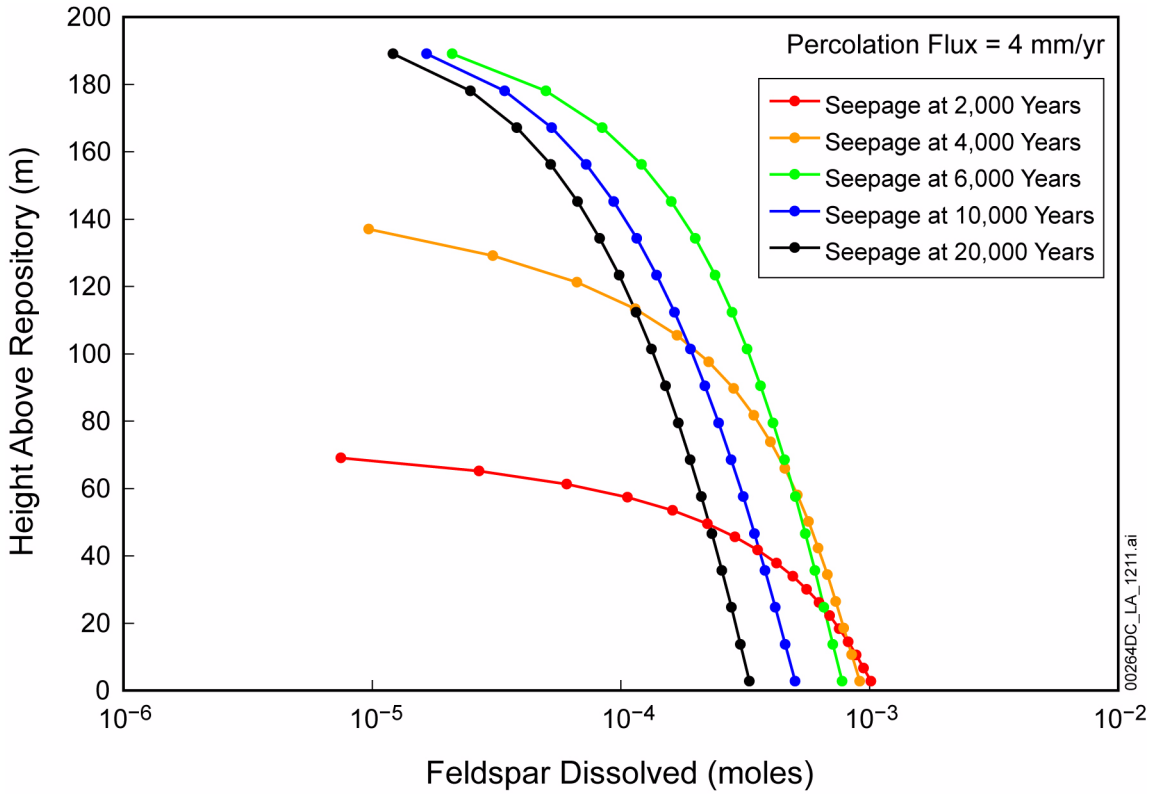

Figure 2.3.5-19. Cumulative Amount of Feldspar Dissolved as Water Percolates along the Temperature-Flow Paths

NOTE: Temperature-flow paths are given in Figure 2.3.5-18

Source: SNL 2007b, Figure 6.3-10.

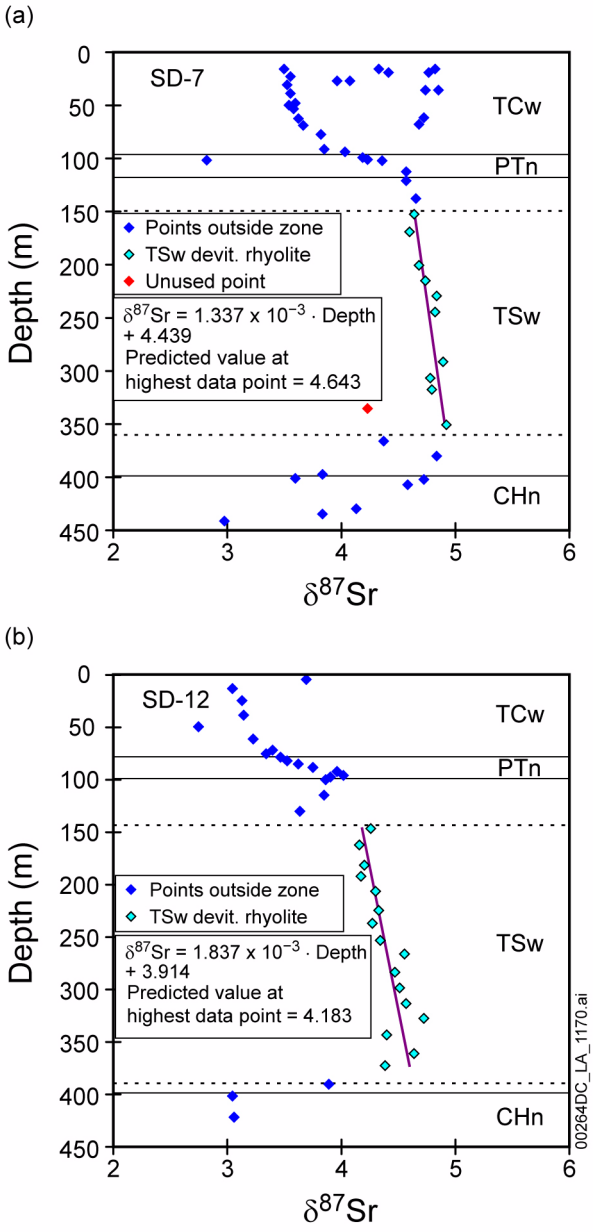

Figure 2.3.5-20. Pore-Water $\delta^{87}Sr$ Values Systematically Increase with Depth Through the Devitrified Rhyolitic Center of the TSw

NOTE: Data for Boreholes SD-7 and SD-12. One point in the interval for SD-7 was not included in the fit.

Source: SNL 2007b, Figure 7.1-3.

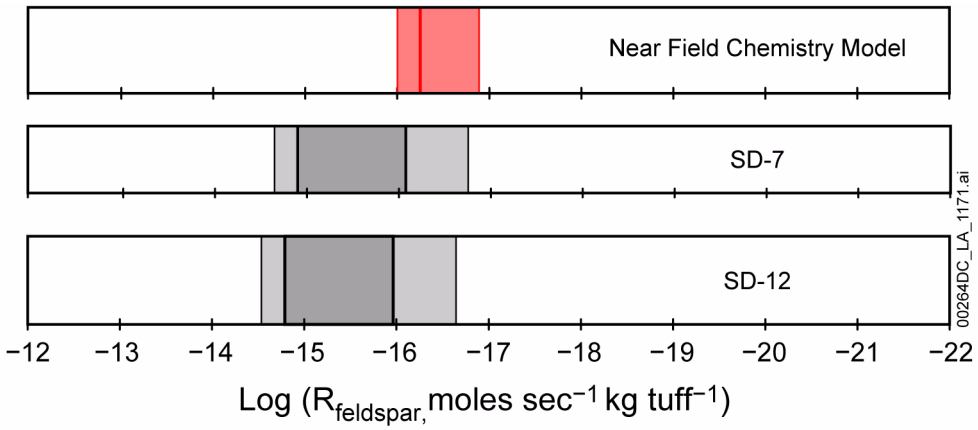

Figure 2.3.5-21. Comparison of the Near-Field Chemistry Model Feldspar Dissolution Rates with Rates Calculated from Pore-Water Strontium Isotopic Data, Boreholes SD-7 and SD-12

NOTE: The near-field chemistry model implements a range of values, as shown. The heavy line represents the mean value. Rates calculated from strontium isotopic data are a function of assumed percolation flux, with the darker regions representing flux rates from 1 mm/yr (lowest rate) to 15 mm/yr (highest rate); lighter regions indicate the expanded range if uncertainty in estimated parameters is included.

Source: SNL 2007b, Figure 7.1-4.

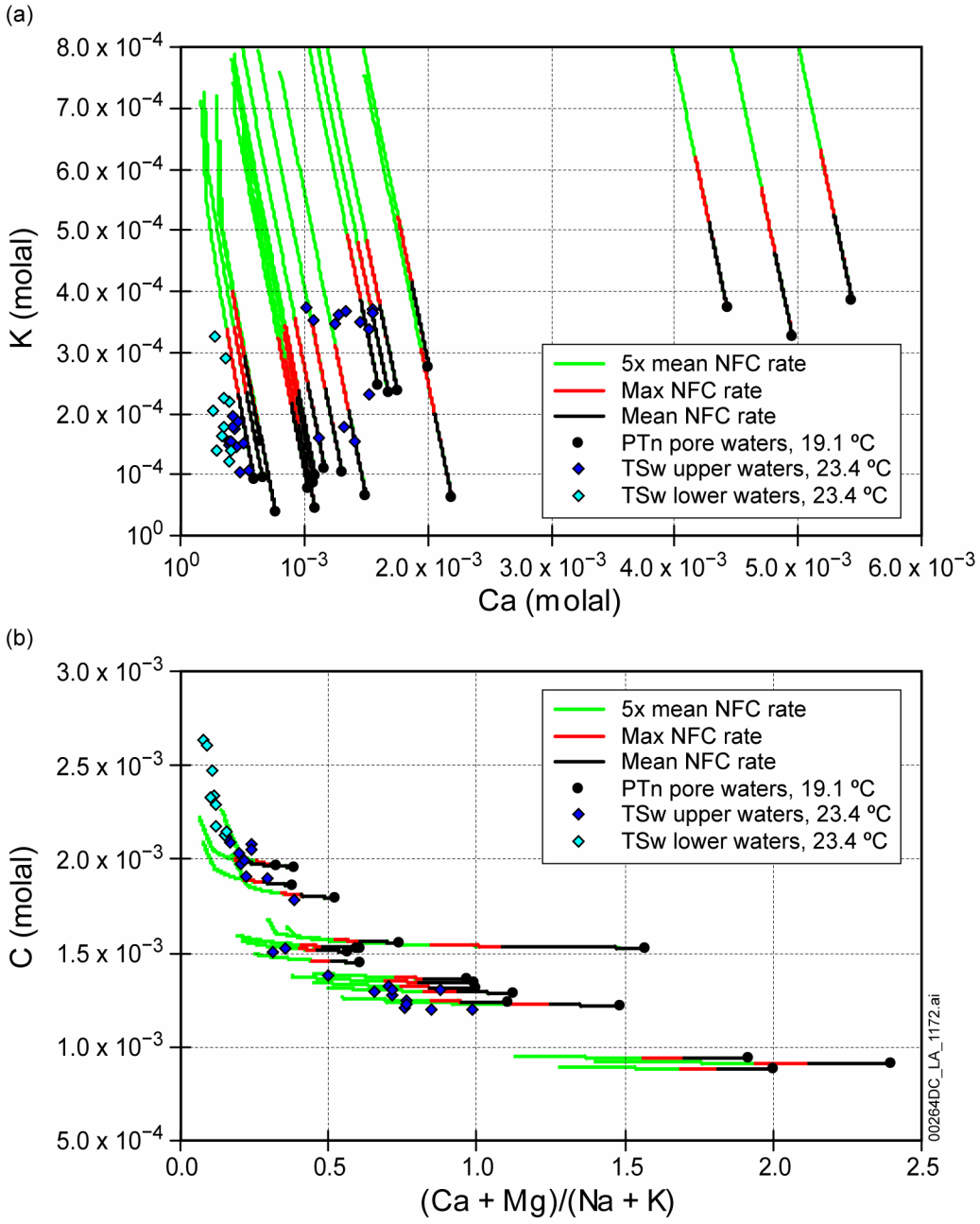

Figure 2.3.5-22. Plot of (a) Potassium Versus Calcium Molalities and (b) Divalent/Monovalent Cation Ratio Versus C Molality for TSw and PTn Pore Waters, Showing Predicted Evolutionary Pathways for the PTn Waters at Three Different Feldspar Dissolution Rates

Source: SNL 2007b, Figures 7.1-6 and 7.1-8.

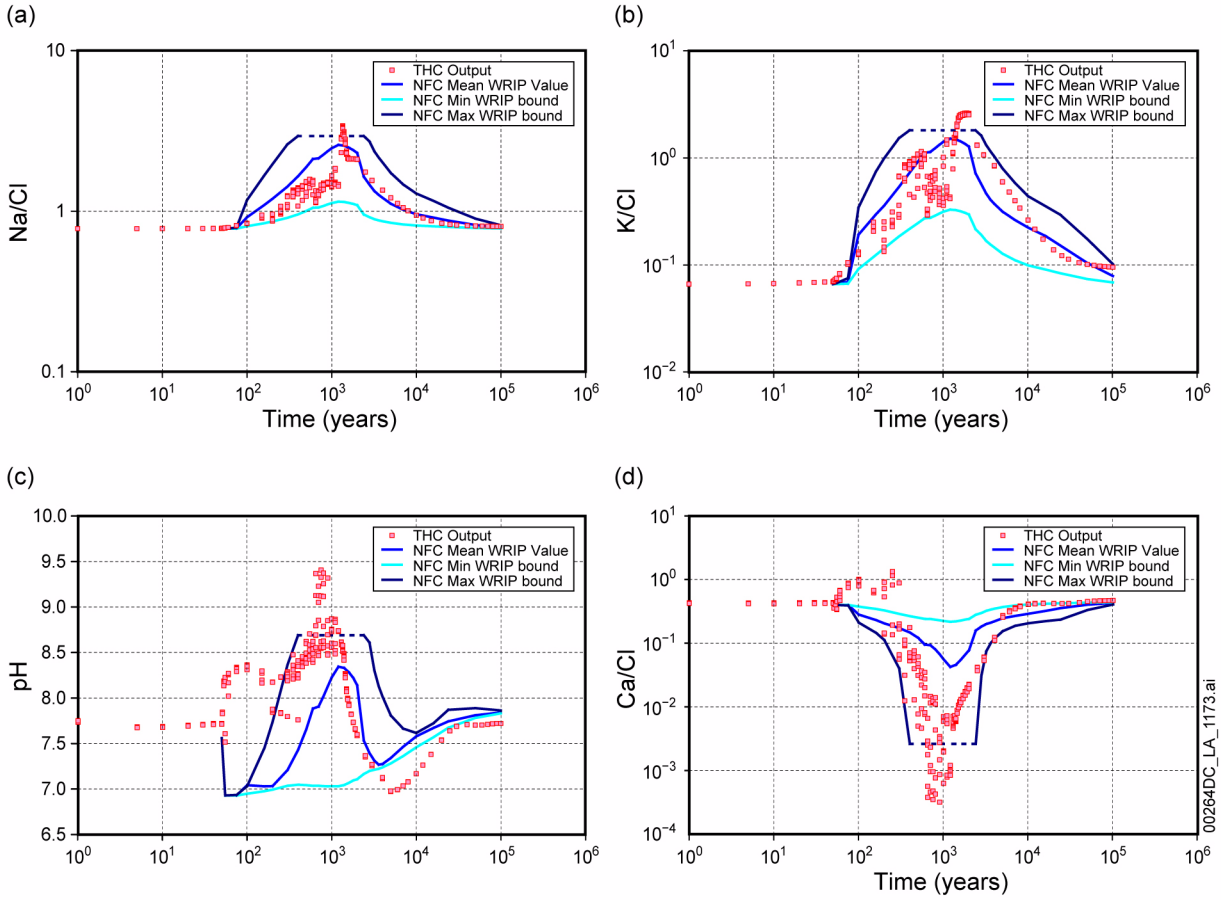

Figure 2.3.5-23. Comparison of Potential Seepage Water Compositions Predicted by the Near-Field Chemistry and Thermal-Hydrologic-Chemical Seepage Models for the Group 3 Representative Water

NOTE: Thermal-hydrologic-chemical data are from the six highest-flux nodes above the drift. The near-field chemistry model incorporates an uncertainty range on the water–rock interaction parameter value; the near-field chemistry results shown here are for the mean, maximum, and minimum water–rock interaction parameter values at each time step. The near-field chemistry results are not predicted if the water–rock interaction parameter value exceeds the maximum amount evaluated by the near-field chemistry model.
WRIP = water–rock interaction parameter.

Source: SNL 2007b, Figure 7.1-11.

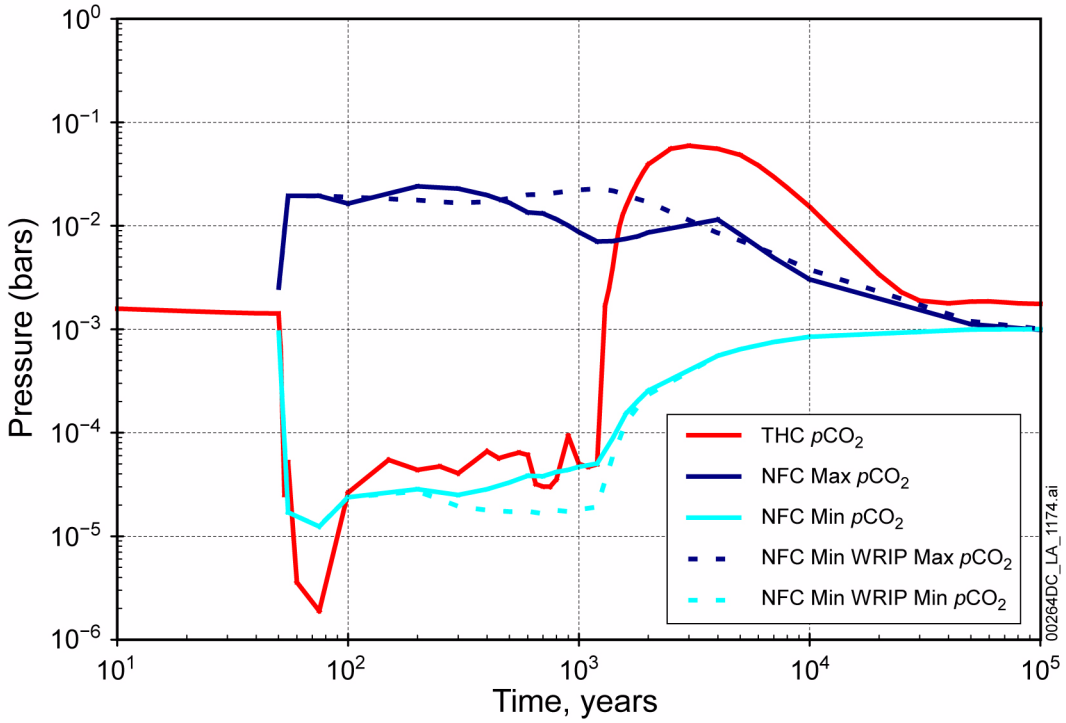

Figure 2.3.5-24. Comparison of In-Drift CO_2 Partial Pressures Predicted by the Near-Field Chemistry and Thermal-Hydrologic-Chemical Seepage Models

NOTE: The near-field chemistry model range does not entirely bound the thermal-hydrologic-chemical seepage model range.

Source: SNL 2007b, Figure 7.1-12.

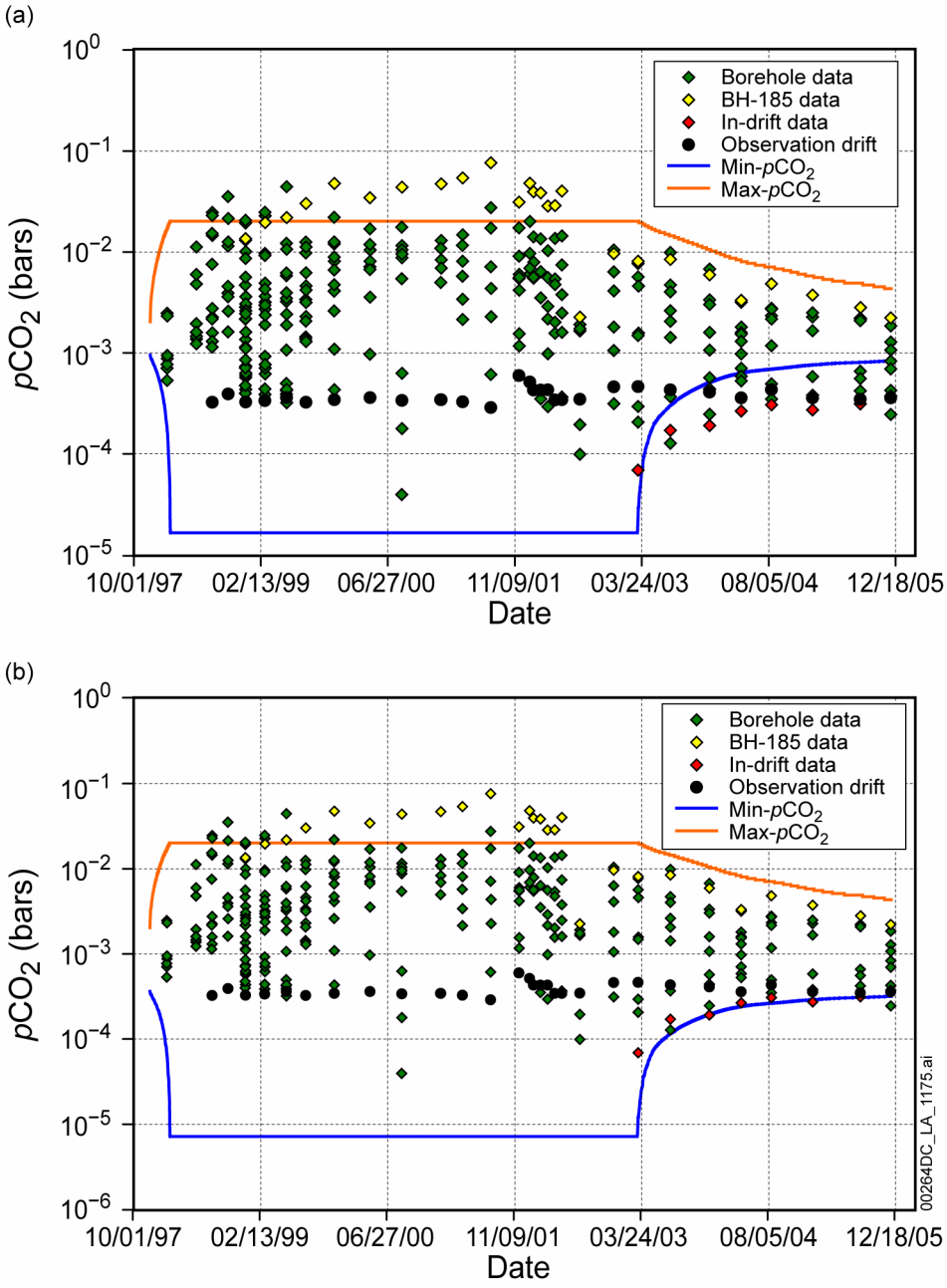

Figure 2.3.5-25. Comparison of Predicted Near-Field Chemistry Model pCO_2 Range and Measured Gas-Phase CO_2 Concentrations in and around the Drift Scale Test: (a) Near-Field Chemistry Model Range, Assuming Ambient $pCO_2 = 10^{-3}$ bars, the Repository-Level Value In the Rock; (b) Near-Field Chemistry Model Range Assuming Ambient $pCO_2 = 10^{-3.42}$ bars, the Current Atmospheric Value

NOTE: CO_2 concentrations have been corrected for condensation of water vapor from the gas phase during sampling. The predicted CO_2 ranges are based on the Group 4 representative water.

Source: SNL 2007b, Figure 7.1-15.

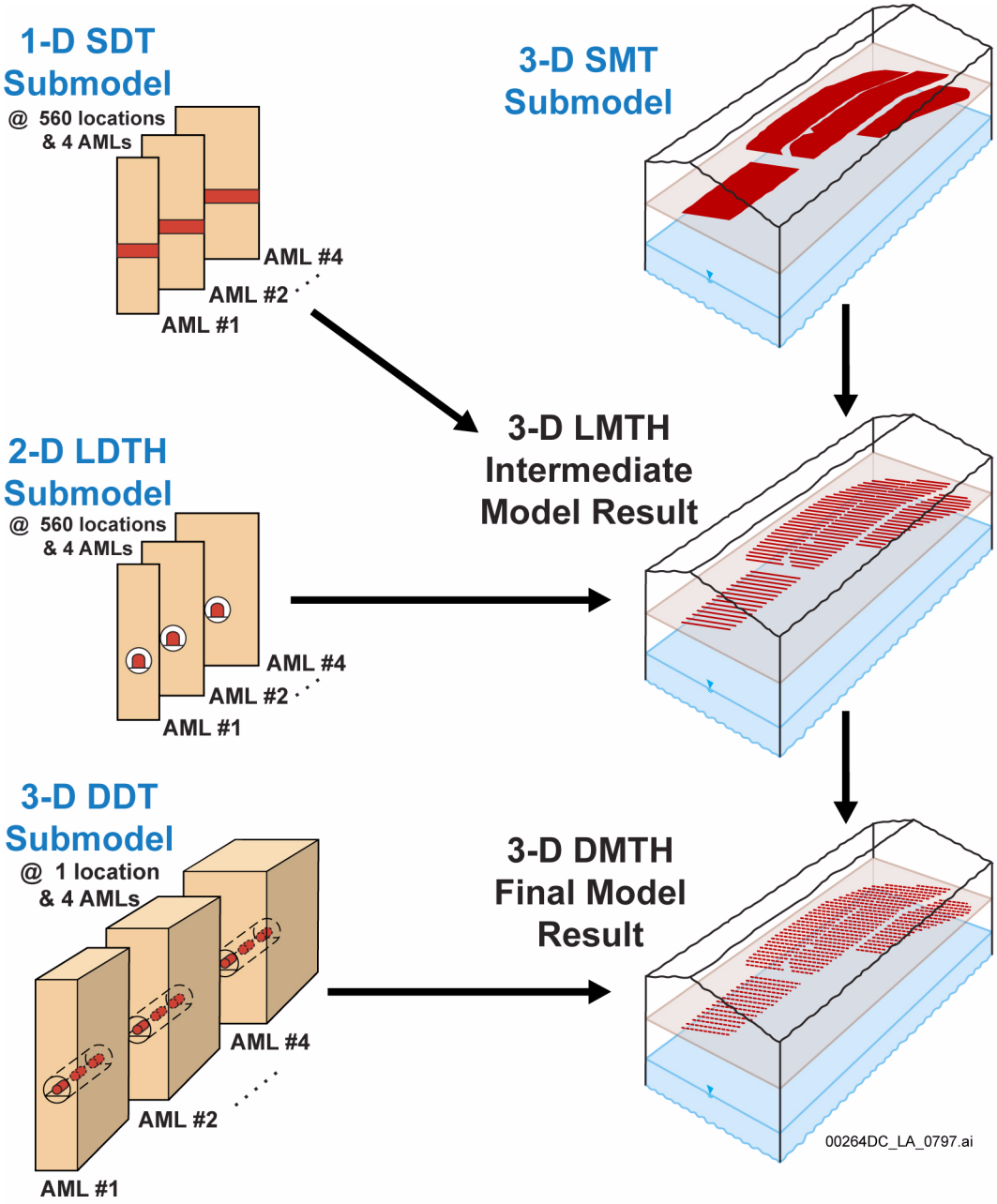

Figure 2.3.5-26. Conceptual Diagram Showing Information Flow Between Submodels, Intermediate Model Results, and Final Model Results of the Multiscale Thermal-Hydrologic Model

NOTE: The SMT submodel smears the heat source of the 108 drifts, as indicated by the heated region in the SMT diagram.
AML = areal mass loading; DDT = discrete-heat-source, drift-scale, thermal-conduction-radiation; DMTH = discrete-source, mountain-scale, thermal-hydrologic; LDTH = two-dimensional, line-averaged-heat-source, drift-scale, thermal-hydrologic; LMTH = line-source, mountain-scale, thermal-hydrologic; SDT = smeared-source, drift-scale, thermal-only; SMT = smeared-source, mountain-scale, thermal-only.

Source: SNL 2008a, Figure 1-1, Sections 6.2.4 to 6.2.9, and Sections 6.2.14[a] to 6.2.17[a].

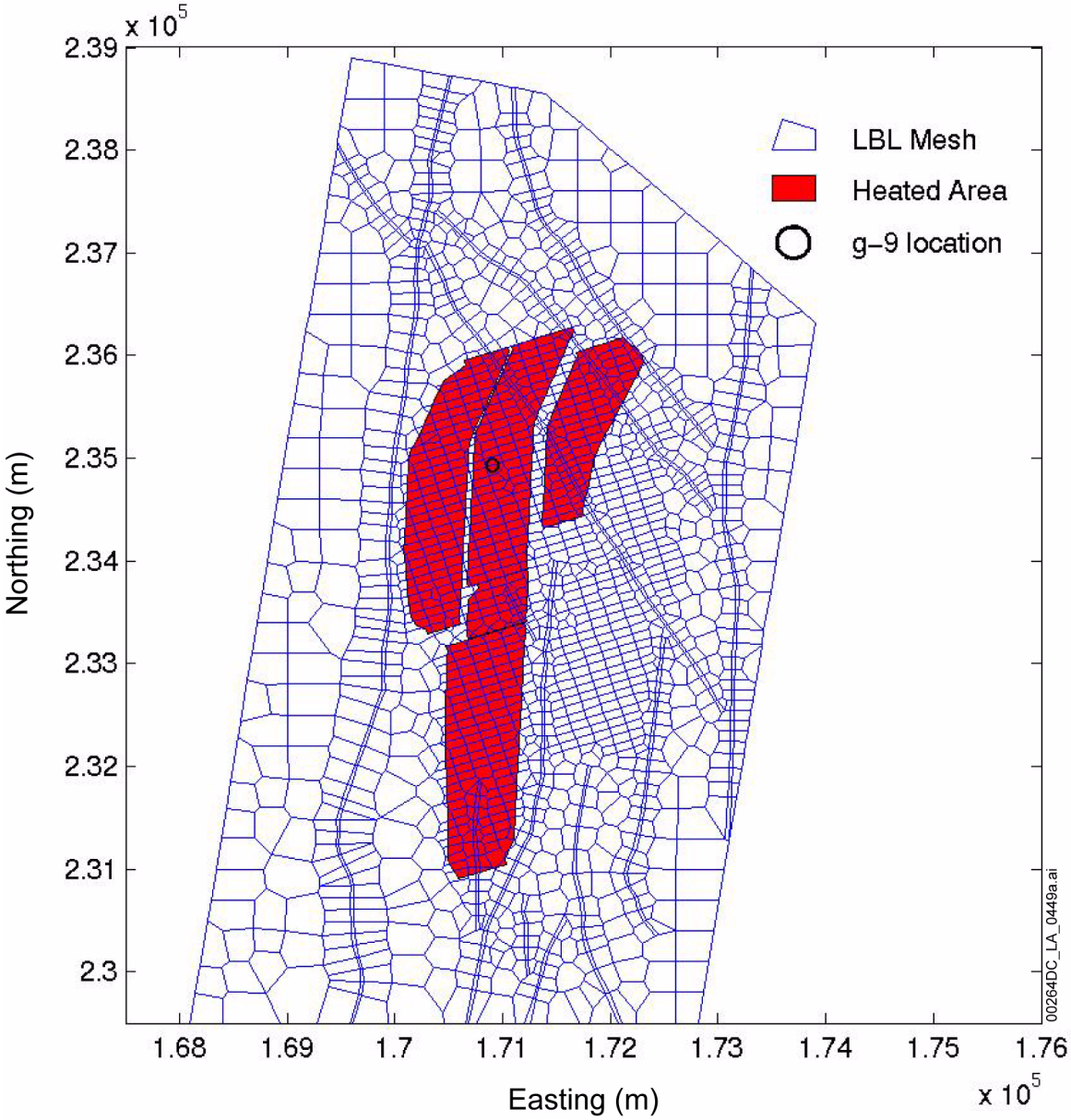

Figure 2.3.5-27. Heated Repository Footprint of the SMT-Submodel Mesh, Overlain on the Unsaturated Zone Flow Model Mesh, and Showing the g-9 Location Used for Sensitivity Studies

NOTE: Heated repository footprint shown as colored fill (SNL 2008a); unsaturated zone flow model grid shown as mesh of colored lines (SNL 2007h).

Source: SNL 2008a, Figure 6.2-17[a].

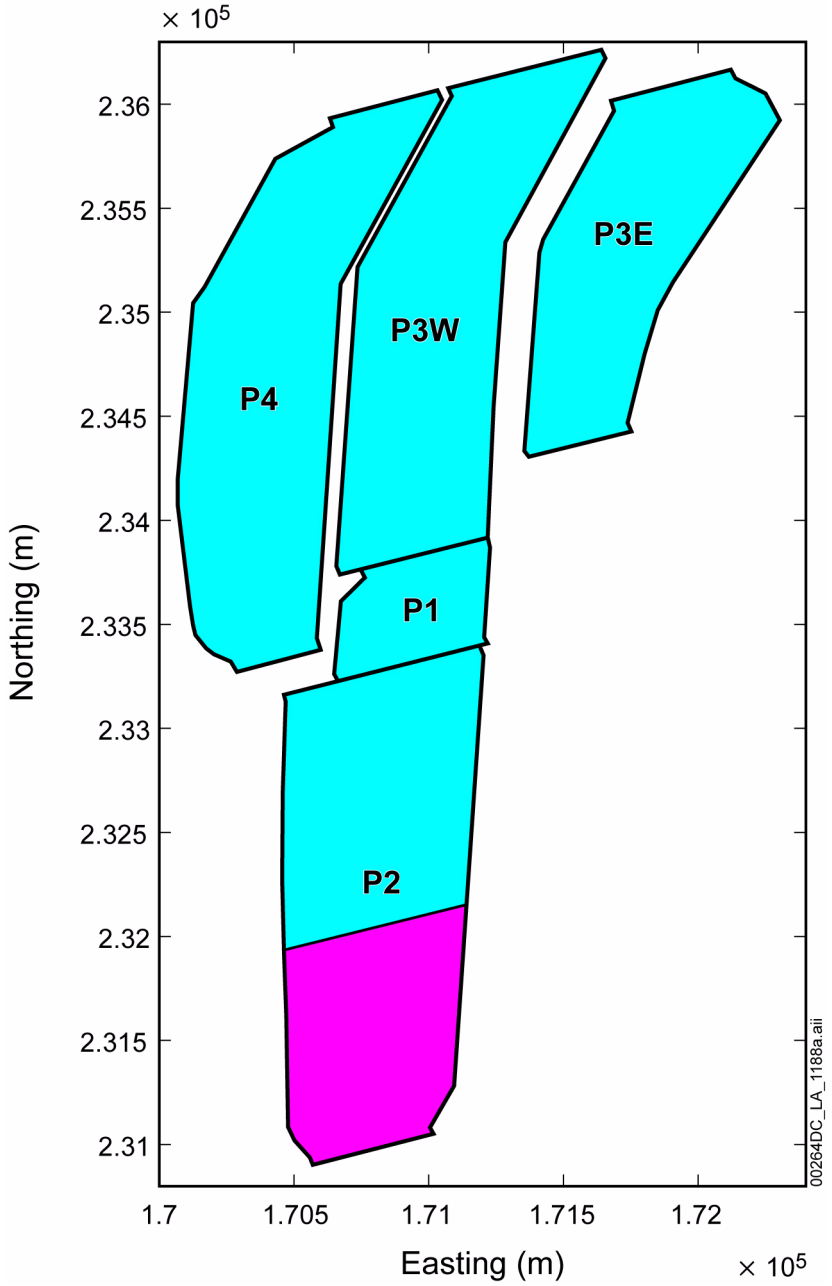

Figure 2.3.5-28. Heated Repository Footprint of the SMT-Submodel Mesh, Panel Numbers, and Contingency Drifts at the South End of Panel 2

NOTE: The relative availability of contingency area among the 108 emplacement drifts is represented by the southern shaded area, although contingency area has not been allocated to particular drifts (as discussed in Section 1.3.2.2).

Source: SNL 2008a, Figure 6.2-19[a].

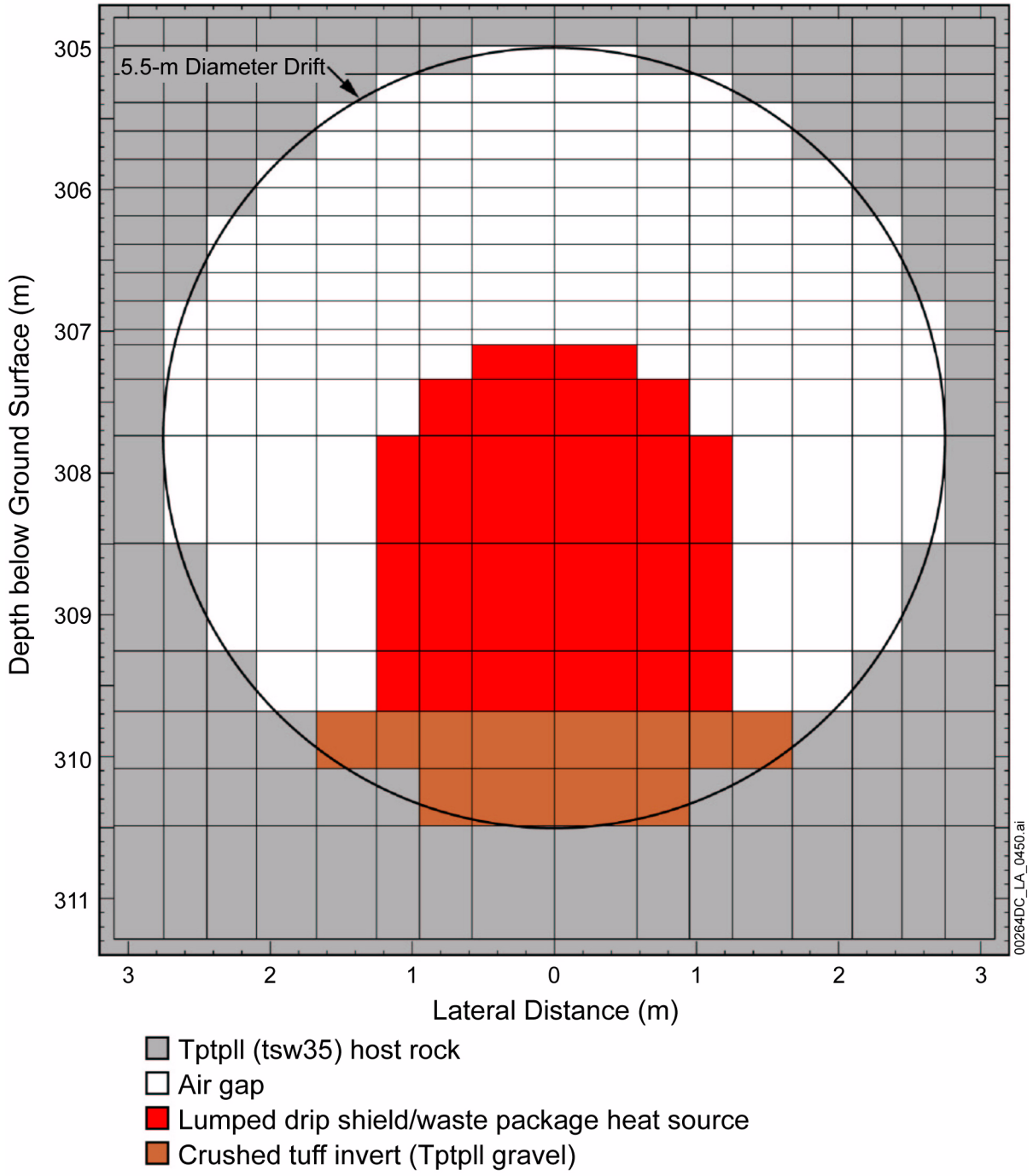

Figure 2.3.5-29. Cross-Sectional View of the Numerical Mesh Describing the Drift Used for Line-Source, Drift-Scale, Thermal-Hydrologic Submodel Runs

Source: SNL 2008a, Figure 6.2-6.

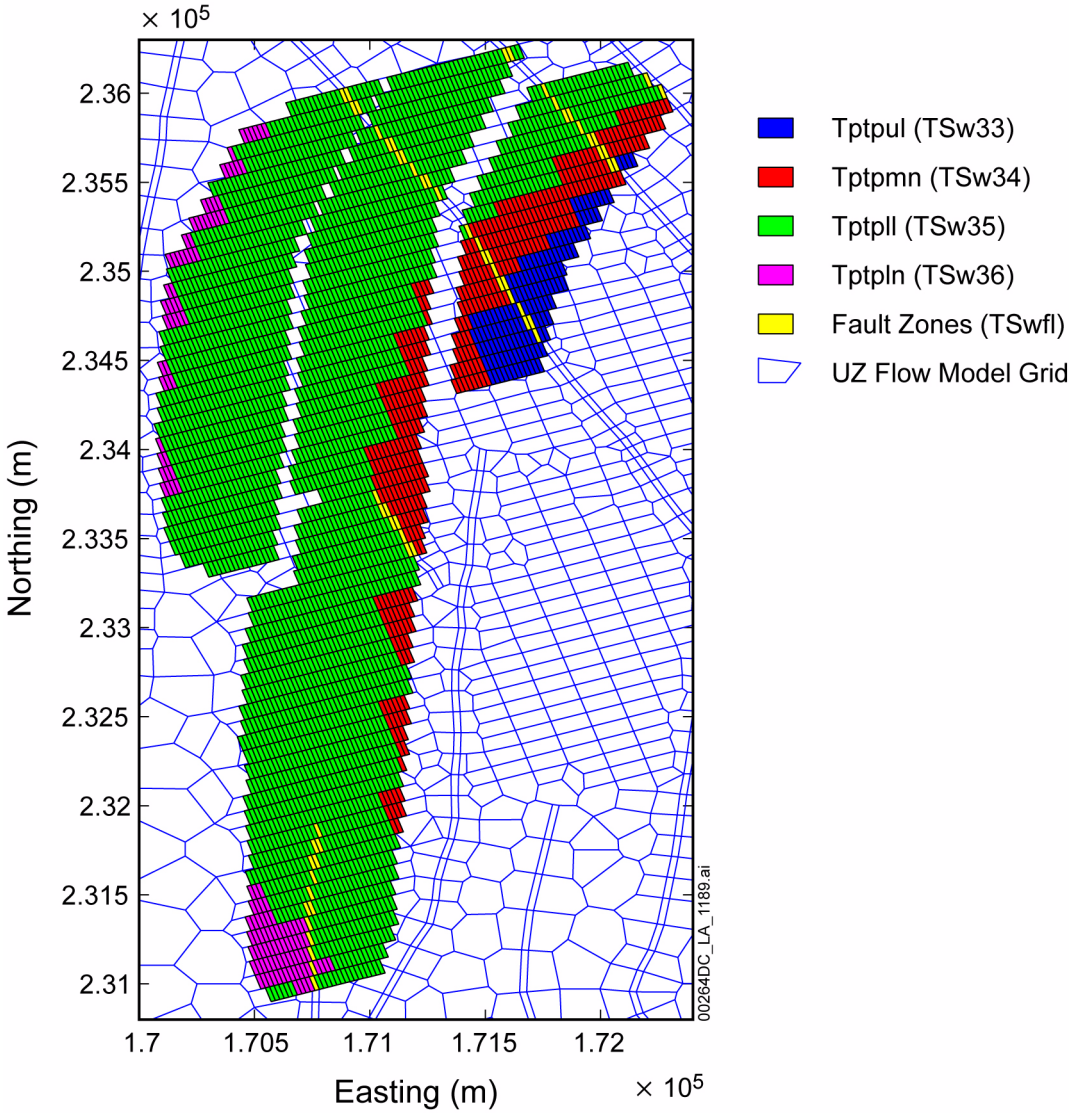

Figure 2.3.5-30. Distribution of Host-Rock Units Within the Repository Footprint

Source: SNL 2008a, Figure 6.2-18[a].

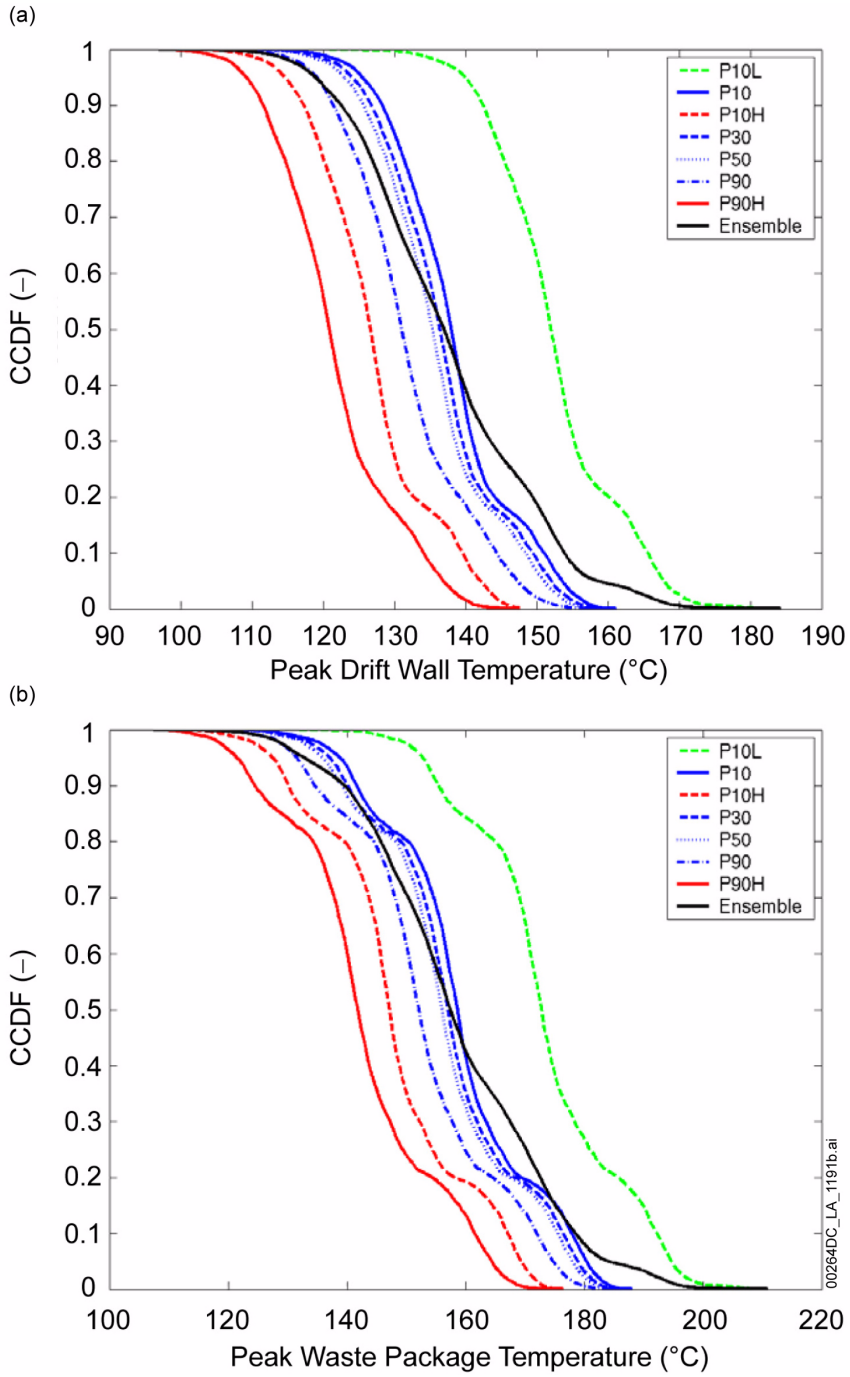

Figure 2.3.5-31. Complementary Cumulative Distribution Functions for Peak Temperature (a) on the Drift Wall and (b) on the Waste Packages

NOTE: Each of the seven complementary cumulative distribution function plots represents 26,112 values, which are the product of eight different waste package types at 3,264 locations across the repository. These are the peak temperatures from the 182,784 temperature histories. The ensemble curve is based on all of the data from the seven uncertainty cases, using the weights for the three thermal conductivities and four infiltration cases (five of the cases are represented by surrogate cases from the seven that were run; see the text near the end of Section 2.3.5.4.1.3.2 for a description of the surrogate case approach).

Source: SNL 2008a, Figure 6.3-77[b].

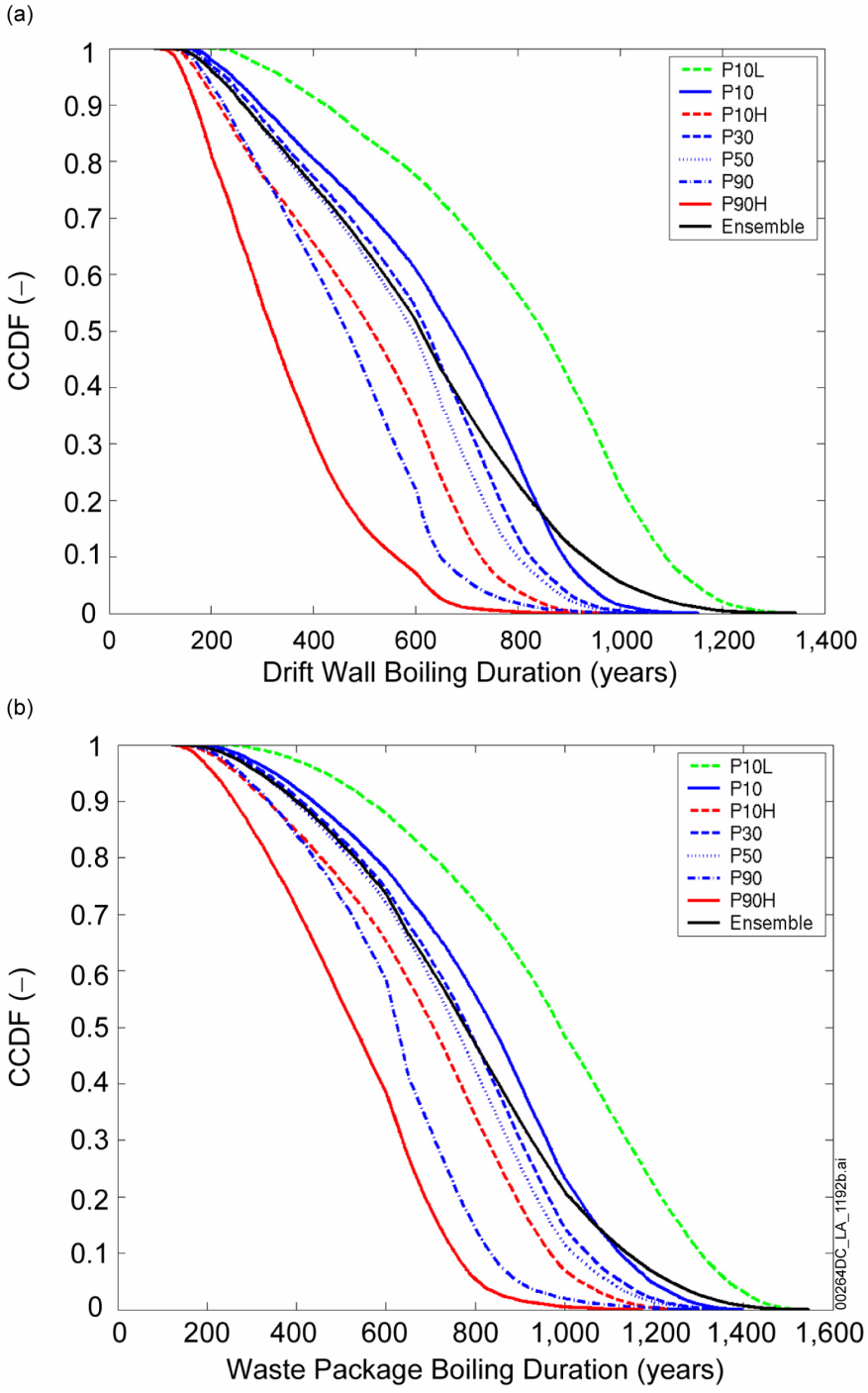

Figure 2.3.5-32. Complementary Cumulative Distribution Functions for the Time When Boiling Ceases (a) at the Drift Wall and (b) at the Waste Package

NOTE: Each of the seven complementary cumulative distribution function plots represents 26,112 values, which are the product of eight different waste package types at 3,264 locations across the repository. These are the times when boiling ceases for each of the 182,784 temperature histories. The ensemble curve is based on all of the data from the seven uncertainty cases, using the weights for the three thermal conductivities and four infiltration cases (five of the cases are represented by surrogate cases from the seven that were run).

Source: SNL 2008a, Figure 6.3-78[b].

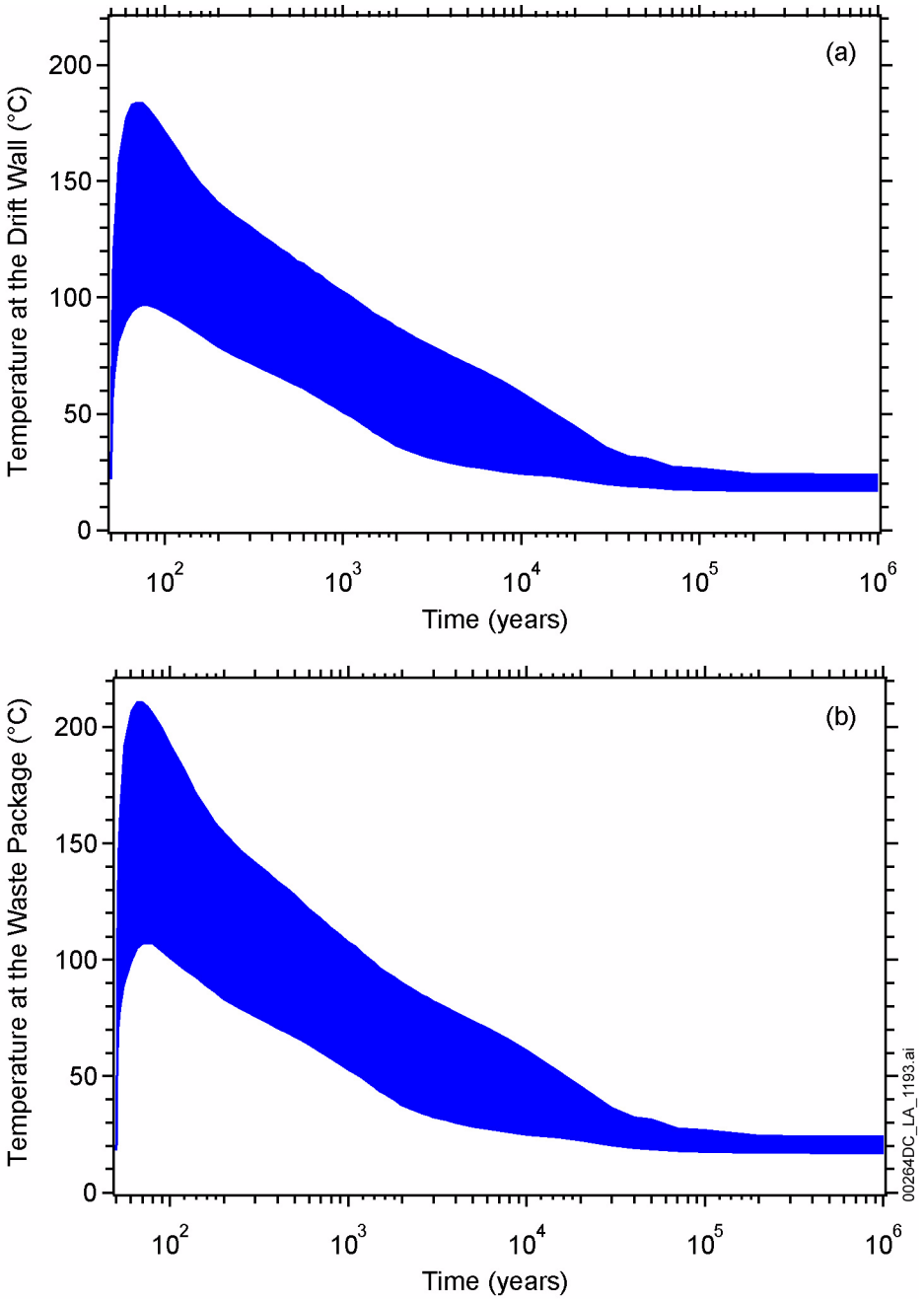

Figure 2.3.5-33. Range of Temperature Histories for (a) the Drift Wall and (b) the Waste Package

NOTE: The areas shown in blue represent “horsetail plots” of 182,784 temperature histories, a number which is the product of eight waste package simulated, 3,264 locations across the repository, and seven uncertainty cases. The minimum and maximum values represent either a minimum or maximum value for all 182,784 histories at any point in time.

Source: SNL 2008a, Figure 6.3-76[a].

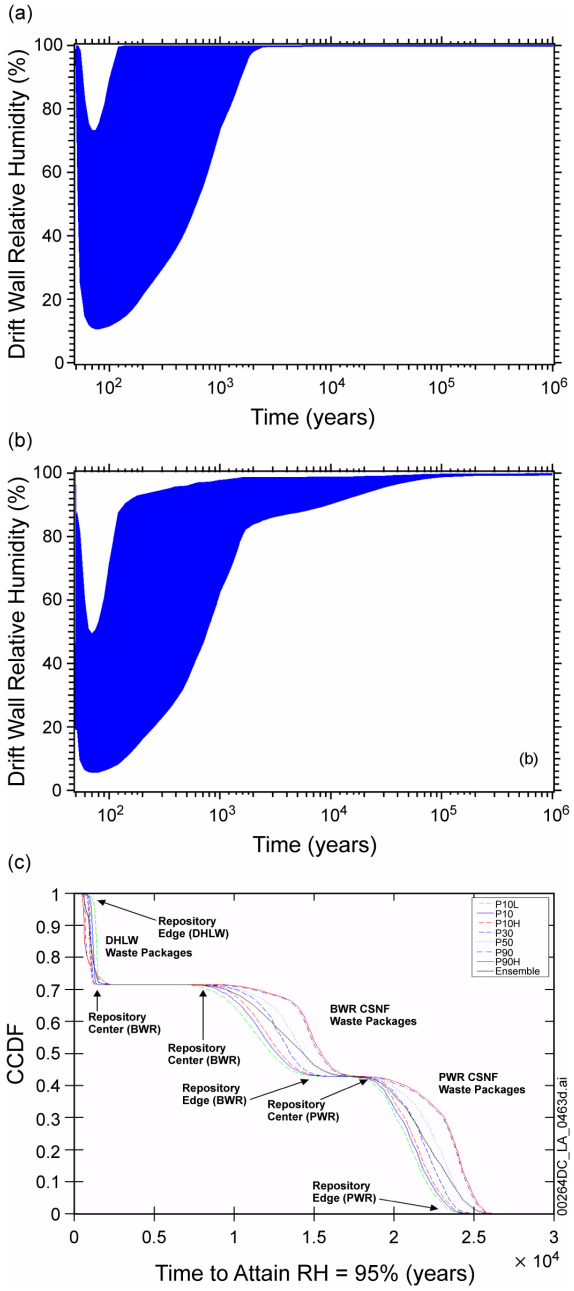

Figure 2.3.5-34. Range of Relative Humidity Histories for (a) the Drift Wall, (b) the Waste Package, and (c) Complementary Cumulative Distribution Function for the Time Required for Waste Package Relative Humidity to Attain a Value of 95%

NOTE: The areas shown in blue represent “horsetail plots” of 182,784 relative-humidity histories, a number which is the product of eight waste package simulated, 3,264 locations across the repository, and seven uncertainty cases. The minimum and maximum values represent either a minimum or maximum value for all 182,784 histories at any point in time. The inset detail for waste package relative humidity expands the humidity range for which threshold conditions are identified that control radionuclide transport in the engineered barrier system (Sections 2.3.7.11 and 2.3.7.12).
CCDF = complementary cumulative distribution function; CSNF = commercial SNF; DHLW = DOE HLW; RH = relative humidity.

Source: SNL 2008a, Figures 6.3-81[a], and 6.3-98[b].

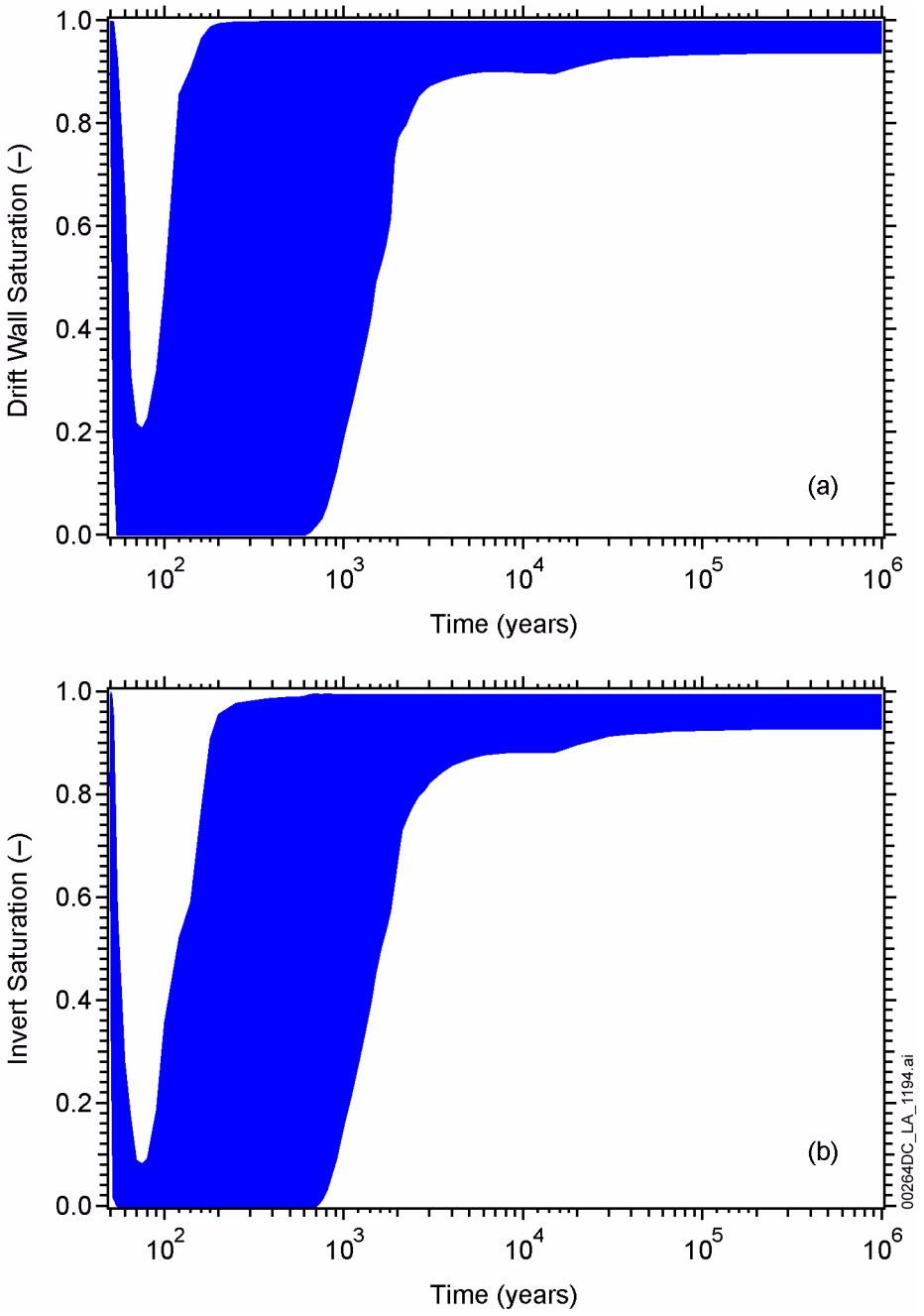

Figure 2.3.5-35. Ranges of Histories for Liquid Saturation at (a) the Drift Wall and (b) the Invert

NOTE: The areas shown in blue represent “horsetail plots” of 182,784 liquid-phase histories, a number which is the product of eight waste package simulated, 3,264 locations across the repository, and seven uncertainty cases. The minimum and maximum values represent either a minimum or maximum value for all 182,784 histories at any point in time. The liquid-phase saturation pertains to the matrix continuum in the host rock at the drift wall and in the intragranular porosity of the crushed tuff in the invert.

Source: SNL 2008a, Figure 6.3-80[a].

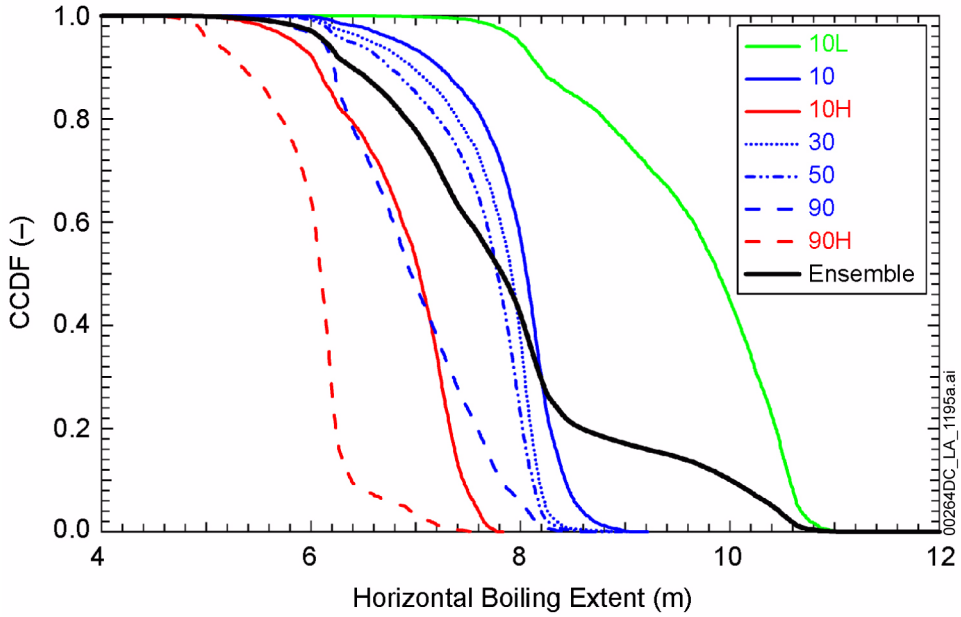

Figure 2.3.5-36. Complementary Cumulative Distribution Functions of the Maximum Lateral Extent of the Boiling-Point Isotherm (96°C) from the Drift Centerline for the Range of Parametric Uncertainty Addressed by the Multiscale Thermal-Hydrologic Model

NOTE: Each of the seven complementary cumulative distribution function plots represents 26,112 values, which are the product of eight different waste package types at 3,264 locations across the repository. These are the maximum lateral extents of boiling corresponding to the 182,784 temperature histories. The ensemble curve is based on all of the data from the seven uncertainty cases, using the weights for the three thermal conductivities and four infiltration cases (five of the cases are represented by surrogate cases from the seven that were run).

Source: SNL 2008a, Figure 6.3-79[a].

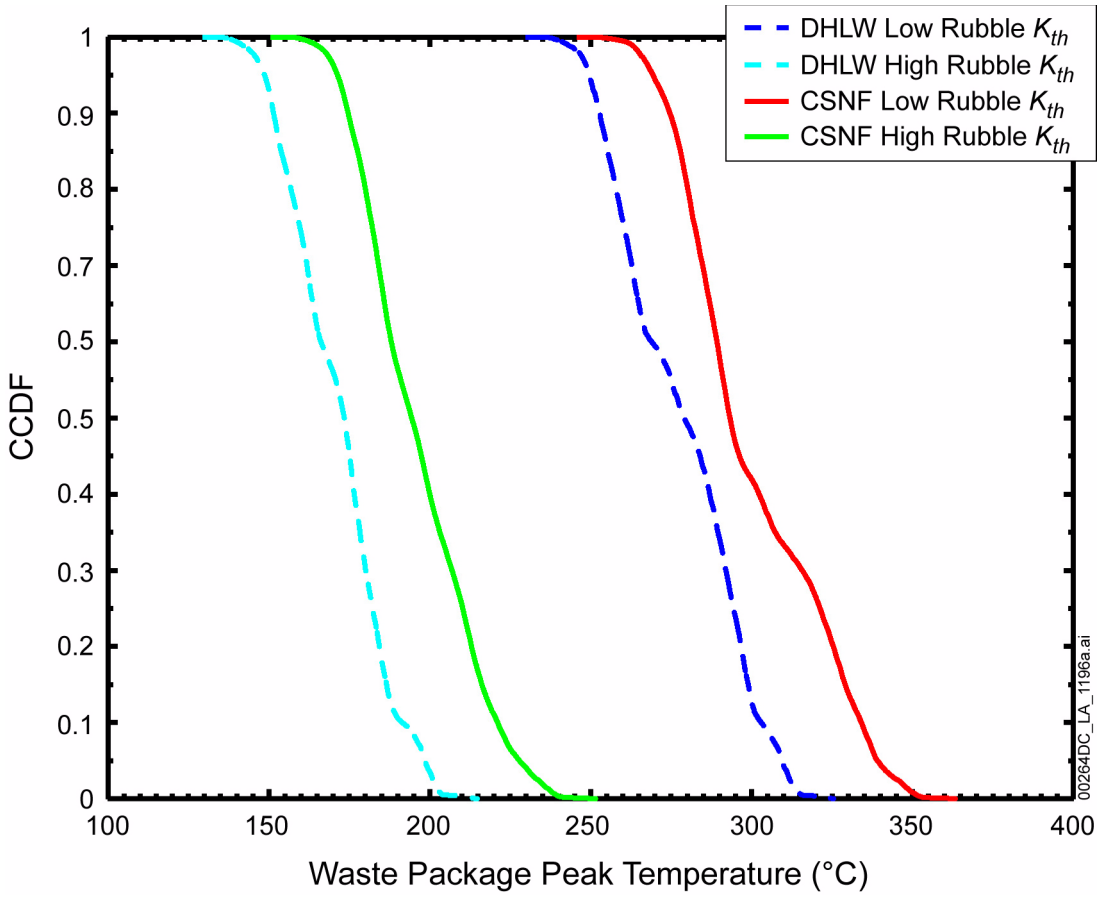

Figure 2.3.5-37. Complementary Cumulative Distribution Functions for Peak Waste Package Temperatures for Commercial SNF and DOE HLW Waste Packages for Collapsed-Drift Cases Subject to Low and High Rubble Thermal Conductivity

NOTE: Each commercial SNF curve represents 137,088 temperature histories (six commercial SNF waste packages at 3,264 locations and seven uncertainty cases). Each DOE HLW (codisposal waste package) curve represents 45,696 temperature histories (two DOE HLW waste packages at 3,264 locations and seven uncertainty cases.)

Source: SNL 2008c, Figure 6.4.2-29.

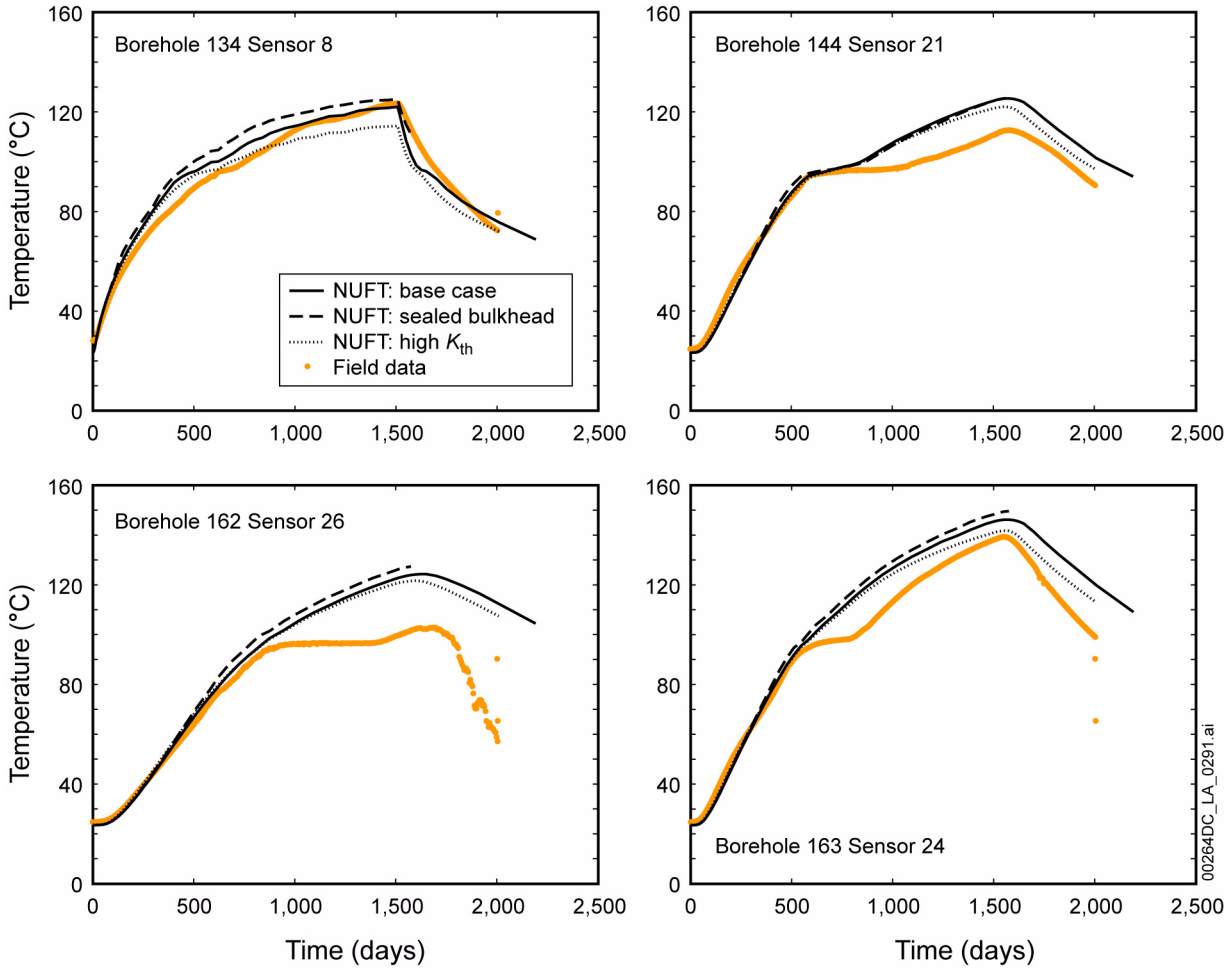

Figure 2.3.5-38. Comparison of Measured and Simulated Temperature Histories for Boreholes 134, 144, 162, and 163

NOTE: NUFT is the software used within the multiscale thermal-hydrologic model.

Source: SNL 2008a, Figure 7.4-14.

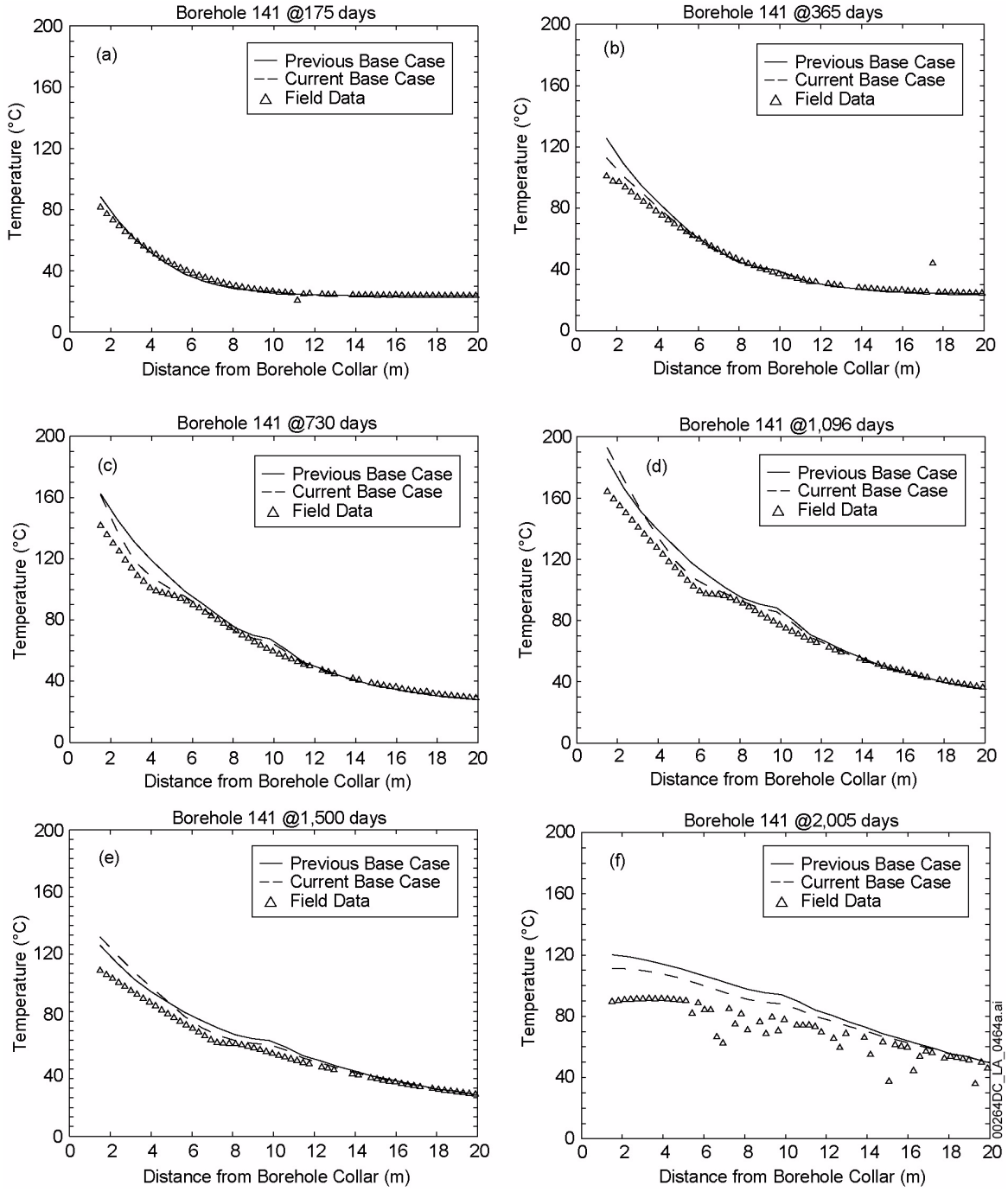

Figure 2.3.5-39. Comparison of Measured and Simulated Temperature Spatial Profiles for Borehole 141

NOTE: The behavior exhibited at 2,005 days is typical of either sensor degradation or condensation shedding (SNL 2008a, Section 7.4). The NUFT simulations are for the two indicated cases. The “current base case” uses the same updated thermal and hydrologic property values as are used in the multiscale thermal-hydrologic calculations that directly support the TSPA. The “previous base case” is presented for comparison and is based on earlier work using different values for thermal and hydrologic properties (SNL 2008a, Section 7.4.3).

Source: SNL 2008a, Figure 7.4-21[a].

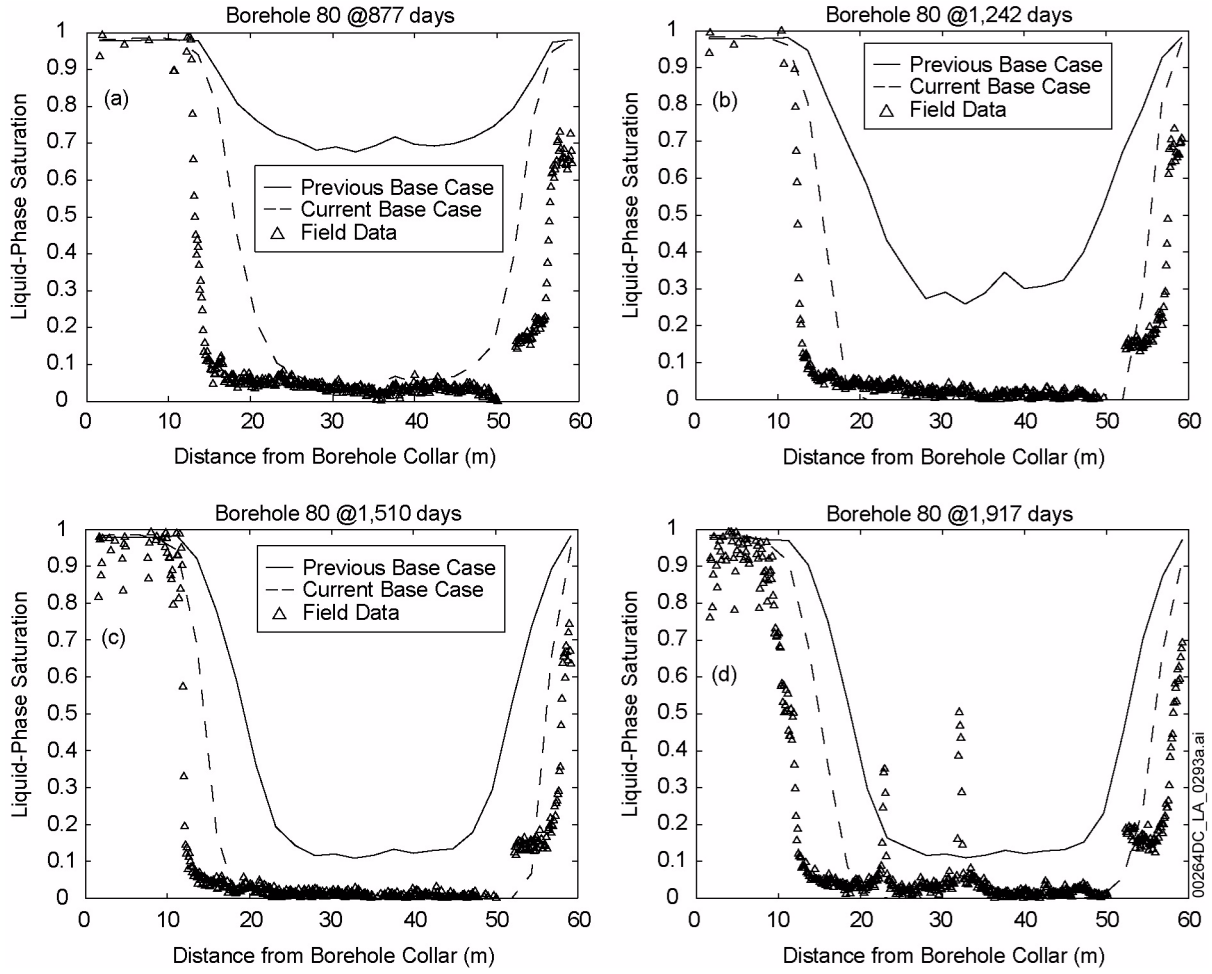

Figure 2.3.5-40. Comparison of Measured and Simulated Liquid-Phase Saturations for Borehole 80

NOTE: The NUFT simulations are for the two indicated cases. The “current base case” uses the same updated thermal and hydrologic property values as are used in the multiscale thermal-hydrologic calculations that directly support the TSPA. The “previous base case” is presented for comparison and is based on earlier work using different values for thermal and hydrologic properties (SNL 2008a, Section 7.4.3).

Source: SNL 2008a, Figure 7.4-37[a].

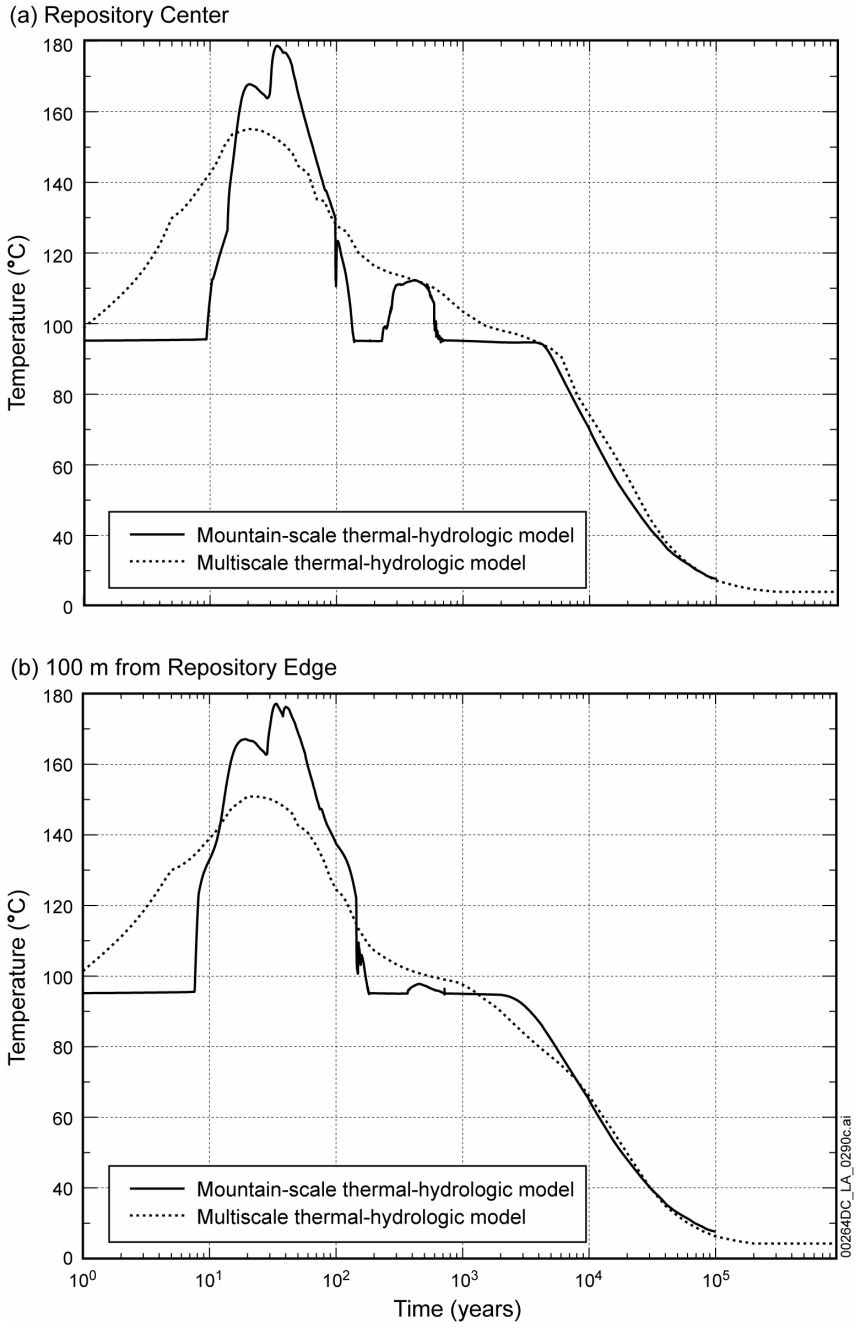

Figure 2.3.5-41. Comparison of Drift Wall Temperatures Predicted by the Multiscale Thermal-Hydrologic Model and an East–West, Mountain-Scale, Thermal-Hydrologic Model

NOTE: This comparison of predicted temperatures at (a) a repository-center location, and (b) 100 m from the edge of the repository, with a nominal average infiltration flux of 7.8 mm/yr (SNL 2008a, Section 6.4). The multiscale thermal-hydrologic model is used to predict drift-wall temperature adjacent to an “average” 21-PWR medium-heat commercial SNF waste package at each of these locations. The east–west cross-sectional mountain-scale thermal-hydrologic model (Haukwa et al. 1998) is used to predict the drift temperature, which is averaged over the cross section of the drift, arising from a line-averaged heat-source representation of waste package decay heat.

Source: SNL 2008a, Figure 6.4-1.

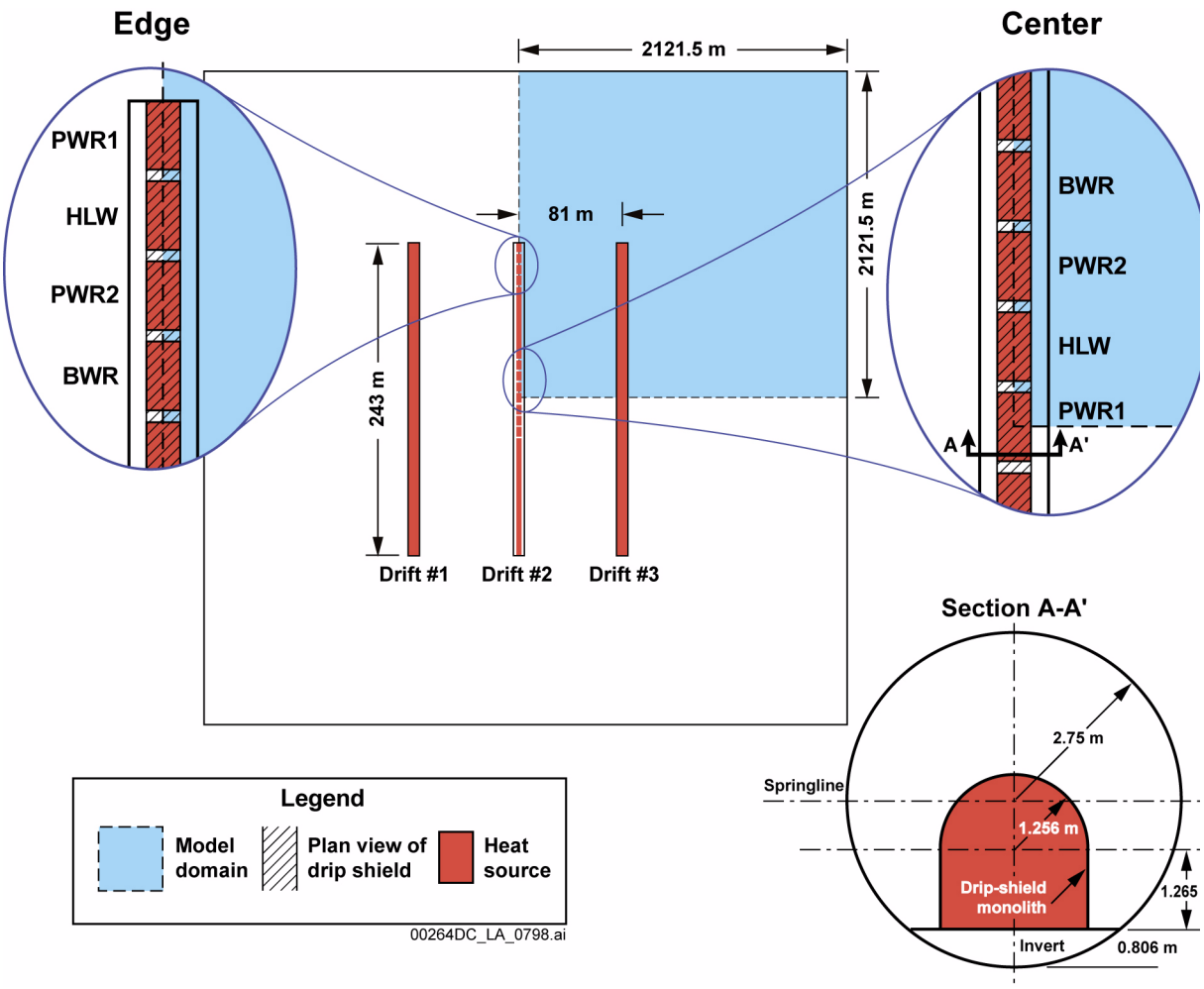

Figure 2.3.5-42. Conceptual Schematic for the Three-Drift Test Case

NOTE: To the upper left is the plan view of the three-drift test case; highlighted in blue is the zone of symmetry. To the upper right is a close-up of the Drift #2 waste package sequencing. To the bottom right is the vertical cross section of the modeled drift with the drip shield and waste package lumped together as a heat source.

Source: SNL 2008a, Figure 7.5-1.

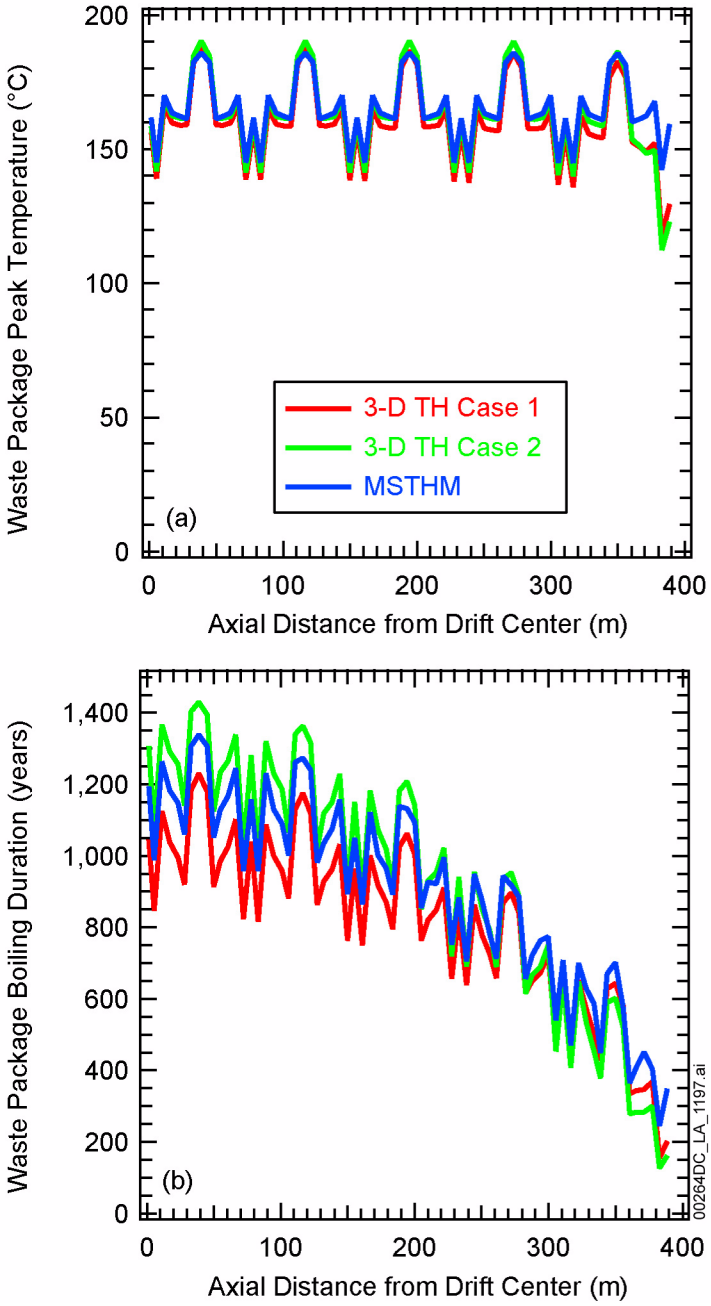

Figure 2.3.5-43. Thermal-Hydrologic Conditions Predicted by the Multiscale Thermal-Hydrologic Model and Three-Dimensional, Pillar-Scale, Thermal-Hydrologic Model Compared along the Drift, Including (a) Peak Waste Package Temperature and (b) Time When Boiling Ceases on the Waste Package

NOTE: For the three-dimensional pillar-scale, thermal-hydrologic model, Case 1 allows advective and diffusive vapor transport along the drift, while Case 2 does not. These results are for 71 waste packages along an emplacement drift with a heated half-length of 391.57 m. The sequence of waste packages in the unit cell is repeated ten times, starting with the pwr1-1 waste package at the repository center and ending with the pwr1-1 waste package at the repository edge.

Source: SNL 2008a, Figure 7.8-1[a].

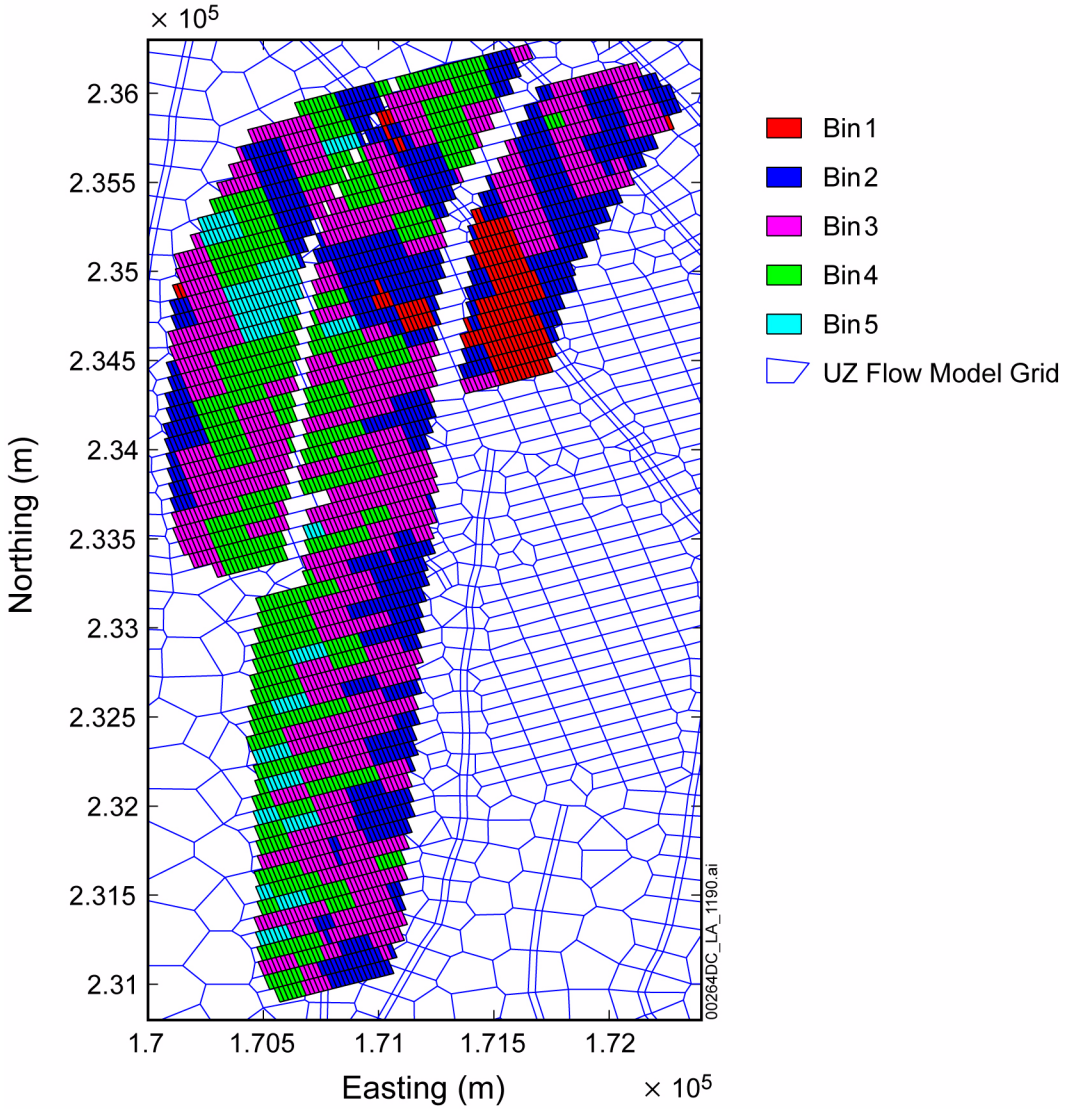

Figure 2.3.5-44. Correlation of the Five Percolation Flux Bins with Locations Within the Repository Footprint

Source: SNL 2008a, Figure VIII-1[a].

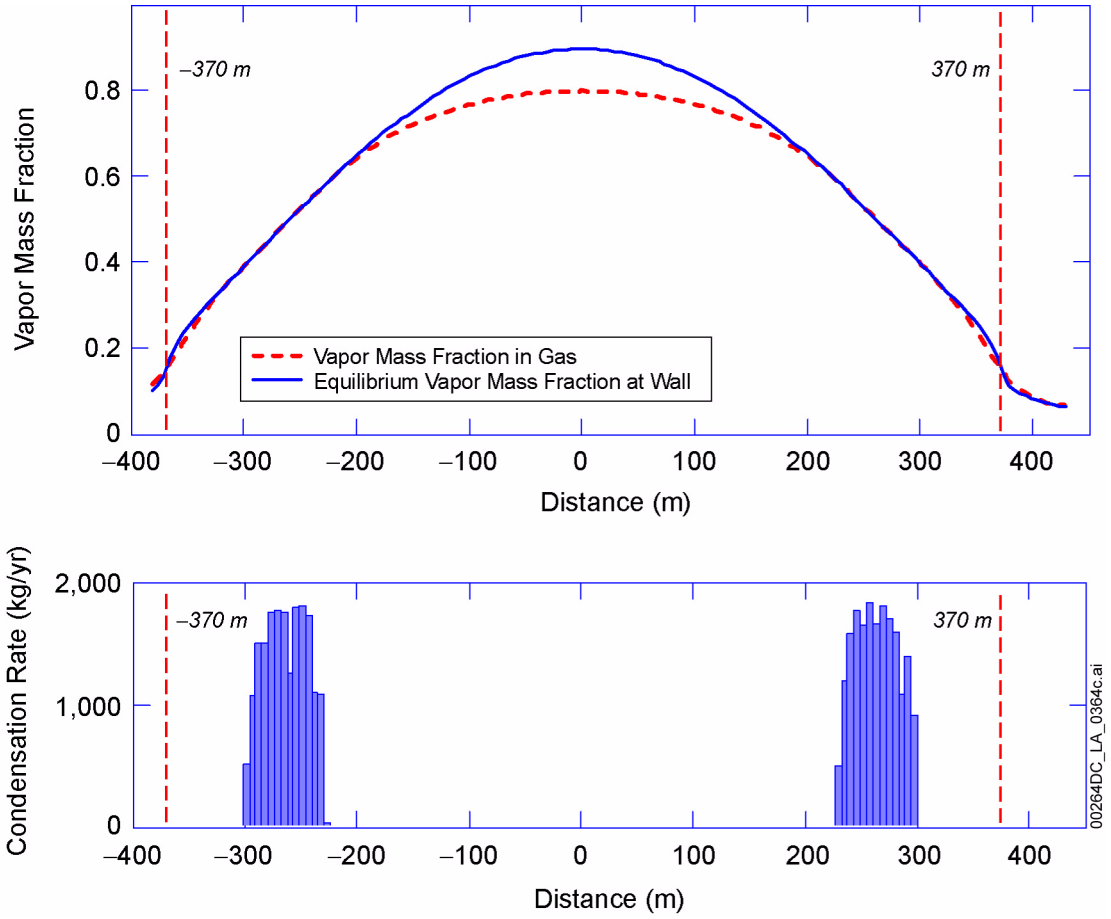

Figure 2.3.5-45. Vapor Mass Fraction in Gas and Condensation Rate on Drift Wall: Drift Choice #7, 1,000 years, High Percolation Rate, Well-Ventilated Drip Shield, Low Invert Transport, High Dispersion Coefficient

NOTE: Top: Vapor mass fraction in gas and equilibrium vapor mass fraction at the drift wall. Bottom: Condensation rate on drift wall (condensation in access/exhaust regions not shown).

Source: SNL 2007e, Figure 6-7[a].

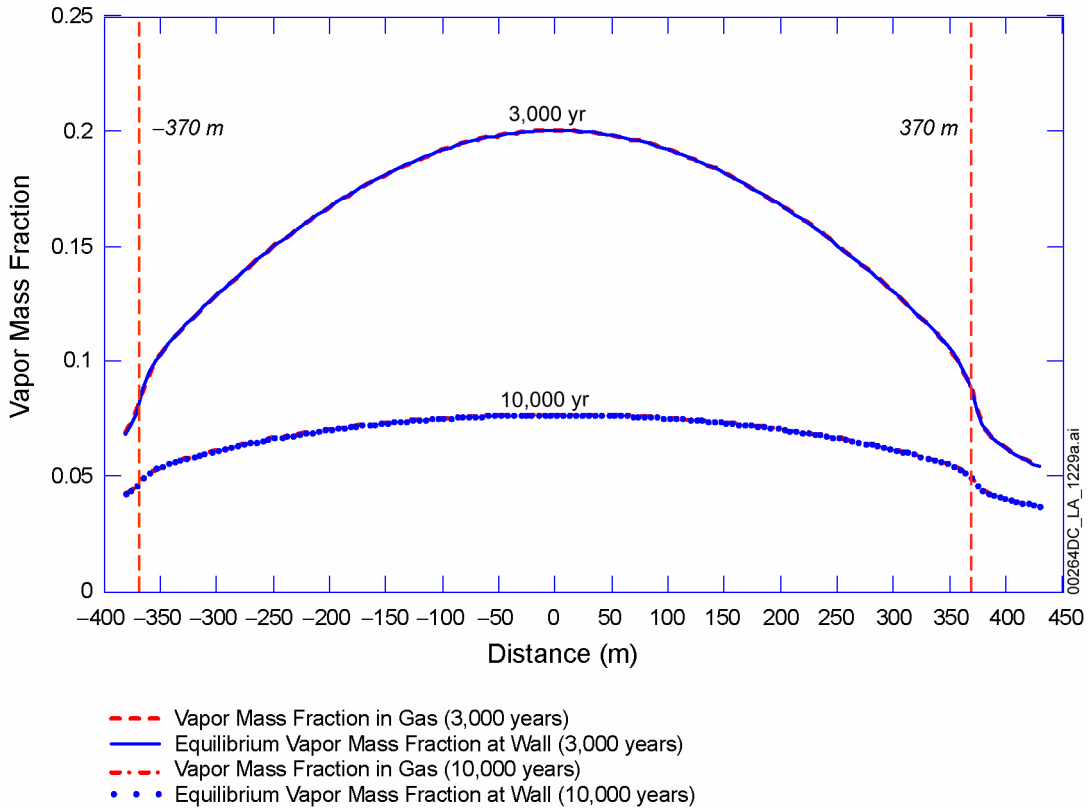

Figure 2.3.5-46. Vapor Mass Fraction in Gas at 3,000 Years and 10,000 Years: Drift Choice #7, High Percolation Rate, Well Ventilated Drip Shield, Low Invert Transport, Low Dispersion Coefficient

NOTE: Top lines: Vapor mass fraction in gas at 3,000 years. Bottom lines: Vapor mass in gas at 10,000 years.

Source: SNL 2007e, Figure 6-8[a].

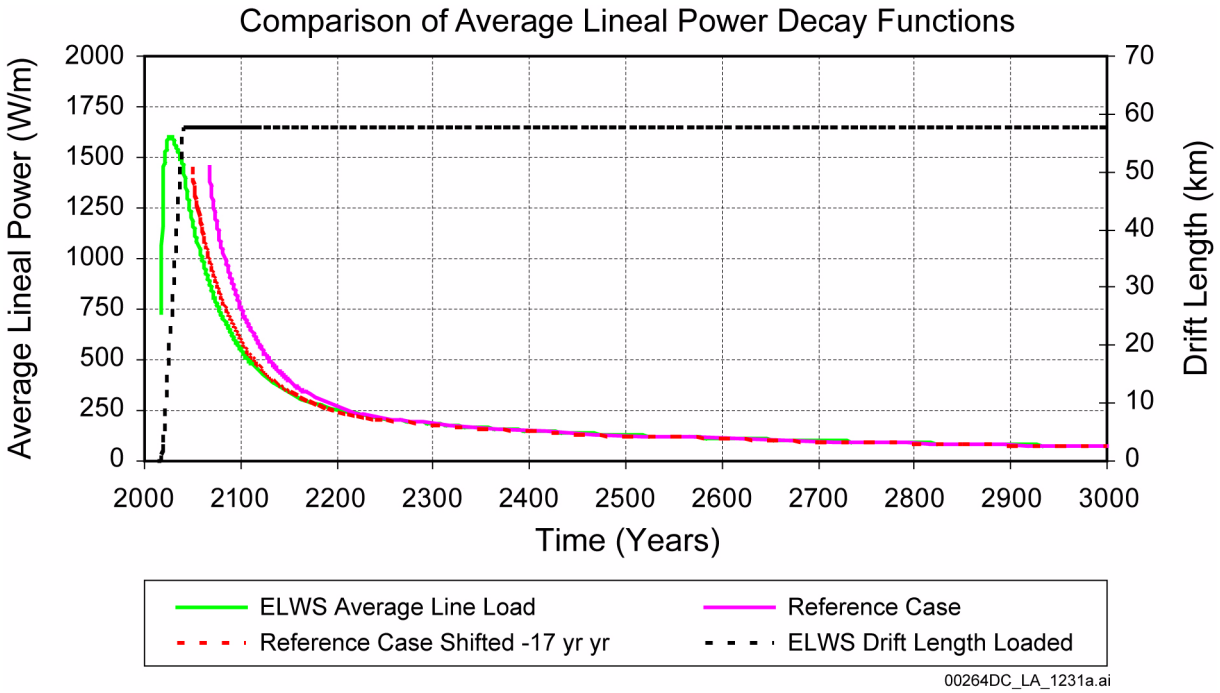

Figure 2.3.5-47. Comparison of Average Lineal Power Decay Functions for the Estimated Limiting Waste Stream and the Postclosure Thermal Reference Case

Source: SNL 2008c, Figure 6.1-1.

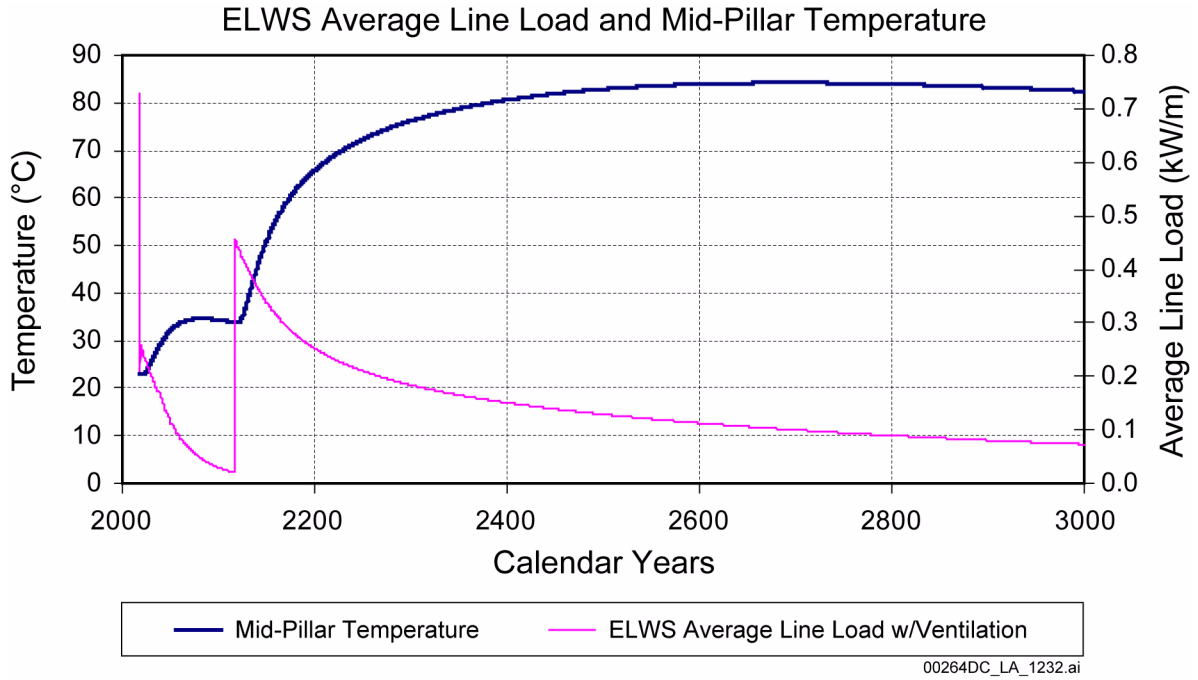

Figure 2.3.5-48. Estimated Limiting Waste Stream Average Line Load and Calculated Mid-Pillar Temperature History

NOTE: Mid-pillar temperature calculated using the mean wet thermal conductivity for the lower lithophysal host-rock unit.

Source: SNL 2008c, Figure 6.1-2.

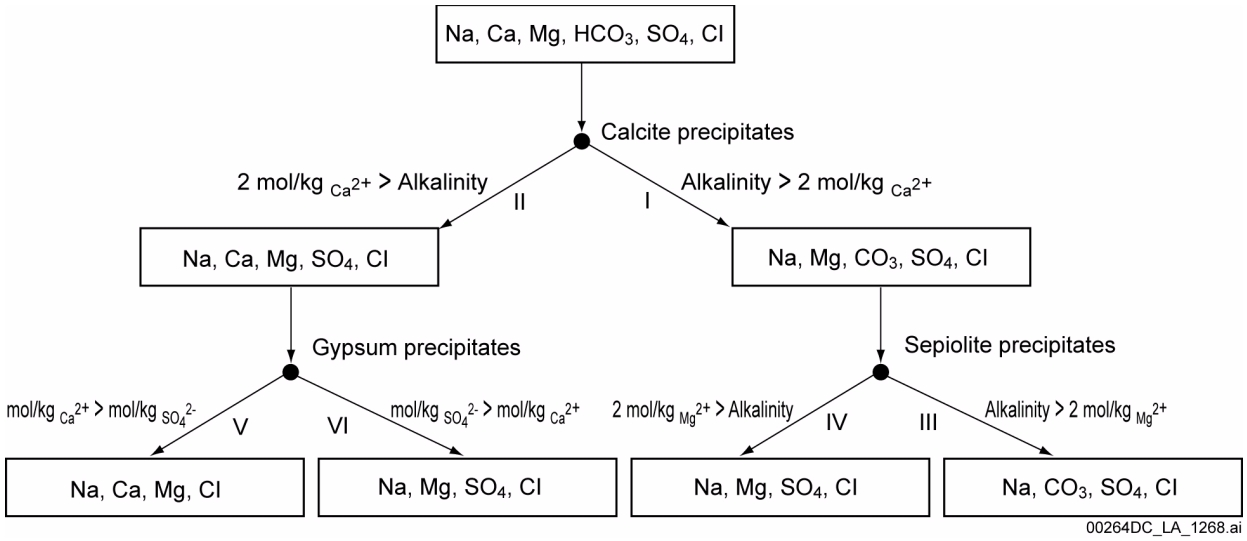

Figure 2.3.5-49. Simplified Chemical Divide Diagram Based on Evaporative Concentration of Dilute Starting Waters to Form a Suite of Naturally Occurring Lake Waters

NOTE: Drever identifies dolomite or another magnesium-bearing carbonate as a possible alternative to sepiolite in this diagram. This figure does not explicitly include NO_3, because it is not generally a significant component in natural surface waters. However, its behavior would be similar to that of chlorine.

Source: Drever 1997a, p. 331; SNL 2007b, Figure 6.3-15.

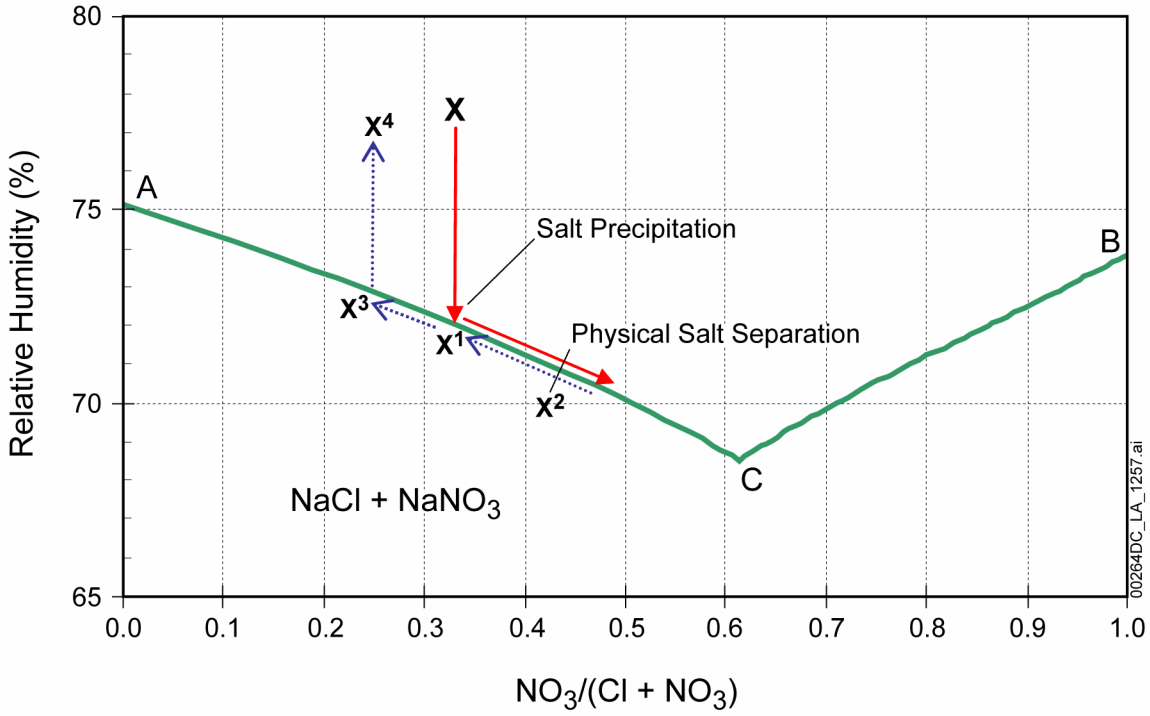

Figure 2.3.5-50. Schematic Representation of the Conceptual Process of Salt Precipitation and Separation

Source: SNL 2007b, Figure 6.15-3.

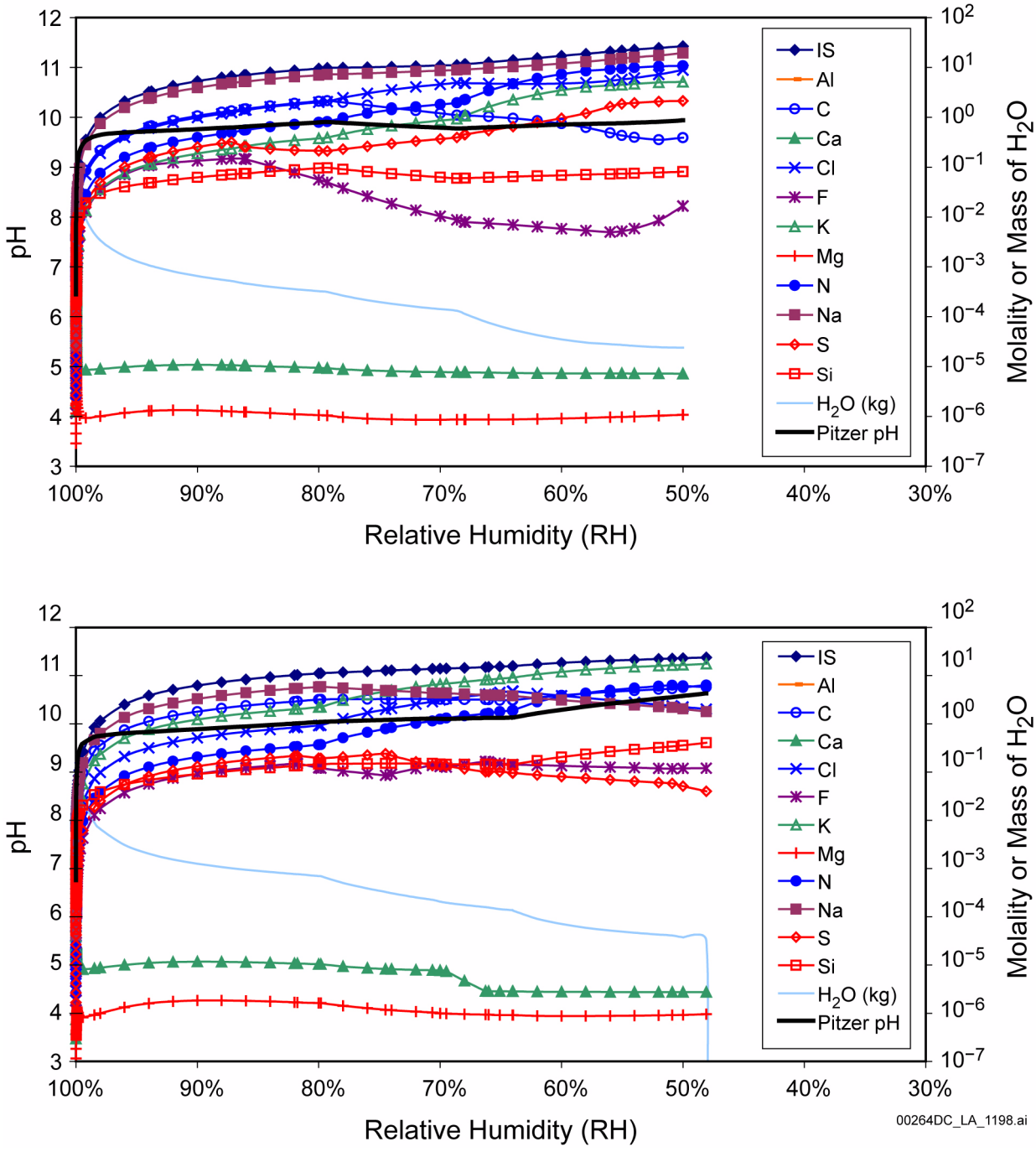

Figure 2.3.5-51. Predicted Compositional Evolution of Group 1 Water at 70°C, No Water–Rock Interaction and pCO_2 10^{-3} bar (upper); Predicted Compositional Evolution of Group 1 Water at 70°C, High Water–Rock Interaction and pCO_2 10^{-3} bar (lower)

NOTE: IS = ionic strength.

Source: SNL 2007b, Figure 6.9-1.

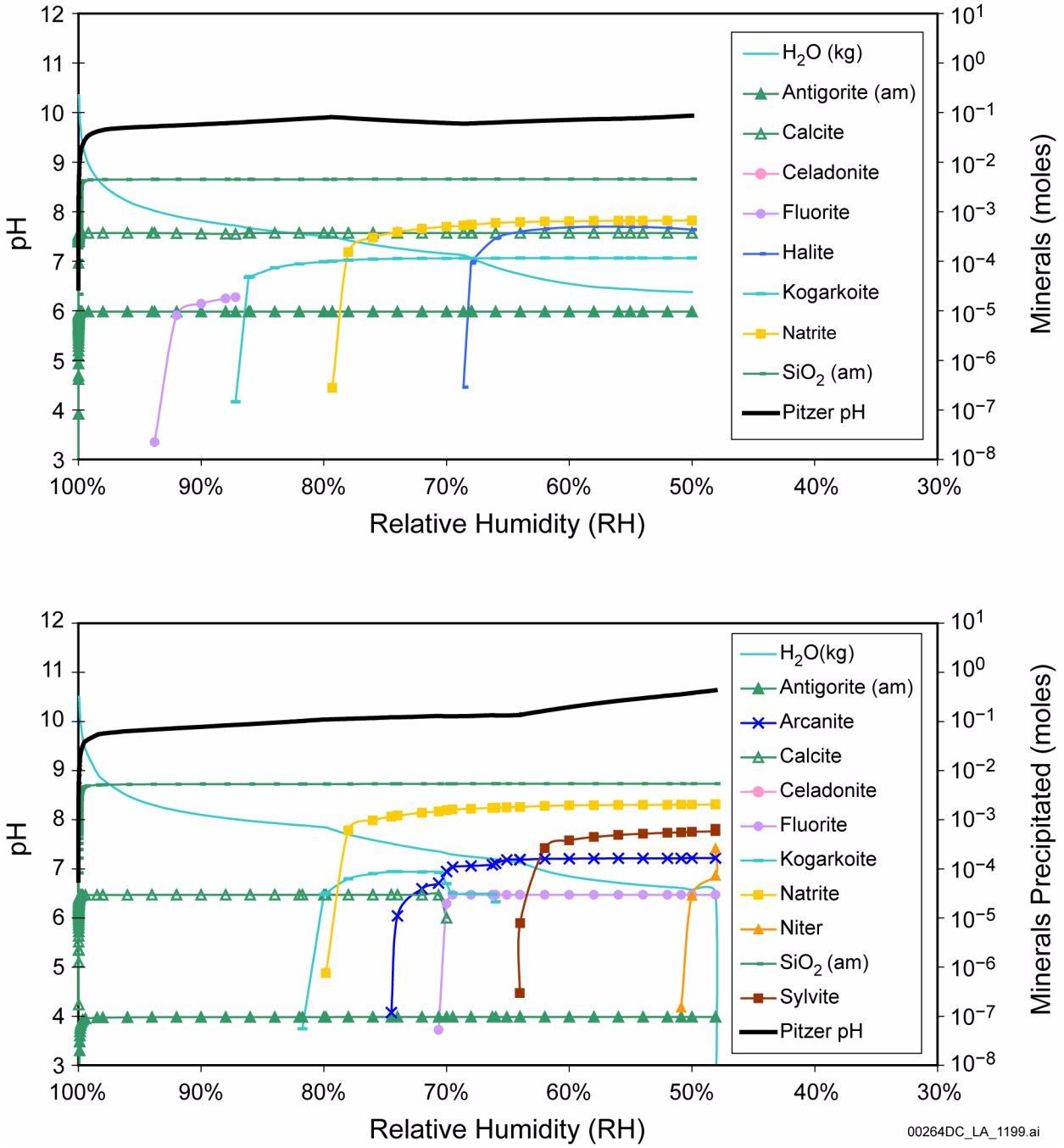

Figure 2.3.5-52. Predicted Mineral Precipitation as Group 1 Waters Evaporate at 70°C, No Water–Rock Interaction and pCO_2 10^{-3} bar (upper); Mineral Precipitation as Group 1 Waters Dilute/Evaporate at 70°C, High Water–Rock Interaction and pCO_2 10^{-3} bar (lower)

Source: SNL 2007b, Figure 6.9-3.

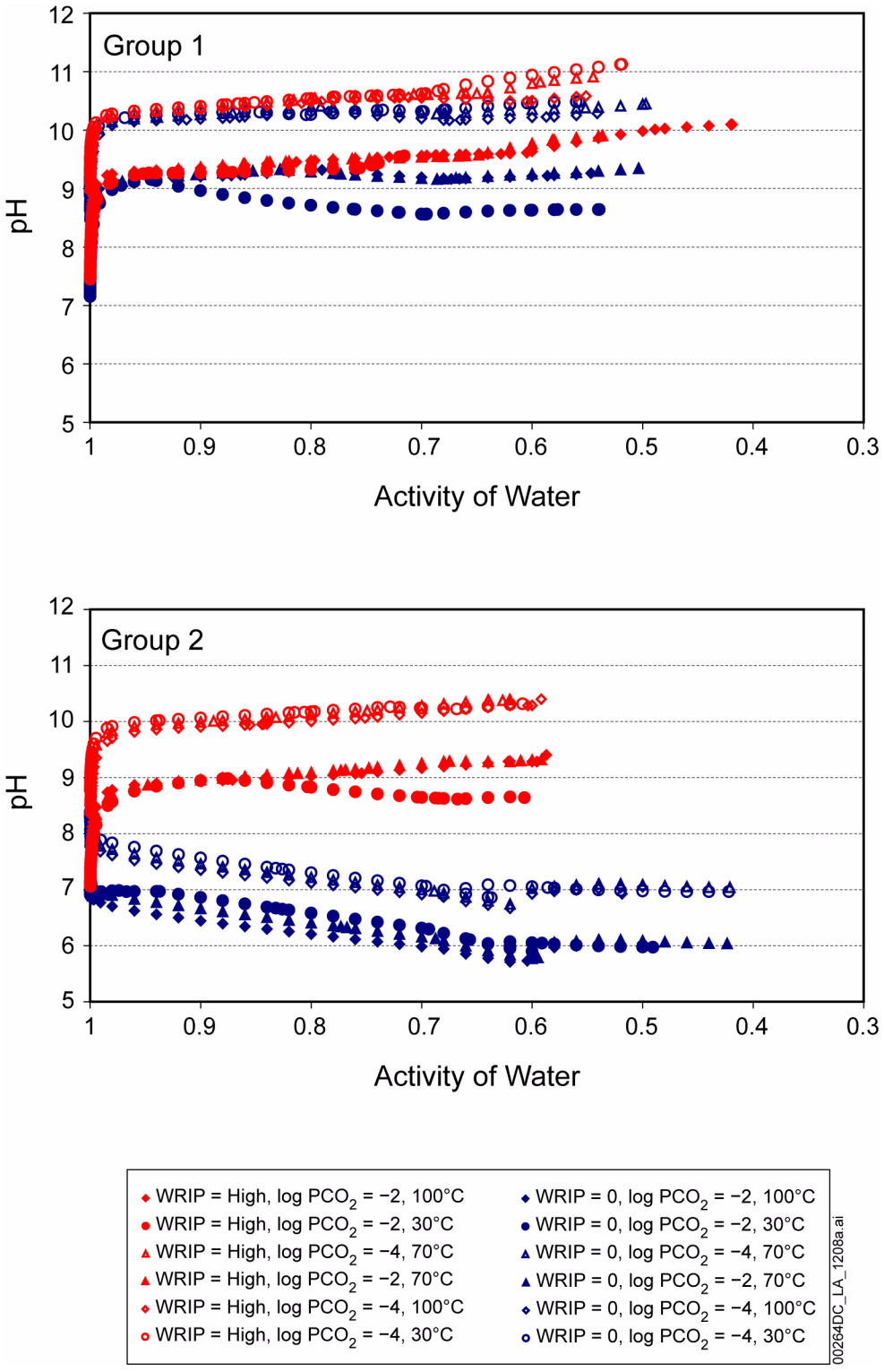

Figure 2.3.5-53. pH Range for Group 1 (upper) and Group 2 (lower) Waters, for No Water–Rock Interaction and High Water–Rock Interaction at pCO_2 10^{-2} to 10^{-4} bar and at T = 30°C, 70°C, and 100°C

Source: SNL 2007b, Figure 6.13-5 and Figure 6.13-6.

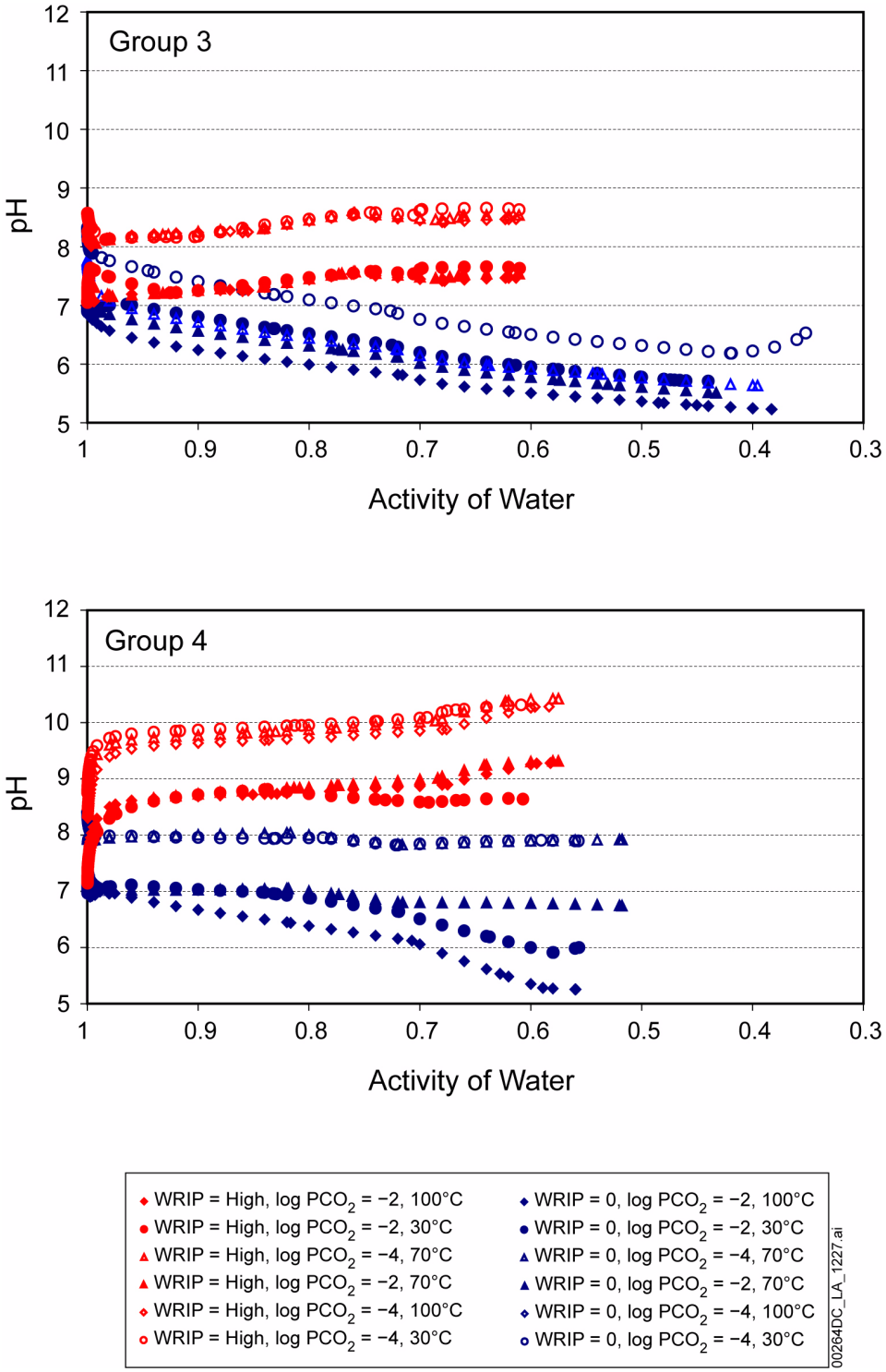

Figure 2.3.5-54. pH Range for Group 3 (upper) and Group 4 (lower) Waters, for No Water–Rock Interaction and High Water–Rock Interaction at pCO_2 10^{-2} to 10^{-4} bar and at T = 30°C, 70°C, and 100°C

NOTE: WRIP = water–rock interaction parameter.

Source: SNL 2007b, Figure 6.13-7 and Figure 6.13-8.

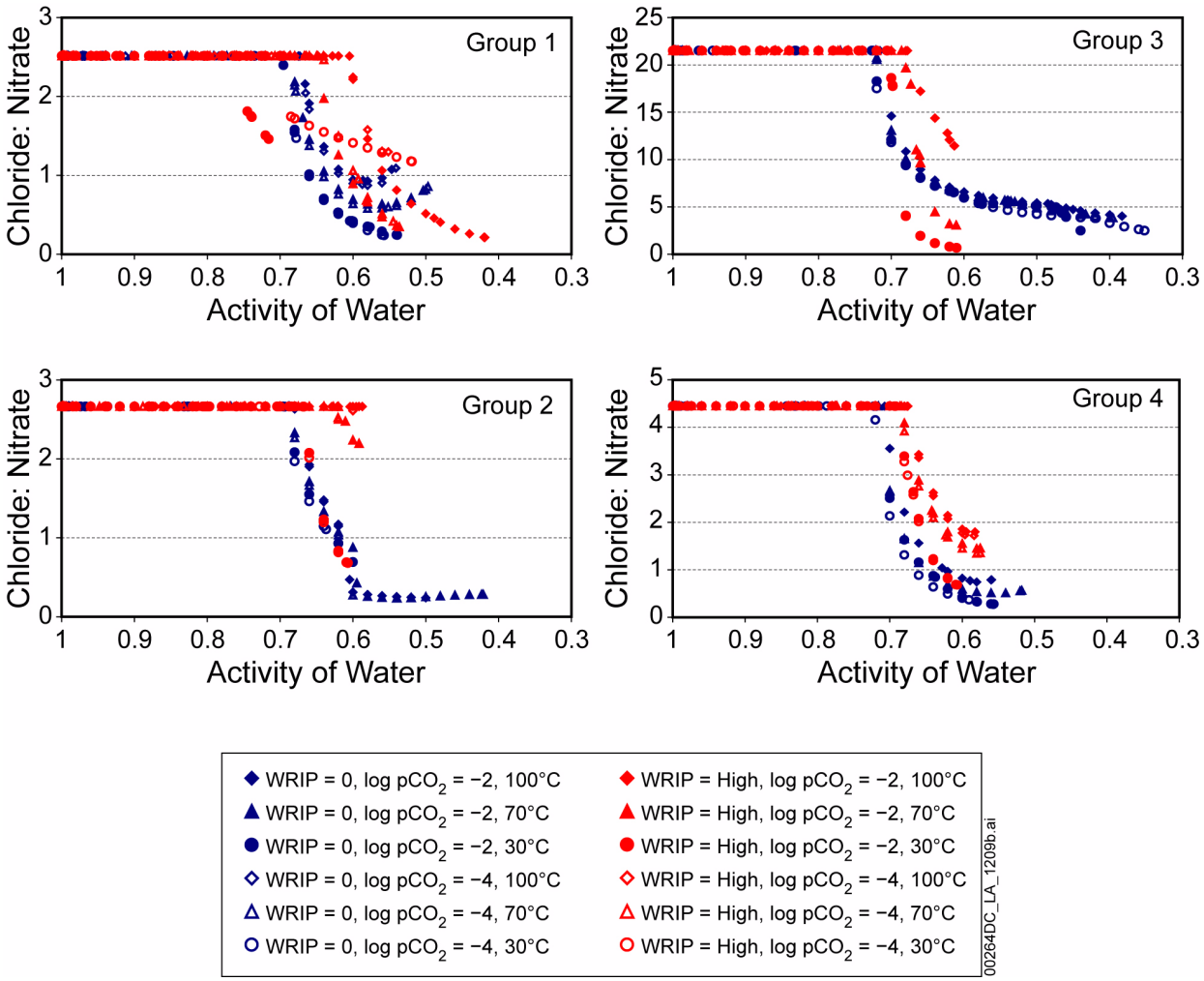

Figure 2.3.5-55. Range of Cl^-/NO_3^- Ratio Versus Relative Humidity for the Evaporation Lookup Tables Representing Groups 1 to 4

NOTE: Evaporation of the waters is shown at two different degrees of water–rock interaction (none and high), and each possible combination of three temperatures (40°C, 70°C, and 100°C) and two pCO_2 values (10^{-2}, and 10^{-4} bars). The pO_2 is fixed at the atmospheric level. These graphs are intended to show that Cl^-/NO_3^- ratios do not change as waters evaporate, until saturation with respect to chloride or nitrate salts is reached. Chloride salts are always predicted to precipitate first, or very shortly after nitrate precipitation. In all cases, the Cl^-/NO_3^- ratio drops rapidly with further evaporation. Note that the initial Cl^-/NO_3^- ratios shown in these pots are for the representative waters for each group; the actual range of values used, at activities of water (relative humidity values) above that of salt separation, is determined by sampling a discrete distribution of Cl^-/NO_3^- ratios for each group. At activities of water below salt separation, the Cl^-/NO_3^- ratios are taken directly from seepage evaporation lookup tables and correspond to the values shown here (plus uncertainty). WRIP = water–rock interaction parameter.

Source: SNL 2007b, Figure 6.13-9 to 6.13-12.

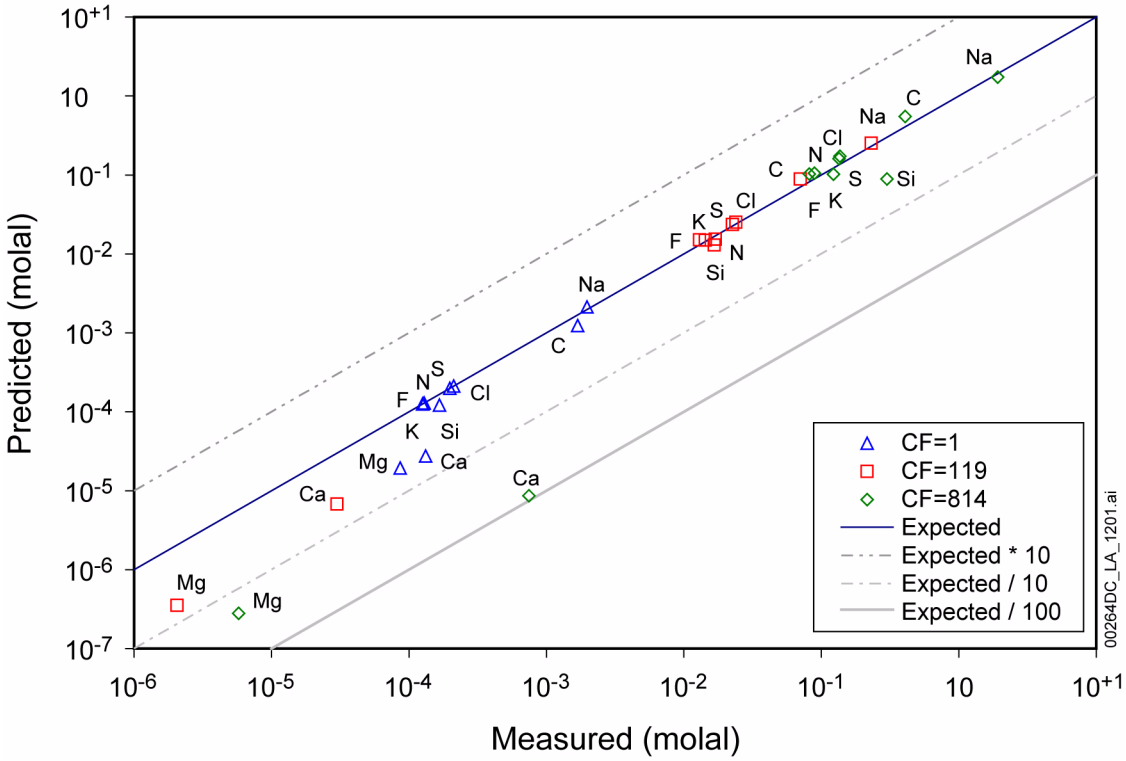

Figure 2.3.5-56. Predicted Versus Measured Concentrations for Synthetic J-13 Water Evaporation Experiment

NOTE: CF = concentration factor.

Source: SNL 2007k, Figure 7-68.

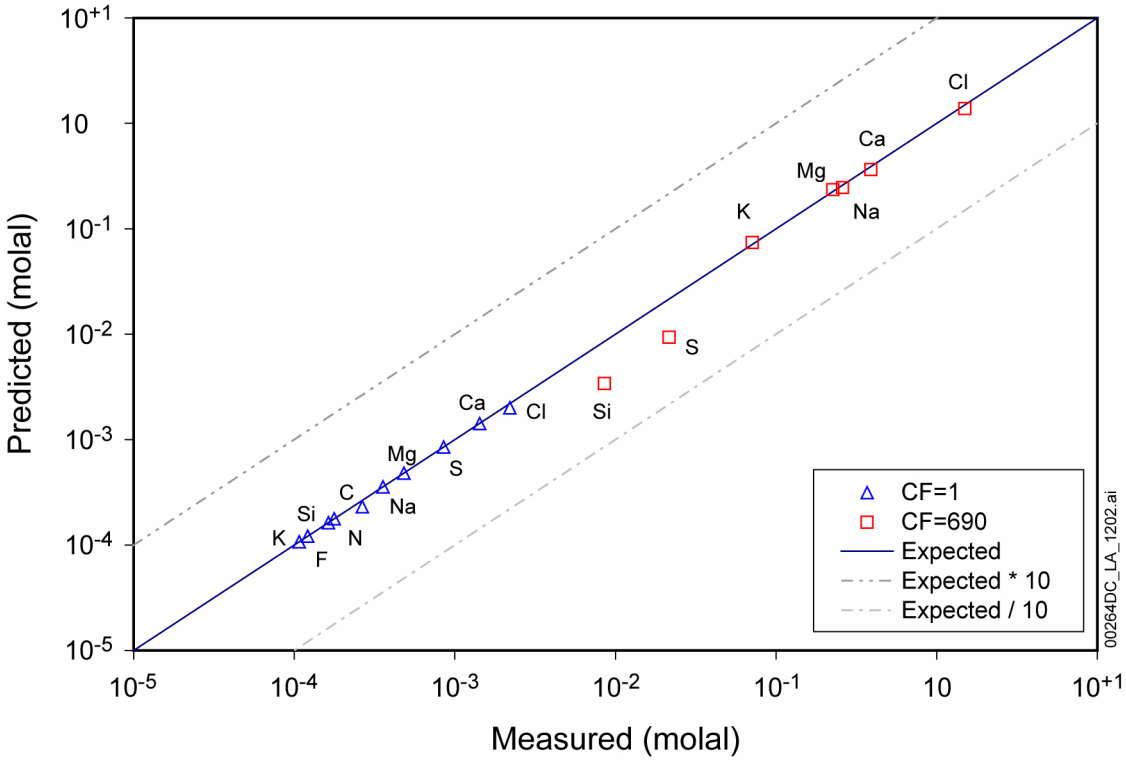

Figure 2.3.5-57. Predicted Versus Measured Concentrations for Synthetic Topopah Spring Tuff Pore-Water Evaporation Experiment

Source: SNL 2007k, Figure 7-75.

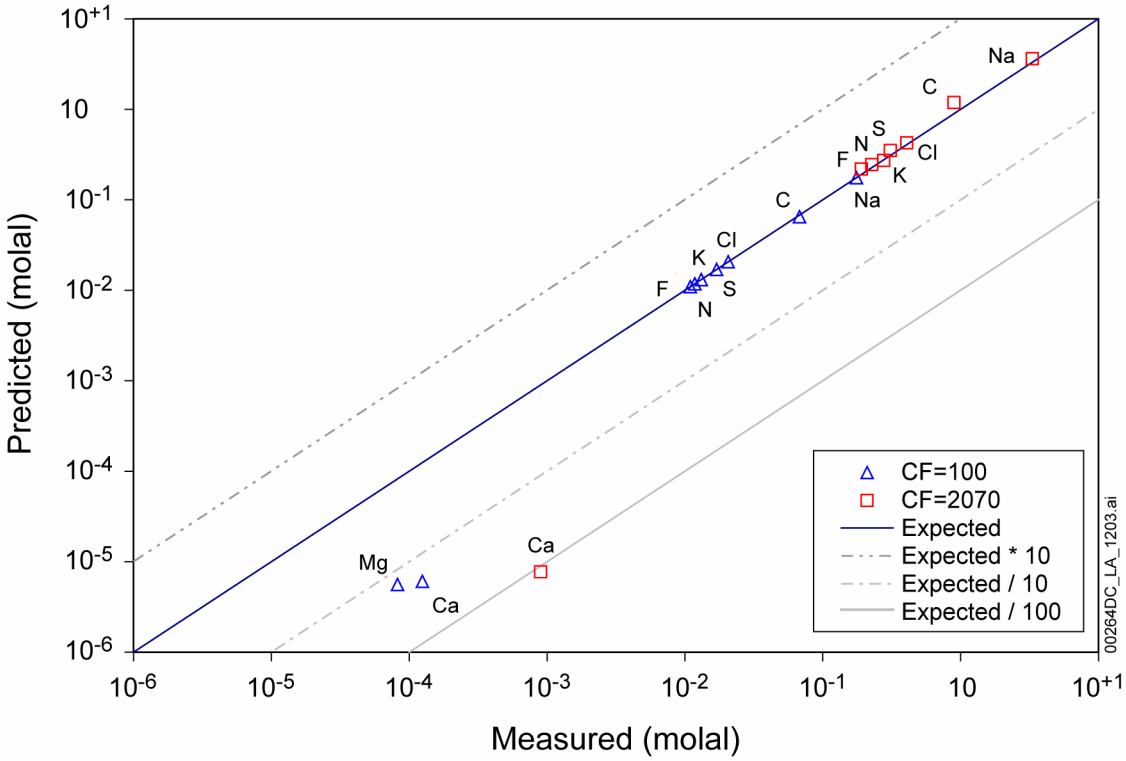

Figure 2.3.5-58. Predicted Versus Measured Concentrations for 100x Synthetic J-13 Water Evaporation Experiment

Source: SNL 2007k, Figure 7-72.

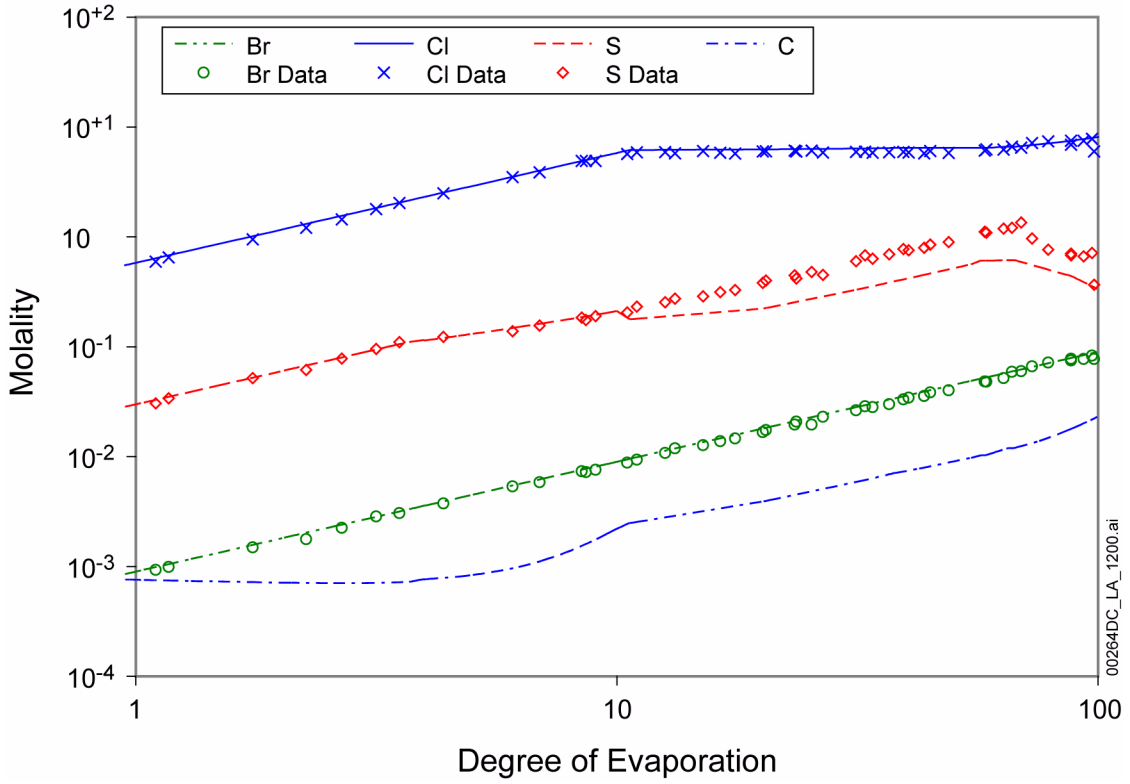

Figure 2.3.5-59. Modeled Concentrations of Br^-, Cl^-, CO_3^{2-} and SO_4^{2-} and Measured Concentrations of Br^-, Cl^-, and SO_4^{2-} from Evaporation of Inagua Seawater

NOTE: Data for CO_3^{2-} were not measured.

Source: SNL 2007k, Figure 7-94.

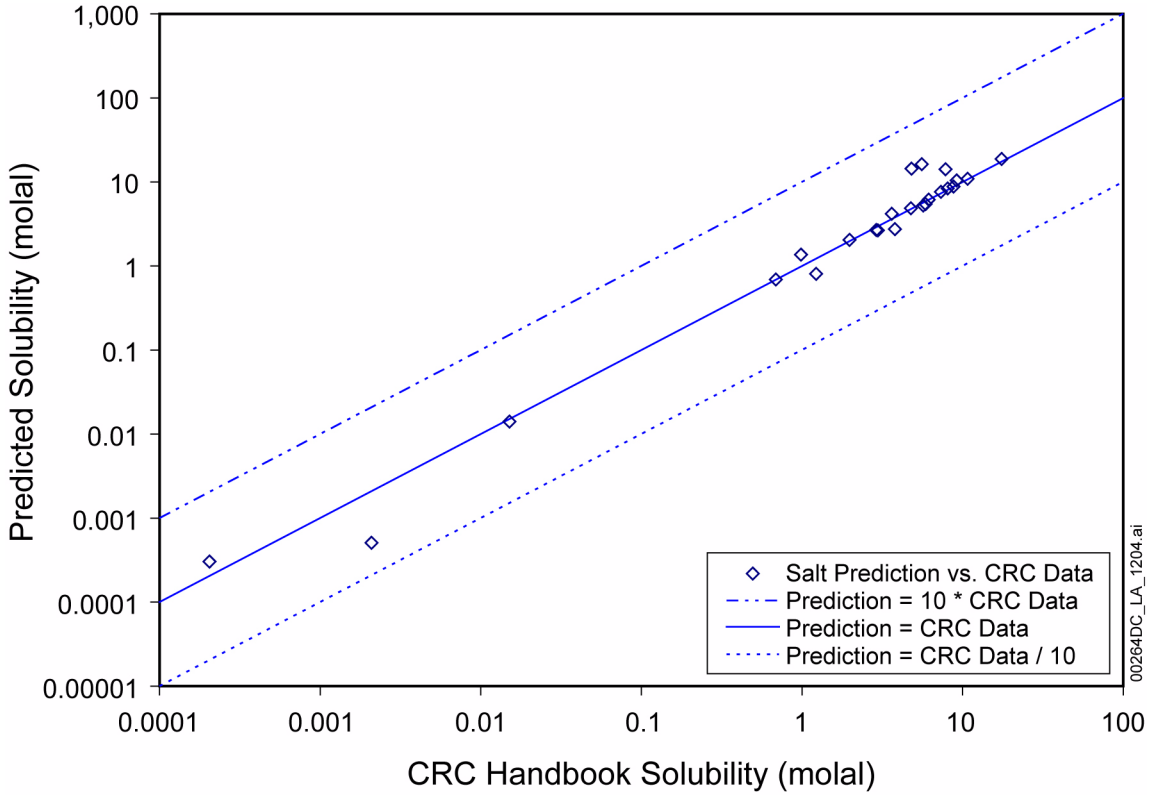

Figure 2.3.5-60. Predicted Versus Chemistry Handbook Mineral Solubilities at 25°C

Source: SNL 2007k, Figure 7-1.

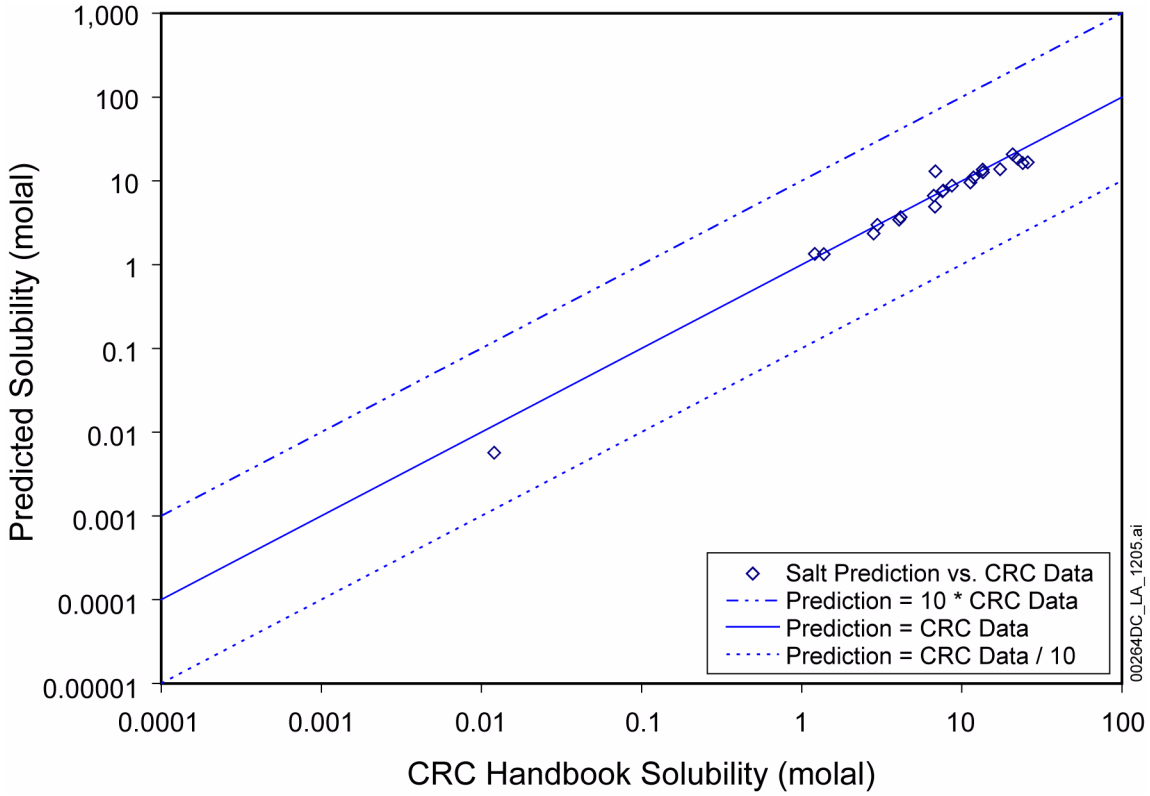

Figure 2.3.5-61. Predicted Versus Chemistry Handbook Mineral Solubilities at 100°C

Source: SNL 2007k, Figure 7-2.

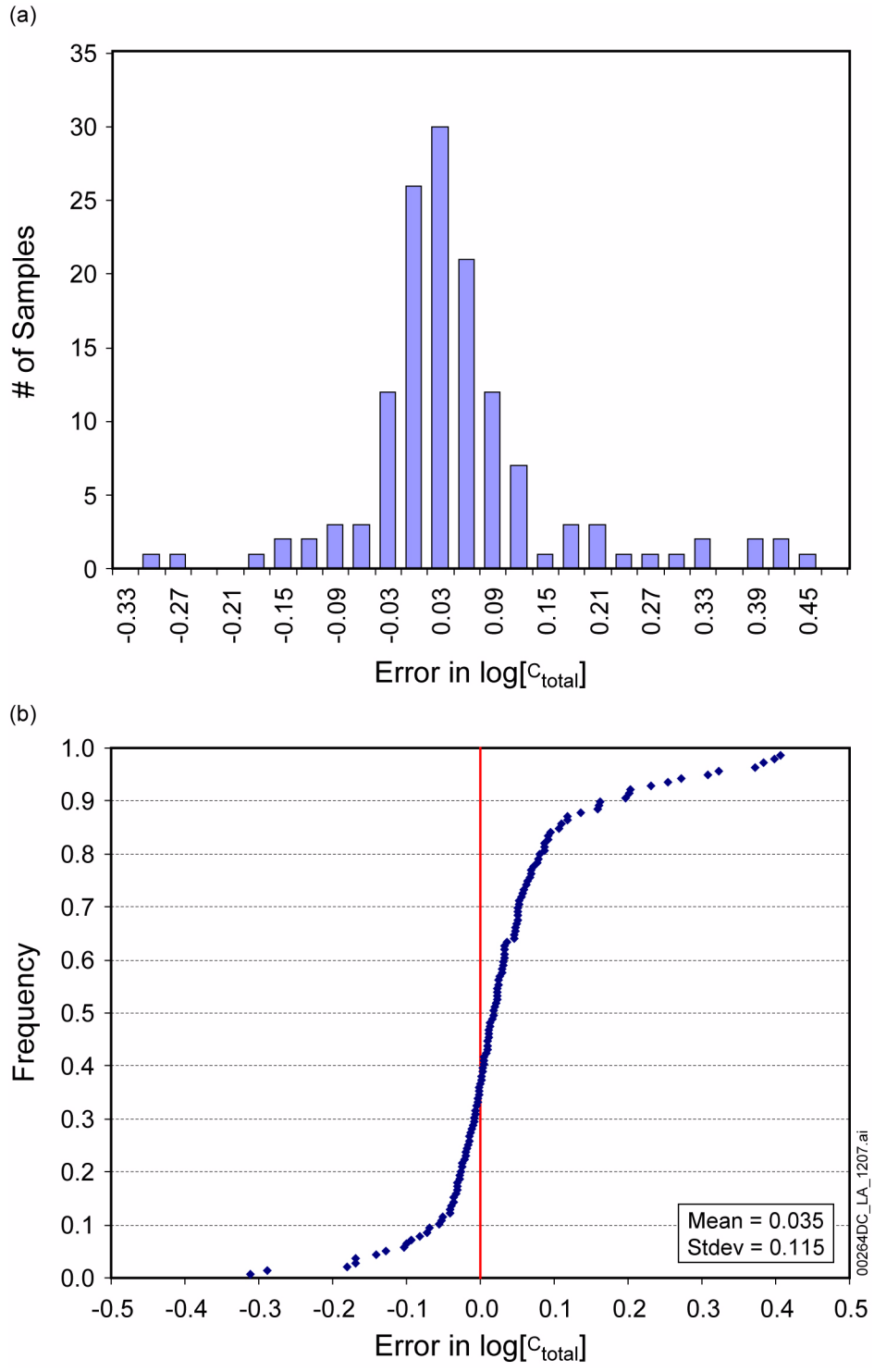

Figure 2.3.5-62. Histogram (a) and Cumulative Distribution Function (b) of Error in $[C]_{total}$

NOTE: The error values form a distribution with a very narrow, high-probability peak, but with scattered higher and lower values. It is slightly offset toward positive values.

Source: SNL 2007b, Figure 6.12-6.

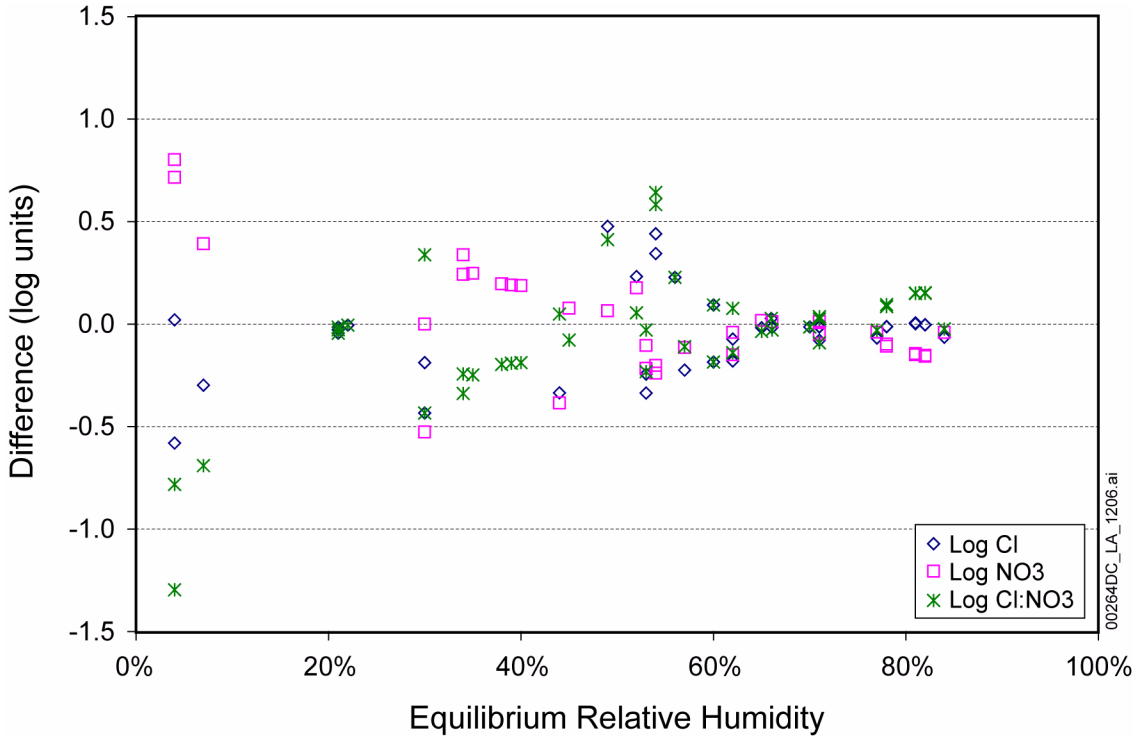

Figure 2.3.5-63. Differences between Measurements and Model Predictions for Ternary Systems and Leg 4 of the Pore-Water Evaporation Experiment at 95°C

Source: SNL 2007k, Figure 7-101.

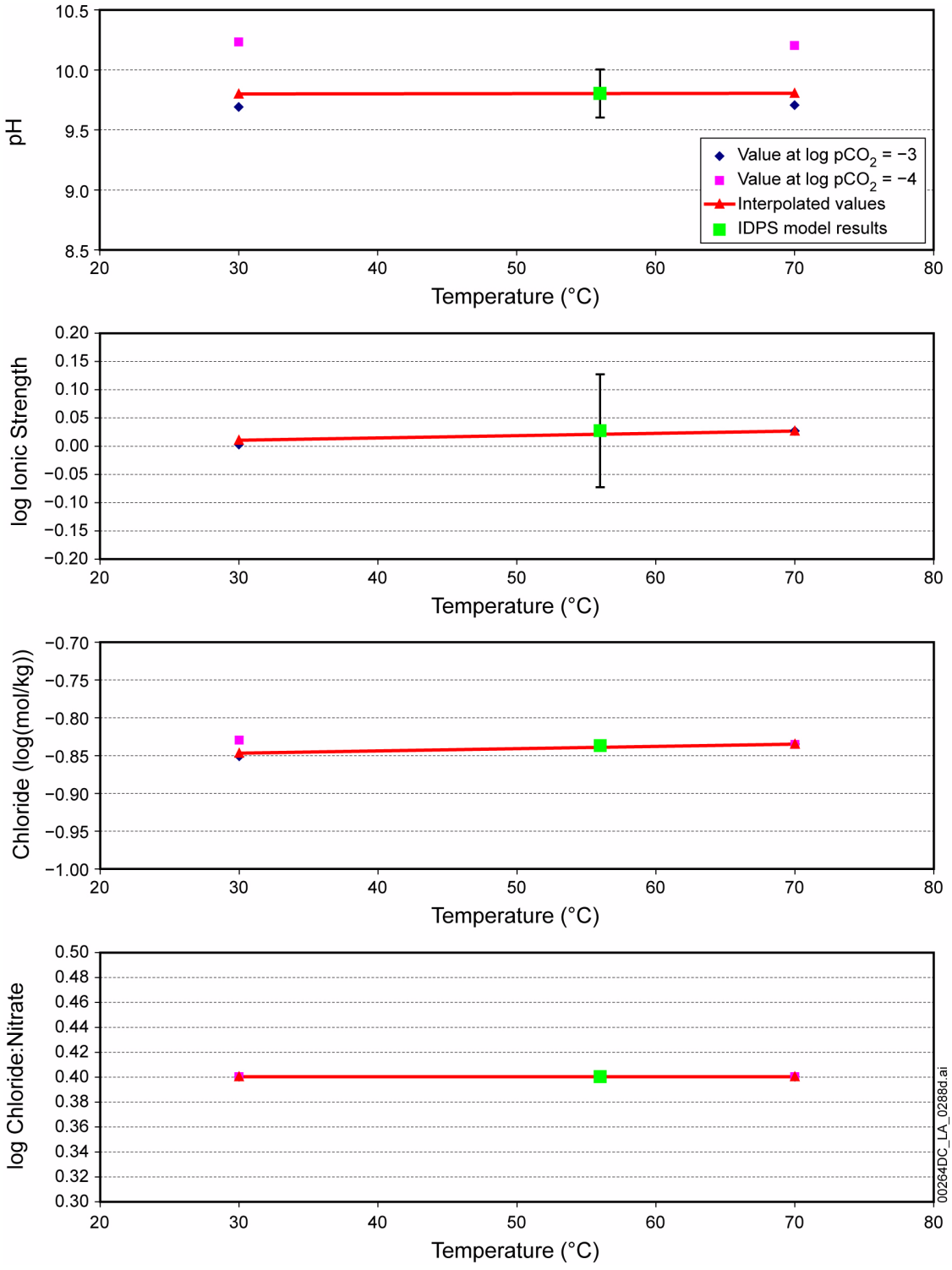

Figure 2.3.5-64. Comparison of In-Drift Precipitates/Salts Model Results with Interpolated Results from Seepage Evaporation Abstraction for 56°C, pCO_2 of $10^{-3.2}$ bar, and 98% Relative Humidity

NOTE: IDPS model = in-drift precipitates/salts model.

Source: SNL 2007b, Figure 7.2-1.